

# Towards NMR imaging of ink penetration in paper

**Citation for published version (APA):**

Nicasy, R. J. K. (2024). *Towards NMR imaging of ink penetration in paper*. [Phd Thesis 1 (Research TU/e / Graduation TU/e), Applied Physics and Science Education]. Eindhoven University of Technology.

**Document status and date:**

Published: 26/06/2024

**Document Version:**

Publisher's PDF, also known as Version of Record (includes final page, issue and volume numbers)

**Please check the document version of this publication:**

- A submitted manuscript is the version of the article upon submission and before peer-review. There can be important differences between the submitted version and the official published version of record. People interested in the research are advised to contact the author for the final version of the publication, or visit the DOI to the publisher's website.
- The final author version and the galley proof are versions of the publication after peer review.
- The final published version features the final layout of the paper including the volume, issue and page numbers.

[Link to publication](#)

**General rights**

Copyright and moral rights for the publications made accessible in the public portal are retained by the authors and/or other copyright owners and it is a condition of accessing publications that users recognise and abide by the legal requirements associated with these rights.

- Users may download and print one copy of any publication from the public portal for the purpose of private study or research.
- You may not further distribute the material or use it for any profit-making activity or commercial gain
- You may freely distribute the URL identifying the publication in the public portal.

If the publication is distributed under the terms of Article 25fa of the Dutch Copyright Act, indicated by the "Taverne" license above, please follow below link for the End User Agreement:

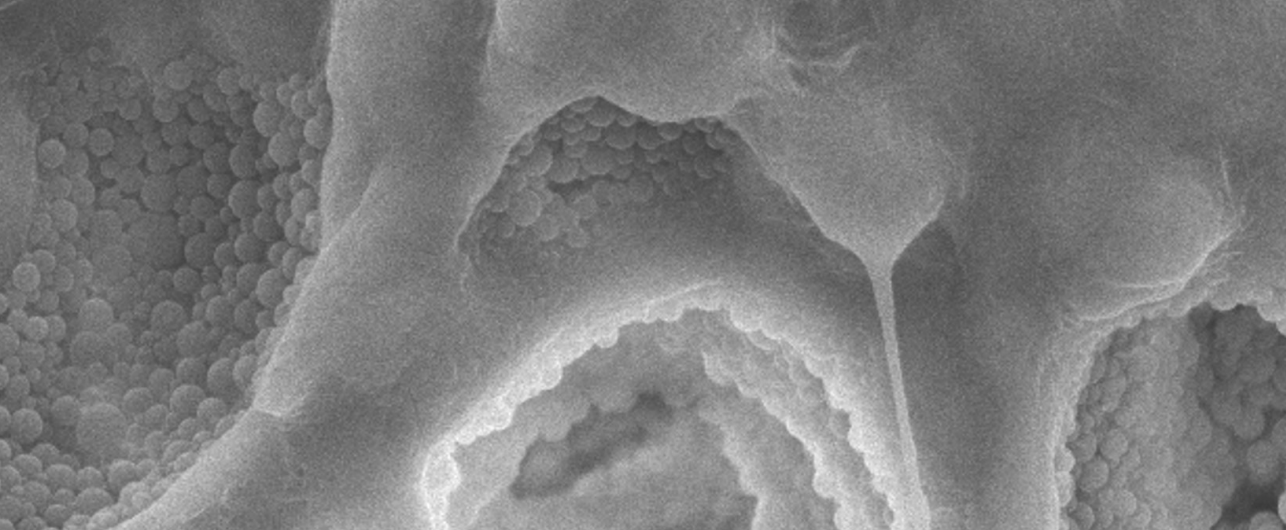
[www.tue.nl/taverne](http://www.tue.nl/taverne)

**Take down policy**

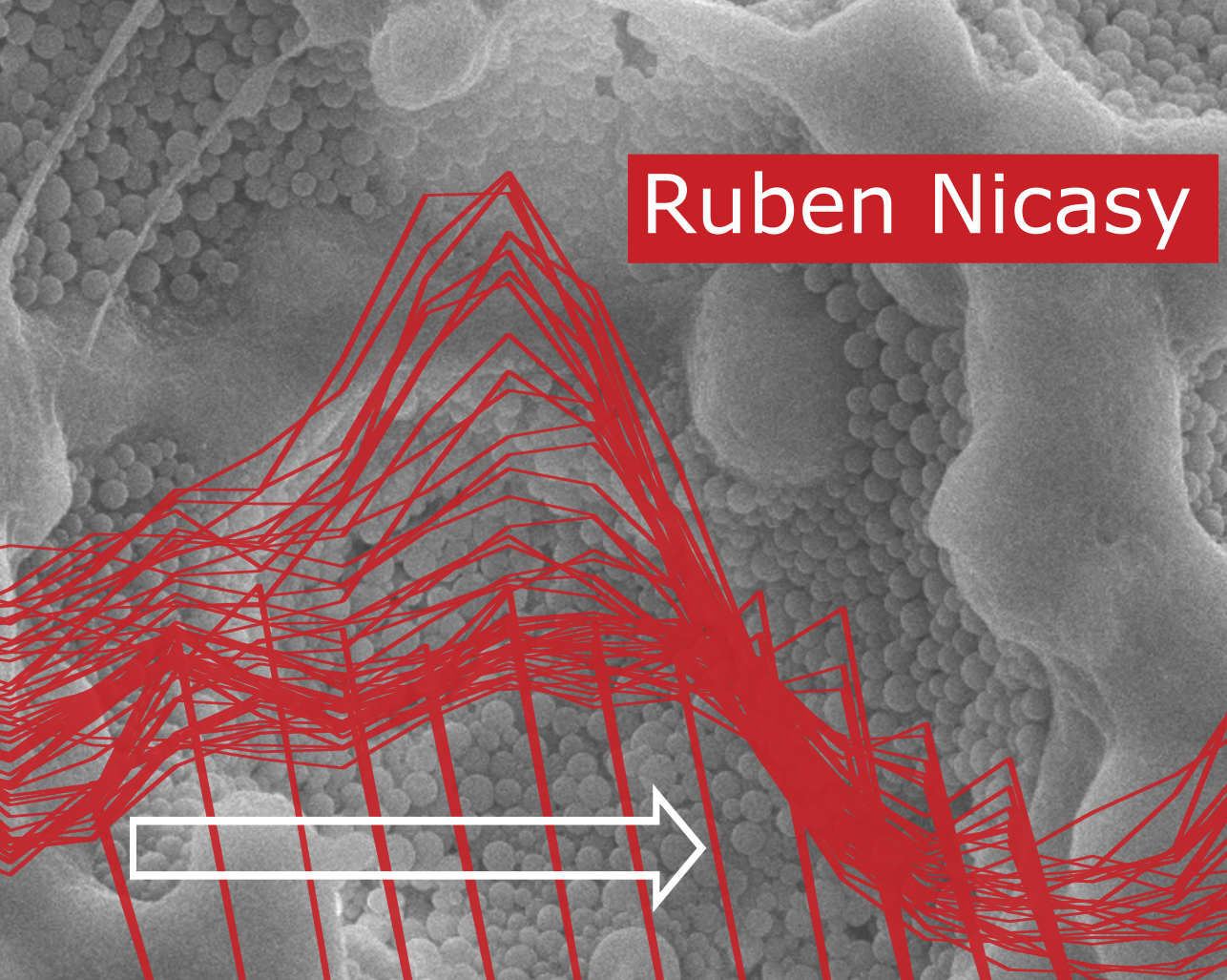
If you believe that this document breaches copyright please contact us at:

[openaccess@tue.nl](mailto:openaccess@tue.nl)

providing details and we will investigate your claim.



# Towards NMR imaging of ink penetration in paper



Ruben Nicasy



# **Towards NMR imaging of ink penetration in paper**

PROEFSCHRIFT

ter verkrijging van de graad van doctor aan de Technische Universiteit Eindhoven, op  
gezag van de rector magnificus prof.dr. S. K. Lenearts, voor een commissie  
aangewezen door het College voor Promoties, in het openbaar te verdedigen op  
woensdag 26 juni 2024 om 11:00 uur

door

**Ruben Jo K Nicasy**

geboren te Bonheiden, België

Dit proefschrift is goedgekeurd door de promotoren en de samenstelling van de promotiecommissie is als volgt:

voorzitter: prof. dr. K. Storm

1<sup>e</sup> promotor: prof. dr. ir. O.C.G. Adan

2<sup>e</sup> promotor: prof. dr. D.W. Bousfield (The University of Maine)

Copromotor: dr. ir. H.P. Huinink

leden: prof. Dr. A.P.M. Kentgens (Radboud Universiteit Nijmegen)

prof. dr. A.A. Darhuber

dr. J.-C. Perrin (University of Lorraine)

prof. dr. dipl.-ing. U. Hirn (Graz University of Technology)

*Het onderzoek of ontwerp dat in dit proefschrift wordt beschreven is uitgevoerd in overeenstemming met de TU/e Gedragscode Wetenschapsbeoefening.*



ISBN:[978-94-6469-995-1]

A catalogue record is available from the Eindhoven University of Technology Library

Cover design by Ruben Nicasy, photo from Hamid Mansouri

Printed By: [www.proefschriftmaken.nl](http://www.proefschriftmaken.nl)

The research described in this thesis was carried out in the group Transport in Permeable Media at the Eindhoven University of Technology, Department of Applied Physics.

This publication is part of the project PQP (Print Quality and Particles) (Project No. 17099) of the research collaboration program High Tech Systemen en Materialen (HTSM) 2018 TTW, which was (partly) financed by the Dutch Research Council (NWO). Additional funding is provided by Covestro and Canon Production Printing

---

# Contents

---

<b>1. Introduction .....</b>	<b>1</b>
1.1 Topic of this thesis .....	1
1.2 Motivation for paper and ink research .....	1
1.3 Studying ink penetration .....	3
1.3.1. Models and simulations .....	3
1.3.2. Experimental methods .....	3
1.3.3. Scientific questions in ink penetration .....	4
1.3.4. NMR as a promising experimental technique .....	5
1.4 Objectives and outline of the thesis .....	6
<b>2. History of paper and printing .....</b>	<b>9</b>
2.1 Paper .....	9
2.1.1. Paper arrives in Europe .....	10
2.1.2. Modern paper production .....	11
2.1.3. The invention of the paper-making machine .....	12
2.1.4. The introduction of commercial cardboard .....	12
2.1.5. An industrialized and sustainable process .....	13
2.2 Ink and printing .....	14
2.2.1. Start of modern printing .....	14
2.2.2. Types of printing .....	14
<b>3. NMR imaging of reaction and transport in thin layers .....</b>	<b>19</b>
3.1 Introduction .....	19
3.2 Basic NMR principles .....	21
3.2.1. NMR relaxation .....	24
3.2.2. Pulse Sequences .....	28
3.3 High-Resolution spatial Encoding .....	29
3.3.1. Resolution and field of view .....	30
3.4 High-gradient NMR setups .....	32
3.4.1. STRAFI (STRAY Field Imaging) .....	32
3.4.2. GARField (Gradient At Right Angles to Field) .....	34
3.4.3. MOUSE (Mobile Universal Surface Explorer) .....	35
3.4.4. Guideline .....	35
3.5 Applications .....	36
3.5.1. Structure and Structural Evolution .....	36
3.5.2. Film Formation Drying .....	40
3.5.3. Film Formation Curing .....	42
3.5.4. Film Formation Coalescence .....	43
3.5.5. Diffusion and Penetration .....	46
3.5.6. Thins Films on Site: Cultural Heritage .....	48
3.6 Conclusions .....	49
<b>4. Ultra-Fast Imaging (UFI) NMR method: liquid uptake .....</b>	<b>51</b>
4.1 Introduction .....	51
4.2 Liquid Absorption in thin, porous media .....	52
4.2.1. Liquid front as a function of time for a sharp front .....	52



4.2.2. Darcy's Law, From 3D to 1D .....	55
4.3 Materials and Methods .....	55
4.3.1. Membrane samples .....	55
4.3.2. Liquid solutions.....	56
4.3.3. Automatic scanning absorptometer .....	57
4.4 Ultra-Fast Imaging (UFI) method .....	58
4.4.1. Echo summation .....	58
4.4.2. $T_1$ shortening.....	59
4.4.3. UFI Signal characterization and calibration .....	60
4.4.4. Selecting the right contrast agent .....	62
4.4.5. Experimental procedure .....	62
4.4.6. NMR coil profile correction.....	63
4.5 Applying UFI for liquid uptake.....	64
4.5.1. The relation between signal and contrast agent .....	64
4.5.2. Signal calibration in porous media .....	66
4.5.3. Measuring liquid penetration with UFI .....	67
4.5.4. ASA Experiments .....	70
4.6 Conclusions.....	70
<b>5. Imaging iron oxide nanoparticles during capillary suction .....</b>	<b>73</b>
5.1 Introduction .....	73
5.2 Materials and methods .....	74
5.2.1. Styrene- $\text{Fe}_3\text{O}_4$ -hybrid particles.....	74
5.2.2. Liquid solutions.....	75
5.3 Theoretical particles signal calibration .....	76
5.4 Typical NMR signal profiles for different cases.....	77
5.4.1. A pure liquid without particles (A) .....	78
5.4.2. Homogeneous movement of liquid and particles (B) .....	79
5.4.3. The particle front lags behind the liquid front (C) .....	79
5.4.4. Particle cannot enter the porous media (D) .....	79
5.5 Experimental details.....	79
5.6 Characterization of iron-oxide latex particles .....	81
5.7 Characterization of liquid solutions .....	82
5.8 NMR characteristics of latex particles.....	83
5.8.1. Effect of $\text{Fe}_3\text{O}_4$ -content on the relaxation behavior .....	83
5.8.2. Effect of particle concentration on the relaxation behavior.....	84
5.8.3. Calibration curves .....	85
5.9 Measuring particle concentration profiles during imbibition .....	86
5.10 Conclusions.....	90
5.11 Appendix A: NMR decay curves as a function of $\text{Fe}_3\text{O}_4$ content.....	91
5.12 Appendix B: Decay curves as a function of particle concentration .....	92
<b>6. Effect of particle concentration on capillary uptake.....</b>	<b>95</b>
6.1 Introduction .....	95
6.2 Capillary uptake in function of particle concentration (UFI-signal profiles) ..	97
6.3 Influence of particle concentration on particle penetration depth .....	99
6.4 Influence of particle concentration on liquid imbibition speed.....	104
6.5 Conclusions.....	106

<b>7. Penetration, swelling and air displacement in cellulose sheets. ....</b>	<b>109</b>
7.1 Introduction .....	109
7.2 Materials & methods.....	110
7.2.1. Substrate.....	110
7.2.2. Liquid uptake experiments .....	111
7.3 NMR signal: the various hydrogen pools in wet paper .....	113
7.4 Water uptake in cellulose fiber networks: a three-phase process.....	115
7.4.1. Phase I : liquid penetration .....	118
7.4.2. Phase II: swelling .....	118
7.4.3. Phase III: trapped air release leads to further moisture increase ...	120
7.5 Discussion.....	122
7.6 Conclusions.....	123
7.7 Appendix A: $T_1$ and $T_2$ relaxation times in paper during phase III .....	124
<b>8. Liquid penetration in hydrophobized and calendered paper sheets. ....</b>	<b>127</b>
8.1 Introduction .....	127
8.2 Materials.....	129
8.2.1. Substrates .....	129
8.3 Effect of calendering.....	130
8.4 Liquid penetration .....	131
8.5 Swelling.....	132
8.6 Moisture content.....	134
8.7 Liquid front vs swelling .....	134
8.8 Effect of hydrophobization.....	135
8.9 Moisture content.....	136
8.10 Swelling vs moisture content.....	138
8.11 Highly hydrophobized papers.....	139
8.12 Conclusions.....	142
<b>9. Particle dynamics in hydrophilic uncoated paper sheets .....</b>	<b>145</b>
9.1 Introduction .....	145
9.2 Materials and methods .....	146
9.3 UFI signal profiles during capillary uptake .....	146
9.4 Influence of particles on liquid dynamics and swelling.....	147
9.5 Particle penetration depth .....	148
9.5.1. Signal profiles.....	149
9.5.2. Particle concentration inside the paper sheet .....	150
9.6 conclusions .....	151
<b>10. Conclusions .....</b>	<b>153</b>
<b>11. Outlook.....</b>	<b>157</b>
11.1 Determining particle concentrations during penetration and swelling .....	157
11.2 Finding the relation between delay time and paper hydrophobization.....	157
11.3 The effect of increasing substrate complexity .....	159
11.3.1. Effect of particles on liquid transport in hydrophobized paper .....	159
11.3.2. Effect of hydrophobicity on particle transport.....	161
11.3.3. The influence of a coating layer on liquid penetration .....	162
11.3.4. The effect of a primer on ink penetration .....	163
11.4 The effect of particle properties on ink penetration.....	164

---

11.4.1. Clarifying the influence of multi-sized particles on ink penetration .	164
11.4.2. The effect of glass transition temperature on ink penetration.....	164
11.4.3. The effect of surface charge on ink penetration.....	165

<b>References .....</b>	<b>167</b>
-------------------------	------------

<b>Summary.....</b>	<b>181</b>
---------------------	------------

<b>Samenvatting .....</b>	<b>183</b>
---------------------------	------------

<b>Acknowledgements / Dankwoord .....</b>	<b>187</b>
---	------------

<b>List of publications .....</b>	<b>189</b>
-----------------------------------	------------

<b>Curriculum Vitae .....</b>	<b>191</b>
-------------------------------	------------

# 1

## Introduction

---

### 1.1 Topic of this thesis

Equation Section (Next) This thesis deals with the complex processes involved in printing: liquid penetration, particle penetration and deformations. The interaction of ink with paper is of great importance as it determines the quality of the final print and other properties such as durability and gloss. Present day investigative methods to characterize the penetration of components during printing all have limitations that severely limit the amount of information that can be gathered about the printing process experimentally. The aim of this study is to develop a novel NMR-based method for studying the printing process, with a primary goal of advancing our understanding of the complex processes involved in printing.

In recent decades, printing has evolved into a common practice found in every facet of our lives, such as sanitary, which makes up 10% of our daily usage, printing and writing equals 24%, and packaging, which accounts for 54%. Besides our daily life, the paper industry plays an important role in multiple industries, including the food and pharmaceutical industries, where it is often used as a filter or packaging media. Other rising applications of the print and paper industry are lab-on-chip devices, used for detection of, for example, pregnancy or COVID, and the usage of inkjet printing in applications such as thin-film transistors, light-emitting diodes, sensors or even solar cells [1]. Even in construction, pulp and paper has been introduced as a renewable material in the form of laminates [2]–[4], gypsum boards [5] or even thermal insulation [6].

The quality of print products is determined by factors such as paper structure, ink compositions, and physical processes like fluid penetration, particle penetration, and structural deformations. The complexity of these processes and paper media drive a constant development within the printing industry. This thesis aligns with this trend to consistently improve the print quality, lower production cost, and increase stability of pulp and paper products.

### 1.2 Motivation for paper and ink research

Research on ink-paper interactions remains important as our society shifts to digital printing and expands the use of printing to enable new technology. Furthermore, significant changes are required to meet the Net Zero Emission (NZE) by 2050, a strategy formally adopted by the European Union to limit global warming to 1.5 degrees

Celsius. All changes in the industry should guarantee print quality, which requires innovation and research.

Contrary to the belief that digitalization decreases the demand for paper and print products, the industry is, in fact, expanding. While there is a decline in printing, writing grades, and newspapers, other sectors such as sanitary or packaging are compensating for these losses. Figure 1.1 shows how the global paper and paperboard production increased between 1992 and 2018. The overall market is expected to continue its growth and reach an annual production of 490 million metric tons at the end of 2023.

According to the International Energy Agency (IEA), the pulp and paper sector was responsible for just under 2% of all emissions from industry in 2022, and not on track to meet the NZE. To meet climate goals, the production process requires some major changes to reduce CO<sub>2</sub> emission. This can be achieved by introducing renewable energy sources such as biomass and improving efficiency.

Other ways to reduce environmental impact of paper products include incorporating recycled fibers and minimizing the use of harmful chemicals such as colorants, inks, bleaching agents, and hydrophobization (sizing) agents. Research offers critical support to the aim of decreasing ink usage. Further, research focuses on replacing these substances with environmentally friendly alternatives, such as transitioning to water-based inks. However, water-based inks have quality issues compared to solvent based inks. This calls for more research into water-based inks. Furthermore, efforts should also aim to decrease ink usage. Finally, introducing recycled fibers in support of the transition towards a circular economy helps combat deforestation. However, recycled fibers have inferior papermaking properties and therefore multiple studies are devoted to the use of recycled fibers and their effect on product quality [7]–[9].

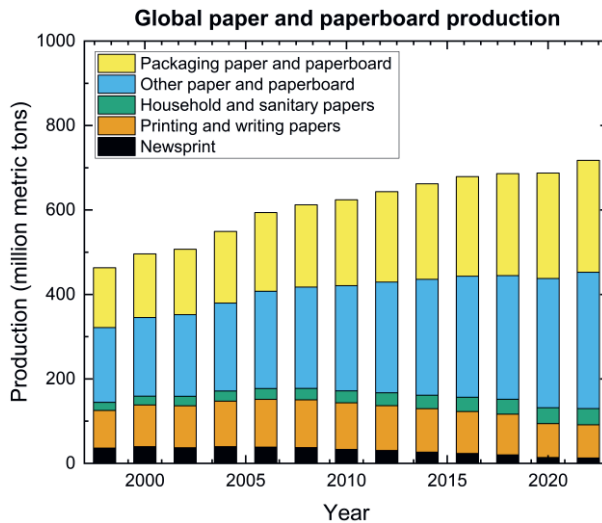


Figure 1.1 Global paper and paperboard market from 1998 to 2022, in million metric tons. FAO. Forestry Production and Trade. License: CC BY-NC-SA 3.0 IGO. Extracted from: (<https://www.fao.org/faostat/en/#data/FO>. Data of Access: 26-02-2024)

In addition to research designed to improve the climate impact of paper and printing products, new research opportunities arise due to the ban of non-biodegradable materials, such as plastics. Paper has numerous limitations compared to plastic in many applications. To compete with the existing plastic counterparts, the design of new characteristics such as water repellency, anti-counterfeiting or anti-microbial properties is required. Additionally, these novel technologies may be realized by extending inkjet printing beyond common graphic printing to use as a technique to deposit and make patterns of functional materials onto a substrate [1], [10], [11].

It is clear that the paper industry faces significant challenges, including changing and reducing energy consumption, changing raw materials, and the rise of new applications. These adaptations threaten to reduce quality and performance. Research on ink penetration is essential to investigate the effects of these changes on pulp, paper and print products.

### **1.3 Studying ink penetration**

The study of ink penetration in complex porous media such as paper is a challenging task. The studies are mostly focused on liquid transport, particle transport and swelling/deformation of the paper medium. These processes can be studied either by models or simulations or by experimental measurement techniques. Although existing methods have their own merits, measurements on paper applications, e.g. paper sheets, are exceptionally challenging for several reasons. Firstly, paper is non-transparent foreclosing light-based techniques. Secondly, liquid uptake in paper sheets occurs on timescales below 1 s. Thirdly, the thickness of a paper sheet is around 100  $\mu\text{m}$ . Taken together, these difficulties prescribe sub-second temporal resolution and spatial resolution below 100  $\mu\text{m}$  in a measurement environment applicable to non-transparent media.

#### **1.3.1. Models and simulations**

The first way to study ink penetration is through theoretical models and simulations that try to mimic particle transport [12], [13], liquid transport [14] or swelling/deformation [15], [16]. However, simulating these processes in complex media such as paper is challenging for several reasons. First, the relative contributions of processes such as transport through fibers, along fibers, transport within the pore space and swelling are dependent upon the specific ink and paper type used and are mostly unknown. Second theoretical models to accurately describe the varying transport and deformation processes are mostly missing or incomplete. Therefore, experimental verification is required to validate, improve, and extend the existing models.

#### **1.3.2. Experimental methods**

The second way to study ink penetration utilizes experimental techniques. Three general approaches to ink penetration studies are reflected in the literature: liquid absorption, particle retention studies and microscopic techniques.

A first group of experimental techniques that can measure liquid transport with a sub second temporal resolution are Ultrasonic Liquid Penetration (ULP) [17], [18], Drop Absorption (DA) [17], [19], the Bristow Wheel [20], [21], weight measurements [22]

or Automatic Scanning Absorptometer (ASA) [23], [24]. In the commonly used Bristow Wheel test, paper samples are mounted on top of a rotating wheel while the test liquid is poured into a liquid container. During the test, the wheel starts to rotate, and the liquid container comes in contact with the paper sample. Liquid is allowed to escape through an opening at the bottom of the container, which leaves behind a liquid strip onto the sample. By changing the rotation speed and recording the volume change in the liquid container, the total amount of transferred liquid per surface area over a specific time can be calculated, which gives data about the total transferred volume.

While these techniques meet the temporal resolution and are able to measure within non-transparent media, they provide no spatial information. Therefore, only effects on the total liquid absorption speed can be investigated. There have been efforts to interpret this information into characteristics of the fluid redistribution inside paper: i.e. the location of the absorption front or the liquid distribution. However, assumptions about the fluid movement have to be made beforehand, which makes precludes translation of global information to local information very difficult. In a complex system such as paper, interpretation of the data becomes particularly difficult due to effects like hydrophobicity, swelling and film flow.

A second group of experiments to study particle transport are retention studies [25]–[27]. In a retention study, a particle suspension is injected and pushed through a porous media. Data is gathered by analyzing the residue with a breakthrough curve, which represents the particle concentration as a function of the input liquid volume. These studies allow to determine the in-situ deposition rate of the particles within a non-transparent porous media, but are unable to give spatial resolved information.

A third group of experimental techniques to investigate with sufficient spatial resolution are microscopic techniques such as optical microscopy [28], [29], confocal laser scanning microscopy (CLSM) [30][31], [32], Scanning Electron Microscopy (SEM) [33], Focus Ion Beam (FIB) [34] and Cryo-SEM [35]. However, these techniques are unable to measure in-situ, measure within non-transparent media and have issues measuring cross sectional information. Cross sections can only be measured post-mortem by cutting the paper, which introduces undesired artefacts within the measurements.

### 1.3.3. Scientific questions in ink penetration

Due to the absence of an effective technique for in-situ measurements within non-transparent media with sufficient temporal and spatial resolution, a complete picture about ink transport is still lacking, leading to multiple unsolved questions.

First, it is still unclear if liquid penetration in thin, porous media can still be described by well-known models such as Darcy [14], [23], [36] or Washburn [36]–[39], both describing the flow of liquids in a porous media. While these models hold for larger penetration depths [40], the use of these equations in thin, porous media is still not validated and may fail to adequately account for swelling, inertial effects, film flow, and vapor transport.

In addition to liquid transport, particle transport in thin membranes can also benefit from spatially and temporal resolved in-situ measurements. However, imaging particles at such high temporal and spatial resolutions has not yet been realized. Current

literature reports effects of flow rate [41], [42], porosity [43] and particle size, but a deep understanding is lacking. Therefore, it remains unclear if penetration of liquid with added particles still follows laws such as Darcy or Washburn.

Moreover, the mechanisms that affect liquid penetration are not well understood at these timescales. At larger scales, such as columns, particles alter the permeability of porous media, which significantly influences liquid penetration. It remains an open question whether this is still the case for droplet penetration on short timescales.

Additionally, the formation of a filter cake during ink penetration [44], a phenomenon in which particles (pigment or latex) are trapped at the surface of the paper, resulting in reduced permeability and particle clogging, remains inadequately understood. In-situ measurements of particle clogging can illuminate the effects of filter cake formation and its exact location.

Transport in paper, a complex system consisting of a network of wood pulp fibers [45], is mostly described by models such as Lucas-Washburn [36]–[39] or Darcy's Law [14], [23], [36]. Despite their potential, deviations are commonly observed due to the complexity of the paper sheet [37], [46] and processes such as water transport through internal pores within the fibers (lumen) [38], [47], vapor transport, evaporation, inertia effects [48], [49], a precursor front [50] and swelling [51]. Efforts have been made to extend the existing models and incorporate processes such as swelling [52] or liquid uptake by fibers [51]. Due to the short timescale and small sizescale of the liquid penetration, it is difficult to quantitatively capture and analyze these different processes and their effects in real time. Identifying the crucial processes and determining their significance for various paper types remains a daunting task.

To enhance the print quality of cellulosic materials like paper, the material is modified to alter the penetration behavior, strength, and smoothness. Two commonly used processes are calendering, which influences the porous structure by compressing the paper sheet, and sizing, which changes the surface chemistry of the fiber to modify the hydrophobicity. Most research focuses on the penetration of water into materials such as paper [53], cellulosic materials [54] and random fiber network [55], [56]. Research is scarce on effects such as calendering and sizing. Nonetheless, several studies address the effects of sizing and calendering on phenomena such as dot spreading [57], [58], wettability [59], [60], mechanical strength [61], changes in local roughness [62], ink-setting behavior [63] and printability [64]. Although these studies offer information about the effect on parameters such as printability, gloss and water resistance, they provide limited insight into mechanisms of penetration and the importance of processes such as transport along fibers and swelling. These details are key in understanding print quality in these particular media.

#### 1.3.4. NMR as a promising experimental technique

To measure liquid transport, particle transport and swelling within pulp and paper applications such as paper sheets, an improved experimental technique should meet several criteria:



1. The technique should have sufficient temporal ( $< 0.1$  s) and spatial resolutions ( $< 20$   $\mu\text{m}$ ) to measure within thin paper sheets.
2. The technique should be able to measure within non-transparent media.
3. The technique should give information about all three processes (particle transport, liquid transport and swelling) simultaneously. This allows detection of phenomena such as particle-liquid front splitting, effects of swelling on the penetration behavior.

A good candidate to meet all these criteria is nuclear magnetic resonance (NMR) [40], [65]–[67]. Conventional NMR systems are, unfortunately, still unable to meet the high spatial and temporal resolution required to measure the fast liquid and particle transport within thin paper sheets. To gain more spatial resolution, high-gradient NMR setups have shown promising results. Unfortunately, measuring liquid and particles during uptake inside porous layers of about 100  $\mu\text{m}$  (i.e. single paper sheets) demands temporal resolution of several milliseconds as liquid uptake can go faster than 0.1 s [68].

## 1.4 Objectives and outline of the thesis

*The main goal of this thesis is to develop an NMR-based experimental technique that allows the study of ink penetration in paper with a primary goal of advancing our understanding of the complex processes involved in printing. To achieve this, the technique should measure with sufficient temporal ( $< 25$  ms) and spatial resolution ( $< 25$   $\mu\text{m}$ ) and should be able to measure: **1: transport of complex fluids in a thin, porous layer, 2: particle transport, and 3: transport and deformation within paper sheets.***

Such a technique will help to answer the questions raised in section 1.3, and thereby improve knowledge about ink penetration.

The main research questions of this thesis are:

- 1. How does liquid transport in thin, porous media; are models such as Darcy or Washburn still able to describe these processes?**
- 2. How do particles penetrate in paper and how do particles influence the overall uptake of liquid?**
- 3. How does a complex liquid penetrate paper?**

This thesis tries to give an answer to these questions by first developing a proper NMR-based measurement technique, followed by studies on liquid penetration and particle transport in thin well characterized media. Thereafter, transport of liquid and particles in paper, a more challenging media, will be studied. Consequently, this thesis is outlined in four main parts as shown in Figure 1.2.

How NMR can be used to measure liquid transport in thin, porous media with sufficient temporal and spatial resolution is the topic of chapter 3 and chapter 4. In chapter 3, the basic principles behind NMR and different high-spatial resolution NMR-setups are introduced. Thereafter, in chapter 4, the newly developed, Ultra-Fast Imaging NMR (**UFI-NMR**) method is introduced. In this chapter, transport within thin, porous media is investigated and compared to Darcy's Law.

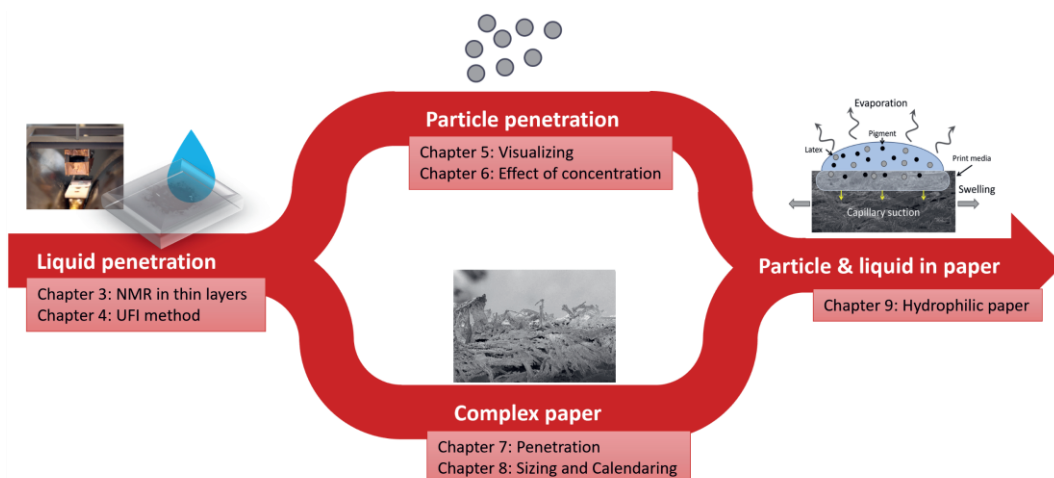


Figure 1.2 Outline of thesis.

The penetration of particle mixtures within thin membranes is studied in chapter 5 and chapter 6. Chapter 5 shows how UFI-NMR is able to image and quantify latex particles tagged with iron oxide, while chapter 6 focuses on the effect of particles on liquid transport and particle penetration depth.

How water penetrates in thin paper sheets is the topic of chapter 7 and chapter 8. Chapter 7 studies the different phases of water penetration and proposes a model for the penetration of water within a hydrophilic paper sheet. How this penetration is changed by post-processing effects, like compression (calendering) or hydrophobization (sizing), is studied in chapter 8.

How particles affect the penetration of complex particle mixtures inside hydrophilic non-coated papers is discussed in chapter 9.

The final results and main conclusions of this thesis are discussed and summarized in chapter 10. Finally, chapter 11 presents an outlook and ideas for further research.



# 2

## History of paper and printing

---

In this chapter, some background about the evolution and current state of the paper and printing industry is given. The aim of this chapter is to provide some more insight into the art of printing and paper making which will help in understanding the research of this thesis. During this chapter, it becomes clear how there is a continuous development within the paper and print industry and how history still defines current processes within the printing industry.

### 2.1 Paper

Equation Section (Next)The history of the paper industry, as we know it today, originates from China and dates back to 105 AD [69]–[71]. At that time, Cai Lun (T'sai Lun) recorded the first paper making process based on single fibers. The first goal of paper was spreading religion and collecting information. Because the production of paper was cheaper and easier compared to its counterparts, such as papyrus and parchment, paper became the main material for writing.

The process introduced by Cai Lun consists of four main steps, which are still part of the paper-making process. Figure 2.1 shows a schematic representation of these four steps. In step 1, see Figure 2.1a, fibers were harvested. The main sources of fiber were bamboo and old synthetics, such as fishing nets or rags. In step 2, the collected fibers were soaked in large wooden or stone vats, see Figure 2.1b. During this process, fibers were separated and transformed into a proper pulp, a process that could take up to three months. To improve fiber separation, the mixture was often pounded, boiled, or both. In step 3, see Figure 2.1c, the pulp was scooped out of the vat and evenly distributed on a mold. This process was carried out by craftsmen as it required a lot of skills to get an evenly distributed layer of pulp. In step 4, see Figure 2.1d, the pulp layer within the mold was dried and compressed to drain out water. Finally, the paper sheet could be peeled off the mold, after which the process could be repeated. The original paper mold used by Cai Lun consisted of a rectangular frame made from wood with an interior that consisted of a woven net through which the water could flow. Because the mold was crucial for the paper making process, the mold was adjusted and optimized many times, including variations like the laid paper mold, Korean molds or Japan molds [70].

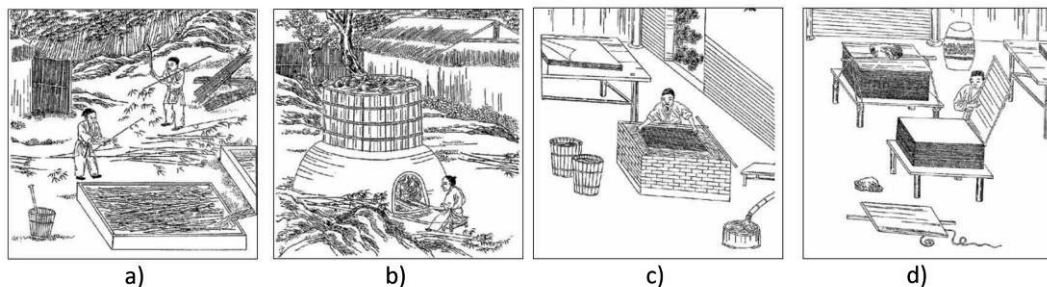


*Figure 2.1 Old Chinese paper making process. A) cutting bamboo, b) soaking the fibers, c) screen dipped in pulp and d) drying and pressing.*  
 (<https://www.printmuseum.org/blog-3/2021-aapi-historymonth-pt1>)

After the introduction of the paper-making process in China around 105 AD, the technology began to spread all over the world. First in Asian countries such as Korea (384 AD) and Japan (610 AD), whereafter it traveled via the Islamic world towards Europe. The road followed by paper technology was similar to the well-known Silk Road, a trade route that went from East Asia to the middle East. During its journey, additions to the paper-making process were made to improve the paper quality. Two crucial additions, still present in modern paper making, include a coating layer for smoothness and shine and paper sizing for water resistance.

### 2.1.1. Paper arrives in Europe

It lasted until the 11<sup>th</sup> century before the paper making process arrived within central Europe. In Europe, the process of pulp and paper was further refined by introducing new molds with metal wires instead of bamboo or horse hairs and introducing a 'deckle'. The deckle was a second screen or fence, which was used to keep the paper within bounds, making it easier to obtain an evenly distributed paper sheet. The biggest improvement was mechanizing the beating process. With large expertise in watermills and abundant waterpower, the water driven stampers were introduced, see Figure 2.2. This powerful beating accelerated the paper making process. In addition to the water driven stampers, European paper makers had to implement a new fiber pretreatment process. Since European paper relied on fibers from old fabrics, such as rags or clothing, which contained bodily fluids, food particles and other non-cellulosic materials that could intervene with the paper quality, the pulp was enzymatic pretreated in a process known as retting. This technique was commonly used between 1300 and 1800 as a cleansing process [72]. The retting process also helped to break down the fibers, which led to a reduction in the beating time. In modern paper making, pretreatment of fibers 'cleaning' is also used to remove unwanted particles and to save energy by reducing pulping time.



Figure 2.2 Picture of wooden stamper. Driven by a watermill. [73]

### 2.1.2. Modern paper production

The real start of modern mechanized paper making occurred around the 16<sup>th</sup>-18<sup>th</sup> century with the invention of multiple machines, like the Hollander beater, the Fourdrinier machine and wood-cut machines. Besides new machines, the pulp and paper industry began to extend beyond traditional paper sheets with the introduction of packaging materials and the invention of cardboard.

The first major innovation came with the Hollander beater around 1680, see Figure 2.3a. The Hollander beater consists of a circular water way with a beater wheel, mostly made from metal plates. The Hollander beater allowed to have more control over the pulp processing by adjusting the roll height of the beater wheel allowing to process fibers with more variance and minimize damage to already separated fibers [74]. While the Hollander beater remains a part of modern paper making, it has evolved to a larger and more industrial scale.

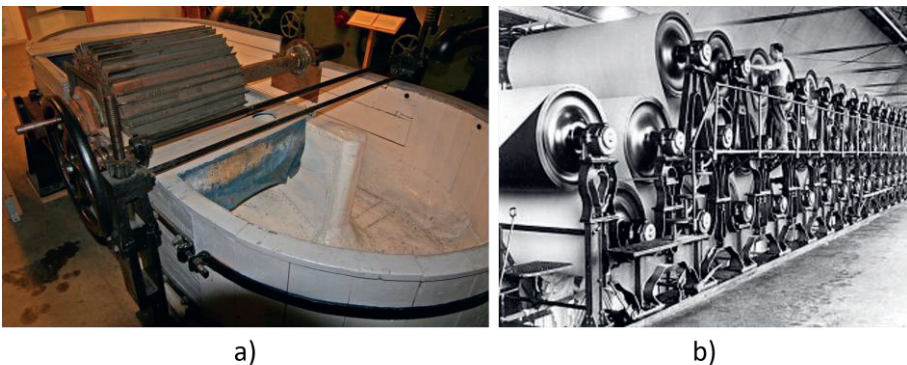


Figure 2.3 Machines used for the pulp and paper industry: a) Hollander beater, invented in 1680 ([https://en.wikipedia.org/wiki/Hollander\\_beater](https://en.wikipedia.org/wiki/Hollander_beater)) and b) the Fourdrinier machine invented in 1806 (<https://www.floridamemory.com/items/show/66958>).

### 2.1.3. The invention of the paper-making machine

The second major innovation came with the invention of the Fourdrinier machine, also called the paper making machine, at the beginning of the 19<sup>th</sup> century, Figure 2.3b. This machine consists of multiple cylindrical rolls, which allow to mass produce paper rolls from pulp. This machine ultimately replaced the old process of sieving the fibers by hand using a mold, see Figure 2.1c. Within the machine, pulp was drained from water by using a combination of drying and compression. The paper machine is still used today in pulp and paper production factories. However, since its invention, the machine has been optimized and scaled-up to meet the daily demand.

### 2.1.4. The introduction of commercial cardboard

Additional to inventions within the paper making process, the use of pulp and paper rose during the 19<sup>th</sup> century due to the invention of the bag making machine in 1852 by Francis Wolle and the first commercial cardboard boxes made from paperboard carton. The first paperboard carton was produced around 1817 by the firm M. Treverton & Son, a so-called non-corrugated box. Somewhat later, around 1840, in France the first corrugated cardboard box was introduced, with the typical zigzag structure.

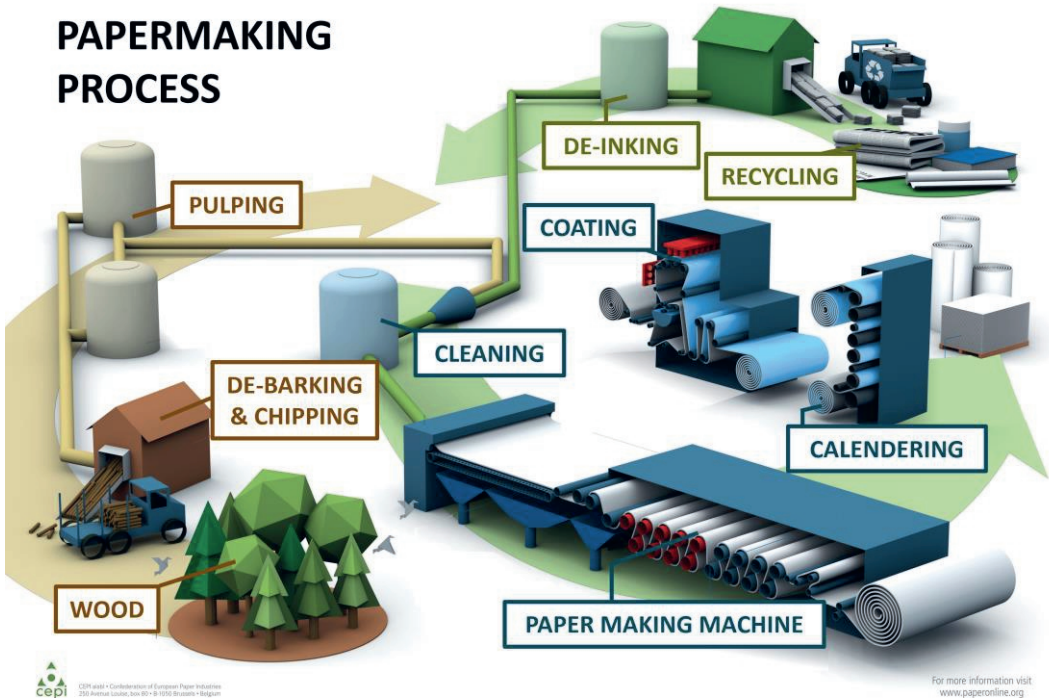


Figure 2.4 Modern paper-making process (<https://www.cepi.org/about-cepi/history-of-pulp-paper/>).

### 2.1.5. An industrialized and sustainable process

Today, paper making is done on a large scale and obtains much of its energy needed from biomass. Figure 2.4 shows a schematic representation of the current paper making process. Most steps and machines involved in the current process are still based upon old principles. The main change in the pulp and paper making process concerns the addition of recycled fibers.

For a long period, almost all fibers came from new materials. However, due to the growing need for more sustainable solutions and stop deforestation, recycling of old fiber sources became more and more important. Currently, recycling of paper is one of the key advantages of paper packaging over its plastic counterparts in terms of sustainability. This results in a huge shift towards paper packaging and a growing need for recycled fibers.

The current pulp and paper making process starts with the collection of wood, which is debarked and chipped, before it can be turned into pulp. By adding water to the fibers pulp is made. Subsequently, this is processed either mechanically or chemically, or a combination of both, to separate the fibers from lignin and other unwanted components. Lignin is an unwanted component as it tidily holds the cellulose fibers together and often causes discoloration of the final paper. The final pulp is cleaned and sometimes bleached with chemicals such as chlorine or peroxide to make the pulp even more white. Another type of pulp can be made from recycled fibers. This process involves similar steps, such as pulping and cleaning, but also contains additional steps, such as collecting recycled fiber sources and de-inking. The finished pulp, either recycled or wood based, is then diluted with water and fillers such as  $\text{CaCO}_3$  may be added. Thereafter, the pulp is poured on top of a conveyor belt via a flow box and goes through the paper making machine. In this machine, the pulp is transferred into a roll of paper by a combination of dewatering, pressing, and drying.

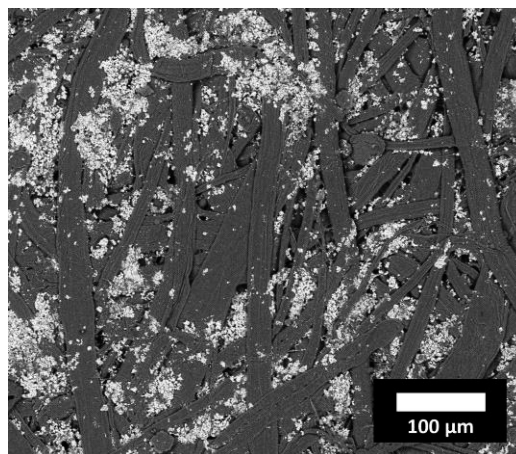


*Figure 2.5 SEM image of an industrially produced uncoated printing paper. The fibers are seen in gray while calcium carbonate fillers are shown in white.*



A detailed description of the paper making process can be found in dedicated textbooks [70], [71]. After the roll of paper is made, the paper can be modified depending on its application. Modifications refer to: applying a coating layer to make the surface of the paper smoother and brighter [75], calendering [76], [77] to make the paper thinner and sizing [78], [79] to make the paper more hydrophobic.

After these steps, a paper sheet consists of multiple components, making paper a complex porous media. For example, a typical paper used in our printers consists of around 70-75 wt% of fibers, 20-25 wt% mineral additives such as  $\text{CaCO}_3$ , 4-5 wt% water and 0-1 wt% of extra components such as sizing components and pigments. Figure 2.5 shows a Scanning Electron Microscopy (SEM) image of the surface of an industrially produced uncoated printing paper. The image shows the fibers in gray and the calcium carbonate fillers in white. The image clearly shows the complexity of the paper sheet with its multiple components and the varying fiber shapes and orientations.

## 2.2 Ink and printing

To create a print, various printing techniques can be used. This chapter gives an overview of various printing methods and will shortly introduce the origins of printing. More information about various printing methods can be found in dedicated textbooks [80].

### 2.2.1. Start of modern printing

Modern printing is commonly attributed to Gutenberg's introduction of the printing press in 1436 [81]. This method involved arranging individual letters into a holder. After correct positioning the letters, ink was applied on the letters and a paper was placed on top. Thereafter, a plate was used to exert pressure on top of the paper to firmly apply the ink. This way of printing is known as letter press printing and belongs to a group of printing technologies that uses an intermediate carrier for image formation. Conventional offset printing also belongs to this category and is mostly used for mass-production, because of the significant cost of the print plates, making it less economical for smaller quantities. From the late 20<sup>th</sup> century, other types of printing arose which were the non-impact printing techniques, such as inkjet or laser jet printing, which do not necessitate an intermediate to transfer the print. These non-impact or digital printing techniques do not require an intermediate and are ideal for smaller quantities.

### 2.2.2. Types of printing

#### *Conventional printing – offset printing (using an intermediate)*

In conventional printing, the ink is transferred indirectly via a printing plate (roller) onto the print media. While the principles behind this technique are very similar, depending on the intermediate print layer, different types of conventional printing techniques exist. The main types are letterpress and gravure printing.

In letterpress printing, the printing elements or letters are raised compared to the base plate. When the printing plate is inked, the ink sticks to the raised parts, which can later be transferred to the substrates. When the print plate is made flexible, the printing process is called flexography. This type of printing is less accurate than letterpress

printing, but due to the flexibility allows to press on very thin flexible media such as plastics which is often used in packaging.

In gravure printing on the other hand, the printing elements are engraved into the surface of the print plate. Prior to printing, the entire plate is inked. Thereafter, ink is removed from the surface with a blade, so that the only ink that remains is situated within the holes of the print plate. Finally, the ink is transferred from the plate to the substrate.

All these conventional printing methods are based upon the principles of rolling cylinders against cylinders. These rolling motions can be extremely fast, which leads to very high productions speeds. However, the main drawback of these techniques is that the image carriers are fixed and are unable to be changed. Therefore, the high productions speeds can only be achieved by reproducing the same image many times.

If small quantities of print are required, the print method should be very adaptable, which requires digital printing.

### *Digital printing*

In digital printing, an image can be printed directly from a digital-based image and does not require using intermediates. This type of printing is mostly used for desktop printing. The cost per page is higher than offset printing methods, but for small quantities, the production of a highly costly print plate can be avoided, which reduces the overall price. There mainly exist two types of digital printing: laser printing and inkjet printing.

In laser printing, a charged cylinder is used. During the printing process, the laser is used to transfer an image onto the cylinder by defining regions with an opposite charge. These regions will then attract a powdered ink "toner" which is then transferred onto the paper.

In inkjet printing, ink is deposited directly on the substrate, which allows to transfer the print to the substrate with a minimum of functional elements. There are mainly two types of inkjet inks: liquid-based inks and hot-melt inks. Both inks contain pigment or dye particles. For liquid-based inks, being liquid at room temperature, ink becomes solid through drying. In this process, solvent (solvent-based inks) or water (water-based inks) evaporates or is absorbed by the medium allowing the particles to settle. To help evaporation, ink can be heated after applying. Other liquid-based inks are UV inks which are cured using UV light. In hot melts, which are solid at room temperature, the ink is heated within the nozzle to make it fluid. After the ink contacts the paper, the temperature drops, and the ink droplet becomes solid.

For all types of inkjet printing, the final print consists of a combination of multiple individual droplets. In the last decades, droplets became smaller and smaller, which resulted in more control, improved print quality and lower costs. Current inkjet printers can reach resolutions as high as a few 1000 DPI (Dots Per Inch). This allowed inkjet printing to compete with other techniques and became one of the most used printing techniques. Depending on droplet generation, there are two main inkjet technologies: continuous (CIJ) and drop-on-demand (DOD). Both are shown in Figure 2.6.

Both techniques are quite similar, in that they create droplets that fall onto the print media. However, in continuous inkjet, Figure 2.6b, a continuous stream of ink is pushed through the nozzle which is broken up by electric charges. Differently, in drop on demand printing, Figure 2.6a, droplets are created on demand. Depending on the way a droplet is created, three types of DOD printing exist, namely thermal, piezoelectric and electrostatic. In thermal ink jet, the ink is heated until it vaporizes, and creates a pressure that forces a droplet out of the nozzle. In piezo inkjet, a droplet is created due to changes in the ink supply chamber. Finally, in electrostatic inkjet, an electric field is build up between the paper and ink chambers exerting a force on the liquid, which forces ink droplets out.

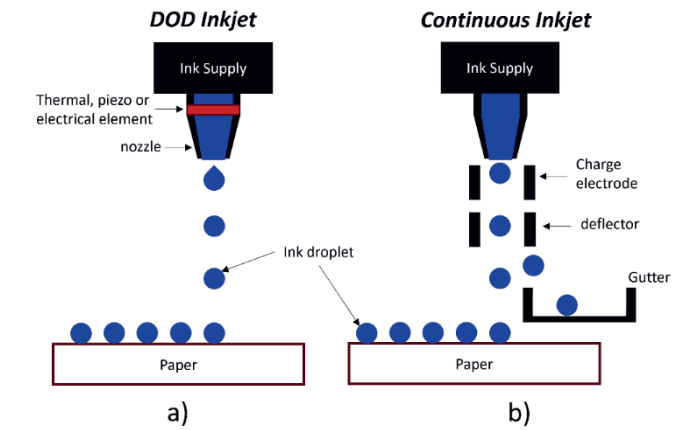


Figure 2.6 a) Drop On Demand (DOD) inkjet printing and b) Continuous inkjet printing.

In both techniques, no contact takes place between the print elements and the substrate. Prints are made by ink droplets falling onto the media. The processes that follow after the droplet hits the paper sample are extremely important in determining the final print quality. Figure 2.7 shows a schematic representation of an ink droplet penetrating a print media and some of the most important processes. Once an ink droplet hits the paper, it penetrates the pores of the media due to capillary suction. Suction pulls particles, such as latex particles and pigments, into the media. The degree of penetration will determine the ink density and mechanical properties of the ink spot. Therefore, the penetration process is inherently coupled to the print quality of the porous media. Understanding the different processes and their contributions is necessary to be able to influence and control pigment deposition in an ideal regime for maximizing print quality.

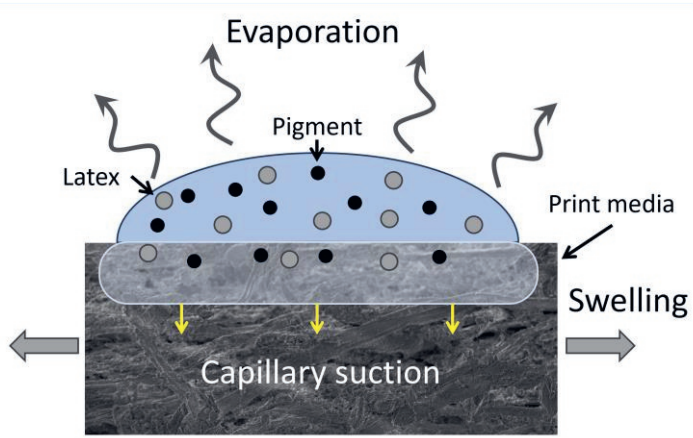
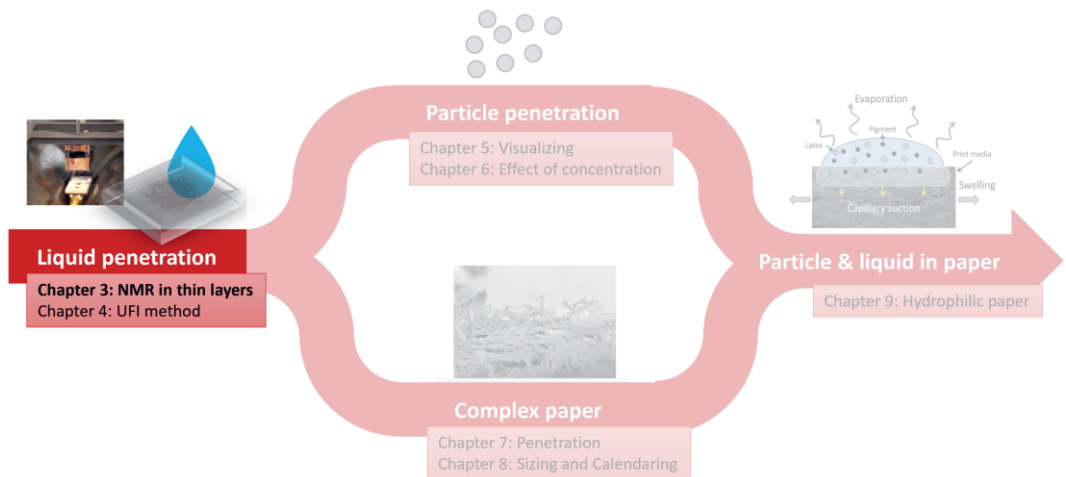


Figure 2.7 Schematic representation of a droplet penetrating a paper substrate.



# 3

## NMR imaging of reaction and transport in thin layers

---

Reactions, transport, and deformation phenomena in thin layers between 10 and 1000  $\mu\text{m}$  are important in many applications. To measure transport processes and structural changes in thin layers such as liquid transport or swelling in paper, this study uses a NMR-based imaging technique. NMR is a non-destructive imaging technique that uses nuclear spins such as the  $^1\text{H}$  atom to gather information. To use NMR within thin, porous media, a high spatial resolution is required. Therefore, special high-gradient NMR setups are required such as STRAFI, GARField or the NMR-MOUSE. This chapter will cover the use of high-gradient NMR setups within thin, porous media and how it becomes different compared to conventional NMR imaging. The first part of this section introduces the basic principles behind NMR and how it allows to gather spatial resolved information about transport processes and structural changes. Thereafter, these basic principles will be extended towards systems with high magnetic gradients. Three possible high gradient NMR setups will be discussed (STRAFI, GARField and the NMR-MOUSE) and a guideline to select the best high-gradient setup for specific measurements will be provided. To illustrate how these high-gradient NMR setups can be used to measure information about reaction, transport and structural changes, a review about multiple types of experiments is given.

*Adapted from:*

*R. Nicasy, H. Huinink, B. Erich, and O. Adan, "NMR Profiling of Reaction and Transport in Thin Layers: A Review," Polym. 2022, Vol. 14, Page 798, vol. 14, no. 4, p. 798, Feb. 2022, doi: 10.3390/POLYM14040798.*

### 3.1 Introduction

Reaction and transport in thin layers (10–1000  $\mu\text{m}$ ) are very important in the printing industry [17], [68], [82] but also in a broad range of other applications [83] that can be found in building materials [84], energy storage [85], [86], photovoltaic devices [87], [88], art [89], [90], flexible electronics [91], optics [92], and coatings [93]–[95]. The focus of this chapter does not lie only on the printing process but on reaction and transport phenomena in general. Performance and stability of these thin layers will be determined by their final structure and underlying physical processes. In literature, the study of these processes is mostly categorized in different groups belonging to polymer or non-polymer thin layers. Here, we also differentiate between polymer and non-polymer films. Within polymer films, we identify two main groups of processes, firstly,

the ones during film formation and, secondly, processes that occur when the film is formed. The process of film formation is a multistage process which in literature is defined in different ways. In this chapter, we categorize two types of film formation, both starting with the evaporation of the solvent followed by either curing or coalescence. After the film has formed, other processes such as transport of liquid and chemical reaction take place. In non-polymer films, such as cements or printing paper, liquid uptake and deformation are the most important processes. A more fundamental understanding of these processes will lead to more cost-effective, efficient, and stable applications.

Film formation [96], [97] is crucial in determining the final structure of the film and its stability. If film formation happens incorrectly, the layer can suffer from non-uniformities, skin formation [98], [99], precipitation [100], chemical differences and other mechanical malfunctions [101] that all reduce performance. In most cases, applying thin layers starts with a liquid solution that covers the surface, containing both the film material (polymer, latex) and a solvent [96]. In the mid-1900s, volatile organic components were mostly used as solvent. However, since 1950, concerns about their toxicity [102], flammability and environmental effects [103], [104] have led to a change towards using water as solvent [105]. When the layer is applied, film formation happens in a two-stage process where first the solvent must evaporate, allowing close contact between the polymers, followed by a type of mechanism to overcome their mutual repulsion and form a rigid layer. The rate of solvent evaporation is critical for film formation and depends on multiple factors [106], [107]. First, the rate of evaporation will depend on vapor pressure, temperature, surface area and airflow. In a second stage, the release of solvent becomes limited by transport through the thin layer [106], [108]. If the solvent evaporates too quickly, the polymer will not have time to adhere to the surface or form a continuous film. In contrast, a slow evaporation rate will induce over wetting in the subsurface. When enough solvent has evaporated, a continuous layer is formed by curing (cross-linking) or coalescence in the case of latex [109], [110]. Both cross-links and coalescence will be responsible for the strength and characteristics of the initial thin layers. A wide variety of studies focus on cross-linking [111]–[113], and coalescence [97] to gain a better understanding and improve the final structure.

Processes after film formation such as liquid transport [114], [115] and reactions within these films are responsible for performance, degradation, and instabilities. A wide variety of degradation processes can be identified, including biodegradation [116], photodegradation by light [117] and chemical degradation. Studies on the penetration and diffusion of liquids and the corresponding effect on the film morphology are the focus of a large group of studies and will be discussed in this chapter [118].

Other types of non-polymer thin layers can be found in the printing industry [119]–[121] (printing paper with a thickness of 100  $\mu\text{m}$ ). In these printing papers, the penetration of ink is of great importance as it influences the final print quality [82], [122]. The wide variety of coatings [123], hydrophobicity [64] and basis weight found in these papers will all influence the printing process and the resulting print quality. Another type of thin layer can be found in the human skin [124], [125] where layers such as the stratum corneum and viable epidermis, both around 50  $\mu\text{m}$  thick, can be found. In these skin layers, processes such as the penetration of skin care products [126] or oils take place. As a final example, in cement pastes [127], [128] used in

building applications, strength is based upon the internal morphology and transport of ions.

Experimental techniques able to study film formation, reaction and transport processes are necessary to gain the insights allowing improvement of performance and stability. Since many processes in thin layers such as diffusion, curing and chemical reactions will happen with a so-called front, gaining spatial and time-dependent information is a crucial requirement. As described in the introduction, high-spatial-resolution MRI has the potential to be a versatile tool for studying these processes.

MRI has made its way into material research, as well as in polymer research [97], [129]–[132]. NMR can be used to measure density profiles, atoms' mobility, and probe their environment which enables them to study reactions and transport processes in thin layers. Reactions in thin films, such as cross-linking [133]–[135], glass transitions, curing and many more chemical reactions, will all influence the mobility of the atoms, which is visible in the NMR signal. Additionally, transport processes can be studied by measuring time-dependent density profiles.

Characterizing polymers with NMR has been the focus of many studies. Most research is conducted with NMR spectroscopy which is already well known and described in many books [136]–[139]. Here, the focus lies upon the different high-resolution NMR setups that are able to extract information with high spatial resolution. Three different high-gradient NMR setups exist with resolution in the micrometer range that are able to extract physical and chemical information about thin films: STRAFI (STRay Field), GARField (Gradient-At-Right-angles to Field) and MOUSE (MOBILE Universal Surface Explorer).

This chapter will begin by explaining the basic theory behind NMR and how hydrogen atoms can be used to extract spatial information. Thereafter, the GARField [140], STRAFI [141] and MOUSE [142] setup will be discussed, where an overview will be given about their similarities and differences. Lastly, different thin layer studies will be discussed to demonstrate how chemical and physical information of thin layers (between 10 and 1000  $\mu\text{m}$ ) such as polymer films or paper can be extracted using high-spatial-resolution NMR setups.

## 3.2 Basic NMR principles

Equation Section (Next)The existence of a nuclear spin was demonstrated by Bloch and Purcell in 1946 when they measured for the first time nuclear magnetic resonance (NMR) [143], [144]. They received the Nobel Prize in Physics for this work in 1952. The basics of NMR are often explained using a classical vector model [131]. In this classical model, the nuclei are described by small magnetic dipoles with magnetic moment  $\vec{\mu}$  [ $\text{Am}^2$ ], also known as "spin". The nuclear spin  $\vec{\mu}$  is the consequence of moving charges within the atom's nucleus. A relation exists between the angular momentum  $\vec{b}$  [ $\text{kgm}^2\text{s}^{-1}\text{rad}$ ] and the magnetic moment of the nucleus  $\vec{\mu}$ ,

$$\vec{\mu} = \gamma \vec{b}, \quad (3.1)$$

where the proportionality constant  $\gamma$  [ $\text{rads}^{-1}\text{T}^{-1}$ ] is the gyromagnetic ratio. The most studied nucleus (abundant in water, polymers and biopolymers) is hydrogen ( $^1\text{H}$ ) where



$\gamma/2\pi = 42.58$  [MHzT<sup>-1</sup>]. Although hydrogen is the most abundant and well known atom, there also exist studies on other elements such as fluorine [145] (40.08 MHzT<sup>-1</sup>) or carbon-13 (10.71 MHzT<sup>-1</sup>) [146]. When nuclear spins are situated in external applied magnetic field  $\vec{B}_0$  [T], they will experience a torque  $\vec{\tau}$  [Nm] related to the magnetic field by,

$$\vec{\tau} = \mu \times \vec{B}_0. \quad (3.2)$$

Because the torque equals the time derivative of the angular momentum, equations (3.1) and (3.2) can be combined to:

$$\frac{d\vec{\mu}}{dt} = \gamma(\vec{\mu} \times \vec{B}_0). \quad (3.3)$$

All nuclei will experience this same time dependence in their magnetic moment  $\vec{\mu}$ . Therefore, they will start to align and precess around the applied magnetic field  $\vec{B}_0$ , which by normal convention is pointing in the  $z$ -direction. This precession is called Larmor precession. A schematic picture of this precession is shown in Figure 3.1a. The frequency  $\vec{f}$  [Hz] depends on the magnetic field and is given by,

$$\vec{f} = \frac{\vec{\omega}}{2\pi} = \frac{\gamma}{2\pi} \vec{B}_0, \quad (3.4)$$

where  $\vec{\omega}$  [rad/s] is the Larmor frequency. To excite and manipulate the atoms, a second magnetic field,  $\vec{B}_1$  [T], is used. This magnetic field is applied by a radiofrequency (RF) pulse sent by an RF-coil. A frequently used design is the Helmholtz coil [147]. The excitation is best when the radio frequency (RF) pulse coincides with the Larmor frequency  $\vec{\omega}$  from Equation (3.4). As a response, the hydrogen atoms will precess along the new established magnetic field. In most cases, this manipulation is used to bring the magnetic moments in the  $xy$ -plane. In an NMR measurement, the total magnetization  $\vec{M}$  along this  $xy$ -plane can be measured using the same or another RF-coil, which is a sum of all the individual magnetic moments,

$$\vec{M} = \sum_i \vec{\mu}_i. \quad (3.5)$$

Measuring this signal can be done in multiple ways. The most common way is by using spin echoes, firstly introduced by Hahn [148], [149] in 1950. After a combination of pulses, the signal is recorded at some echo time  $t_e$  [s]. This and other pulse sequences will be discussed in section 3.2.2 Pulse Sequences.

One advantage of NMR is the ability to achieve spatial resolution along the  $y$ -direction, perpendicular to the thin layer. Encoding spatial information is achieved by applying a magnetic field gradient  $\vec{G} \equiv (\partial B_z / \partial x, \partial B_z / \partial y, \partial B_z / \partial z)$  perpendicular to  $\vec{B}_0$ , see Figure 3.1b.

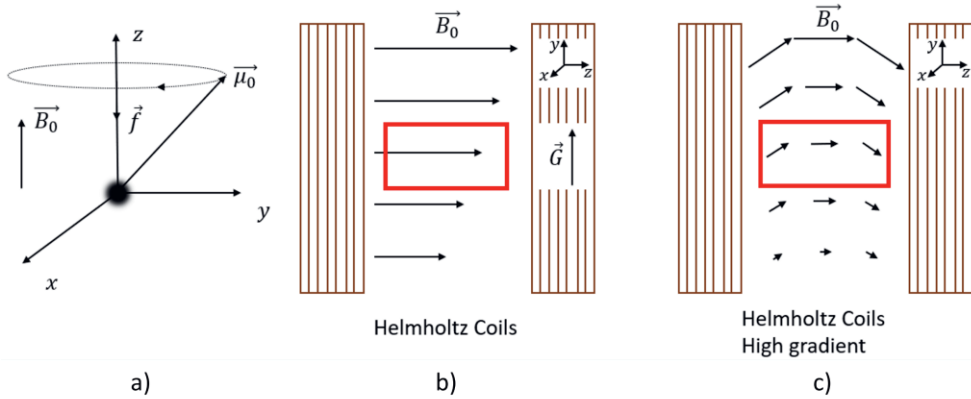


Figure 3.1 a) Larmor frequency, b) conventional NMR setup (Helmholtz coil) with condition  $|B|/G \gg 1$  where the gradient field  $\vec{G}$  and applied magnetic field  $\vec{B}_0$  are shown and approximated by straight lines because the radii of curvature are negligible. Depicted in red is the measurement area used in NMR experiments. c) The same Helmholtz coils as in b, but with  $|B|/G \ll 1$ . In this case, the radius of curvature cannot be neglected which can be seen in the filed lines from  $\vec{B}_0$ .  $\vec{G}$  is not drawn because it lies on the contrary to the middle figure, not in one direction, which would make the graph too complicated.

This gradient changes the magnetization along the  $y$ -direction, indicated by the black arrows in Figure 3.1b, which leads to a spatial dependent Larmor frequency along the  $y$ -direction given by,

$$\omega(y) = 2\pi f(y) = \gamma(B_0 + G_y \cdot y), \quad (3.6)$$

with  $G_y$  the gradient of the  $z$ -component of the magnetic field along the  $y$ -direction ( $\partial B_z / \partial y \approx \partial B_0 / \partial y$ ) and  $f$  the frequency amplitude. The total measured NMR signal is a combination of all different nuclei that resonate with different Larmor frequencies. When applying a Fourier transform on the recorded echo, the separate contributions of all different Larmor frequencies can be extracted and linked to a specific  $y$ -position through equation (3.6), providing the spatial density distribution  $\rho(y)$ . After excitation, the total signal intensity  $S(y, t_e)$  decays over time due to spin-spin or  $T_2$  relaxation and spin lattice or  $T_1$  relaxation with characteristic timescales  $T_2^*$  [s] and  $T_1$  [s]. As explained before, signal is recorded with echoes at a specific time  $t_e$ . The  $T_2$  relaxation time determines how fast a signal decays as function of  $t_e$  and can therefore be deduced from the signal decays directly. The  $T_1$  relaxation on the other hand, determines how fast a signal recovers to its original state after excitation. Maximum signal is achieved when atoms, at the beginning of an experiment, are aligned with  $\vec{B}_0$ . Therefore, signal is a function of the time between multiple pulsed experiments  $t_r$  [s], also called the repetition time and the time they need to relax back to their equilibrium  $T_1$ . The final signal intensity is also proportional to the density of hydrogen atoms  $\rho$  [ $\text{kgm}^{-3}$ ] and is given by,

$$S(y, t_e) \propto \rho(y) \left( 1 - \exp\left(-\frac{t_r}{T_1}\right) \right) \left( \exp\left(-\frac{t_e}{T_2^*}\right) \right). \quad (3.7)$$

Depending on the gradient strength ( $G$ ) and magnetic field strength ( $|B_0|$ ), two different regimes exist: low gradients with  $|B|/G \gg 1$  and high gradients with  $|B|/G \ll 1$ . In conventional NMR setups with low gradients,  $|B|/G \gg 1$ , see Figure 3.1b, the curvature of the magnetic field lines is so small that the following assumptions can be made: 1) the magnetic field is constant, pointing in the  $z$  direction, and 2) the gradient along the  $y$ -direction can be assumed to be constant and equal to  $\partial B_z / \partial y$ . In this case, eq. (3.6) can be used.

However, to measure within thin, porous media, a high gradient is required and therefore  $|B|/G \ll 1$ . This makes the situation more complicated due to huge curvatures within the magnetic field lines, see Figure 3.1c. This special case will be discussed in section 3.3.

### 3.2.1. NMR relaxation

In the previous section, the formula for the signal intensity (equation (3.7)) shows two relaxation processes with two characteristic timescales  $T_2^*$  and  $T_1$ . These relaxation times depend on the environment of the nuclei and provide valuable information about the nuclei's surroundings. In this section we will describe these relaxation times, which depend on multiple factors, such as: the substance, the porous media, diffusion and contrast agent concentration, will be described in this section.

There are two typical characteristic relaxation processes called  $T_1$  or spin-lattice relaxation and  $T_2$  or spin-spin relaxation. In case of  $T_1$ , energy between the hydrogen spins and the surroundings is exchanged. This energy exchange relaxes the spins back to their original  $z$ -direction. How fast  $M_z$  is restored is characterized by the  $T_1$  time. The energy transfer is most effective when the surrounding atoms vibrate or rotate at the Larmor frequency. The second relaxation process accounts for losses in the transversal component of the magnetization vector ( $M_{xy}$ ). The rate at which this relaxation occurs is defined by the  $T_2^*$  relaxation time. Both relaxation times are influenced by different local factors. To understand how these times can be used to gain physical information, a deeper look at both relaxation times is needed.

The  $T_2^*$  and  $T_1$  relaxation time can be rewritten as the contribution of different factors as [150],

$$\frac{1}{T_2^*} = \frac{1}{T_2} + \frac{1}{T_{2i}} = \frac{1}{T_{dip.}} + \frac{1}{T_{2pores}} + \frac{1}{T_{2dif}} + \frac{1}{T_{2contrast}} + \frac{1}{T_{2i}} \quad (3.8)$$

$$\frac{1}{T_1} = \frac{1}{T_{1dip}} + \frac{1}{T_{1pores}} + \frac{1}{T_{1contrast}} \quad (3.9)$$

where  $T_2^*$  and  $T_1$  are the relaxation times found in Equation (3.7). Here,  $T_2^*$  is a combination of both  $T_2$  and  $T_{2i}$ , where the second one is attributed to inhomogeneities in the magnetic field introduced by the setup [151]. In most pulse sequences such as the Hahn spin echo [148], [149] or Carr-Purcell-Meiboom-Gill sequence (CPMG) [152], [153], one can compensate for field inhomogeneities and the  $T_{2i}$  contribution can be

avoided. Within this thesis, the pulse sequences will always compensate for the field inhomogeneities and therefore,  $T_2^*$  is replaced by  $T_2$ .

### *Dipolar interaction – Bulk relaxation*

The first relaxation mechanism is induced by dipolar interactions ( $T_{2dip}$ ,  $T_{1dip}$ ) and can be used to identify the bulk component e.g., the molecule or phase. Dipolar interactions between neighboring atoms induces small differences in the magnetic field [154]. These local variations lead to variations in the Larmor frequency and dephasing of the spins which leads to a faster relaxation. This relaxation mechanism can be linked to molecular mobility, quantified by a motional correlation time ( $\tau_c$ ) which defines the average time necessary for a molecule to rotate one radian. The relation between the correlation- and relaxation- time was introduced by Bloembergen, Purcell and Pound in 1948 [155], known as the BPP theory, given by,

$$\frac{1}{T_{2dip}} = \frac{3}{20} \frac{\gamma^4 \hbar^2}{r^6} \left[ \frac{5\tau_c}{1 + \omega_0^2 \tau_c^2} + \frac{2\tau_c}{1 + 4\omega_0^2 \tau_c^2} \right], \quad (3.10)$$

$$\frac{1}{T_{1dip}} = \frac{3}{10} \frac{\gamma^4 \hbar^2}{r^6} \left[ \frac{\tau_c}{1 + \omega_0^2 \tau_c^2} + \frac{\tau_c}{1 + 4\omega_0^2 \tau_c^2} \right]. \quad (3.11)$$

Figure 3.2a shows both relaxation times as a function of the correlation time. These relaxation times can be used to discriminate between different polymer and biopolymer motional regimes inside a thin film, provide information about different structures, mobility, chemical reactions, and mechanical responses. In rigid environments, with low correlation times (solids or polymers below their glass transition temperature), hydrogen atoms experience the same deviations in magnetic field for a longer time, leading to a larger phase difference in their Larmor frequencies and faster  $T_{2dip}$  decay times (gray line in Figure 3.2a). On the contrary, when molecules are mobile (large correlation times), for example in liquid water, the differences in magnetization will be averaged out over time leading to longer  $T_{2dip}$  relaxation time. These relaxation times can be used to observe any difference between materials where the molecular mobility of the studied atoms are different such different polymer substances [132], crosslinked and non-crosslinked materials, water and cellulose within a paper sheet [156], [157], and skin layers within polymer films [158], [159].

Also the  $T_1$  relaxation will be influenced by the dipolar interaction (eq. (3.11)). Because  $T_1$  relaxation depends on the energy transfer between the spins and their environment which is most effective when vibrations are similar to the Larmor frequency, the effect of the dipolar interaction will be strongest when  $\tau_c = \omega$ . This explains the shape of the black line in Figure 3.2a.

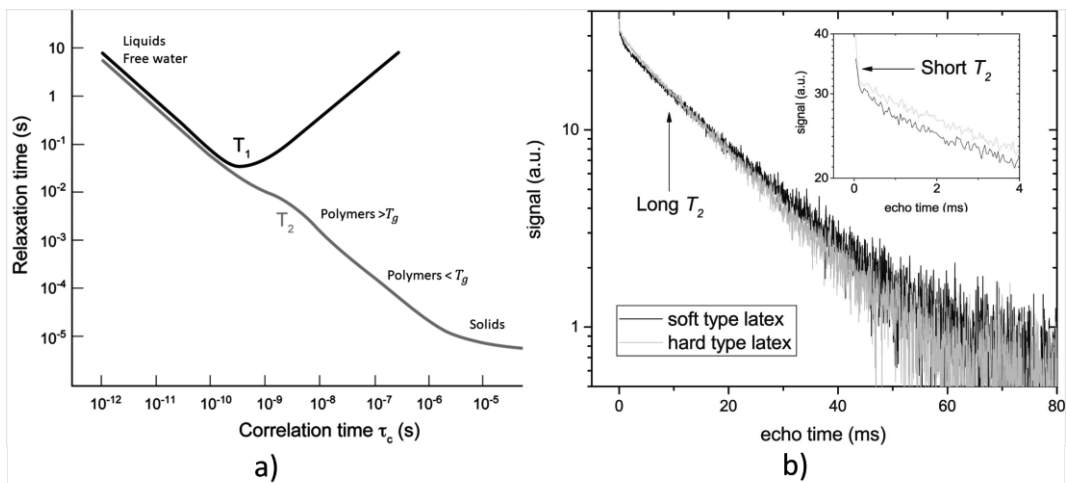


Figure 3.2 a) Dependence of  $T_1$  and  $T_2$  upon  $\tau_c$  (Reproduced from Chem. Soc. Rev., 2014,43,1627–1659 with permission from the Royal Society of Chemistry.) [160]. b) Signal decay of a latex film measured with a GARField NMR. Both soft and hard-type latex are visible and show a multi-exponential decay where the short and long  $T_2$  component are marked. The short relaxation time is attributed to hydrogen atoms within the polymer, while the long relaxation time comes from free water. (Reprinted from Progress in Organic Coatings, Volume 123, Benjamin Voogt, Henk Huinink, Bart Erich, Jurgen Scheerder, Paul Venema and Olaf Adan, Water mobility during drying of hard and soft type latex: Systematic GARField  $^1\text{H}$  NMR relaxometry studies, Pages 111–119, Copyrights 2018, with permission from Elsevier [161]).

### Porous matrix relaxation

The second term appearing in both relaxation times, is the relaxation caused by a porous matrix ( $T_{2\text{pores}}$ ,  $T_{1\text{pores}}$ ) which was described in detail by Brownstein and Tarr [162]. Due to diffusion, atoms encounter the pore surface, where relaxation due to dipoles or other effects occur. How effectively this surface relaxation is, depends on multiple factors such as the pore surface material, quantified by the surface relaxivity  $\sigma$  [ $\text{ms}^{-1}$ ] [163]–[167], the diffusion constant  $D$  [ $\text{m}^2\text{s}$ ] and the pore radius  $r$  [m]. Different motional regimes exist, which are determined by the value of  $\sigma r/D$  [168]. When  $\sigma r/D \ll 1$ , the fast diffusion regime, diffusion is fast enough, and surface relaxation will become the dominant relaxation mechanism. On the contrary, in the slow diffusion regime, when  $\sigma r/D \gg 1$  atoms are unable to diffuse towards the pore surface in a sufficient time and as a consequence surface relaxation can be neglected. Here, the factor  $r/D$ , relates to the number of encounters with the surface. Surface relaxation will become important when either the surface relaxivity is high enough or there are many encounters with the porous surface. In the fast diffusion regime, Brownstein and Tarr found that  $1/T_{2\text{pores}}$  and  $1/T_{1\text{pores}}$  can be approximated by,

$$\frac{1}{T_{2\text{pores}}} = \sigma_2 \frac{S}{V}, \quad (3.12)$$

$$\frac{1}{T_{1pores}} = \sigma_1 \frac{S}{V}, \quad (3.13)$$

where the factor  $S/V$  is the pore surface-to-volume ratio. These relaxation times can be used to gain useful information about the porous matrix [150], [163]–[166] and possible changes over time when subjected to different environmental factors.

### *Diffusion relaxation*

A third parameter only found in  $T_2$  relaxation comes from diffusion of molecules. When atoms diffuse, they encounter different field strengths due to the setup's gradient. This leads to dephasing and a lower  $T_2$  time. This effect depends on the gradient strength, diffusion constant and diffusion time (the time between two pulses,  $t_e$ ), which is described by the following formula [169], [170],

$$\frac{1}{T_{2dif}} = \alpha \gamma^2 G^2 t_e^2 D. \quad (3.14)$$

The parameter  $\alpha$ , is a constant which is defined by the evolution of coherent pathways for a given pulse sequence as described by Hurlimann [170].

### *Contrast agent relaxation*

In some cases, the relaxation time can also be adjusted by using contrast agents, which is represented by  $1/T_{2contrast}$  and  $1/T_{1contrast}$ . Contrast agents are substances, mostly used in medical NMR, to enhance the contrast of structures and liquids by effecting their relaxation time. Commonly used contrast agents are gadolinium based contrast agents such as Clariscan™ [171], [172] or  $\text{CuSO}_4$  [173]. The effect of the contrast agents depend on their concentration  $C$  [ $\text{m}^3$ ] and relaxation rates or relaxivity  $R_2$  [ $\text{S}^{-1} \cdot \text{m}^3$ ] and  $R_1$  [ $\text{S}^{-1} \cdot \text{m}^3$ ] [174], [175], given by,

$$\frac{1}{T_{2contrast}} = R_2 C, \quad (3.15)$$

$$\frac{1}{T_{1contrast}} = R_1 C. \quad (3.16)$$

### *Multiple relaxation times*

Probing relaxation times can also be useful for studying different pools of atoms at the same time, a trick commonly used in thin film studies [176]–[180]. Every pool of hydrogen nuclei will have their own characteristic  $T_2$  and  $T_1$  relaxation time given by equation (3.8) and (3.9) which depend on the different processes earlier described. The signal for one hydrogen pool is given by equation (3.7). In case of multiple hydrogen pools, the signal is a contribution of every individual pool which can be represented by,

$$S(y, t_e) \propto \sum_{i=1}^{\beta} \rho_i(y) \left( 1 - \exp\left(-\frac{t_r}{T_{1i}}\right) \right) \left( \exp\left(-\frac{t_e}{T_{2i}}\right) \right), \quad (3.17)$$

where the summation runs over all different pools of hydrogen nuclei ("i"), having their own relaxation times  $T_{2i}$  and  $T_{1i}$ . In case the relaxation times of different hydrogen groups are far enough apart, a multi-exponential decay is observed and their relative contributions to the signal can be separated. Figure 3.2b, demonstrates this principle by showing a decay of a latex film [181]. The decay clearly shows a two-component exponential decay. From the BPP-theory we know that the latex can be attributed to the short relaxation time while the long  $T_2$  relaxation time can be linked to free water.

By exploiting this method, the relative contribution and relaxation time of different pools of hydrogen atoms can be followed over time using the same experiment. This is by far the most powerful tool in studying thin films over time [182]. Using this technique, M.R.Halse [183] showed that they could follow three groups of hydrogen atoms in a decane/rubber system at the same time: dry rubber ( $T_2 = 0.7$  ms), swollen rubber ( $T_2 = 1.8$  ms) and solvent ( $T_2 = 200$  ms).

### 3.2.2. Pulse Sequences

To gather information about the nuclei density  $\rho$  and the  $T_2$  and  $T_1$  relaxation time, different pulse sequences are used, which will be discussed in this section.

Before any pulses are given, the magnetization vector is in equilibrium, pointing in the same direction as the main magnetic field  $\vec{B}_0$ . Creating an NMR signal is achieved by bringing the magnetization out of equilibrium using a radio frequency (RF) wave. This RF irradiation will have a magnetic component ( $\vec{B}_1$ ) along the  $xy$ -plane exerting a torque on the magnetization, Equation (3.2). Applying this RF-field for a certain amount of time is called an "RF-pulse". The angle by which the magnetization will rotate is called the "flip angle" ( $\alpha$  [°]) and depends on both the pulse time ( $t_p$  [s]) and the magnitude of the RF-field ( $|B_1|$ ) given by

$$\alpha = \gamma B_1 t_p \quad (3.18)$$

Applying different RF-pulses is referred to as a pulse sequence and can be used to measure the signal intensity, relaxation times and diffusion which will be briefly discussed in the remainder of this section. For a more in-depth discussion about the pulse sequences, we refer to more advanced studies [43,88,110] and reviews [83,111].

#### *Signal intensity*

Measurements of the signal intensity are mostly performed using Hahn spin echoes [148], [149] with the following pulse sequence [ $90_x^\circ - \tau - 180_y^\circ - \tau - \text{echo}$ ]. At  $t = 0$ , a  $90^\circ$  pulse rotates the spins around the  $x$ -axis into the  $xy$ -plane. After this pulse, the transverse magnetization starts to dephase due to the environment, field inhomogeneity and the gradient according to equation (3.8). At  $t = t_e/2$ , a second  $180^\circ$  pulse is given, which rotates the spins around  $y$ -axis and refocuses them. At  $t = t_e$ , the spins are refocused, and a so-called spin echo is created from which the transverse magnetization can be measured.

### $T_2$ relaxation time

To measure the  $T_2$  relaxation, two measurements are used, the Carr–Purcell–Meiboom–Gill sequence (CPMG) [152], [153] and the Ostroff–Waugh (OW) pulse sequence [184]. The most frequently used sequence is the CPMG sequences which start the same as the Hahn spin echo but is followed by a train of  $180^\circ$  pulses  $[90_x^\circ - \tau - (180_y^\circ - \tau - \text{echo} - \tau)_n]$ . Every  $180^\circ$  pulse refocuses the spins, resulting in a series of spin echoes. The echo intensity drops due to  $T_2$  relaxation. The signal intensity at the  $n^{\text{th}}$  echo is given by,

$$S(nt_e) = S_0 \exp\left(-\frac{nt_e}{T_2}\right), \quad (3.19)$$

from which the  $T_2$  relaxation time can be calculated. Another option for measuring the  $T_2$  relaxation time is using the Ostroff–Waugh (OW) pulse sequence which is an adaption of the CPMG sequence. Within the OW sequence, the  $180^\circ$  pulse is exchanged by another  $90^\circ$  pulse. In high-gradient measurements, this sequence is chosen above the more conventional CPMG sequence, for reasons that will be explained section 3.3.1.

### $T_1$ relaxation time

To measure the  $T_1$  relaxation time, the saturation recovery [185], [186] and inversion recovery [131], [186], [187] sequence are used. However, in the high-resolution setups described in this review, the saturation recovery sequence is chosen for reasons that will be explained in section 3.3.1. The pulse sequence of the saturation recovery sequence is given by  $[\alpha_y^\circ - \tau_I]_m - \tau_2 - 90_x^\circ - \tau - 180_y^\circ - \tau - \text{echo}$  [188], where  $m$  denotes the amount of saturation pulses. The measurement starts by saturating the nuclear spins, setting the magnetization in the transverse plane to zero. This is achieved by  $m$  pulses with a certain angle  $\alpha$ . After complete saturation, Hahn spin echoes will be measured at different time intervals specified by  $\tau_2$ . The measured echo intensity is then given by,

$$S(\tau_2) = S_0 \left(1 - \exp\left(-\frac{\tau_2}{T_1}\right)\right), \quad (3.20)$$

from which the  $T_1$  relaxation time can be calculated.

## 3.3 High-Resolution spatial Encoding

To profile thin porous media with a high-enough resolution, a high gradient is required, see equation (3.6). Three NMR setups can generate high-enough gradients to profile porous media between 10–1000  $\mu\text{m}$ , namely, STRAFI (STRAY FIeld) [189], GARField (Gradient-At-Right-angles-to-Field) [140] and MOUSE (MOBile Universal Surface Explorer) [190]. In these high-gradient setups, where  $|B|/G \ll 1$ , previously made assumptions regarding the constant magnetic field in the  $z$ -direction and the constant gradient along the  $y$ -direction ( $G_y = \partial B_z / \partial y$ ) are no longer valid. Consequently, equation (3.6) cannot be used anymore due to the significant curvatures within the magnetic field lines, see Figure 3.1c. To understand this, we need to consider Maxwell in free space with a static magnetic field and no current,



$$\nabla \times \vec{B} = 0. \quad (3.21)$$

According to this condition, the following relation should hold for the gradient in the  $y$ -direction,

$$\frac{\partial B_z}{\partial y} = \frac{\partial B_y}{\partial z}. \quad (3.22)$$

Therefore, by introducing a gradient in the  $y$ -direction ( $\partial B_z/\partial y$ ), there must be a gradient in another direction ( $\partial B_y/\partial z$ ). This results in a curvature into the mean magnetic field, which is of the order of  $|B|/G$  [140]. In conventional NMR setups with a low gradient, this curvature is around  $10^2\text{m}$  and can be neglected. When the gradient becomes much larger, this curvature should be taken into account. Consequently, it follows from equation (3.6) that,

$$\vec{f}(\vec{r}) = \frac{\gamma}{2\pi} (\vec{B}_0 + \vec{G} \cdot \vec{r}), \quad (3.23)$$

where we use a vector notation to account for the fact that the Larmor frequency is different along the same horizontal plane. As signals are excited and resolved according to their respective Larmor frequency, this inhomogeneous Larmor frequency will lead to some problematic effects within high-resolution setups. The RF-pulses that normally excite a rectangular region will now excite curved slices that depend on the shape of the magnetic field lines. The curvature in STRAFI, for example, is around  $0.1\text{ m}$  [140], much lower than in conventional NMR setups ( $10^2\text{m}$ ). Figure 3.3 shows the sensitive region of an original NMR-MOUSE where a clear curvature can be observed [191].

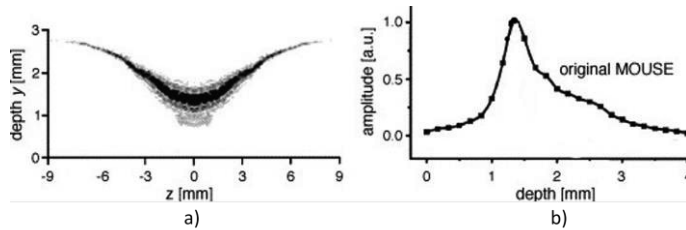


Figure 3.3 a) sensitive region of an original NMR-MOUSE. b) Slice thickness of the signal amplitude for a conventional NMR-MOUSE (Reprinted from *Magnetic Resonance Imaging, Volume 23, Issue 2*, Bernhard Blümich, Federico Casanova, Juan Perlo, Sophia Anferova, Vladimir Anferov, Kai Kremer, Nicolae Goga, Klaus Kupferschläger, Michael Adams, *Advances of unilateral mobile NMR in nondestructive materials testing*, pages 197–201, Copyright 2005, with permission from Elsevier [191]).

### 3.3.1. Resolution and field of view

In the previous section, we discussed how a gradient is used to encode spatial information. The final resolution  $\Delta z$  is mostly determined by the gradient strength and its ability to encode and read out spatial information. However, there are some other limitations that determine the maximum achievable resolution. Another important

parameter is field of view (FOV) which provides the maximum area that can be measured with the NMR setup. This section will cover some of the most important factors that determine the final resolution and FOV. Both parameters will be discussed for two measurement strategies: 1) a Fourier measurement and 2) a slice selective pulse measurement. In the Fourier measurement, spatial information is collected via a Fourier transformation of the NMR signal, mostly found in GARField [181], [192] and sometimes in STRAFI [193]. In the slice selective pulse measurement, a slice selective pulse collects the NMR signal of a thin slice without the need for a Fourier transformation. Here, the profile is built up slice-by-slice which requires a mechanical movement of the sample or magnet, mostly found in STRAFI [194] and MOUSE [195].

In a Fourier measurement, the maximum theoretical resolution is determined by the lowest frequency difference ( $\Delta f$ [Hz]) that can be differentiated. This frequency difference depends on the window width or acquisition time ( $\Delta t_a$ [s]) of the measurement ( $\Delta f \approx 1/\Delta t_a$ ) [189]. The spatial dimension  $\Delta z$  [m] that corresponds to this frequency difference is determined by the gradient [189] by,

$$\Delta z = \frac{1}{\gamma G_z \Delta t_a}. \quad (3.24)$$

Thus, for a gradient of 40 T/m and an acquisition time of 100  $\mu$ s, the maximum achievable resolution becomes 5.9  $\mu$ m. To increase the maximum theoretical resolution either the gradient or acquisition time should be increased. However,  $\Delta t_a$  should always be lower than the  $T_2^*$  found in Equation (3.8). When  $\Delta t_a > T_2^*$ , the signal is limited by a fast  $T_2^*$  relaxation instead of the acquisition time. As a result,  $\Delta t_a$  in Equation (3.24) should be replaced by  $T_2^*$ . Because typical acquisition times of high-gradient setups are around 100  $\mu$ s, much lower than conventional NMR setups, these cases almost never appear.

In the slice selective measurements, the resolution is determined by the frequency bandwidth ( $\Delta f$ ) of the RF-pulse. The frequency bandwidth from the RF-pulse is inversely proportional to the pulse length ( $t_p$ ). Thus, for a 10  $\mu$ s pulse time, the excited frequency bandwidth ( $\Delta f$ ) is around 0.1 MHz which for a gradient of 40 T/m would excite a slice of 58.7  $\mu$ m = ( $\Delta r \approx 1/t_p \gamma G_z$ ). A problem arises in high-gradient fields, because of the curvature induced on the magnetic field that limits the homogeneity of  $|\vec{B}_0|$  and therefore the resolution. In the STRAFI and MOUSE setup, these inhomogeneities will be the limiting factor for the resolutions. These experimental resolutions are determined by measuring the profile of a thin slice, containing NMR active atoms, and analyzing the resulting profile [85]. An example of such measurement is shown in Figure 3.3a, where the sensitive area for a normal NMR-MOUSE is shown. Figure 3.3b shows the corresponding depth profile. In most cases, the experimental resolution is determined by taking the half-width of this profile which in this case would be around 1 mm. As will be explained later, GARField introduces specially designed poles to increase the homogeneity of  $|\vec{B}_0|$  [140]. For this reason, the achievable resolution in GARField is not limited by inhomogeneities and is determined by equation (3.24), mostly higher than in a STRAFI and MOUSE setup.

The high gradients also affect the FOV by inducing a large spread in resonance frequencies and unlike a conventional NMR imaging setup, the gradients cannot be switched off. The spread in resonance frequencies can be of the order of 25 MHz  $\text{cm}^{-1}$ [196]. This severely limits the single-shot FOV that can be achieved with one RF-pulse. In a Fourier measurement, the theoretical FOV is determined by the slice selective pulse ( $\Delta r \approx 1/t_p \gamma G_z$ ) which can be increased by lowering the pulse time.

Now, we can explain why in a high-gradient setup, an OW-sequence and saturation recovery sequence are chosen above the more conventional CPMG sequence and inversion recovery sequence. Since the OW- and saturation recovery sequences use only  $90^\circ$  pulses, always the same volume will be excited. In a CPMG- and inversion-recovery sequence where  $90^\circ$  and  $180^\circ$  pulses are used, this is not the case. Another problem in the case of the inversion recovery arises in the first pulse, used to invert the magnetization from  $M_z$  to  $M_{-z}$ , which will not be exactly  $180^\circ$  throughout the sample which can interfere with the  $T_1$  measurement. In saturation recovery measurement, the signal is saturated by a series of pulses which circumvent this problem.

In real measurements, limitations in the FOV arise because the sensitivity drops significantly when moving away from the RF-coil. In a GARField setup for example, this sensitivity drop limits the FOV to around 500  $\mu\text{m}$  depending on the signal-to-noise ratio. In a slice selective measurement, which can be performed by STRAFI and MOUSE, the sample can be moved through the sensitive area which in essence could result in a limitless FOV. However, the setup design will mostly be the limiting factor leading to a FOV in the order of a few millimeters. The slight differences between the three setups will lead to slight changes into the achievable resolution and FOV. A more detailed explanation can be found in section 3.4 where the setups are discussed separately. However, in most cases, the achievable resolution and FOV can be approximated using the above-mentioned formulas.

### 3.4 High-gradient NMR setups

In this section, the three mentioned high-resolution NMR setups (STRAFI, GARField and MOUSE) will be discussed in more detail. The goal is to provide a general guideline that helps in deciding which setup is most suitable for studying a specific application or material.

#### 3.4.1. STRAFI (STRAY Field Imaging)

Stray field imaging was introduced by A. A. Samoilenko et al. in 1988 [141]. The STRAFI technique uses the stray field (fringe field) of a superconducting magnet to produce its high gradient. Figure 3.4a is a schematic representation of a STRAFI setup. Indicated with black dotted lines are the field lines of the main magnetic field  $\vec{B}_0$  from the superconducting magnet. The measurement area lies in the stray field just below the superconducting magnet where a large gradient can be found that lies along the same direction as  $\vec{B}_0$ . Typical gradients that can be achieved are between 30 and 60 [ $\text{T}\cdot\text{m}^{-1}$ ] [189]. Indicated with red lines are the field lines from the RF-pulse. From here there exist mainly two different ways to acquire a complete profile, leading to two types of STRAFI, conventional STRAFI [197], [198] and Fourier transform STRAFI [193]

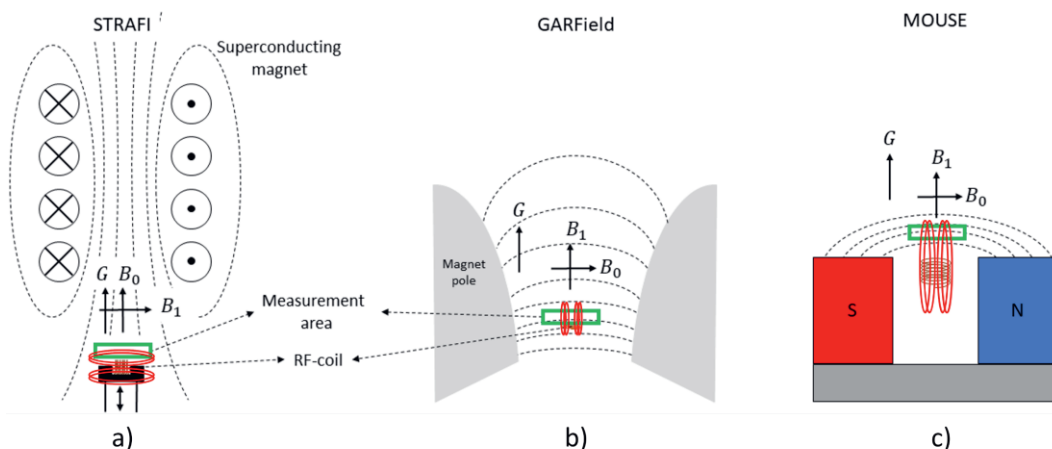


Figure 3.4 Schematic representation of a) STRAFI, b) GARField, and c) MOUSE. In all figures, the measurement area is depicted with a green rectangle. The magnetic field lines are indicated with black for the  $B_0$ -field while the ones from the RF-pulse are indicated with red. In all setups, the direction of the gradient ( $G$ ), main magnetic field ( $B_0$ ) and RF-pulse ( $B_1$ ) in the measurement area are indicated with black arrows.

In conventional STRAFI, profiles are acquired by recording the NMR signal slice-by-slice [197], [198]. One method for imaging slice-by-slice is by moving the sample, which can be seen in Figure 3.4a. As slices are imaged separately, no Fourier transform is required, which leads to a resolution that is limited by the frequency bandwidth of the excitation pulse, see section 3.3.1. The pulse-time dependent resolution results in some drawbacks and limitation. As the pulse lengths can never be longer than the  $T_2^*$  of the material, the resolution for polymers and materials with very short  $T_2^*$  times is limited. Since the frequency bandwidth of the pulse is inversely proportional to the pulse time, this method allows to have rather good resolutions at the expense of long measurement times. Another time restraint comes from the mechanical movement required in slice-by-slice measurements. This becomes problematic when measuring fast dynamic processes. However, there are some tricks to lower measurement time of a single profile. For example, during the repetition time, one can already start to measure other slices which means that the time is limited by the  $T_1$  of the sample [196]. As slices are measured separately, changing some parameters will always influence measurement time. For example, increasing the resolution or sample thickness results in higher measurement times as more slices need to be measured. Therefore, for slow processes, good resolution can be achieved, while for fast processes, the measurement time is too long. Thus, measuring with STRAFI is easier for slow processes and lower resolutions (above  $50 \mu\text{m}$ ).

In the special case, when the frequency bandwidth of the excitation pulse is large enough to capture the complete sample, a Fourier transform STRAFI can be implemented [193]. Here, the echo is collected from the whole sample and the profile is reconstructed by a Fourier transform. Using this method, measurements are only limited by  $T_1$  and not because of mechanical movement. This technique was mostly used to image thin films below  $400 \mu\text{m}$ . The theoretical resolution in these measurements are determined by Equation (3.24). However, the resolution is mostly limited by the shape of the sensitive

area and should be determined experimentally. A major drawback of STRAFI is that the sensitive area where the  $B_0$  field is most homogeneous does not coincide with the optimum gradient position. Therefore, the actual gradient is mostly lower than the maximum gradient that is reported for the particular electromagnet. After a trade-off between measurement speed and resolution, the most encountered studies reported resolutions between 50 [199]– 450 [197]  $\mu\text{m}$ .

### 3.4.2. GARField (Gradient At Right Angles to Field)

To solve the high-curvature problem found in STRAFI that limits the maximum resolution, the GARField NMR was introduced in 1999 by P. M. Glover et al. [140]. In this setup, the researchers changed from a gradient along one component ( $y$ -direction) to a gradient in the magnetic field amplitude  $|B_0|$ . To achieve this, the setup uses electromagnets with specially designed pole tips. The specific shape was calculated using a specific solution of the Laplace equation  $\Delta^2\varphi=0$  where  $\varphi$  is the scalar potential defined by  $B=\text{grad } \varphi$ . For a detailed calculation, we refer to the original paper [140]. The specially designed pole tips from the electromagnets are able to generate a horizontal plane where  $|B_0|$  is constant along the  $xy$ -plane and perpendicular to the gradient, Figure 3.4b. Consequently,  $\partial|B|/\partial z=C$  and  $\partial f/\partial z=C$  which results in in-plane uniformity. When using these pole tips, the ratio  $G/|B|$  is always constant and independent of  $y$  and  $z$ . This allows to operate with different gradient strengths without losing the in-plane uniformity of the magnetic field, allowing for an easy adaptation of the resolution. Shown in Figure 3.4b, is a schematic representation of the setup where the shape of the magnetic pole tips can be seen. Implementing these magnetic poles was only possible when the orientation of the magnetic field and gradient were slightly different compared to STRAFI. Where in STRAFI the  $B_0$  and  $G$  are aligned, they are perpendicular in the GARField setup. As the RF-pulse should be perpendicular to the main magnetic field, the RF-coil from the STRAFI and GARField will have different orientations. The highest sensitivity is obtained when the sample is placed at the end of the RF-coil. This is only possible in the GARField setup. In STRAFI, this arrangement is impossible and the sample should be placed apart from the RF-coil, which lowers the sensitivity.

Compared to conventional STRAFI and MOUSE, a depth profile is measured in one single measurement without repositioning the sample or magnet. The time required to measure a single profile depends on the different parameters used in the pulse sequence but is typically shorter than in STRAFI. A drawback, however, is the limited FOV. Without the possibility to reposition the sample, the FOV is mostly limited by the reduced sensitivity when moving away from the coil, mostly around 500  $\mu\text{m}$ .

As some applications such as coatings are mostly used on metallic surfaces, a special note should be made. Metallic surfaces interfere with the magnetic signals in the setup, which introduces artifacts in the measurement. Artifacts can be the result of differences in magnetic susceptibility between polymer and metal and from eddy currents generated in the metal. To address this problem, H. Zhu et al.[200] investigated the effect of metal substrates on the NMR signal. The researchers found through simulations and experimental work that magnetic susceptibility can be neglected when measuring with a GARField NMR, but that the eddy currents interfere with the pulse field. Therefore, it was calculated that measuring metallic surfaces requires more pulse power to manage these eddy currents.

### 3.4.3. MOUSE (Mobile Universal Surface Explorer)

Different from the STRAFI and GARField, the NMR-MOUSE is a portable device invented to investigate large objects in a non-destructive manner [89], [90]. The NMR-MOUSE consists of a compact permanent magnet (red and blue in Figure 3.4c), which generates the  $B_0$  field. Inside the magnets, the magnetic field is homogeneous but when moving to the fringe field, the field starts to become more inhomogeneous, creating a rather high gradient of about 22 T/m depending on the specifics of the magnets [89]. The small size and low weight make it suitable for on-site testing in a non-destructive manner. This makes the NMR-MOUSE suitable to carry out measurements on large surfaces such as walls or paintings without the need for collecting samples and destroying the object.

The magnetic field is typically quadratic along the  $x$ - and  $z$ -direction and with a main gradient along the  $y$ -direction. This variation in the  $y$ -direction can be used to extract depth profiles of a specific material. The  $B_1$ -field is obtained from a built-in RF-coil, see Figure 3.4c. By calculating the exact magnetic field, it has been found that there is a sensitive region just outside the device [201]. Just like conventional STRAFI, slice-selective pulses are used to extract spatial information, therefore, recording a signal is fully equivalent to STRAFI. However, the sensitive region lies outside the magnets, which limits the final depth that can be measured. Different devices are available to measure depths ranging from 3 to 25 mm [89]. Selecting the best device depends on the application as more depth coincides with a lower sensitivity.

A drawback of the simple magnetic design is the fact that the sensitive region is oddly shaped, varying in thickness, see Figure 3.3a. This results in low sensitivity and huge restrictions on the maximum achievable resolution. Spatial resolutions better than half a millimeter are hard to achieve [202], [203]. Attempts have been made to reduce the resolution. J. Perlo et al. [204] reported resolutions as low as 2.3  $\mu\text{m}$  by making a new magnetic geometry with four permanent magnets. Measuring with these high resolutions in a slice-selective manner is, however, very time consuming. Another drawback of the design is the limitation of the sensitive volume, which limited the FOV to 50  $\mu\text{m}$ .

### 3.4.4. Guideline

Choosing the proper setup depends on multiple parameters, such as the sample material, required resolution and measurement time.

When resolution is most important, GARField is the best option. By solving the curvature problems found in STRAFI, GARField will have the best resolution of all setups. The most reported resolutions lie somewhere between 5 and 15  $\mu\text{m}$  (Table 3.1). In addition to a good resolution, the Fourier measurements used in GARField, offer faster measurement times than slice-selective measurements (Table 3.1). Profiles are mostly measured between 1 and 10 minutes. It should be mentioned that STRAFI also has a Fourier implementation, but with lower resolutions (most reported resolutions between 24–60  $\mu\text{m}$ ) and lower sensitivity coming from the RF-coils orientation. Therefore, for a dynamical process or if a high resolution is required, GARField would be the best option. A drawback of GARField is the rather low FOV (< 500  $\mu\text{m}$ ) with a sensitivity that lowers when moving away from the RF-coil.

When larger samples should be measured, STRAFI would be a better choice. Due to the slice-selective excitation, samples can be moved through the sensitive area, making the FOV, in essence, limitless. While at 400  $\mu\text{m}$  the GARField already loses a lot of sensitivity, the STRAFI does not encounter this signal loss. In these measurements, resolution always comes with a trade-off towards measurement time. Higher resolutions require measuring more slices when keeping the FOV constant.

When measurements are required on-site or if a small piece of the sample is not available, MOUSE is the only suitable option. For most applications such as walls, oil/water wells [205]–[207], PE pipes [191] or paintings, samples small enough for STRAFI or GARField are not available, leaving MOUSE as the only option.

An overview of the most frequently encountered parameters is given in Table 3.1. It should be mentioned that in all cases, trade-offs between different parameters are made. Therefore, the best achievable resolution is almost never achieved. However, the table should give an idea about different ranges that are commonly used for the different setups.

Table 3.1 Most important characteristics of STRAFi, GARField and MOUSE setup.

	$ \vec{B}_0 $ [T]	$ \vec{G} $ [T/m]	Measure time [min]	Resolution [ $\mu\text{m}$ ]	Portable	Sample size [ $\mu\text{m}$ ]
<b>STRAFi</b>	2.3-7	30-60	>3	24-60	No	Limitless
<b>GARField</b>	0.7-1.4	17-44	1-10	5-15	No	50-400
<b>MOUSE</b>	0.025-0.7	11.5	60	50-1000	Yes	50-1000

## 3.5 Applications

The following section will provide a deeper look at some common types of experiments that are performed by these three NMR setups in thin layers. Every section starts with a discussion of the general principles using a representative study as an example. Thereafter, a summary of related studies is given showing the variety of samples and materials that can be studied.

### 3.5.1. Structure and Structural Evolution

In most cases, the high-gradient NMR setups are used to gain information about the internal structure and structural evolution. Therefore, multiple NMR-experiments performed on thin layers aim to determine the moisture content and different polymer states such as crystallinity or cross-linking. Three main parameters are used to identify the internal structure: the signal intensity, diffusivity and  $T_1$ ,  $T_2$  relaxation times. All these parameters provide information about the hydrogen content, their environment, and microstructures, as described in section 3.2.1.

In studies performed by P. J. McDonald et al. [127], [128], the researchers characterized hydrated cement pastes using different  $T_1$  and  $T_2$  relaxation studies.  $T_1$  and  $T_2$  relaxation times were determined using a saturation recovery and OW- sequence with a GARField-setup. A slice selective measurement was performed 10 mm below the surface of the

sample with a slice thickness of 0.6 mm. When plotted in a  $T_1$ - $T_2$  correlation spectrum, the researchers could relate the relaxation times to different groups of hydrogen atoms with varying pore radii (Equations (3.12) and (3.13)). Figure 3.5 shows the  $T_1$ - $T_2$  correlation spectrum for a white cement sample cured under water. Based on this data, the following pores were identified: gel pores ( $T_2 = 400 \mu\text{s}$ ) and multiple capillary pores ( $T_2 > 400 \mu\text{s}$ ) with different pore sizes. Observing the different relaxation times, they found that after 6 days (Figure 3.5b), 2 peaks are visible, both with low  $T_1$  and  $T_2$  times corresponding to gel pores. At day 7, capillary pores with longer relaxation times also start to become visible (Figure 3.5c). Characterizing bulk properties like this can also be performed using a normal NMR spectrometer [208]. In this case, the researchers identified the correlation maps at a specific location of 10 mm below the surface. The advantage of the GARField NMR could be to perform the correlation maps at different positions and study the different pore fraction at different positions, however, this was not done in this study.

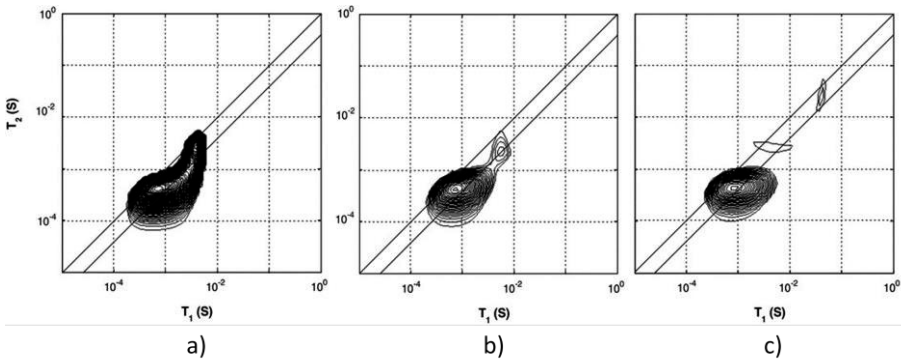


Figure 3.5  $T_1$ - $T_2$ -correlation maps of white cement with water-cement ratio of 0.4. Figures are taken from the curing process under water after a) 2 days, b) 6 days and c) 7 days. A development in pore space can be observed by the separation of the single peak into smaller peaks when approaching 6 and 7 days. (Reprinted from *Magnetic Resonance Imaging, Volume 25, Issue 4*, Peter J. McDonald, Jonathan Mitchell, Michael Mulheron, Luc Monteilhet, Jean-Pierre Korb, *Two-dimensional correlation relaxation studies of cement*, pages 470–473, Copyrights 2007, with permission from Elsevier [127]).

In a follow-up study [128], the dynamic porosity in cement paste during water up-take and drying was studied, using  $T_2$  relaxation. Three main groups were found that correspond to different pore sizes: hydrates inner layers of 1 nm ( $T_2 = 120 \mu\text{s}$ ), gel pores of 3–5 nm ( $T_2 = 360 \mu\text{s}$ ) and capillary pores larger than 5 nm ( $T_2 = 1080 \mu\text{s}$ ). The final signal intensity will be a contribution of all hydrogen pools as given by equation (3.17). Figure 3.6a, shows a typical signal decay where the solid line is the total decay and marked with dashed lines are the contributions of the different pores. For completeness, the authors added a dotted line representing the part coming from the crystalline solid. Using this multi-exponential decay, the researchers could follow the different types of hydrogen atoms during evaporation (Figure 3.6b) and moisture uptake (Figure 3.6c). Red corresponds to water in capillary-sized pores, green to gel-sized pores and blue for



interlayer pores and black is the total amount of moisture. The authors observed that after 1 hour, the moisture uptake already reaches 90% of its total amount. A striking fact is that they saw for the first time that moisture will start to redistribute between the different pores. In this research, they only looked at a particular part in the layer, however, with GARField, MOUSE or STRAFI, the same information is available at every position in the layer.

Studies on cement like-materials such as pastes and Portland cement have also been performed on STRAFI [209]–[211] and MOUSE [210], [212]. In other studies, this separation based on relaxation times was used to separately study water and polymer contribution in latex films [181], [213], human skin [214] and polymers such as Polyurethane coatings [215], plasticizing of nylon-6 [216], [217], semi-crystalline polyethylene [218] and photo-polymerization of methacrylate [219]. Additionally, medical applications, such as the binding behavior of collagen-binding liposomes, have been studied [220], [221]. Even layers with very low relaxation times, such as ice ( $T_2=3.5 \mu\text{s}$ ), have been imaged during melting using a STRAFI setup [197].

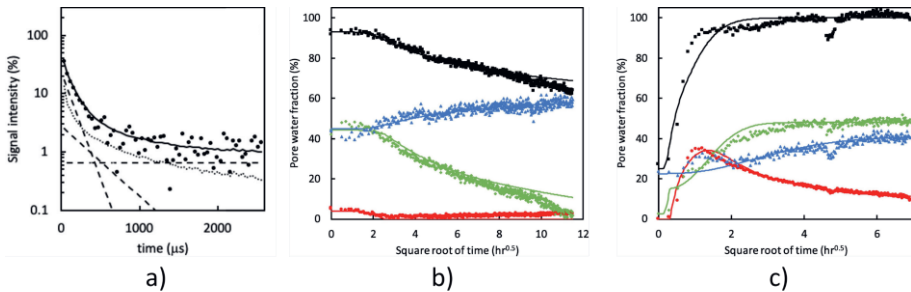


Figure 3.6 a) Signal intensity decay measured by a quadrature echo train. The solid line is the total fit. The dashed lines represent the fractions with different  $T_2$  times ( $120 \mu\text{s}$ ,  $360 \mu\text{s}$  and  $1080 \mu\text{s}$ ). b) and c) Pore water fractions measured  $600 \mu\text{m}$  below the surface during drying (b) and wetting (c). Red corresponds to water in capillary pores, green to gel sized pores and blue to interlayer spaces. Black represents the total hydrogen content. (Reprinted from *Cement and Concrete Research*, Volume 133, Peter J. McDonald, Ors Istok, Magdalena Janota, Agata M. Gajewicz-Jaromin, David A. Faux, Sorption, anomalous water transport and dynamic porosity in cement paste: A spatially localised  $1\text{H}$  NMR relaxation study and a proposed mechanism [128]).

In addition to  $T_2$  and  $T_1$  relaxation, another way to characterize the structure of thin layers is via the diffusion coefficient  $D$  of the hydrogen atoms. In materials, water can be present in a wide variety of states with different diffusion coefficients such as free water, water confined in pores or water bound to the polymer matrix. When materials undergo a structural transition, the water diffusivity will be altered, giving insight into the internal structure of the layer. A study performed by B. Voogt et al. [213] demonstrates this principle. The researchers used the proton local mobility and diffusivity to characterize the structure of hard and soft latex during drying. By measuring the  $T_2$  relaxation time with different echo times, the diffusion coefficient was determined, see Equation (3.14). Figure 3.7 shows the diffusion coefficient measured at different times steps during drying. From  $t = 30 \text{ min}$  onward, the diffusion constant was too low to be determined. As a result of drying, the particles' mobility will be restricted,

lowering the auto-diffusion  $D$  (Figure 3.7) and the  $T_2$  of the atoms. The  $T_2$  of latex remained rather constant around 0.1 ms, indicating that the proton mobility is constant. By analyzing the diffusion constants and relaxation times, they found that water changes from a free state towards pore water and finally, water that is physically bound to the polymer matrix. The researchers also observed a difference in packing between the soft and hard type of latices. The relative concentration of the polymer increased in the soft type but remained constant in the hard type. This indicates that in the soft type, the particles come closer together, forming a close packed structure, while for the hard type, this is not possible due to the hardness. These measurements clearly show the restricted movement of the hydrogen atoms.

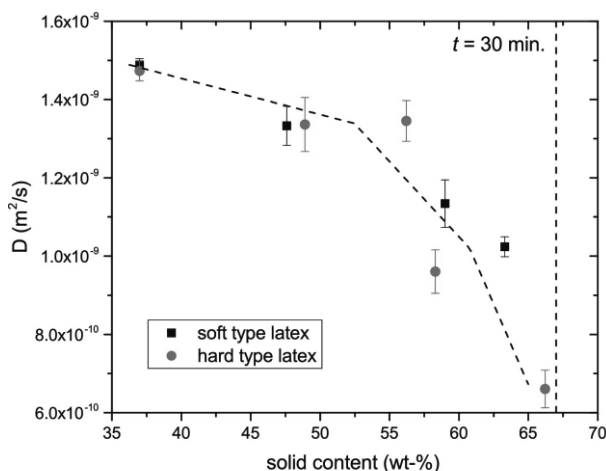


Figure 3.7 Diffusion coefficient of free water within the hard- and soft-type latex. (Reprinted from *Progress in Organic Coatings*, Volume 123, Benjamin Voogt, Henk Huinink, Bart Erich, Jurgen Scheerder, Paul Venema and Olaf Adan, *Water mobility during drying of hard and soft type latex: Systematic GARField  $^1H$  NMR relaxometry studies*, Pages 111–119, Copyrights 2018, with permission from Elsevier [161]).

In a similar study performed by V. Baukh et al. [217], multilayered coatings were investigated. The authors found that the diffusion coefficient increased with water content and that binding of water to the polymer was stronger at low water concentrations. In other studies, diffusion coefficients were measured in order to determine the amount of bacteria [198] or structural changes in water-swollen cellophane [222].

As the diffusion coefficient depends on the structure of the material, it can also be used to differentiate layers in heterogeneous structures. P. J. McDonald et al. [125] used this method to determine the diffusion constants and profiles of the human skin in vivo. The measurements revealed a clear contrast between the stratum corneum and viable epidermis. This contrast was largely attributed to a difference in diffusion constant between both layers. Comparable studies on human skin that characterized the different skin layers were performed on GARField [124], [223] and MOUSE [214], [224]. In addition to water and polymers, studies on small penetrants such as toluene and n-hexane in PE pellets have also been performed [225].

### 3.5.2. Film Formation Drying

Film formation is the process in which a polymer emulsion or colloidal dispersion will overcome their stabilizing forces to form a continuous film. These stabilizing forces can be overcome when the continuous liquid phase evaporates, forcing the emulsion droplets or polymer particles together. The evaporation of excess liquid is referred to as the drying phase of the film formation process. When enough liquid has evaporated, the polymers or colloidal particles need to form a continuous film. After solvent evaporation, there are two types of processes: curing and coalescence [226]. In the curing process, a stable film is formed by cross-links between reactive polymers. On the other hand, in coalescence, the polymer particles will first coalesce and deform to form a close packed structure. In order to form a homogeneous film, deformation is followed by entanglement of the polymer chains. Particle boundaries disappear, which will lower the film roughness [97]. All these combinations of drying, curing and coalescence make film formation a complicated process. Since most applied films and coatings undergo film formation, this section is dedicated to studies that are focused on this topic. First, drying experiments and then the subsequent processes are discussed.

During drying, water or solvent evaporates from the polymer film, mostly reducing the overall thickness. A representative example of a study on the drying processes of waterborne colloidal films was performed by J.-P. Gorce et al. [227]. Measurements were performed on a GARField setup using an OW-sequence with a 8.7  $\mu\text{m}$  resolution. Profiles of the NMR signal measured at different times are shown in Figure 3.8. The width of the signal corresponds to the thickness of the polymer film. First of all, evaporation leads to film shrinkage due to the disappearance of hydrogen atoms. When all water has evaporated, the profile reaches its final thickness, corresponding to 150  $\mu\text{m}$ . This decrease in profile thickness can be used to characterize a drying front and a corresponding drying rate. Secondly, the maximum signal intensity reduces over time from 0.7 to 0.4. To understand the reduced signal, we need to introduce two hydrogen pools  $\rho_a$  and  $\rho_b$ , setting  $\beta=2$  in equation (3.17). The signal intensity is then determined by,

$$S \propto \rho_a \exp\left(-\frac{t_e}{T_{2a}}\right) + \rho_b \exp\left(-\frac{t_e}{T_{2b}}\right) \quad (3.25)$$

where we have left out the  $T_1$  term. Here, the signal is split into a term coming from the solvent ( $\rho_a, T_{2a}$ ) and one coming from the polymer or colloidal particles ( $\rho_b, T_{2b}$ ). When solvent is released, the total active hydrogen atoms  $\rho$  is almost unchanged as hydrogen atoms from the water are replaced by the ones from the polymer. Therefore, the signal decrease cannot be attributed to a loss in active hydrogen atoms. However, the relative contributions do change, where during drying  $\rho_a$  reaches zero,  $\rho_b$  reaches its maximum. As the mobility of the polymer is much lower than that of free water, the  $T_2$  of the polymer is lower than that of free water by at most one order of magnitude (see section 3.2.1). Faster relaxation leads to a lower signal, where the final signal amplitude is closely related to the mobility of the polymer phase which in this case was very low. In the beginning, the signal intensity (0.7) is dominated by the solvent ( $\rho_a \exp(-t_e/T_{2a})$ ); after drying, the signal will be determined by the polymer ( $\rho_b \exp(-t_e/T_{2b})$ ) which due to a faster decay will have a lower signal intensity (0.4).

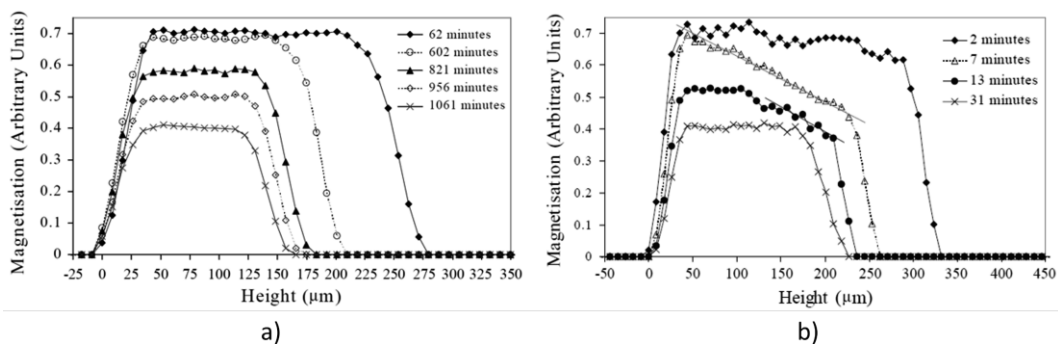


Figure 3.8 NMR profiles measured during film drying of an alkyd emulsion in closed environment with  $P_e = 0.2$  (a) and with  $P_e = 16$  (b). The water fractions were determined for every profile. In figure a, the fraction were 0.48 (62 min), 0.33 (602 min), 0.23 (821 min), 0.15 (956 min) and 0.09 (1061 min). In figure b, the fractions were 0.44 (2 min), 0.25 (7 min), 0.15 (13 min) and 0.10 (31 min). (Reprinted by permission from Springer Nature Customer Service Centre GmbH Springer Nature: *The European Physical Journal E—Soft Matter, Vertical water distribution during the drying of polymer films cast from aqueous emulsions*, J.-P.Gorce et al., 2014 [227]).

In the same study, the influence of the Peclet number  $P_e = vL_{ef}/D$  was investigated, where  $v$  [ $\text{ms}^{-1}$ ] is the speed of receding waterfront,  $L_{ef}$  [m] the layer thickness and  $D$  [ $\text{m}^2\text{s}^{-1}$ ] the diffusion coefficient. By controlling the thickness, the speed of the receding waterfront and the diffusion coefficient, the  $P_e$  number could be adjusted. When  $P_e > 1$ , advection dominates, but for  $P_e < 1$ , diffusion is more important. Figure 3.8a shows profiles for the case where  $P_e = 0.2$ , whereas Figure 3.8b shows profiles for the case where  $P_e = 16$ . A difference in profile shape was observed indicating that diffusion towards the surface can keep up with the evaporation (flat profiles) when  $P_e = 0.2$ . On the contrary, when  $P_e = 16$ , diffusion towards the surface cannot keep up with evaporation and a concentration gradient of water molecules is observed near the surface. The formation of this dense polymer layer at the surface decreased diffusion towards the surface, slowing down the evaporation.

In a comparable study performed by P. Ekanayake et al. [228], density profiles of drying colloidal films revealed that the particle concentration gradient inside this dense layer of colloidal particles scales with  $P_e^{0.8}$ . Furthermore, in this study, the GARField setup was chosen as it has the best resolution, allowing to see this thin dense top layer.

In some cases, drying induces the formation of a skin layer that can trap water. These skin layers reduce solvent evaporation and significantly slow down the drying process [98], [99]. E. Ciampi et al. [98] investigated skin formation upon drying of poly(vinyl alcohol) (PVOH). Profiles were measured with a GARField NMR for an initial PVOH content of 10 wt% and 25 wt%. The profiles for the 10 wt% dried similarly to the ones measured by [227]. In case of high-polymer-weight fractions (25 wt%), a skin layer developed that trapped water inside the profile, leading to slower evaporation.

Similar studies of the drying behavior of different polymers, such as alkyd layers [159], [192], [229], [230], latex layers [213], gelatine layers [231] and even dental resins [194], [232]–[234], have been conducted using the GARField, STRAFI and MOUSE NMR setups.

### 3.5.3. Film Formation Curing

In case of reactive compounds, a curing reaction can start when enough water evaporates, and the polymer content is high enough. Measurements with GARField on drying alkyd coatings [229] illustrate the capability to measure the drying–curing film formation process. In this study performed by S. J. F. Erich et al., NMR profiles were measured every 10 min with an OW-sequence as seen in Figure 3.9. The profiles reveal this two-stage process where the polymer layer first dries which results in shrinkage and intensity drop due to solvent evaporation, as explained in previous section. This process is indicated by the arrows in Figure 3.9. After drying, a (reaction) curing front moves into the polymer film. The signal loss due to curing of polymers can be attributed to the loss in mobility of the polymer. When polymers are cured, they become more rigid, the  $T_2$  drops, and signal is lost when the  $T_1$  approaches  $t_e$ .

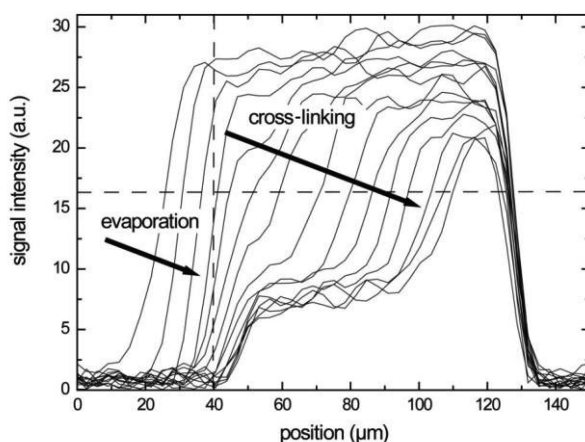


Figure 3.9 Hydrogen profiles of a solvent-borne alkyd sample measured during drying. The top of the coating corresponds to the left side, while the cover glass can be found on the right. The vertical dashed line indicates the top of the film after drying. (Reprinted from S. J. F. Erich, J. Laven, L. Pel, H.P. Huinink, and K. Kopinga, "Dynamics of cross linking fronts in alkyd coatings", *Appl. Phys. Lett.* 86,134105 (2005) <https://doi.org/10.1063/1.1886913>, with permission of AIP Publishing [229]).

In the study of S. J. F. Erich et al. [229], curing experiments were performed on water-borne and solvent-borne alkyds. Both systems showed the same behavior where first, an evaporation and second a curing stage could be distinguished. In a related paper [159], NMR and confocal Raman Microscopy were compared, and the curing could be related to the disappearance of double bonds and the formation of oxidative cross-links. These cross-links lowered the hydrogen mobility and reduced the NMR signal, giving rise to the observed curing front. Tracking these fronts in different environmental conditions revealed that oxygen supply was the limiting factor in the curing front dynamics.

Further, the effect of drying on porous media [192], catalysts [235]–[238] and pigment volume concentrations [239] was studied.

Curing also plays a role in dental resins. By exposing the resin to a light source, it will begin to polymerize and shrink. This polymerization shrinkage (PS) is crucial for the

durability of the material, as it will determine stresses and strains in the film and the uptake of fluids and bacteria. A polymer that is widely used as a dental bonding agent is dimethacrylic acid. Curing studies on this polymer have been performed with a STRAFI NMR [194], [232]–[234]. In an experiment performed by T. Nunes et al. [194], glass vials were filled with a liquid resin. The liquid resin was exposed to light. Different groups of hydrogen atoms could be discriminated based on their  $T_2$  and  $T_1$  relaxation times: mobile molecules (free monomers) with long relaxation times and rigid molecules (cured AB2). It was found that oxygen strongly influenced the kinetic behavior. Using STRAFI, the influence of different cements and curing protocols could be determined and all were shown to affect the curing process, and they should be chosen with care in medical applications.

Other curing measurements can be found for the curing of wood glue layers [230] and gelatine layers (biopolymer) [231].

### 3.5.4. Film Formation Coalescence

In some applications, film formation involves coalescence (e.g., with latex particles). In case of latex dispersions, film formation occurs due to deformation and the interdiffusion of polymer chains rather than curing. Well-known applications are water-based paints [240]–[243] or pressure-sensitive adhesives [99], [244]. The deformation and interdiffusion of these polymers depends on the mobility of the latex particles, reflected by their glass transition temperature ( $t_g$ ) [213]. The sequence of events can overlap in time and the processes can also influence each other. For instance, the water fraction will influence the mobility of the polymer chains [213], [245], leading to a decrease in deformation and interdiffusion upon drying [152]. Studying these processes with NMR can give crucial information, leading to a better understanding of unwanted effects such as film cracking [246], trapped water [99] and irregular particle formation [247].

To illustrate the use of high-resolution NMR for studying latex film formation, we use a study by B. Voogt et al. [213] as an example. In this study, drying of both soft ( $t_g <$  room temperature) and hard ( $t_g >$  room temperature) latices were studied inside a GARField NMR. Measurements were performed with an OW-sequence with  $t_e = 2\tau = 40$   $\mu$ s. Figure 3.10 shows profiles measured during drying of both soft- (a) and hard-type (b) latices at an RH of 80%. As discussed in section 3.5.2, a stepwise process is observed where first evaporative drying takes place. This will induce film shrinkage due to water evaporation which can be observed via a receding drying front. This leads to a higher concentration of latex particles. In both films, thickness ( $d$ ) and maximum signal intensity ( $S_{max}$ ) decreased over time. It was observed that the hard-type latex dried much faster. Hard-type latex thickness decreased until 20 min, while for the

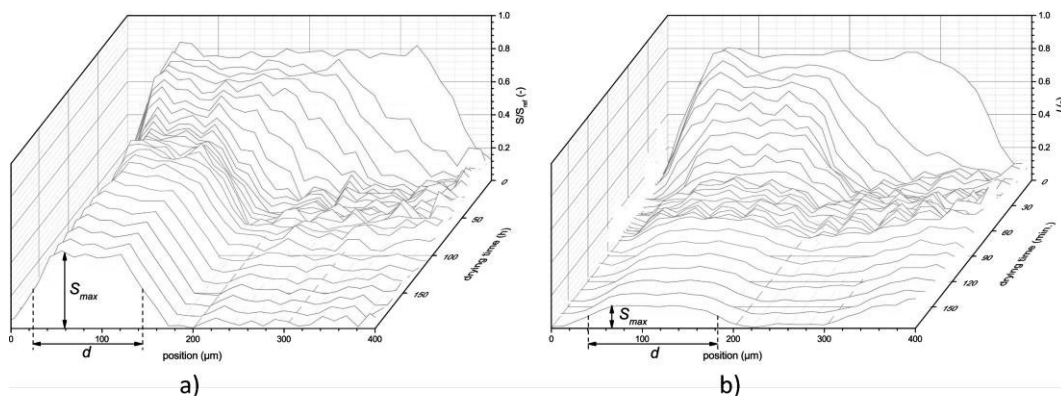


Figure 3.10 NMR signal intensity profiles during drying of a) soft and b) hard type latex.  $S_{max}$  and  $d$  are the coatings maximum signal intensities and thicknesses. (Reprinted from *Progress in Organic Coatings*, Volume 123, Benjamin Voogt, Henk Huinink, Bart Erich, Jurgen Scheerder, Paul Venema and Olaf Adan, *Water mobility during drying of hard and soft type latex: Systematic GARField  $^1\text{H}$  NMR relaxometry studies*, Pages 111–119, Copyrights 2018, with permission from Elsevier [161]).

soft latex, this only happened at 40 min. The maximum intensity of the hard-type latex also lowered faster and ended lower at around 0.2, while for the soft latex a signal intensity of 0.6 was observed, both leveling off at 40 min. The difference in leveling off between  $S_{max}$  and  $d$  for hard latex suggests a continuation of bulk water evaporation, while the latex particles are fixed in position and are not able to keep concentrating. This is understandable as particles below their  $t_g$  will form brittle and porous networks [97] and are unable to form a continuous film.

In this study by B. Voogt et al., the protons in free water and polymer were studied simultaneously, using a multi-exponential decay analysis. A typical OW-decay is shown in Figure 3.2b. For both latices, a clear multi-exponential decay was observed where the short relaxation time could be linked to the polymer and the long relaxation time to the free water phase. Both short relaxation times are fixed at 0.1 ms, showing that both latices have proton pools with mobilities that are not affected by drying. These are the protons embedded within the latex.

Using this multi-exponential decay, the different concentrations could be followed over time. The researchers found that a loss of free water ( $\rho_{long}$ ) due to evaporation was independent of the lattice type. However, the latex fraction showed an increase for the soft latex type ( $\rho_{short}$ ), indicating a further increase in concentration. This effect was not observed in the hard latex type. The increase in proton density was the consequence of coalescence of the particles. When film formation happens above the polymers  $t_g$ , the polymer mobility is high enough that the polymer chains can interdiffuse and form a polymer film. This indicates that the  $t_g$  of latex has a huge influence on the film formation processes and the coalescence of the particles.

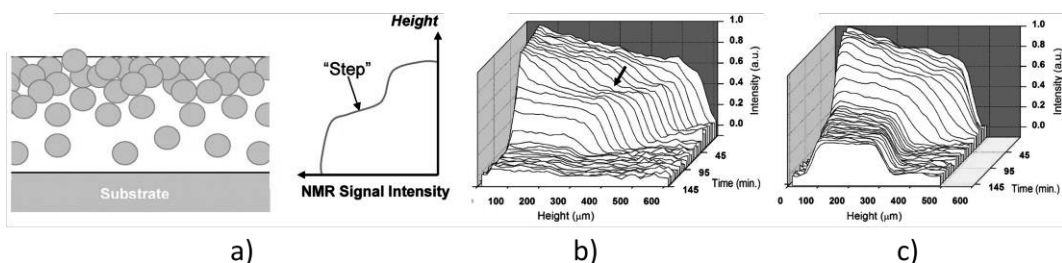


Figure 3.11 a): schematic representation of latex packing near the surface accompanied by a representation of the corresponding NMR signal. NMR profiles measured over time for (b) acrylic copolymer latex (SM0) and (c) 25 wt% PDMS on the acrylic monomer (SM25) (Reprinted with permission from *Macromolecules* 2008, 41, 22, 8537–8546. Copyright 2008 American Chemical Society [248])

Other studies have focused on the coalescence of particles at the liquid–air interface, leading to a “skin-layer” [99], [248]. In certain compositions, coalescence appears near the liquid–air interface during the drying stage. This is schematically represented in Figure 3.11a. This skin-layer will block the evaporation, leading to trapped water within the film. R. Rodriguez et al. [248] studied the film formation for different compositions: acrylic copolymer (SM0), a hybrid latex containing 25 wt% PDMS (SM25), and a blend of the acrylic (SM0) with 11 wt% PDMS emulsion. Drying measurements on two of these compositions are shown in Figure 3.11, namely, SM0 (b) and SM25 (c). The SM0 polymer had a much lower mobility than the SM25. Therefore, the signal intensity for SM0 was almost zero after drying, while for the SM25 there was still signal. By setting the echo time to 180 μs, the researchers made sure that almost no signal was attributed to the SM0 polymer and the signal could be attributed to free water. In both drying experiments, the signal intensity increased in the depth of the film. This increase was also observed in other studies [99] and was attributed to a gradient in free water. In the neat acrylic dilution (SM0), a deviation from this linear behavior was observed where a layer with lower signal intensity appeared at the top. This indicated a step in the free water concentration and a denser packing of latex particles at the surface (Figure 3.11a) which showed to increase in thickness over time. This drastic step in particle density was not observed in the SM25, see Figure 3.11c. Here, a more uniform profile was observed that reached its final form at 55 min.

Other studies used similar NMR measurements to study the effect of glass transition temperature [249], surfactant [244], tackifying resins (TR) [99], salts [250], different amounts of carboxylic acid functional groups [181] and the Peclet number [227] on the film formation process. GARfield NMR seems to be the best technique for these processes, as it has a high-enough FOV to cope with the latex films and can give the best resolution. However, measurements with a MOUSE were also performed on latex films [195]. This, however, led to lower resolutions (30 μm) and was hampered by long measurement times.



### 3.5.5. Diffusion and Penetration

Liquid uptake and diffusion in thin layers are important for coatings, the printing industry or sustainability of materials. Water and solvents can weaken interactions between neighboring polymers and ultimately lead to failure of the thin layer by softening or cracking. Both liquid content and penetration speed are crucial parameters in characterizing the stability of thin layer. In this section, it will be shown how NMR profiling has been used to measure liquid penetration over time. A crucial parameter for solvent penetration is the diffusion coefficient ( $D[\text{m}^2\text{s}]$ ). This parameter is, however, difficult to measure because it depends on morphology such as crystallinity [251] or temperature.

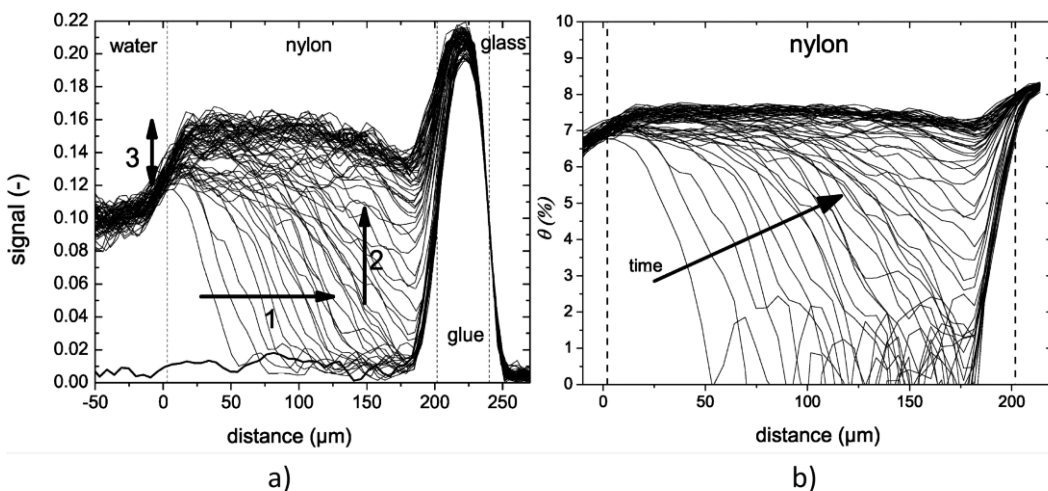


Figure 3.12 a) Liquid profiles measured during uptake of water into 200  $\mu\text{m}$  thick nylon membranes. b) same profiles as in the middle graph but after replacing the signal intensity with the moisture content. (Reprinted with permission from *Macromolecules* 2012, 45, 4, 1937–1945. Copyright 2012 American Chemical Society. [252]).

To illustrate the capability of high-resolution NMR depth profiling in studying penetration and diffusion experiments, a study by N. J. W. Reuvers et al. [252] is used.

In this study, the water uptake in thin nylon-6 films was measured with a GARField NMR using an OW-sequence. Figure 3.12a shows the profiles measured during the water uptake within a 200  $\mu\text{m}$  thick nylon-6 membrane. When going from right to left, the glass plate, glue layer, nylon and water can be observed. While the glass plate cannot be imaged by the NMR, a clear difference between the silicon glue, nylon film and water is observed. The observed differences in signal intensities could be linked to varying  $T_2$  and  $T_1$  times. Shown with a bold line is the signal intensity measured before the experiment. The researchers distinguished three different processes. (1) liquid front development, traveling towards the bottom of the layer ( $t < 6 \text{ h}$ ), (2) water distributes equally over the film ( $6 \text{ h} < t < 10 \text{ h}$ ) and (3) a slower process occurred where a small signal increase is observed near the glass–polymer interface. Using these profiles, the researchers determined the actual diffusion coefficient within the layer. To be able to do this, the researchers needed to convert the NMR signal intensity to moisture content ( $\theta$ ). They could link the NMR signal to a moisture profile using a gravimeter calibration [252].

The resulting relationship was nonlinear and was attributed to plasticization and a change in relaxation of free water. The NMR signal profiles in Figure 3.12 can be viewed as a superposition of a liquid front and plasticization front. Using the relation between moisture content and NMR signal, the original NMR profiles (Figure 3.12a) are converted to moisture content profiles (Figure 3.12b). The small signal increase observed before (3) could be attributed to polymers that become more mobile and contribute to the signal.

The moisture profiles were used to extract the diffusion coefficient of water within the nylon film. The calculated diffusion coefficients are shown in Figure 3.13a. The diffusion coefficient increased with increasing moisture content.

To study the signal change due to plasticizing, the excess water was replaced by  $D_2O$ .  $D_2O$  has the same characteristics as water but will not contribute to the NMR signal. Half the NMR signal in the profiles was linked to hydrogen atoms of water and half of the signal to mobilized polymer. Additionally, the glass transition temperature and  $T_2$  relaxation could be linked with moisture content (Figure 3.13b). In a follow-up study, it was found that the plasticization lags behind the water migration in these nylon-6 thin films [253].

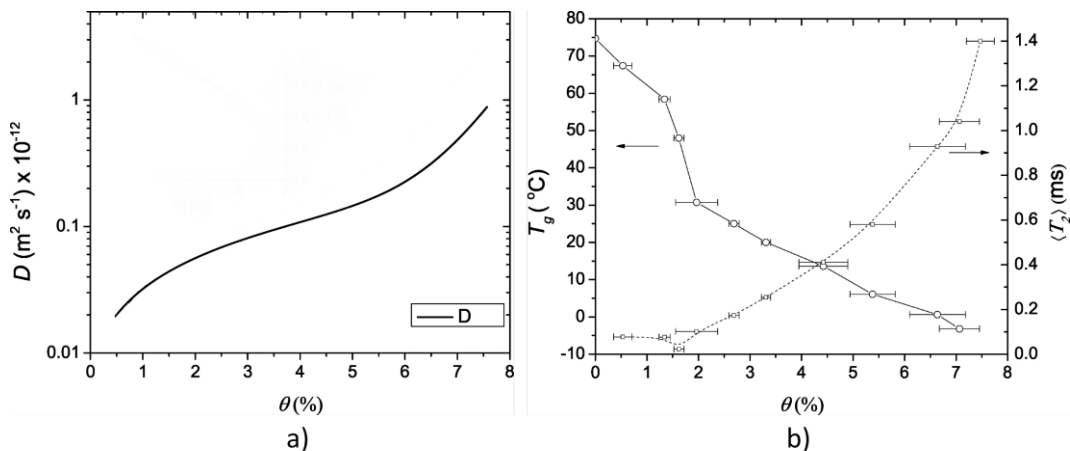


Figure 3.13 a) the diffusion coefficient ( $D$ ) in function of moisture content. b) The glass transition temperature ( $t_g$ ) and average relaxation time ( $T_2$ ) in function of moisture content. (Reprinted with permission from *Macromolecules* 2008, 41, 22, 8537–8546. Copyright 2012 American Chemical Society [252]).

Similar penetration studies have been performed on dental resins. Using STRAFI, G. Hunter et al. [234] studied the uptake of water and water/ethanol mixtures into a commercial dental resin. Measurements with different ethanol concentrations revealed that the diffusion coefficient increased with ethanol content. Additionally, transport in ceramic substrates [254], multilayer coatings [217], [255], glassy pellets of the starch polymer amylose [199], cement pastes [211] glue lines [230], vulcanized rubber [256] and nylon-6 [216], [217] have been studied. In addition to the penetration of water, the transport of different ions such as  $Mn^{2+}$  and  $Cu^{2+}$  [257], different salt solutions [258] and the ingress of vapors [259], [260] have also been studied with the NMR setups. Finally, the influence of stress on the penetration behavior was studied by V. Baukh et al. [261].

### 3.5.6. Thins Films on Site: Cultural Heritage

In some applications, measurements of thin layers need to be performed outside the lab because it is impossible to collect small samples or to recreate a similar structure. As the STRAFI and GARField setups are located within the lab and require samples of a specific shape and size, measurements on site are performed by NMR-MOUSE. The portability of the NMR-MOUSE makes it possible to measure samples with infinite lateral dimensions where limits are mostly bound because of time constraints. One big category of such applications studied with the NMR-MOUSE is cultural heritage [262]: for example, in case of paintings on wood. A significant issue with cultural heritage is structural damage during conservation. Using the NMR-MOUSE, the internal structure of paint layers can be studied. These studies can help in characterizing different sources of damage and identifying the best conservation environment.

Damage of cultural heritage is mainly caused by moisture uptake which, for example, in wooden painting or walls, can cause degradation over time. Measuring the moisture distribution can provide information on the conditions in which the painting should be stored and can help in preserving cultural heritage [90]. In this section, a closer look at some analysis methods will be given, demonstrating the use of the NMR-MOUSE on cultural heritage.

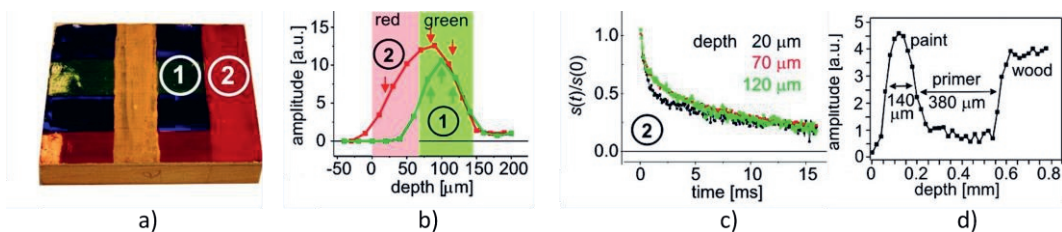


*Figure 3.14 a) Easel painting model with a wooden background covered by a primer and one (1) or two (2) paint layers. b): measured depth profiles for the position marked in a. A clear difference in thickness is observed between both layers where one layer is thinner than the two layers. c) Signal decay measurements at position 2 for different depths. d) Complete depth profile through the painting indicating the different layers. (Reprinted with permission from Acc. Chem. Res. 2010, 43,6, 761–770. Copyright 2010 American Chemical Society [89]).*

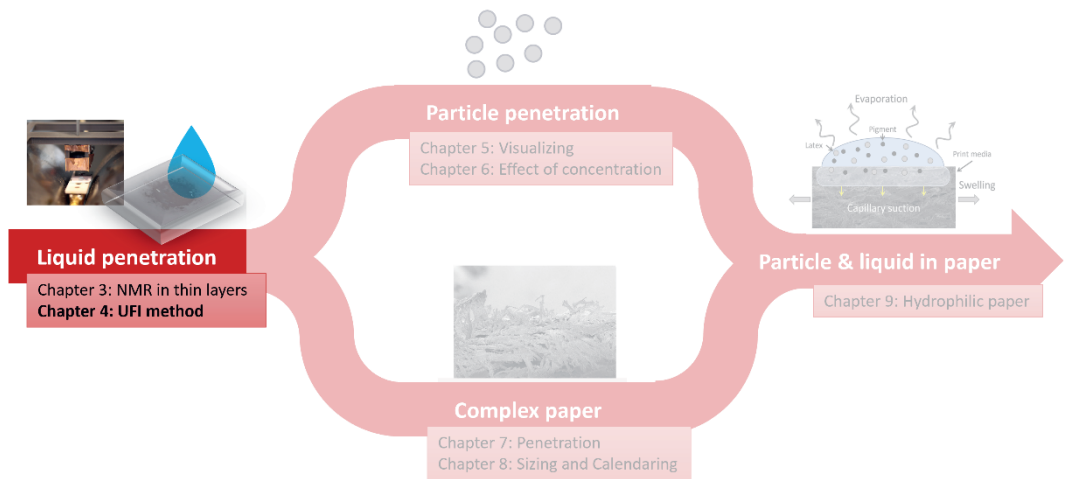
B. Blümich et al. [89] demonstrated the use of the NMR-MOUSE for studying the layered structure of paintings. The researchers started with a wood panel covered by a primer and one or multiple layers of paint. They tried to mimic the structure found in old paintings. Figure 3.14a shows a picture of the structure where two positions are marked with either one (1) or two (2) layers of paint. Depicted in Figure 3.14b are the depth profiles measured by an NMR-MOUSE of the two positions shown in Figure 3.14a. Both paint layers had good signal and the thickness of the layers was also reflected in the width of the NMR signals. Imaging different layers was performed both with total amplitude measurement (Figure 3.14b) and characterizing the signal decays (CPMG Figure 3.14c). In Figure 3.14d, the total NMR signal was measured along the thickness of the painting revealing a layered structure of paint, primer and wood. Using this method, the thickness of the different layers could be monitored at different points, revealing damage at certain positions. The CPMG could give information about changes within the layers over time.

In the same paper, the authors also demonstrated the ability to characterize old paper structures by measuring the hydrogen atoms in the cellulose fibers, time- dependent water uptake and drying in stone. Even old master violins such as a Stradivari were investigated in this way. The study revealed that the master violins' wood density increased with age, which determined the quality of the instrument. This measurement technique was also used for the ancient Roman fresco and bricks in the walls of the cryptoporticus at Colle Oppio in Rome [263], the degradation of historical paper [142] and the conservation treatments on paintings [264]-[266].

### 3.6 Conclusions

In this chapter, three different high-resolution NMR setups able to study thin layers between 10 and 1000  $\mu\text{m}$  were reviewed, namely, STRAFI, GARField and MOUSE. These NMR techniques are all able to give spatial and time-resolved information about structural changes and transport in thin layers. The setups used two different acquisition methods: slice-selective pulse- and Fourier-measurements. In the slice-selective pulse measurements performed by MOUSE and in conventional STRAFI, the signal is recorded in a stepwise manner, whereby the pulse excites the region of interest. In this case, the resolution is determined by the pulse length given by  $\Delta r \approx 1/t_p \gamma G$ . High resolution can be achieved at the expense of long measurement times. The advantage of the stepwise acquisition is that sample size is only limited by the aperture used. Unfortunately, the resolution is limited by the large curvatures found in the main magnetic field  $\vec{B}_0$  of both STRAFI and MOUSE and should be determined experimentally. In GARField and in some cases in STRAFI, the acquisition is achieved by a Fourier analysis. The sample is excited with one pulse (limiting the total measurement area) where the resolution is determined by the acquisition time, given by  $\Delta r \approx 1/t_a \gamma G$ . As the sample is measured using one pulse, measurements are much faster. In GARField, the problem with the inhomogeneous field is solved by specially designed poles leading to the best space and time resolution found in all the setups. Moreover, Fourier STRAFI exists, which can measure much faster than conventional STRAFI. However, due to the arrangement of the magnetic field, a solenoid-shaped coil is needed that compared to the surface coil in GARField will always have lower sensitivity. A drawback of this special design is that GARField lacks the ability to measure samples larger than 400  $\mu\text{m}$ . To measure larger samples, STRAFI would be more appropriate. Finally, the NMR-MOUSE has proven to be valuable in cultural heritage because it is the only mobile device able to measure depth profile on-site in a non-invasive manner.

A variety of applications such as drying, film formation, penetration, structural changes and measurements on cultural heritage have been reviewed illustrating the potential of these NMR-profiling tools. By measuring hydrogen profiles over time, the setups were able to follow drying, curing and penetration fronts. Using these profiles, the diffusion coefficient and front kinetics could be determined for a wide variety of parameters. Detailed structural information about thin layers could be gathered by measuring  $T_2$  and  $T_1$  relaxation times and signal intensities. The information could be used to follow film formation, film degradation, penetration, and diffusion experiments.



# 4

## Ultra-Fast Imaging (UFI) NMR method: liquid uptake

To measure moisture distributions during fast transport processes in thin, porous media, a novel Ultra-Fast Imaging (UFI) NMR method is used which is able to measure with a 14.5  $\mu\text{m}$  spatial and 10 ms temporal resolution. This chapter gives a detailed explanation about the methodology and the interpretation of the signal intensity. It is shown that there exist specific conditions for the  $T_1$  and  $T_2$  relaxation times to achieve optimal signal-to-noise ratios. In most cases, a contrast agent is required to optimize these relaxation times. In this chapter, two contrast agents are studied as possible candidates:  $\text{CuSO}_4$  and Clariscan. Furthermore, it is shown that the signal intensity can be linked to the moisture in porous films that contain water-based liquids. The UFI-method is then tested by performing penetration experiments on porous PVDF and nylon-6,6 membranes. Finally, these penetration experiments will be compared to automatic scanning absorptiometry which showed a good agreement with the NMR experiments and Darcy based penetration behavior.

*Adapted from:*

1) R. J. K. Nicasy, H. P. Huinink, S. J. F. Erich, O. C. G. Adan, and N. Tomozeiu, "Ultra-Fast Imaging NMR method for measuring fast transport processes in thin, porous media," *Magn. Reson. Imaging*, vol. 103, pp. 61–74, Nov. 2023, doi: 10.1016/j.mri.2023.06.009.

2) R. J. K. Nicasy, H. P. Huinink, S. J. F. Erich, and O. C. G. Adan, "High-speed NMR imaging of capillary action in thin nontransparent porous media," *Phys. Rev. E*, vol. 104, no. 4, p. L043101, Oct. 2021, doi: 10.1103/PhysRevE.104.L043101.

### 4.1 Introduction

Equation Section (Next)The absorption of liquids in thin porous layers such as polymeric membranes and paper is an everyday phenomenon and crucial for applications such as paper-based microfluidics [267]–[269], printing [17], [82], [270], coatings [161], [255], towels or tissues [271], [272] and cooling of micro-electronics [38], [273]. The rapid growth of these technologies demand a better understanding of the physical mechanisms that influence the fluid flow. In most cases, liquid absorption is driven by the capillary pressure, in which case the liquid uptake can be described by models such as Lucas-Washburn's [274], [275] and Darcy's law [276]. However, experimental data

revealed deviations from these theoretical models [46], [277]. In the past decades, a wide variety of studies was performed towards the applicability of these laws for different porous systems such as paper [278]–[280] leading to refinements of the models. However, as explained in the introduction, experimental verification during capillary uptake is challenging for a few reasons. Firstly, in case of fast capillary uptake the time scales of interest often go below 1 s. Secondly, in the case of paper sheets or membrane filters, the thicknesses of around 100  $\mu\text{m}$  form a challenge. Therefore, the measurement techniques should have a sufficient spatial and temporal resolution to cope with this.

How NMR can cope with high spatial resolutions was the main topic of chapter 3. The goal of this chapter is to demonstrate that by combining the GARField setup (introduced in chapter 3) and an ultra-fast imaging (UFI) method, it is possible to measure in real time, fluid redistributions in thin, porous media with a resolution between 14.5–18  $\mu\text{m}$  and a minimum temporal resolution of 10 ms.

The goal of this chapter is to provide an in-depth discussion of the UFI NMR technique. The UFI technique will be used as a consistent method for measuring liquid and particle redistributions throughout this thesis. The in depth-discussion within this chapter will establish the foundation necessary to understand the measurements performed within the remainder of this thesis. The chapter starts by introducing the common models used to describe capillary uptake followed by a theoretical analysis of the signal intensity, were the two main ingredients: summation of the echoes which ensure a rapid increase in the signal-to-noise ratio and shortening of the  $T_1$  relaxation time of the solution by adding a contrast agent will be discussed. information about the echo summation and  $T_1$  shortening. In the results section, the usage of contrast agent to optimize the signal intensity is demonstrated. Finally, liquid distribution measurements during uptake in PVDF and nylon-6,6 membranes are discussed, which are compared with Automatic Scanning Absorptometer (ASA) experiments.

## 4.2 Liquid Absorption in thin, porous media

To describe liquid penetration in thin, porous media, different theoretical models can be used. In this chapter, Darcy and Washburn, two of the most commonly used models to describe the fluid front position as a function of time are introduced.

### 4.2.1. Liquid front as a function of time for a sharp front

When assuming that in the porous media, liquid moves with a liquid front  $l$  [m], and assuming mass conservation, the simplest form to describe the relation between volume flux  $\vec{q}$  [ $\text{m s}^{-1}$ ] throughout the media and the front position is by,

$$\vec{q} = \phi \frac{dl}{dt}, \quad (4.1)$$

where  $\phi$  is the porosity of the porous media. To solve this equation for  $l$ , we need a relation for the volume flux  $\vec{q}$ . A commonly used model for the volume flux in a porous media is Darcy's Law, which relates the volume flux  $\vec{q}$  in 3D [ $\text{ms}^{-1}$ ] to the exerted forces, and is given by,

$$\vec{q} = -\frac{k}{\eta} \nabla P, \quad (4.2)$$

with  $k$  [ $\text{m}^2$ ] the permeability of the porous medium,  $\eta$  [ $\text{Pa s}$ ] the viscosity, and  $\nabla P$  [ $\text{Pa}$ ] the pressure gradient. In this equation, gravity has been neglected.

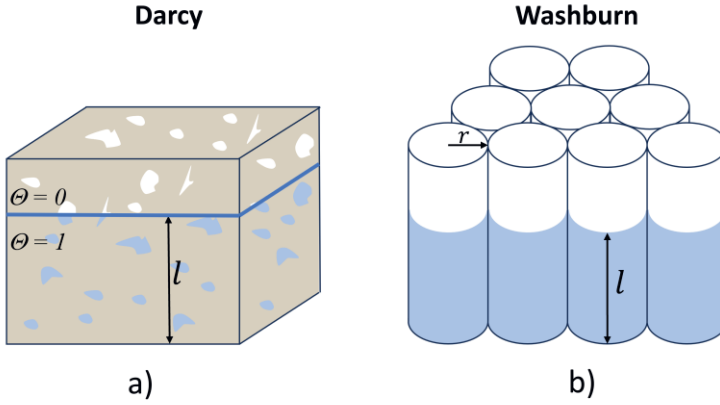


Figure 4.1 Schematic visualization of a) Darcy, b) Washburn.

Darcy's law, schematically represented in Figure 4.1a, describes the flow on length scales larger than the representative elementary volume (REV), where the material can be seen as homogeneous. In Darcy's Law, all the complex information and properties effecting the flow are captured inside the permeability  $k$ . In Darcy's Law with a sharp front formalism, it is assumed that the liquid is incompressible and that the material can be divided in two zones: dry ( $\theta=0$ ) and fully saturated ( $\theta=1$ ). Based on these assumptions, it follows from mass conservation that,

$$\nabla \cdot \vec{q} = -\nabla^2 P = 0. \quad (4.3)$$

Darcy's law is an equation which can be used within any 3D porous system. However, in case of a 1D fluid front, eq (4.3) can be rewritten as,

$$q = -\frac{k}{\eta} \frac{\Delta P}{l}. \quad (4.4)$$

The validity of this 1D model in thin, porous media and why this form can be used within this thesis is explained in section 4.2.2. When combining this equation with equation (4.1) and performing integration by parts, the fluid front can be given by,

$$l^2 = \frac{2k\Delta P}{\eta\phi} t + C. \quad (4.5)$$



In Darcy's Law, information of the pore geometry is captured by the permeability  $k$ . Other models describe fluid flow in simplified media such as a cylindrical tube (Hagen-Poiseuille) or a series of cylindrical tubes (Washburn), see Figure 4.1b.

In case of Washburn, a commonly used model for describing capillary fluid flow in systems such as paper, the porous media is simplified by assuming a series of parallel tubes with a perfectly cylindrical shape as seen in Figure 4.1b. To acquire a relation for the flux within this system, we use the uptake  $Q$  [ $\text{m}^3 \text{s}^{-1}$ ] in a single cylindrical tube, as described by Hagen-Poiseuille, and multiply it by the number of cylinders  $N$ . The resulting flow rate is given by,

$$NQ = -N \frac{\pi r^4}{8\eta} \frac{\Delta P}{l} = Aq. \quad (4.6)$$

After rearranging, this becomes,

$$q = -\frac{N\pi r^2}{A} \frac{r^2}{8\eta} \frac{\Delta P}{l} = -\phi \frac{r^2}{8\eta} \frac{\Delta P}{l}, \quad (4.7)$$

where we have set  $\phi = N\pi r^2/A$ , the porosity of the system. By rearranging this equation, it can be seen that this equation is similar to equation (4.4) by setting the permeability to,

$$k = \frac{1}{8} \phi r^2 = K_0 r^2. \quad (4.8)$$

This shows how Washburn is in essence identical to Darcy, but that it described a particular sub-class of simplified porous systems. Furthermore, equation (4.8) shows how both porosity and pore radius are a key parameter in determining the permeability of a porous media.

In Darcy, which describes the flow in a general porous media,  $k$  is often replaced by  $K_0 r^2$ , so that the effects of pore radius are taken out of the permeability [281].

In case of capillary uptake inside thin, porous media, the pressure difference can be described by the Young-Laplace equation for capillary pressure,

$$P_c = \frac{2\sigma \cos(\theta)}{r} \quad (4.9)$$

where  $r$  [m] is the pore radius,  $\sigma$  [N/m] is the surface tension, and  $\theta$  [°] is the liquid-surface contact angle. By implementing the capillary pressure from equation (4.9) in equation (4.5) and replacing  $k$  by  $K_0 r^2$ , an expression for the fluid front can be extracted which is given by [23],

$$l^2(t) = \frac{4K_0 \cos(\theta)}{\phi} \frac{\sigma r t}{\eta}. \quad (4.10)$$

### 4.2.2. Darcy's Law, from 3D to 1D

In previous section, Darcy's Law was implemented in 1D (equation (4.4)). In this section we will show that this holds for the thin, porous media used in this thesis.

As the pressure gradient scales with liquid penetration see equation (4.2), we need to compare the pressure gradients in all directions. As the main pressure component in spontaneous imbibition is the capillary pressure  $P_c$ , the maximum pressure drop observed in any direction should be similar to  $P_c$ .

We start with equation (4.3), which is based on mass conservation. After rewriting it in cylindrical coordinates and leaving out the angular coordinate, because the droplets used in this study are axisymmetric, we obtain,

$$\nabla^2 P = \frac{1}{R^2} \frac{1}{r'} \frac{\partial}{\partial r'} r' \left( \frac{\partial P}{\partial r'} \right) + \frac{1}{d^2} \frac{\partial^2 P}{\partial z'^2} = 0, \quad (4.11)$$

where we have introduced normalized coordinates  $r' = r/R$  and  $z' = z/d$  with the droplet radius  $R$  [m] and membrane thickness  $d$ . After rewriting this expression, we end up with,

$$\varepsilon \frac{1}{r'} \frac{\partial}{\partial r'} r' \left( \frac{\partial P}{\partial r'} \right) + \frac{\partial^2 P}{\partial z'^2} = 0, \quad (4.12)$$

where  $\varepsilon = (d/R)^2$ . From this equation, it becomes clear that the problem can be assumed 1D when the following condition is met:  $\varepsilon \ll 1$ . By comparing a typical droplet radius of our experiments (2 mm) and the membrane thicknesses (110-165  $\mu\text{m}$ ),  $\varepsilon$  can be estimated to be below 0.0068, showing that the process can be considered as a 1D process, which validates to use of equation (4.4) and therefore equation (4.10).

## 4.3 Materials and Methods

### 4.3.1. Membrane samples

The membranes used in this study are hydrophilic Durapore polyvinylidene fluoride (PVDF) membrane filters and Whatman nylon-6,6 membranes. The physical properties of the membranes are given in Table 4.1. The mean pore diameter and pore size distributions of the membranes were measured with mercury intrusion porosometry (MIP), using an AutoPore IV 9500 V1.05 instrument from Micromeritics Instrument Corporation, and can be seen in Figure 4.2. The pressure in the experiment was varied between 0.0007 en 227.5270 MPa with an equilibrium time of 20 s.

Table 4.1 Physical properties of the porous membranes used in this study.

Sample	Material	Thickness [ $\mu\text{m}$ ]	Avg. pore diameter [ $\mu\text{m}$ ]	Porosity [%]
<b>PVDF Membrane I</b>	PVDF	110	0.41	65
<b>PVDF Membrane II</b>	PVDF	110	1.4	65
<b>nylon Membrane I</b>	nylon-6,6	165	0.42	62
<b>nylon Membrane II</b>	nylon-6,6	165	0.53	67

Scanning electron microscopy (SEM) image of the top surface of PVDF membrane I and nylon membrane II are shown in Figure 4.3. Samples are prepared by taking 18 by 18 mm pieces out of the membrane filters and fixing them on top of a glass cover slip with double sided tape.

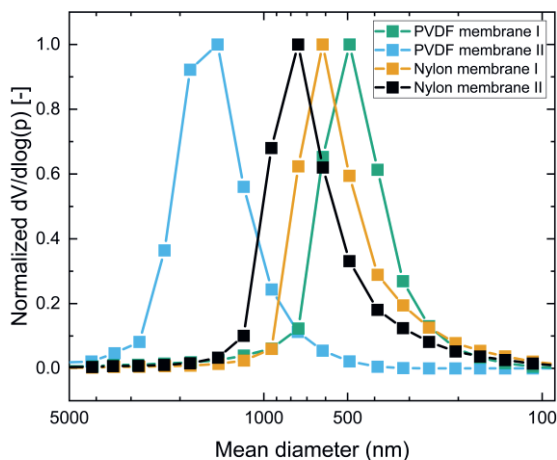


Figure 4.2 Pore size distributions for PVDF membrane I (green), PVDF membrane II (blue), nylon membrane I (orange) and nylon membrane II (black), measured by MIP

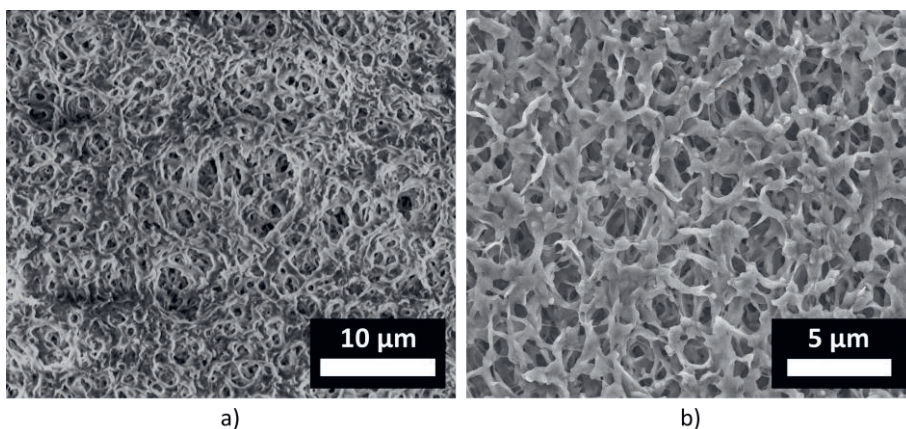


Figure 4.3 SEM image of the top of a) nylon membrane II and b) PVDF membrane I.

#### 4.3.2. Liquid solutions

The liquid solutions used in this study are shown in Table 4.2. The solutions are made by mixing demineralized water type 1, glycerol and in case of the NMR-experiments a watery solution containing either Clariscan or  $\text{CuSO}_4$ . The glycerol (> 99.0 % purity) has a density of  $1.26 \text{ g/cm}^3$  and is used to tune the viscosity of the liquid solutions.

Clariscan ( $\text{C}_{16}\text{H}_{25}\text{GdN}_4\text{O}_8$ ) and  $\text{CuSO}_4$  are both contrast agents that are added to manipulate the NMR-characteristics of the solution.  $\text{CuSO}_4$  (99,7% purity) is provided by Merck in powder form and Clariscan is a Gadolinium based contrast agent used in medical

MRI [171]. The Clariscan comes from GE Healthcare and is provided by Máxima MC in a water like solution with a concentration of 279.3 mg/ml, which is equivalent to 0.5 mmol/ml. It has a pH between 6.5 - 8, a density of 1.349 g/ml and a viscosity of 3.0 mPa.s at room temperature [282].

Viscosity and surface tension for the  $\text{CuSO}_4$  solutions are taken from literature [283]. For the Clariscan solutions, the viscosities are measured with an Anton Paar MCR302 rheometer (20°C) while the surface tension are determined using the pendant drop method [284]. The surface tension for the Clariscan solutions are 5-7 % lower than the one found for a pure water-glycerol mixture. This is however due to a systematic error within the pendant drop method because pure water-glycerol mixtures gave the same lower values.

Table 4.2 The liquids used in this study and their physical properties.

	<b>Contrast agent [M]</b>	<b>Glycerol [wt%]</b>	<b>Viscosity [mPa.s]</b>	<b>Surface tension [mN/m]</b>
<b>CuSO<sub>4</sub></b> based liquids	0.1	0	0.89	72.3
	0.1	25	1.89	70.7
	0.1	50	5.38	68.5
	0.1	70	20	66.1
<b>Clariscan</b> based liquids	0.048	0	1.09	67.3
	0.016	25	2.18	66.46
	0.008	50	6.24	64.9
	0.007	70	24.10	62.95

#### 4.3.3. Automatic scanning absorptometer

Automatic Scanning Absorptometer (ASA) [23] is a device that allows to measure the total amount of absorbed liquid and is similar to the more know Bristow wheel [285]. The ASA setup used in these experiments is the Kumagai Riki Kogyo (KM 500 win). The device is able to measure the absorbed liquid on timescales ranging from 10 ms to 10 seconds. ASA setup uses a spiral-scan device, meaning that the tracks that are made are spiral in nature.

In the experiment, a glass capillary is filled with the desired liquid followed by the fixation of the porous sample on a turntable. Thereafter, the liquid within the glass capillary will be brought in contact with the porous sample by using a scanning head. Due to capillary forces, the liquid starts to penetrate inside the membrane and is drawn out of the glass capillary. During the measurement, a sensor will track the movement of the liquid as meniscus in the glass capillary. This sensor movement together with the inner diameter of the glass capillary are then used to calculate the transferred liquid (TLV), which has penetrated in a specific area ( $A$  [m<sup>2</sup>]) during a specific contact time ( $t$  [s]). By accelerating the turntable, the time can be varied between 10 ms and 10 s. The area of absorption ( $A$ ) is equal to the dimensions of the nozzle which in this research had a width of 1 mm and a length of 5 mm. The same nozzle is used for all experiments.

## 4.4 Ultra-Fast Imaging (UFI) method

To measure liquid distributions with sufficient temporal resolution, our method combines two main ingredients: summation of the echoes which ensures a rapid increase in the signal-to-noise ratio and shortening of the  $T_1$  relaxation time of the solution by adding a contrast agent. Both the echo summation and the shortening of the  $T_1$  relaxation time will be discussed in more detail in this section.

### 4.4.1. Echo summation

The first ingredient for the UFI method is the summation of multiple echoes which ensures a fast increase in S/N-ratio. The echo summation is carried out by performing a specific pulse sequence which will be discussed within this section.

To measure the signal intensity during fast liquid uptake, UFI uses an adaptation of the OW-pulse sequence [184], which is given by:  $90_x^\circ - \tau - [90_y^\circ - \tau - (\text{echo}) - \tau - 90_y^\circ - \tau - (-\text{echo}) - \tau]_N$ , where  $N$  is the amount of repetitions within one measurement. Figure 4.4 gives a schematic representation of the pulse sequence. The difference compared with the OW-sequence is alternating between positive ( $90_y^\circ$ ) and negative ( $90_{-y}^\circ$ ) flip angles instead of using only positive flip angles. Consequently, positive, and negative echoes are created in alternating fashion.

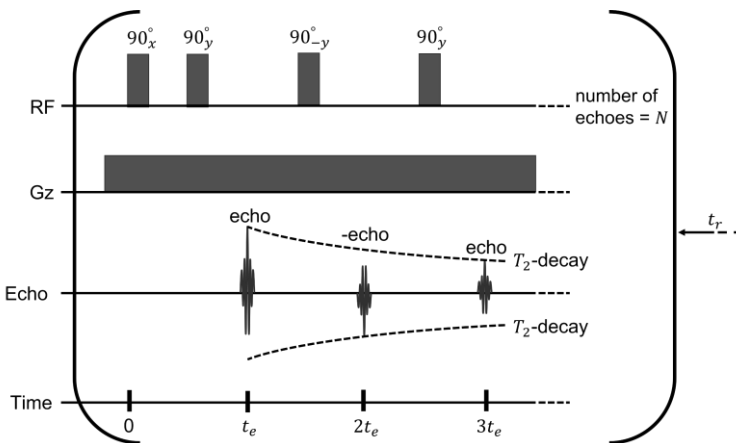


Figure 4.4 Schematic representation of the UFI-pulse sequence.

The final UFI signal intensity is then calculated by adding all  $N$  positive and negative echoes together. Because the signal is measured in one single measurement, in the presence of a constant gradient, a Fourier transformation is required to transfer the signal into signal profiles. The reason for adding up the different echoes is to have a fast increase in S/N-ratio while flipping the echoes ensures that after addition, the constant background noise is cancelled. The downside of doing a summation over all echoes is that the measured profiles will become  $T_2$  weighted. In a CPMG measurement, see section 3.2.2, the different echoes can provide information about multiple hydrogen pools by discriminating between varying  $T_2$  times. This becomes impossible within our UFI-measurement.

The total signal intensity measured by UFI can be deduced from equation (3.7), by adding the signal intensity of  $N$  echoes together which results in:

$$S = \rho \left( 1 - \exp\left(-\frac{t_r}{T_1}\right) \right) \sum_{n=1}^{2N} \exp\left(-n \frac{t_e}{T_2}\right). \quad (4.13)$$

This equation is a geometric series and can be rewritten into:

$$S = \rho \left( 1 - \exp\left(-\frac{t_r}{T_1}\right) \right) \left[ \frac{\exp\left(-\frac{t_e}{T_2}\right) - \exp\left(-\frac{(2N+1)t_e}{T_2}\right)}{1 - \exp\left(-\frac{t_e}{T_2}\right)} \right]. \quad (4.14)$$

In our experiments  $N$  was set to 16 leading to the summation of 32 echoes (16 positive and 16 negative echoes). In this study, the pulse length ( $t_{90}$ ) was equal to 1  $\mu$ s and the echo time ( $t_e = 2\tau$ ) was equal to 50  $\mu$ s which resulted in a total measurement time ( $t_p$ ) of 1.6 ms for one moisture profile.

To turn the acquired signal (equation (4.14)), which represent the signal as a function of time, into moisture profiles, a Fourier transformation is needed. The Fourier transformation will extract the different Frequencies which contribute to the measured signal together with their relative intensities. When using equation (3.23), the frequency points can be turned into relative positions and the signal can be turned into a signal profile as a function of position. By comparing the relative signal to a known sample with a known hydrogen concentration, these signals can be related to a moisture content.

#### 4.4.2. $T_1$ shortening

A second ingredient for the UFI-method is  $T_1$  shortening. The reason behind  $T_1$  shortening and the effect on the measurement will be discussed within this section.

Before a next profile can be measured, the hydrogen nuclei need to relax back to their equilibrium condition, where the repetition time ( $t_r$ ) should be  $t_r > 3T_1$ . This condition is chosen instead of the more frequently used condition  $t_r > 5T_1$ , because waiting an extra  $2T_1$  would only increase the signal intensity from 95% to 99% but almost doubles the measurement time. Because in our case measurement time is the most important factor, the first condition is chosen. The time between two profiles is therefore  $t_m = 3T_1 + t_p = 3T_1 + 1.6$  ms. From eq. (4.13), it becomes clear that for fast imaging, a low  $T_1$  and long  $T_2$  are required. When profiles are required for example every 25 ms, the signal intensity of normal water ( $T_1 \approx 3$  s) will reduce to zero because of a  $T_1$  factor of 0.0083. Therefore, no signal can be measured using normal water, similar to most liquids. To solve this problem, an NMR-contrast agent is added to decrease the  $T_2$  time to meet the condition  $t_r \geq 3T_1$  which ensures a 95% signal recovery. A second condition for the  $T_2$  time should ensure that the signal intensity of the  $2N^{\text{th}}$  echo is still high-enough to be measured. For simplicity, a signal intensity of 37% is chosen, leading to the condition:  $2Nt_e \geq T_2$ .

**Measurement conditions:**

- Time between profiles =  $t_r \geq 3T_1$
- Time to measure one profiles =  $2Nt_e \geq T_2$

This results in a measurement time of  $t_m = t_r + 2Nt_e \geq 3T_1 + T_2$ . To find the optimum signal intensity, the impact of the concentration of contrast agent should be investigated, this is discussed in the following sections.

**4.4.3. UFI Signal characterization and calibration**

In this section, a better understanding of the signal intensity and the corresponding signal optimum is given. Because the signal intensity is  $T_2$  weighted and the  $T_1$  condition ( $t_r \geq 3T_1$ ) cannot always be simultaneously fulfilled, the resulting signal intensity is a function of contrast agent concentration. Our first step is a theoretical discussion on the effect of a contrast agent on the signal intensity measured with the UFI method. In section 4.5.1, a comparison will be made with experiments.

Contrast agents are used to control the  $T_1$ - and  $T_2$ -relaxation time. The effect on both relaxation times is given by equations (3.15) and (3.16). By implementing these relations in equation (4.13), the signal intensity as function of the contrast agent concentration is known and given by,

$$S(C) = \rho \left( 1 - \exp \left( -t_r \left[ \frac{1}{T_1^{ref}} + R_1 C \right] \right) \right) \sum_{n=1}^{2N} \exp \left( -nt_e \left[ \frac{1}{T_2^{ref}} + R_2 C \right] \right) \quad (4.15)$$

A closer look at this equation will help in selecting the best concentration of contrast agent to achieve the highest signal intensity.

*Table 4.3 NMR-relaxation properties of Clariscan and CuSO<sub>4</sub> in different water-glycerol mixtures, found in eq. (3.15) and (3.16).  $T_2^{ref}$  and  $T_1^{ref}$  are the relaxation times for pure water-glycerol mixture (no contrast agent added).*

	<b>Glycerol (wt%)</b>	$T_2^{ref}$ (ms)	$T_1^{ref}$ (ms)	$R_2$ (ms <sup>-1</sup> M <sup>-1</sup> )	$R_1$ (ms <sup>-1</sup> M <sup>-1</sup> )
<b>Clariscan</b>	0	10.7	2480	5.13±0.54	4.48±0.32
	25	15.00	1480	9.29±0.34	7.66±0.16
	50	22.9	980	17.10±1.15	23.52±1.34
	70	31.9	300	46.34±0.54	34.35±1.65
<b>CuSO<sub>4</sub></b>	0	10.7	2480	0.74±0.03	0.62±0.02
	25	15.00	1480	1.25±0.04	0.99±0.03
	50	22.9	980	2.91±0.10	1.91±0.18
	70	31.9	300	5.34±0.08	4.16±0.17

An experiment starts by selecting the proper repetition time ( $t_r$ ) which determines the window between two measured liquid profiles and depends on the speed of the physical process. Other parameters such as the ones found in eq. (3.15) and (3.16) are dependent on the type of contrast agent and can be found in Table 4.3 for Clariscan and CuSO<sub>4</sub>. The relaxation terms  $T_1^{ref}$  and  $T_2^{ref}$  in Table 4.3 reflect the relaxation times without a contrast agent. When looking at equation (3.8) and (3.9), it can be seen that

$1/T_1^{ref} = 1/T_{1dip} + 1/T_{1diff}$  and  $1/T_2^{ref} = 1/T_{2dip} + 1/T_{2diff}$ , in the remainder of this section,  $T_1^{ref}$  and  $T_2^{ref}$  will be used for simplification.

Selecting the proper contrast agent will depend on the type of experiment that is performed and will be discussed in chapter 4.4.4.

For the theoretical discussion on the impact of a contrast agent on the signal intensity, relaxivity rates for commonly used contrast agents are used:  $R_1 = 3200 \text{ M}^{-1} \text{ s}^{-1}$  and  $R_2 = 3500 \text{ M}^{-1} \text{ s}^{-1}$  [286].  $T_2^{ref}$  and  $T_1^{ref}$  are set to 10 ms and 3 s respectively which are the values for water found within our GARField NMR-setup. Using these values in eq. (4.15), the signal intensity for different combinations of repetition time and contrast agent concentration  $C$  can be determined. Figure 4.5 shows a contour plot of the signal intensity in function of both parameters. The figure shows that faster measurement times will lead to a lower signal intensity and require more contrast agent to achieve the maximum achievable signal intensity.

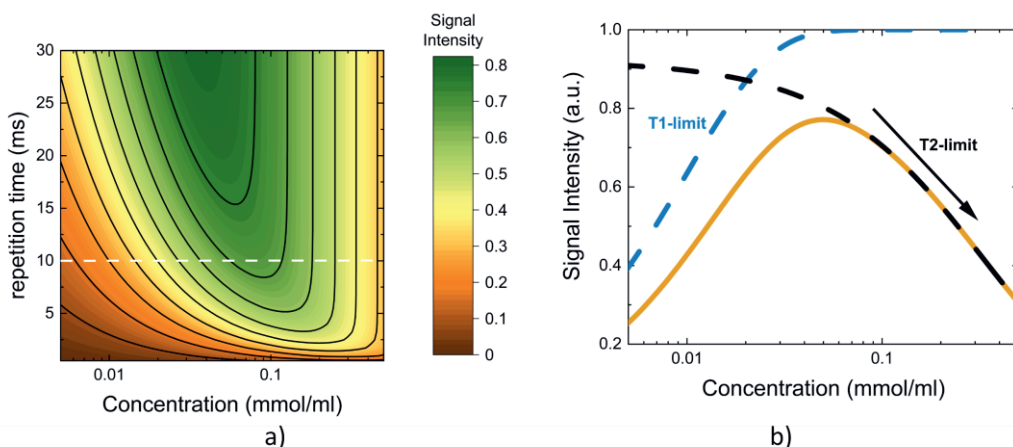


Figure 4.5 a: Contour plot showing the theoretical signal intensity in function of the repetition time (ms) and concentration of contrast agent (mmol/ml) for a fictive contrast agent having the following relaxation characteristics:  $1/T_2 = 1/0.010 + 3500C$  and  $1/T_1 = 1/3 + 3200C$ . b: Signal intensity in function of contrast agent concentration for a repetition time of 10 ms, which corresponds to the white line in figure a. Shown in dotted blue and black lines are the  $T_1$  and  $T_2$  factor found in equation (4.13).

To explain the occurrence of an optimum in the signal intensity for a specific concentration of contrast agent, a closer look is taken to the signal intensity for  $t_r = 10$  ms, marked with a white line in Figure 4.5a. Figure 4.5b shows the signal intensities corresponding with this line for different concentrations. Figure 4.5b also shows the  $T_1$  (blue) and  $T_2$  (black) contributions to the signal intensity. With increasing concentration of contrast agent, the signal first increases. This can be explained by an increase in the  $T_1$  term found in eq. (4.15). By increasing the concentration of contrast agent and thus lowering the  $T_1$  time, the  $T_1$  condition imposed earlier ( $3t_r > 3T_1$ ) will become more and more fulfilled. When comparing the signal intensity to the  $T_1$  term in blue, it can be seen that the signal at low concentrations is  $T_1$  limited. From the moment the  $T_1$  condition is met, which in this case is around 0.05 mmol/ml, 95% of the signal will be recovered.



Besides lowering the  $T_1$  time, increasing the amount of contrast also lowers the  $T_2$  time, which explains why, at a certain concentration, the signal intensity starts to decrease again. These lower  $T_2$  times lead to lower echo intensities resulting in a decrease in the  $T_2$  term found in eq. (4.15), plotted in black in Fig. 4b. By comparing the total signal intensity with the  $T_2$  term, it can be seen that the signal intensity is dominated by the  $T_1$  effect at higher concentrations.

This simultaneous decrease in  $T_2$  and  $T_1$  time when increasing the contrast agent concentrations explains the optimum in the signal intensity. Therefore, the proper concentration of contrast agent should be determined for every liquid mixture in order to have the best Signal-to Noise ratio.

#### 4.4.4. Selecting the right contrast agent

Before solutions can be used within a UFI experiment, they sometimes are adjusted to optimize the measurement results. Figure 4.6 shows a decision tree which helps in preparing your liquid solution.

Preparing a solution for UFI experiments starts by identifying the typical timescale of the physical process  $t^*$ [s] that wants to be investigated and the  $T_1$  time of the liquid solution. When  $t^* > 3T_1$ , no contrast agent is required because signal recovery is fast enough to ensure 95% signal intensity. If  $t^* < 3T_1$ , initial signal recovery is too slow and contrast agents are required to decrease  $T_1$ .

In this project, two contrast agents were used, i.e.  $\text{CuSO}_4$  and Clariscan. These contrast agents were chosen because they are well characterized in literature and commonly used as contrast agents [171], [172], [173]. If the liquid is stable in a salt like environment,  $\text{CuSO}_4$  is preferable because it has the smallest effect on viscosity and surface tension. However, in case the solution is unstable in a salt-like environment, the case for most colloidal systems, Clariscan will be used. Clariscan will slightly increase the viscosity, but, due to its inert nature, will not interfere with the particle stability and is therefore preferred.

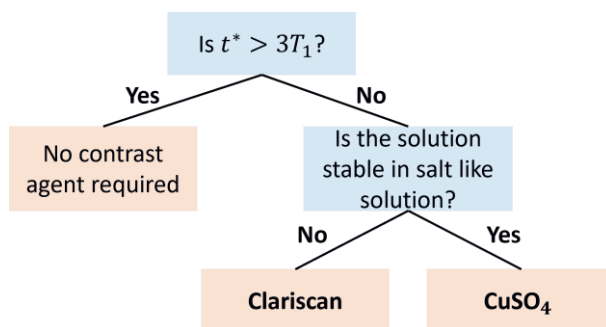


Figure 4.6 Decision tree for deciding which contrast agent should be used.

#### 4.4.5. Experimental procedure

In this thesis, experiments on droplet penetration into membranes and paper samples are conducted. Figure 4.7 illustrates a schematic representation of the experimental setup, featuring the droplet insert and the light sensor to trigger the NMR measurement.

To prevent interference of the light sensor with the measurement, the light sensor is surrounded by a faraday cage. The sample consists of either membrane or paper glued on top of a glass plate using a double-sided tape. The glass plate is used to fixate the sample to prevent curl and to protect the RF-coil from moisture. The RF-coil is located below the droplet insert and has a diameter of 4 mm.

The droplets have a volume ranging from 5-10  $\mu\text{l}$ , effectively covering the entire measurement area. Within the NMR setup, 1D images of the sample can be measured. The area for signal recording is marked with a black square and the corresponding 1D moisture profile is shown on the right. The moisture profile shown in this image is an example from a typical moisture profile measurement conducted within this thesis.

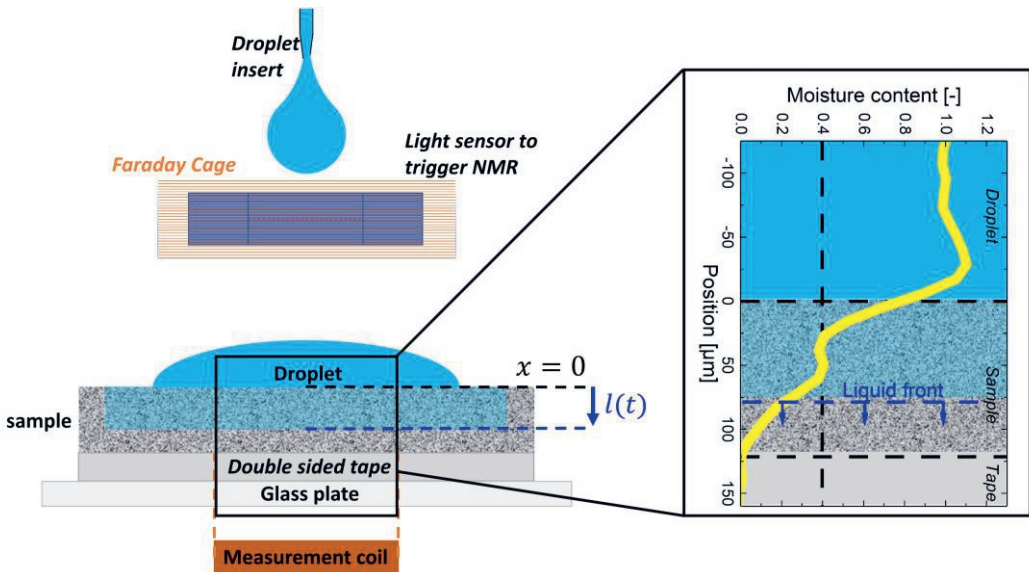


Figure 4.7 Schematic representation of the measurement insert. Shown are the droplet insert, the light sensor to trigger the NMR, the sample with droplet and the RF-coil to measure the signal. A corresponding liquid profile is shown on the right.

#### 4.4.6. NMR coil profile correction

Because profiles are measured using an RF-coil located below the sample (Figure 4.7), the relative position to the measurement coil significantly influences the measured NMR signal. To correct for this, liquid profiles are always corrected using a profile measured with a reference sample. To illustrate this procedure, Figure 4.8a shows UFI signal profiles measured during penetration within a nylon-6,6 membrane without any coil corrections. In these profiles, the droplet-membrane interface is used as the  $x = 0$  position. Figure 4.8a also shows a reference profile in black which shows how the signal intensity is maximum near the coil and diminishes as you move away. To interpret the measured NMR signals and relate them to moisture profiles, the profiles are always corrected by dividing the obtained signals by a reference profile. Figure 4.8b shows the corrected profiles for the area marked with dotted lines in Figure 4.8a. It is important to note that all profiles presented in this thesis are corrected using a reference profile to correct for this coil profile.

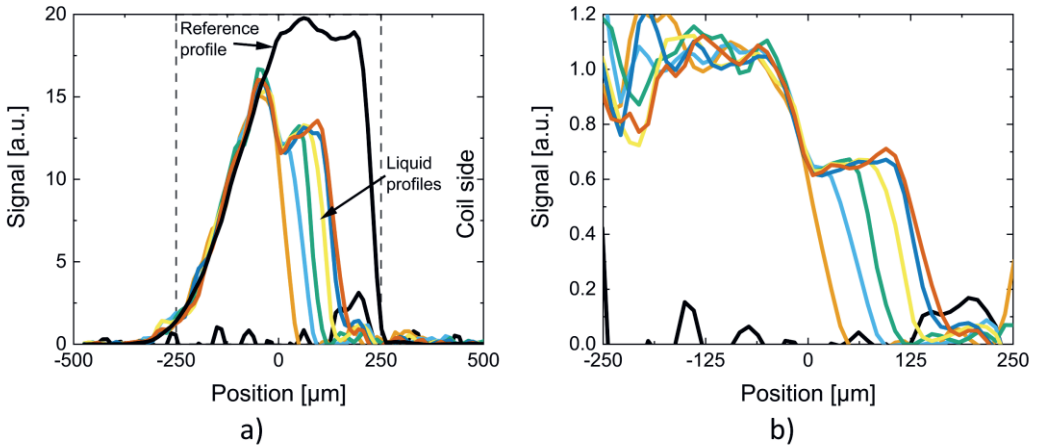


Figure 4.8 a) UFI signal profiles without coil correction. In black is a reference profile and measurements are marked with colors. b) Signal profiles from a, but after coil correction. In both figures,  $x = 0$  is set to the droplet-membrane interface.

## 4.5 Applying UFI for liquid uptake

The aim of this chapter is to use UFI to investigate liquid uptake in thin, porous media, which is the first step towards imaging ink penetration in paper sheets. The section starts by characterizing the signal intensities for a variety of model inks. Finally, UFI will be used to measure the penetration of varying model inks in PVDF and nylon-6,6 membranes. For both membranes, the influence of viscosity, surface tension and pore radius will be investigated.

### 4.5.1. The relation between signal and contrast agent

In section 4.4.3, the effect of a contrast agent on the signal intensity was explained theoretically. In this section, an experimental verification of eq. (4.15) will be given, by comparing UFI measurements of the signal intensity with predictions based on the  $T_1$  and  $T_2$  relaxation characteristics of the liquid. The comparison was performed for water-glycerol mixtures containing varying amounts of Clariscan and  $\text{CuSO}_4$ .

The relaxation characteristics of Clariscan and  $\text{CuSO}_4$  within different water-glycerol mixtures are determined with an OW-sequence ( $t_e = 50 \mu\text{s}$ ,  $t_r = 25$  to  $100 \text{ms}$ ) and saturation recovery.

Table 4.3 gives the results for the different relaxation parameters in eq. (3.15), (3.16) and for the reference relaxation terms. The corresponding relaxation times as a function of concentration can be found Nicasy et al. [24]. It was found that increasing the glycerol content will increase the relaxivity for both Clariscan and  $\text{CuSO}_4$ . This is in line with findings of other research groups, which showed that increasing the viscosity will enhance the effect of contrast agents [155], [287].

Furthermore, it was found that  $T_1^{\text{ref}}$  lowers with decreasing the amount of glycerol, while the opposite happens with  $T_2^{\text{ref}}$ . The increase of the  $T_2$  relaxation time can be related to a decrease in diffusion when adding glycerol. In previous research, it was proven that

with high gradients, the  $T_2$  time can be approximated by  $T_2 \approx 1/\alpha\gamma^2 G^2 D^2 t_e$  [161]. Therefore, the increase in  $T_2$  time is a direct result of the effect of glycerol on the diffusion coefficient. An opposite behavior is observed for the  $T_1$  relaxation time, where increasing the viscosity decreases the relaxation time in accordance with the Bloembergen-Purcell-Pound (BPP) theory [155], [288]. This theory explains that  $T_1$  relaxation is optimal when the frequency of the vibrational and rotational motion (correlation time  $\tau_c$ ) equals the Larmor frequency. In non-viscous liquids such as water, the molecular rotation is much higher than the Larmor frequency, leading to very inefficient  $T_1$  relaxation. By increasing the viscosity, more and more contrast agents have motions and rotations around the Larmor frequency, which results in increased  $T_1$  relaxation.

In most studies, gadolinium-based contrast agents are tested in solutions mimicking blood plasma because of its medical applications. Most reported values are around  $5 \text{ ms}^{-1}\text{M}^{-1}$  [44,47]. The result of normal water is quite close to the reported value, to be expected as blood plasma consists mostly of water.

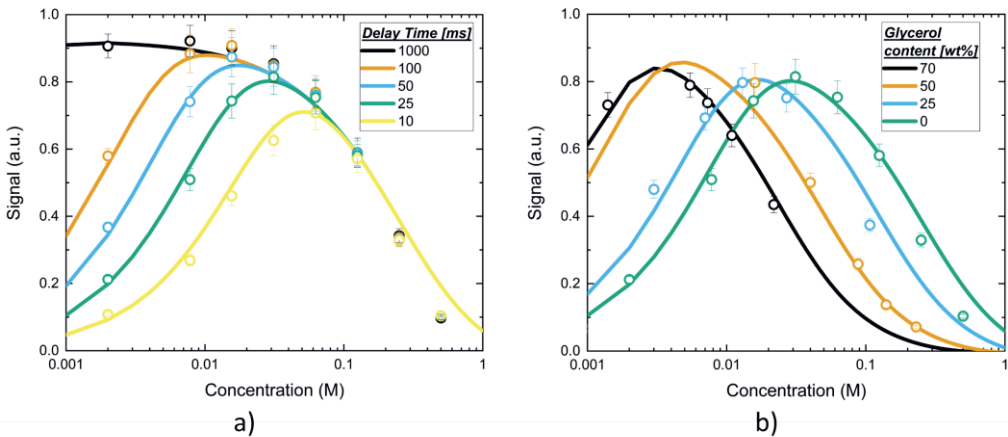


Figure 4.9 a: Comparison between the signal intensity predicted based on the relaxation characteristics of a Clariscan solution of 0 wt% glycerol (lines) and UFI measurements (points). Both are given for different repetition times. b: Same graph as in a but for different water-glycerol concentration, all having the same repetition time of 25 ms.

When the relaxation parameters are known, a prediction of the signal intensity as a function of contrast agent can be made by implementing the values from Table 4.3 in eq. (4.15). Results of this prediction for the water-Clariscan mixture (0 wt% glycerol) are shown by lines in Figure 4.9a. The colors are used to mark different repetition times. Furthermore, Figure 4.9a shows experimental values measured by UFI (marked with dots). This graph shows that there is a good correlation between the prediction (based on the relaxation characteristics of the contrast agent) and the experimental results. Using the graph, the optimum Clariscan concentration can be determined for every desired repetition time. As found in section 4.4.3, lower repetition times results in lower maximum achievable signal intensity and an increase in contrast agent. Similar optimization curves for all different mixtures can be found Nicasy et al. [24].

Figure 4.9b shows the signal intensities for different water-glycerol contents, but for the same repetition time of 25 ms. For the same repetition time, the optimum concentration lowers with increasing glycerol content. Consequently, a lower amount of contrast agent for higher glycerol contents is required to achieve optimal signal intensities.

Because the UFI-method relies on a short  $T_1$  relaxation time, a contrast agent is mandatory in most liquids, as explained in Figure 4.6. In this part, we showed that the method can be used for liquids with a wide variety of viscosities. However, for low viscosity liquids and a high penetration speed, the method breaks down when no soluble contrast agent is available. This puts some limits on the types of liquids that can be used within our UFI-measurements.

#### 4.5.2. Signal calibration in porous media

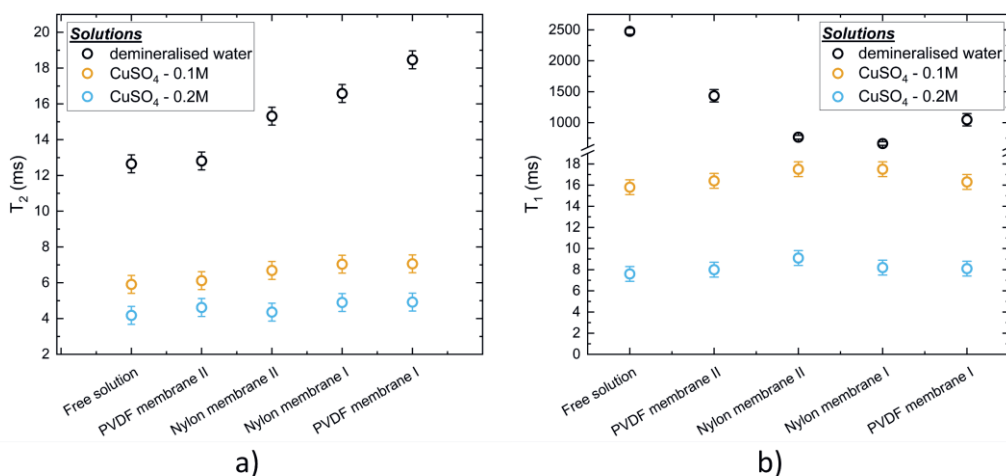


Figure 4.10 a:  $T_2$  relaxation data measured in free solution, PVDF membrane I ( $r = 0.2 \mu\text{m}$ ), PVDF membrane II ( $r = 0.7 \mu\text{m}$ ), Nylon membrane I ( $r = 0.2 \mu\text{m}$ ), and Nylon membrane II ( $r = 0.26 \mu\text{m}$ ) for demi water (black),  $\text{CuSO}_4$  solution 0.1M (orange) and  $\text{CuSO}_4$  solution 0.2M (blue). b:  $T_1$  relaxation data measured in different porous media for demi water (black),  $\text{CuSO}_4$  0.1M (orange) and  $\text{CuSO}_4$  0.2M (black).

The main goal of UFI is to measure liquid distributions in thin media on timescales as low as 10–100 ms. From eq. (4.13), it is known that  $S \propto \rho$  but also depends on  $T_1$  and  $T_2$ . These relaxation times can be influenced by the porous media due to surface relaxation or reducing the diffusion (section 3.2.1). To test if the relaxation times depend on the nature of the porous media, relaxation times of typical solutions used within UFI and demineralized water are determined in different porous media. Figure 4.10 gives the  $T_2$  and  $T_1$  relaxation times measured in solution and within 4 different porous media (Table 4.1).

For demineralized water, the pore space influences the relaxation times and therefore the resulting UFI signal. The  $T_2$  relaxation time for water increases with decreasing pore radius, which is the result of confining the hydrogen atoms and lowering the effective diffusion coefficient. In these measurements, the  $T_2$  relaxation time was measured with an echo time of 50  $\mu\text{s}$ . With a diffusion coefficient of  $2.1 \cdot 10^{-9} \text{ m}^2/\text{s}$ , this results in a

diffusion distance of  $\sqrt{2Dt_e} = 458$  nm. If the pore radius is larger than this diffusion length, which is the case for PVDF-0.65, the relaxation behaves similar to a free solution. For smaller pore radii, the diffusion distance will change to  $\sqrt{2D_{eff}t_e}$ , where  $D_{eff}$  depends on the pore space. The diffusion contribution becomes less profound with higher concentrations of contrast agent. If one would compare the signal intensity of the  $\text{CuSO}_4$  0.2 M solution ( $T_2 = 6$  ms) with the one found in PVDF membrane I ( $T_2 = 7$  ms), the signal measured by UFI would only increase with 1.5% and is much lower than the actual noise found within the system. Therefore, it can be concluded that the pore space will not influence the final signal intensity.

For the  $T_2$  time, the pore space has a negative effect on the relaxation of demineralized water. An increasing surface to volume ratio means more surface relaxation and a lower relaxation time. The measurements reveal that PVDF has less surface relaxivity than nylon, because for the same pore radius, the PVDF has a higher  $T_2$  relaxation time. However, when high amounts of contrast agents are used, the effect of the contrast agent is much more dominant, and the relaxation time will be unchanged for the different pore spaces. Therefore, it can be concluded that the pore space will only influence the relaxation times for demineralized water. However, when contrast agents are added, the effect of the contrast agent is much more dominant, and the pore space has no significant effect on the final signal intensity.

In case of our experiments, the amount of contrast agents is high enough to consider that the  $T_1$  and  $T_2$  times are purely determined by the liquid properties and not by the porous matrix. Therefore, we take that any change in signal intensity can be related to a change in the hydrogen content ( $\rho$ ).

### 4.5.3. Measuring liquid penetration with UFI

#### *Liquid profiles*

Liquid penetration experiments were performed by jetting droplets on top of the membrane filters. After jetting, the UFI method is used to measure liquid distribution profiles during imbibition. By investigating the shape and position of the liquid front and the signal profiles, details about the fundamental processes can be obtained. Liquid distribution profiles of a Clariscan based mixture containing 50 wt% glycerol (Table 4.2) penetrating inside PVDF membrane I with pore size of 0.2  $\mu\text{m}$  are plotted in Figure 4.11a for different times during penetration. The signal intensity is given with respect to a fully saturated sample containing the same test liquid. The profiles are measured every 26.6 ms and are indicated with different colors. The black line with almost no signal is the signal intensity measured just before the droplet hits the membrane. By looking at the profiles, three different regions can be distinguished: the droplet on top of the substrate ( $x < 0$   $\mu\text{m}$ ), the membrane ( $0 < x < 165$   $\mu\text{m}$ ) and the glass plate ( $x > 165$   $\mu\text{m}$ ). Every region has its own signal intensity, the droplet with signal intensity 1, the membrane with signal intensity 0.65 and the tape with signal intensity 0. The droplet has a signal intensity of 1, meaning that the area is fully saturated with liquid. The membrane, however, has a maximum signal intensity of 0.65 indicated with a blue dotted line. Because the signal intensity is independent of the interaction between spins and the membrane, see section 4.5.2, the signal reflects the level of liquid saturation. If a fully saturated porous membrane is assumed, the final signal intensity reflects the porosity of the system which in this case corresponds to 0.65. This value is the same as the

porosity measured by MIP (Table 4.1) which indicates that almost no air is trapped within the porous media after penetration. The profiles show that within PVDF membrane filters, the liquid imbibes with a sharp front.

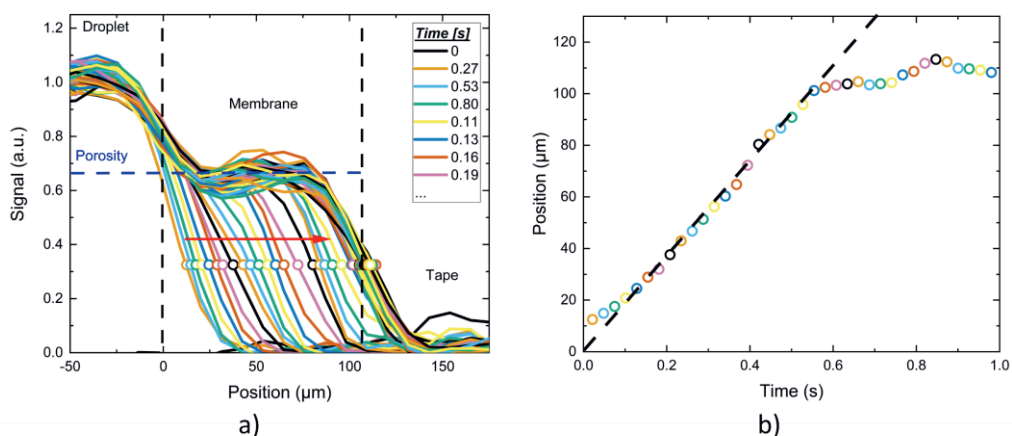


Figure 4.11 a: Moisture profiles measured during penetration of a Clariscan based mixture containing 50 wt% glycerol in PVDF membrane I. b: Front versus  $t$  graph for the liquid profiles shown in a.

#### Liquid front penetration, seen from profiles

Using the UFI liquid profiles, a front position is taken at half the maximum signal intensity (0.33). The front positions for every liquid profile is marked in Figure 4.11a with a circle in the same color as the corresponding liquid profile. In Figure 4.11b, the front is plotted as a function of  $t$  where the same colors are used and where the straight line is drawn as guide to the eye. This plot shows that the penetration follows a linear time behavior which deviates from Darcy's law (eq. (4.10)). The same linear behavior within PVDF membranes was also found by Kuijpers et al. [23].

#### Liquid front penetration as function of pore radius and viscosity

To investigate the effect of viscosity, surface tension and pore radius, the experiment was repeated for all Clariscan containing water/glycerol mixtures (Table 4.2) on both PVDF membranes (Table 4.1) and for all  $\text{CuSO}_4$  containing water/glycerol mixtures (Table 4.2) on both nylon membranes (Table 4.1). Figure 4.12 shows the liquid front positions determined as given in previous section for the experiments on PVDF (Figure 4.12a) and nylon (Figure 4.12b). From this figure, it can be seen that the imbibition speed decreases with increasing glycerol content and with decreasing pore radius for both membranes.

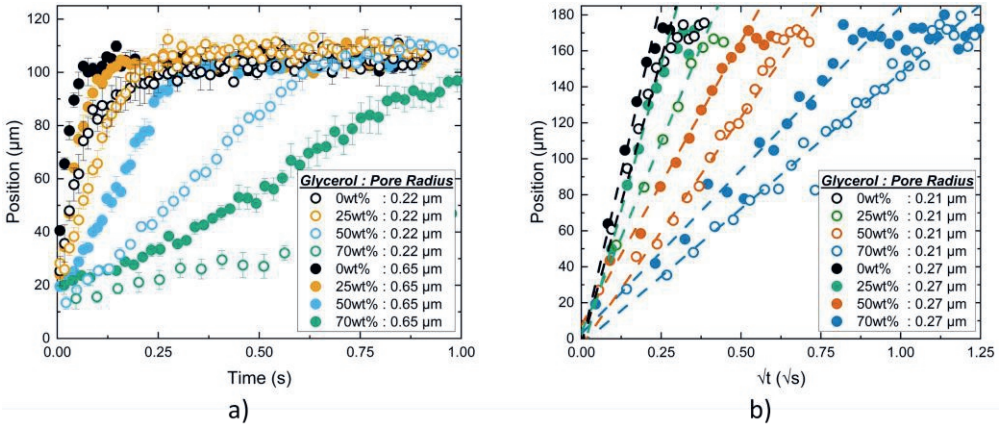


Figure 4.12 Liquid front position as a function of time for a) Clariscan based water-glycerol mixtures on PVDF membrane I ( $r = 0.22 \mu\text{m}$ ) and II ( $r = 0.65 \mu\text{m}$ ) and b)  $\text{CuSO}_4$ . based water-glycerol mixtures on nylon membrane I ( $r = 0.21 \mu\text{m}$ ) and II ( $r = 0.27 \mu\text{m}$ ). In both cases glycerol contents of 0, 25, 50 and 70 wt% were used.

Comparing liquid penetration in nylon-6,6 and PVDF membranes

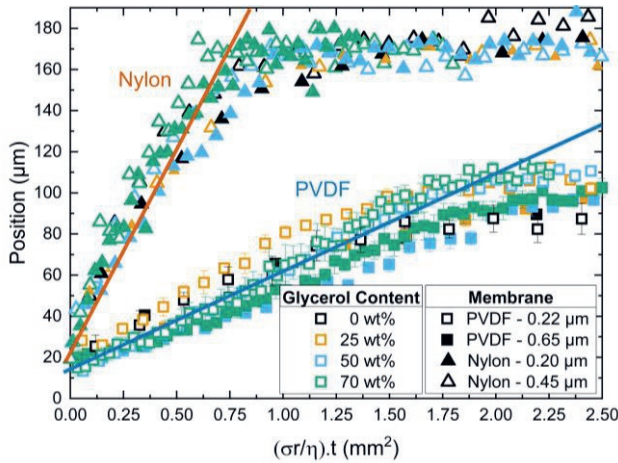


Figure 4.13 Liquid front positions as a function of  $\sigma r t / \eta$  for different water-glycerol mixtures containing 0, 25, 50 and 70 wt% of glycerol on PVDF membranes I and II (pore radius of 0.22 and 0.65  $\mu\text{m}$ ) and nylon-6,6 membranes I and II (pore radius of 0.2 and 0.45  $\mu\text{m}$ ).

To compare the measurement on PVDF and nylon-6,6, the data is plotted as function of  $\sqrt{\sigma r t / \eta}$  in Figure 4.13. The rescaling is based the 1-D Darcy model (eq. (4.10)). It was shown in section 4.2 that in these particular systems, the penetration can be assumed to be 1D. After rescaling, the nylon and PVDF measurement follow two different master curves shown in orange (nylon) and blue (PVDF). In nylon, penetration follows a square root of time behavior as predicted by Darcy, whereas PVDF does not. Kuijpers et al. observed a similar effect when measuring the absorption of water-glycerol mixtures in PVDF membranes with ASA [23].



A second observation is that the penetration inside nylon membranes happens much faster. As the measurements are rescaled with  $\sqrt{\sigma r/\eta}$ , the faster penetration cannot be linked to one of these parameters. Also, both porosity's are quite similar, which was found by the NMR-profiles and MIP results. Therefore, there should exist a difference in  $K_0$  or  $\theta$  between both membranes to explain the observed behavior. Possible reasons could be differences in fiber orientations or tortuosity [289].

#### 4.5.4. ASA Experiments

In the final part of this chapter, the results found by UFI are compared to ASA. Figure 4.14 compares the NMR-data and ASA-measurements, where the NMR data is plotted in orange and the ASA data is plotted in green. The data is shown for both membranes (PVDF and nylon) and for all glycerol contents (0, 25, 50 and 70 wt%). ASA-measurements were performed using liquids with the same water-glycerol ratios, but without the contrast agent on both nylon 6,6 membranes. Data for PVDF membrane I, having a pore radius of 0.22  $\mu\text{m}$  were taken from Kuijpers et al. [23].

This figure shows that the measured liquid fronts for NMR and ASA are in good comparison, underlining again that both techniques show similar results.

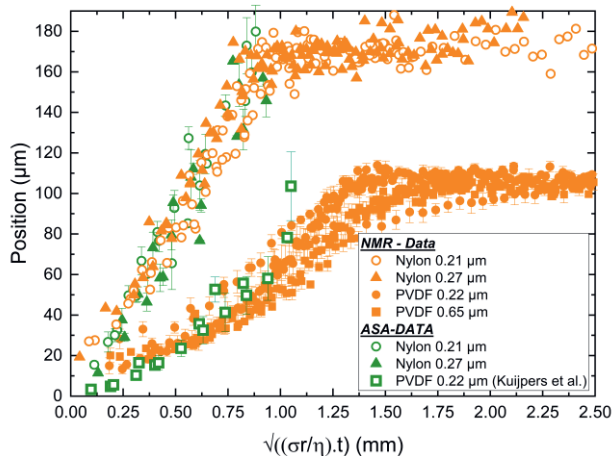


Figure 4.14 Comparison between liquid front positions measured by ASA (green) and UFI (orange) on a rescaled time axis for PVDF- and nylon-membranes. For every membrane and technique, the data for all glycerol contents (0, 25, 50 and 70 wt%) is shown in similar symbols.

## 4.6 Conclusions

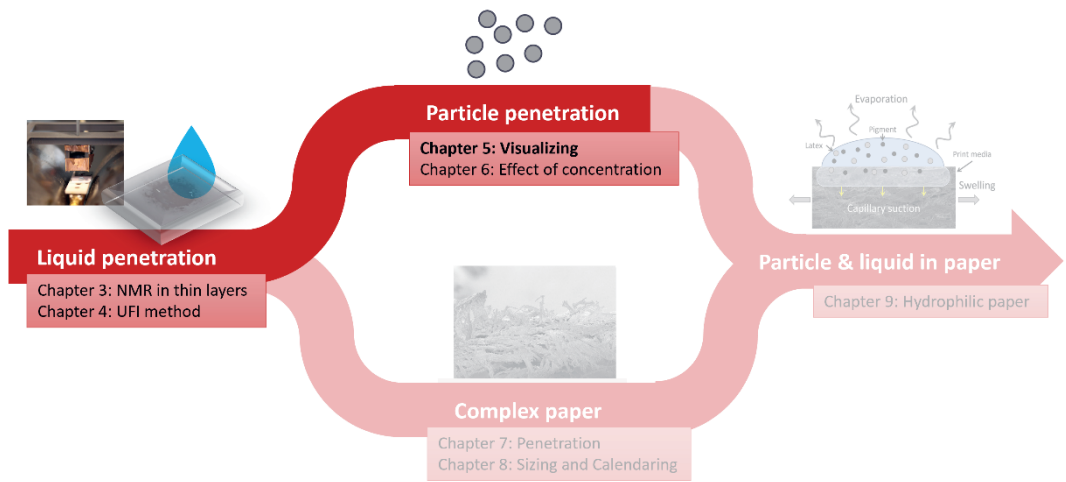
In this chapter, the Ultra-Fast Imaging (UFI) NMR method was introduced that is able to measure moisture profiles during imbibition with a temporal resolution of 10 ms and spatial resolution of 14.5 - 18  $\mu\text{m}$ .

Before a liquid imbibition process can be measured, the signal intensity is optimized by the addition of a contrast agent. Two main contrast agents were studied, namely Clariscan and  $\text{CuSO}_4$ . For both contrast agents, an optimum concentration could be

determined with a theoretical model, which was based on the relaxation characteristics of the corresponding contrast agent. It was also shown that by the addition of those contrast agents, the measured signal intensity was independent of the porous medium and was fully determined by the hydrogen density.

After a clear characterization of the measured signal intensity, penetration experiments were performed on PVDF (pore radii 0.22  $\mu\text{m}$  and 0.65  $\mu\text{m}$ ) and nylon (pore radii 0.21  $\mu\text{m}$  and 0.27  $\mu\text{m}$ ) membranes. In the measured moisture distribution profiles, the droplet, membrane, and tape could be clearly distinguished. From the profiles, the porosity of both membranes could be determined to be 65 % which agreed well with porosity's measured by mercury intrusion porosometry. The liquid distribution profiles in PVDF and nylon revealed a sharp moving liquid front, which could be used to measure the liquid front penetration speed for different water-glycerol mixtures and membrane pore radii. The liquid front penetration speed for the PVDF and nylon membranes decreased with increasing viscosity and decreasing pore radii of the membrane. The liquid fronts measured on nylon-6,6 could be rescaled with  $\sqrt{\sigma r t / \eta}$ , whereas the liquid fronts on PVDF rescaling with  $\sqrt{\sigma r t / \eta}$ . The deviations from the 1D-Darcy model found within PVDF could not be related to the effect of swelling as was proposed by Kuijpers et al. [23]. However further research is required to explain this behavior.

Finally, the NMR-measurements were compared to ASA measurements and showed good agreement. The advantage of the UFI-NMR imaging method however is that a direct moisture profile within the membrane can be measured.



# 5

## Imaging iron oxide nanoparticles during capillary suction

The transport of nanoparticles in porous media has received growing attention in the last decades due to environmental concerns in, for example, the printing industry, filtration, and transport of pollutants. As shown in this thesis, studies on the imbibition of particle dispersions in porous media with sufficiently high spatial and temporal resolution are still challenging. This chapter shows how the Ultra-Fast Imaging (UFI) NMR method developed in 4 can also be used to study  $\text{Fe}_3\text{O}_4$ -latex particles dynamics with a temporal resolution of 15 ms and spatial resolution of 18  $\mu\text{m}$ . In the first part of this chapter, it is shown that a calibration curve between the UFI-NMR signal intensity and the particle concentration exists. In the second part, UFI-NMR is used to study the penetration of particles inside a thin nylon membrane during capillary uptake, which revealed liquid-particle front splitting and an inhomogeneous buildup of the particle concentration. Both the liquid-particle front splitting and inhomogeneous build up could be verified by Scanning Electron Microscopy. Our method allows to determine particle concentration profiles during capillary uptake within thin, porous media. Therefore, the technique can be easily extended to study particle penetrations in a wide variety of systems such thin interfaces, biomaterials, films, and filter media.

*Adapted from:*

*Nicasy, R. J. K. et al. Magnetite-latex nanoparticle motion during capillary uptake in thin, porous layers studied with UFI-NMR. Colloids Surfaces A Physicochem. Eng. Asp. 683, 133011 (2024).*

### 5.1 Introduction

Equation Section (Next)The transport of nanoparticles and colloids within porous media has received growing attention in the last decades in view of a wide variety of applications ranging from filtration processes (bacteria [290], viruses [291], colloids [292] and drinking water [25], [293]), transport of pollutants in soil [26], [27], [294], transport of biomarkers in wearable electronics [295]–[297] and ink penetration [34], [298], [299]. In most applications, particle transport is directly linked to performance or quality; for example the print quality in paper [300], [301] or filtration efficiency of a filter [302], [303]. A better understanding of liquid and particle transport through porous media is of great importance for improving the performance of these applications.

Important parameters are the particle penetration depth, the deposition rate and the separation of particle sizes. A detailed review of the transport of nanoparticles in porous media is given by Boccoardo et al. [304]. One way to study these processes is through theoretical models that try to simulate particle transport [12], [13]. Such models showed that the particle retention was greatly dependent on porosity, flow rate of the carrying fluid and matrix-particle interaction [13]. However, because porosity and permeability depend on the particle deposition within the porous media, the application of these models is very difficult.

Besides theoretical models, there are many experimental methods for studying transport of particles in porous media but as explained in the introduction of this thesis, experimental studies on fast penetration (< 100 ms) in thin-porous media (< 100  $\mu\text{m}$ ) are still challenging.

In previous chapter, an Ultra-Fast Imaging (UFI) NMR proved an ideal tool to study capillary uptake in thin-porous membranes with a high spatial (18  $\mu\text{m}$ ) and temporal (10 ms) resolution. Until now, only the capillary uptake of water-glycerol mixtures was studied, and no studies were performed on the uptake of particle dispersions. The NMR ability to image particles and colloids was already shown in a wide variety of studies [65], [66]. However, these studies are unable to cope with the high temporal and spatial resolution required to measure capillary uptake within thin, porous media.

In this chapter, it will be shown how the UFI-method introduced in 4 can be extended to study the transport of iron oxide nanoparticles during capillary uptake within thin nylon membrane filters. In the first part, it is shown how the iron oxide within the latex particles enables the quantification of the latex particle concentration. Secondly, it is demonstrated how the UFI-NMR method is able to measure the position of latex particles during capillary uptake with a temporal resolution of 25 ms and a spatial resolution of 18  $\mu\text{m}$ . Furthermore, it is shown how particle concentration profiles within the nylon membranes can be determined. Finally, the UFI-NMR results are compared to scanning electron microscopy images. The technique can be easily extended and used to study a wide variety of applications that include penetration of particles and colloids within thin, porous media.

## 5.2 Materials and methods

### 5.2.1. Styrene $\text{Fe}_3\text{O}_4$ hybrid particles

First, iron oxide nanoparticles were synthesized as described by Lu et al [305]. In a 2 L jacketed glass reactor, iron (III) chloride hexahydrate ( $\text{FeCl}_3 \cdot 6\text{H}_2\text{O}$ , 27.02 g) and iron (II) chloride tetrahydrate ( $\text{FeCl}_2 \cdot 4\text{H}_2\text{O}$ , 9.90 g) were dissolved in water (650 g) at 25.0  $^\circ\text{C}$ . Oleic acid (10 g) was dissolved in acetone (60 mL) and added to the reactor and mixed for 30 minutes.  $\text{NH}_4\text{OH}$  (25 wt% solution in water, 75 mL) was added dropwise in 10-15 minutes under  $\text{N}_2$  atmosphere to the reactor and mixed for 1 h. After that the temperature was increased to 85.0  $^\circ\text{C}$  for 1 h. The reaction mixture was cooled down to 70.0  $^\circ\text{C}$  and HCl (2 N solution) was added until pH 2 was obtained. Under the acid pH the nanoparticles coagulated. The nanoparticles were washed with deionized water until the pH of the washing water was 7 and were dried in an oven (at 65.0  $^\circ\text{C}$ ) for 48 h.

In the next step, polystyrene-Fe<sub>3</sub>O<sub>4</sub> hybrid nanoparticle latexes were synthesized by mini-emulsion polymerization, using 100 mL bottles submerged in a water tank and tumbled end over end at 70.0 °C for 24 h. The mini-emulsion was obtained by sonicating the mixture of the water and organic phases in a Branson Digital Sonifier for 20 minutes at 80 % amplitude and a 0.8 s on and 0.2 s off cycle in an ice bath under magnetic stirring. The compositions of the organic and water phases for each polymerization are summarized in table 1. Styrene (S), which is the main monomer, is converted to polystyrene in the final latex. methacrylic acid (MAA) is used as comonomer and sodium dodecyl sulfate (SDS) as surfactant, azobisisobutyronitrile (AIBN) is the initiator and hexadecane (HD) is used as co-stabilizer to keep the stability of the mini-emulsion during the polymerization process. Three latexes of 30 % S.C. were obtained with Fe<sub>3</sub>O<sub>4</sub> concentrations from 0.5 to 5.0 wt% (based on total dispersed phase).

*Table 5.1 Composition of the latex particles in grams. The different components are: Fe<sub>3</sub>O<sub>4</sub>, styrene as the main monomer, Methacrylic acid (MAA) as comonomer, hexadecane (HD) as co-stabilizer, Azobisisobutyronitrile (AIBN) as initiator and sodium dodecyl sulfate (SDS) as surfactant.*

Latex	Organic phase						Water phase	
	Fe <sub>3</sub> O <sub>4</sub> (%)	Styrene (g)	Fe <sub>3</sub> O <sub>4</sub> (g)	MAA (g)	HD (g)	AIBN (g)	Water (g)	SDS (g)
<b>E</b>	7.5	99.4	8.063	3.225	8.600	2.150	250.84	2.72
<b>F</b>	5	102.1	5.375	3.225	8.600	2.150	250.84	2.69
<b>G</b>	2.5	104.8	2.688	3.225	8.600	2.150	250.84	2.69
<b>H</b>	0.5	107.0	0.538	3.225	8.600	2.150	250.84	2.69
<b>I</b>	0.1	107.5	0.108	3.225	8.600	2.150	250.84	2.72

### 5.2.2. Liquid solutions

Liquid solutions are made by mixing demineralized water (type I), glycerol, Clariscan and the Fe<sub>3</sub>O<sub>4</sub>-latex particles as given in Table 5.1. Solutions were coded by GxPyFz where x gives the wt% of glycerol, y the wt% of particles and z the wt% of Fe<sub>3</sub>O<sub>4</sub> within the particles. Clariscan (C<sub>16</sub>H<sub>25</sub>GdN<sub>4</sub>O<sub>87</sub>) is a gadolinium based contrast agent commonly used in medical MRI, provided in a water like solution with a concentration of 279.3 mg/ml (0.5 M) [171]. The solution has a pH between 6.5 and 8, a density of 1.349 g/ml and a viscosity of 3.0 mPa.s at room temperature [282]. The goal of the Clariscan is to change the *T*<sub>1</sub> relaxation time, allowing fast imaging by UFI. The concentration of Clariscan was determined in chapter 4. The glycerol (> 99.0 % purity) has a density of 1.26 g/ml and is used to tune the viscosity of the liquid solutions.

For calibration of the signal, four glycerol contents were used (0 wt%, 25 wt%, 50 wt% and 70 wt%). The actual penetration experiments were only done with mixtures containing 70 wt% (G70) of glycerol and the particles with 0.5 wt% of iron oxide (F0.5). To study the effect of particle concentration, the particle concentration was varied between 0 (P0) and 8 wt% (P8). Experiments with lower viscosities can be performed but would lower the signal-to-noise ratio. When taking the spatial resolution (14.5 μm) and the measurement time (11.6 ms), an estimate about the maximum penetration speed can be given. When the distance that the liquid moves within the measurement time exceeds the spatial resolution, the decrease in signal-to-noise ratio becomes problematic. Therefore, the penetration speed limit for our experiments is 1.25 μm/s.

### 5.3 Theoretical particles signal calibration

Because our NMR equipment is set to measure hydrogen nuclei, the signal originates either from hydrogen nuclei of the liquid solution or from the latex particles. However, because UFI is a  $T_2$  weighted signal and the  $T_2$  time of the polystyrene within the latex particles was as low as 100  $\mu\text{s}$ , the polystyrene will not contribute to the signal intensity measured by UFI. Therefore, the only signal intensity that is measured is that of the liquid solution. The  $\text{Fe}_3\text{O}_4$  within the latex particles will decrease the  $T_2$  relaxation time of the surrounding liquid, which allows for the detection of the particles. Therefore, this section focuses on the effect of the particles on the NMR-signal of the liquid, with the goal to establish a calibration curve to determine the particle concentration. The signal intensity measured by UFI was determined in chapter 4.4 for liquid solutions by equation (4.13).

When  $\text{Fe}_3\text{O}_4$ -latex particles are introduced to the liquid solution, the  $\text{Fe}_3\text{O}_4$  influences the signal of the surrounding nuclei via two processes: shortening of the  $T_2$  time (equation (3.15)) [306], [307] and replacing water (visible with UFI) by latex particles (invisible with UFI). The replacement of water by latex particles can be introduced by replacing  $\rho$  by  $\rho_{\text{max}}(1-aC)$ , where  $\rho_{\text{max}}$  is the density of visible hydrogen nuclei in a pure liquid and  $a$  [ $\text{wt}\%^{-1}$ ] is a constant that represents the decrease in liquid hydrogen nuclei per  $\text{wt}\%$  of latex particles.

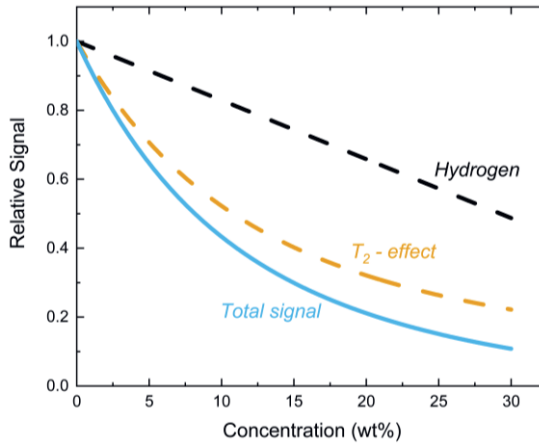


Figure 5.1 UFI NMR signal as a function of the particle concentration (blue). Shown in orange and black dashed lines are the contributions coming from the decrease in relaxation and the decrease of hydrogen atoms respectively.

When introducing both contributions in equation (4.13), the signal intensity becomes:

$$S(C) = \rho_{\text{max}} (1 - aC) \sum_{n=1}^{2N} \exp \left( -nt_e \left[ \frac{1}{T_{2dip}} + R_2 C \right] \right), \quad (5.1)$$

where the  $(1 - e^{-t_r/T_1})$  factor can be neglected due to the addition of Clariscan and its effect on the  $T_1$  time which guarantees that  $t_r/T_1 \ll 1$ . In this equation,  $R_2$  [ $\text{ms wt}\%^{-1}$ ] is the relaxivity of the  $\text{Fe}_3\text{O}_4$ -latex particles and  $C$  ( $\text{wt}\%$ ) the particle concentration.

If the signal intensity is taken relative to the signal of a solution containing no particles  $S(0) = \rho_{\max} \sum_{n=1}^{2N} \exp(-nt_e/T_{2dip})$ . The relative signal becomes:

$$S'(C) = (1 - aC) \sum_{n=1}^{2N} \exp(-nt_e R_2 C), \quad (5.2)$$

where it can be seen that  $S'(0) = 1$ . Here, it is assumed that the  $T_{2dip}$  of the solution does not change by introducing latex particles.

In Figure 5.1, the relative signal intensity  $S'$  is plotted for different concentrations of particles. The relaxation values  $R_2$  and  $a$  are set to  $0.095 \text{ ms}^{-1}\text{wt\%}^{-1}$  and  $0.016 \text{ wt\%}^{-1}$ , respectively. These values correspond to a mixture containing 70 wt% glycerol and particles with 0.5 wt% of iron oxide and are determined in section 3.1.2. For the echo time,  $50 \mu\text{s}$  is used. The signal decrease due to a lowering of the hydrogen atoms is drawn in black-dashed while the  $T_2$  effect is drawn in orange-dashed. The total calibration curve is a combination of both effects and is drawn in blue-solid. The resulting calibration curve allows to extract the particle concentration from the signal.

Within a porous media, the signal intensity decreases due to the porosity of the porous membrane  $\phi$ . When incorporating this effect into equation (5.2), we end up with,

$$S''(C) = \phi(1 - aC) \sum_{n=1}^{2N} \exp(-nt_e R_2 C). \quad (5.3)$$

## 5.4 Typical NMR signal profiles for different cases

When a particle dispersion penetrates in a thin, porous media, three typical situations can occur. Firstly, the particles and liquid move together as a homogeneous mixture and the particle and liquid front coincide. Secondly, the particles move slower than the liquid leading to a splitting of the particle and liquid front. Thirdly, the particles cannot enter the porous membrane, and a particle layers forms on top of the membrane. Because the measured NMR-signal is a function of the particle concentration (eq. (5.2)), all the above-mentioned cases will have their typical NMR-signal profiles. A better understanding of these NMR-signal profiles will help in understanding the measured profiles during uptake experiments. Therefore, a more theoretical discussion about the NMR-profiles will be given in this section.

In the top of Figure 5.2, the different situations are schematically drawn. The figures represent the penetration of liquid (blue) and particles (orange dots) in the nylon membranes (gray). The figures show  $50 \mu\text{m}$  of the droplet on the left followed by the nylon membrane where the interface is marked with a green dashed line. The liquid and particles move from left to right and their corresponding fronts are marked with respectively a black and orange dashed line. The middle figures show the corresponding wt% of liquid (blue-dashed) and particles (red-solid). The lowest figures represent the corresponding NMR-profiles. The NMR-profiles are simulated using MATLAB based on the NMR-system specifications (echo time of  $50 \mu\text{s}$  and a sample rate of 5 MHz), which results in a theoretical spatial resolution of  $14.5 \mu\text{m}$ . To calculate the signal intensities, the calibration curve for a mixture containing 70 wt% glycerol and particles with 0.5



wt% of iron oxide is used (blue-solid line in Figure 5.1). The start concentration of particles used in this discussion is 5 wt%, which corresponds to a relative value of 0.65. In the following subsections, we will discuss these potential situations in more detail.

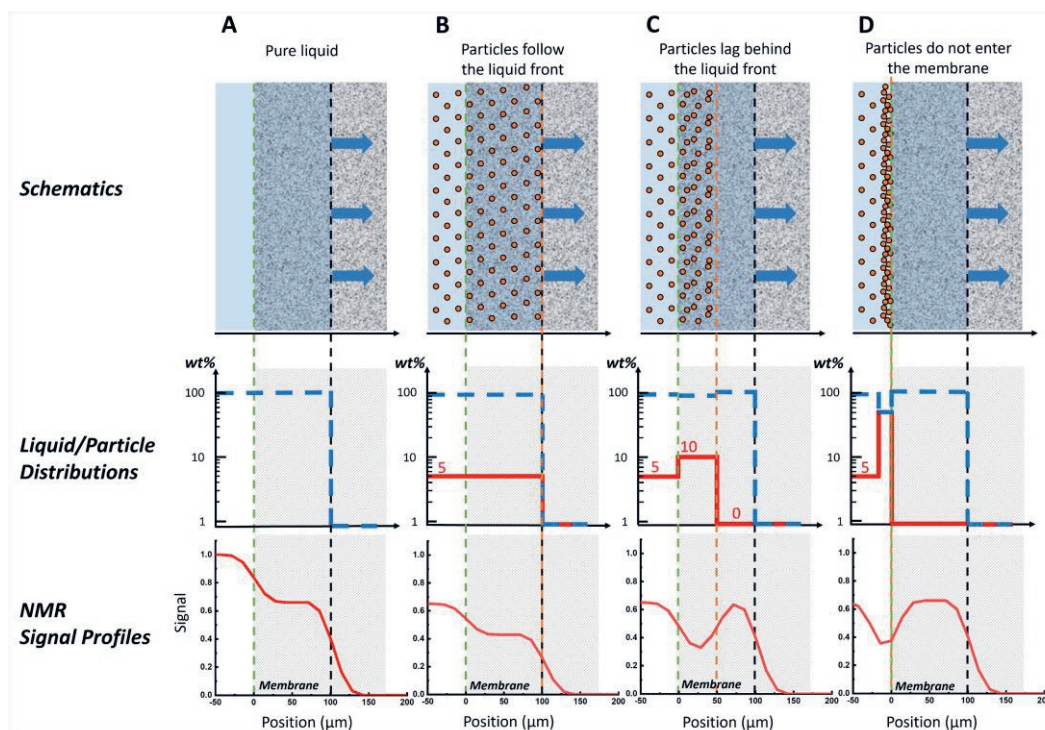


*Figure 5.2 Representation of four different archetypical situations that can occur during particle penetration. From left to right these four situations (top row), corresponding fluid and particle distributions (middle row) and resulting NMR signal profiles (bottom row) are shown. The four situations are A) pure liquid penetration, B) homogeneous movement of liquid and particles, C) splitting between particle and liquid front and D) particles cannot enter the porous media.*

#### 5.4.1. A pure liquid without particles (A)

In Figure 5.2A, the reference situation, where only liquid penetrates the nylon membrane is shown. The liquid content is always 100 wt% but drops to 0 after the liquid front. The corresponding NMR-profile shows first the droplet region with a signal intensity of 1, meaning a fully saturated region with only liquid. Within the membrane, the signal intensity of a fully saturated region drops to 0.65 as a consequence of the porosity (65 %). Ahead of the liquid front ( $x > 100 \mu\text{m}$ ), no liquid is found, which results in a signal intensity of zero. From the reference, it can be observed that the NMR-resolution will have a significant effect on the NMR-profiles, which can be observed in the gradual change in signal intensity at the droplet-membrane and liquid front interface. Experimental measurements of this situation can be found in chapter 4.5.3, where the penetration of water-glycerol mixtures was measured within nylon- and PVDF-membranes.

### 5.4.2. Homogeneous movement of liquid and particles (B)

In the second situation (Figure 5.2B), the particles move together with the liquid and, therefore, the liquid front (black-dashed line) and particle front (orange-dashed line) coincide. In this particular case, the particle concentration was set to 5 wt%. As there is no blocking of particles, at the droplet-liquid interface, the particle concentration everywhere in the liquid phase is 5 wt% (Figure 5.2B, middle). Because the particles are homogeneously distributed, their effect on the signal intensity will be the same at every position. Therefore, the profile is similar to the reference but lowered with a factor of 0.65 due to the presence of particles.

### 5.4.3. The particle front lags behind the liquid front (C)

In the third case, a splitting between the particle front and liquid front occurs. In Figure 5.2C top, the particle front has reached a depth of 50  $\mu\text{m}$  (orange-dashed), while the liquid front has already reached 100  $\mu\text{m}$  (black-dashed line). Figure 5.2C middle, shows the particle concentration throughout the sample starting with 5 wt% in the droplet, 10 wt% until 50  $\mu\text{m}$  followed by a region with no particles. The increased particle concentration in the upper part of the membrane can be attributed to the slower movement of the particles, which results in a buildup of particles. From the calibration curve, we know that the signal will be higher in absence of particles, therefore the signal will start to increase again around 50  $\mu\text{m}$ . The corresponding NMR-profile can be seen in the bottom of Figure 5.2C, where a clear increase in signal intensity is found beyond 50  $\mu\text{m}$ . When the separation between the particle and liquid front is larger than two times the resolution (29  $\mu\text{m}$ ), the signal intensity will increase back to its original intensity found within the reference. In this way, the NMR-profiles could be used to identify a splitting in particle and liquid front. The position of this particle front is situated at the position where the increase in signal intensity is at half maximum (the orange-dashed line).

### 5.4.4. Particle cannot enter the porous media (D)

In the last situation, the particles do not enter the porous membrane, while the liquid penetrates (Figure 5.2D). In this situation, the particles are clogged and stay at the droplet-membrane interface (green-dashed line), where they will create a dense particle layer. In this example, an arbitrary particle layer with thickness of 20  $\mu\text{m}$  and a particle content of 50 wt% was chosen. Inside the medium only water can be found, which can be seen in the middle figure. The dense particle layer results in a decreased NMR-signal intensity on top of the membrane. Similar to the situation where particles lag behind the liquid front, the signal starts to increase to its original value within the membrane ( $x > 0$   $\mu\text{m}$ ), because only liquid is present here. As the particle layer at the top is smaller than 2 times the resolution (29  $\mu\text{m}$ ), the signal at the droplet-membrane interface will not reach zero.

## 5.5 Experimental details

For the NMR measurements, the same GARField NMR as in chapter 4 is used, having specially designed curved poles and a magnetic gradient of 41.5 T/m. Figure 5.3 shows a schematic representation of the setup, similar to Figure 4.7 but now with a membrane

sample during the penetration of a particle suspension rather than only liquid. The measurement area is located above the RF-coil, which has a diameter of 4 mm.

During an experiment, a syringe was used to jet droplets on top of the nylon membrane filter (brown speckled). The droplet was typically around 8 – 12  $\mu\text{l}$ . In all experiments, the droplet covered the entire measurement area. A droplet sensor was used to trigger the NMR and start the UFI pulse sequence. Samples were made by gluing a membrane filter on top of a glass plate (dark grey) using double sided tape (light grey).

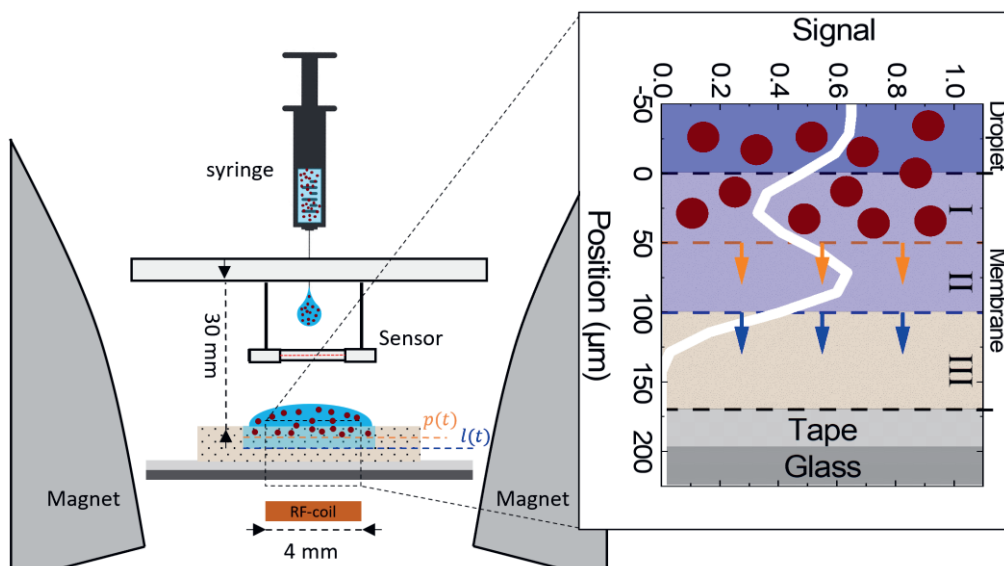


*Figure 5.3 Experimental setup with a typical sample situation and the corresponding 1D - UFI-signal profile as calculated by equation (5.3). Shown are the curved magnetic poles of the GARField NMR, the RF-coil, the syringe and droplet sensor. The sample consists of a droplet, nylon membrane (brown), double sided tape (light grey) and glass plate (dark grey). The liquid within the droplet and membrane is shown in blue and particles are shown with brown circles. The corresponding liquid front  $l(t)$  and particle front  $p(t)$  are marked with orange and blue line respectively. The same markings are used within the 1D-signal profiles.*

In this figure, a typical particle penetration experiment is shown where a liquid-particle mixture with 5 wt% of particles penetrates within a nylon membrane. Within this example, the liquid has partly penetrated the sample and the particle front  $p(t)$  (orange, 50  $\mu\text{m}$ ) lags the liquid front  $l(t)$  (blue, 100  $\mu\text{m}$ ). On the right, the corresponding UFI-signal profile is shown. The signal is shown within the droplet ( $x < 0 \mu\text{m}$ ), membrane ( $0 \mu\text{m} < x < 170 \mu\text{m}$ ), tape ( $170 \mu\text{m} < x < 195 \mu\text{m}$ ) and glass plate ( $195 \mu\text{m} < x$ ). The signal inside the droplet was calculated based on equation (5.3), which for a particle concentration of 5 wt% results in 0.625. Within the membrane, the signal intensity can be split into three regions: region I, with both liquid and particles, region II, with only liquid, and region III without particles and liquid. In region I, the signal intensity drops compared to the droplet because of the porosity  $\phi$  of the membrane. In region II, the signal starts to increase again because of the absence of particles. Finally in region III, the signal intensity drops to zero because no liquid is found.

After the membrane, the tape and glass plate are located which never have signal, because the mixtures are unable to penetrate these regions.

## 5.6 Characterization of iron-oxide latex particles

To characterize the particles, particle size distributions were measured for both the hybrid iron oxide latex particles and the iron oxide particles themselves. Additionally, STEM images of the hybrid iron oxide latex particles are provided which depict both the complete particles and individual iron oxide nanoparticles.

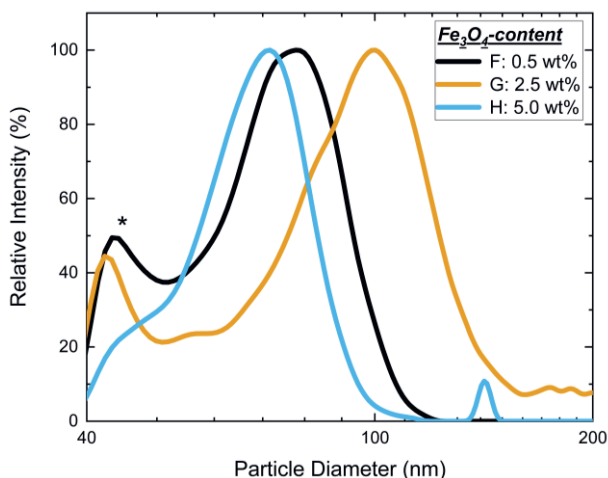


Figure 5.4 Particle size distribution of  $\text{Fe}_3\text{O}_4$ -polystyrene latex particles containing 0.5 wt% (black), 2.5 wt% (orange) and 5 wt% (blue) of  $\text{Fe}_3\text{O}_4$ . The small population observed around 40 nm which is marked with a star, is an artifact due to the signal of the emulsifier, which is not separated from the particles due to its small size.

Figure 5.4 shows the particle size distributions of the  $\text{Fe}_3\text{O}_4$ -polystyrene latex particles containing 0.5 wt% (black), 2.5 wt% (orange) and 5 wt% (blue) of  $\text{Fe}_3\text{O}_4$ . The particle size distribution was measured by capillary hydrodynamic fractionation (CHDF). A CHDF-3000 (Matec Applied Science) was used with an operating flow of 1.4 ml/min at 35.0 °C and detector wavelength at 220 nm. The carrier fluid was 1X-GR500 (Matec). The samples were diluted to 0.5 % S.C. using the carrier fluid and the samples were analyzed using the Matec software v.2.3. The small population observed around 40 nm which is marked with a star, is an artifact coming from the signal of the emulsifier, which is not separated from the particles due to its small size. Furthermore, the particles containing 5.0 wt% of iron oxide (blue line) show a small peak around 150 nm which probably comes from an artefact as the measurement was performed three times and the peak was only observed once.

Scanning transmission electron microscopy (STEM) images of the latex particles containing 7.5 wt% of iron oxide (E in Table 5.1) are shown in Figure 5.5a. In this image, latex particles appear as light gray while iron oxide appears white. The figure shows individual iron oxide latex particles embedded within the latex particles. Using these images, a particles size distribution was obtained for the iron oxide particles which are shown in Figure 5.5b.

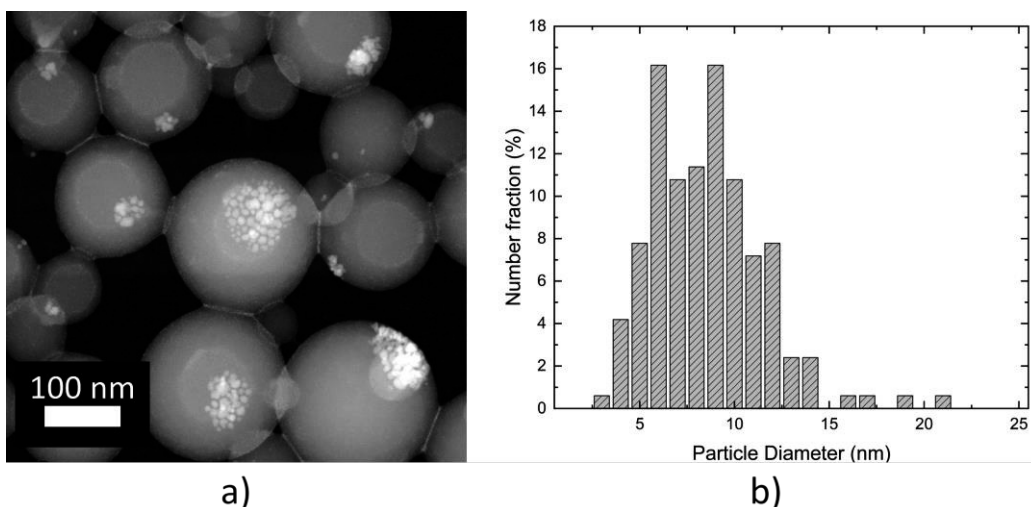


Figure 5.5 STEM image of the  $\text{Fe}_3\text{O}_4$  latex particles containing 7.5 wt% iron oxide (E) latex appears as light gray while  $\text{Fe}_3\text{O}_4$  appears white. B) Particle size distributions of the  $\text{Fe}_3\text{O}_4$  particles, determined from STEM images.

## 5.7 Characterization of liquid solutions

The particle dispersion used in this study are given in Table 5.2, together with their physical parameters. For the complete set of liquids used in signal calibration in section 5.8, we refer to Nicasy et al. [308]. The viscosities of the solutions were measured using an Anton Paar MCR302 rheometer (20 °C), while the surface tension was determined using the Wilhelmy plate method.

The measured data reveals that an increase in particle concentration leads to an increased viscosity and decreased surface tension. The  $T_1$  and  $T_2$  times of the liquid solutions are measured using a saturation recovery and OW sequence respectively.

Table 5.2 The liquids used in the imbibition experiments and their physical properties.

Name	Particles (wt%)	Viscosity (mPa.s)	Surface tension (mN/m)	$T_1$ (ms)	$T_2$ (ms)
<b>G70P0</b>	0.00	23.48	67.60	6.06	4.95
<b>G70P1F0.5</b>	0.99	25.66	63.48	5.37	3.27
<b>G70P2F0.5</b>	2.10	39.09	59.07	5.46	2.51
<b>G70P3F0.5</b>	3.01	32.79	58.80	5.20	2.11
<b>G70P5F0.5</b>	5.03	39.89	57.74	4.52	1.48
<b>G70P8F0.5</b>	7.94	60.27	55.91	3.40	1.10

## 5.8 NMR characteristics of latex particles

Before particles can be followed during imbibition experiments, their NMR characteristics were studied by determining their relaxation characteristics and effect on the signal intensities within the setup. The goal of this section is to select the proper  $\text{Fe}_3\text{O}_4$  latex particle and make particle calibration curves. The section starts by determining the relaxation behavior of latex particles containing varying  $\text{Fe}_3\text{O}_4$  content. Thereafter, the effect of the latex particle concentration on the  $T_2$  relaxation time is studied in order to get values for  $R_2$  and  $a$  (equation 4). The relaxation measurements will be used to determine the calibration curves and select the  $\text{Fe}_3\text{O}_4$  latex particles for the imbibition experiments.

### 5.8.1. Effect of $\text{Fe}_3\text{O}_4$ -content on the relaxation behavior

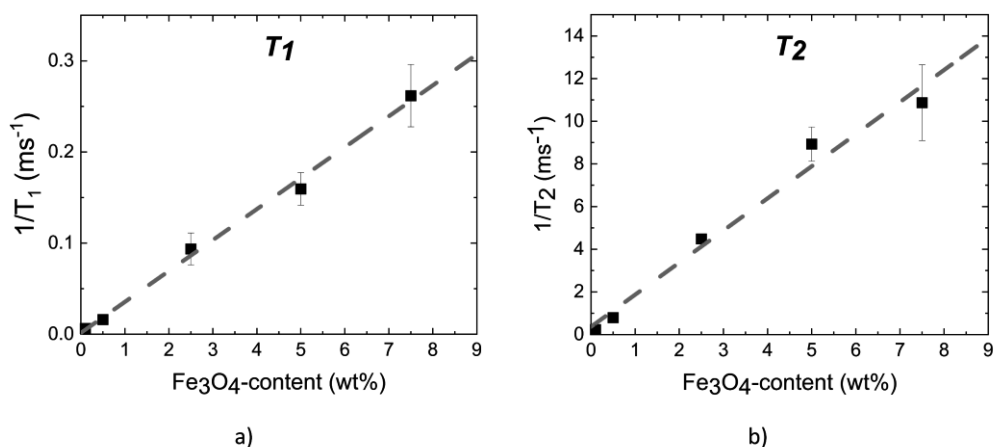


Figure 5.6 Inverse relaxation times as a function of the  $\text{Fe}_3\text{O}_4$ -content in the latex particle's cores. a)  $T_1$  and b)  $T_2$

To characterize the effect of the iron-oxide within the latex particles, the relaxation characteristics of particles containing different amounts of iron-oxide were measured. All solutions contained 70 wt% water and 30 wt% solid content, from which 0.1 wt % to 7.5 wt % was iron oxide.  $T_2$  and  $T_1$  decay curves were measured using an OW-sequence and saturation recovery sequence. Figures of the decay curves can be found in chapter 5.11 (appendix A) and show that increasing the iron-oxide content decreases both the  $T_1$  and  $T_2$  relaxation times. In Figure 5.6, the inverse relaxation times are plotted as a function of the  $\text{Fe}_3\text{O}_4$  content, which shows a linear relationship between both. From this linear relationship, the relaxation rates  $R_2$  and  $R_1$  were determined to be  $1.5 \text{ ms}^{-1}\text{wt}\%^{-1}$  and  $0.034 \text{ ms}^{-1}\text{wt}\%^{-1}$ . Based on this finding, the particles containing 0.5, 2.5 and 5 wt% of  $\text{Fe}_3\text{O}_4$  were selected for further observation. The particles containing 0.1 wt% showed a  $T_2$  relaxation time with too low effect to make them clearly visible, whereas the one containing 7.5 wt% decreased the  $T_2$  relaxation time too much in order to have sufficient signal for UFI measurements.

## 5.8.2. Effect of particle concentration on the relaxation behavior

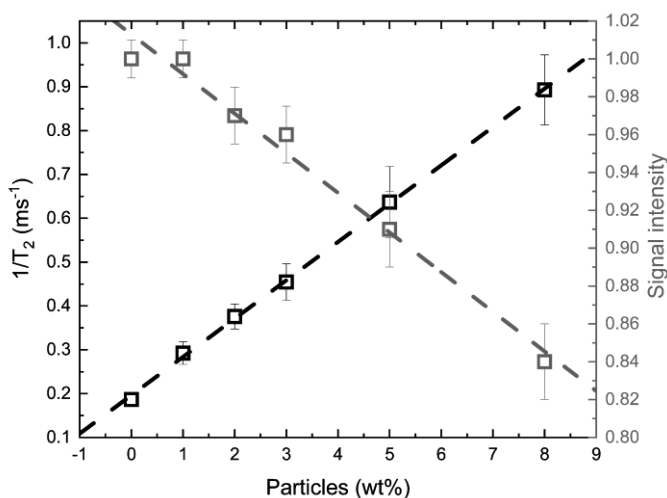


Figure 5.7 Inverse  $T_2$  relaxation time (black) and maximum signal intensity (gray) in function of particle concentration for a dispersion containing 70 wt% of glycerol and particles with 0.5 wt% of  $\text{Fe}_3\text{O}_4$ .

To determine the relaxation characteristics as function of the particle concentration, relaxation times were determined for liquid mixtures containing varying particle concentrations. Because the addition of Clariscan will ensure that the  $T_1$  relaxation time will not influence the signal intensity (eq. (5.2)), only the  $T_2$  decay will be discussed in this section. Information about the effect on the  $T_1$  relaxation time can be found in chapter 5.12, appendix B. This study was performed on solutions containing a varying glycerol content (0 wt%, 25 wt%, 50 wt% and 70 wt%) with the particles containing 0.5 wt%, 2.5 wt% and 5 wt% of iron oxide. A list of all solutions can be found in Nicasy et al. [308].  $T_2$  relaxation times of the solutions were determined by an Ostroff-Waugh pulse sequence with an echo time of 50  $\mu\text{s}$ . The measured decay curves for the solution containing 70 wt% glycerol, 0.005 M Clariscan and 0 - 8 wt% of particles are given in Nicasy et al. [308], Figure 5.7 shows the inverse  $T_2$  relaxation time and maximum signal intensity as a function of particle concentration (particles with 0.5 wt% of iron oxide) for a mixture containing 70 wt% of glycerol. These dispersions will be used for the particle penetration experiments in chapter 6 and 9. It is obviously, increasing the particle concentration increases the inverse  $T_2$  relaxation time, as expected from equation (3.15). The expected linear relationship between  $1/T_2$  and the particle concentration is observed. Furthermore, the maximum signal intensity depends linearly on the particle concentration. Using these data, a value for factor  $a$  ( $0.016 \text{ wt}\%^{-1}$ ) and relaxivity  $R_2$  ( $0.042 \text{ ms}\text{wt}\%^{-1}$ ) can be found. Values for  $a$  and  $R_2$  corresponding to all possible combinations of glycerol content and iron oxide content can be found in chapter 5.12, appendix B.

### 5.8.3. Calibration curves

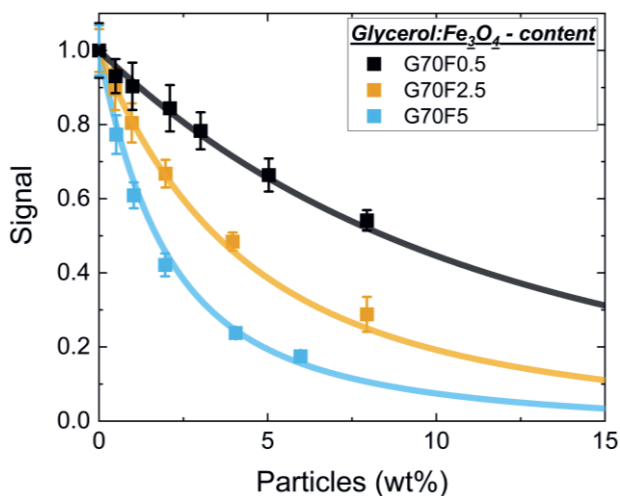


Figure 5.8 Calibration curves for the signal intensity as a function of the particle concentration for varying  $\text{Fe}_3\text{O}_4$  contents but with a similar glycerol content of 70 wt%. Calibration curves, predicted from the obtained values of  $R_2$  and  $a$ , are shown as lines. The data points mark measured UFI-NMR signals from the particle dispersions.

In this section, the relaxation characteristics are used to construct calibration curves that couple the signal intensity with the particle concentration in UFI experiments. These calibration curves allow to determine particle density profiles during capillary uptake.

In this section, calibration curves are determined for solutions containing 70 wt% glycerol and iron oxide contents of 0.5, 2.5 and 5 wt%. Calibration curves for other combinations of glycerol and iron oxide can be made in a similar way using the values found in chapter 5.12, appendix B. To test the theoretical model, signal intensities of all liquid mixtures were measured by UFI. Figure 5.8 shows a comparison between the measured signal (dots) and the predictions (lines) using the theoretical model.

The graph shows the calibration curve for different  $\text{Fe}_3\text{O}_4$  latex particles, containing 0.5 wt%, 2.5 wt% and 5 wt% of  $\text{Fe}_3\text{O}_4$ . As expected, with increasing the  $\text{Fe}_3\text{O}_4$  content, the signal drop is steeper with increasing the particle concentration. It is seen that the measured signal intensities (points) coincide very well with the theoretical signal intensities (lines) found by equation (5.2). The type of  $\text{Fe}_3\text{O}_4$  content that should be used will depend on the type of experiment. The advantage of using a lower iron oxide content, such as 0.5 wt%, is the large range of particle concentrations that can be probed. However, the signal differences are smaller and therefore harder to discriminate. Therefore, when small particle concentrations should be discriminated, particles with a higher  $\text{Fe}_3\text{O}_4$  content are recommended. The downside of the larger signal differences is the smaller range of particle concentrations that can be probed. While with a 0.5 wt%  $\text{Fe}_3\text{O}_4$  content, solution with a particle concentration of 15 wt% still provide enough signal (black line), the particles with 2.5 wt% (orange line) and 5 wt% (blue line) can only be used to probe particle concentrations up until 7.5 wt%, where the signal enters the noise level. In the subsequent study, we performed all measurements on dispersion with particles containing 0.5 wt%  $\text{Fe}_3\text{O}_4$ .



## 5.9 Measuring particle concentration profiles during imbibition

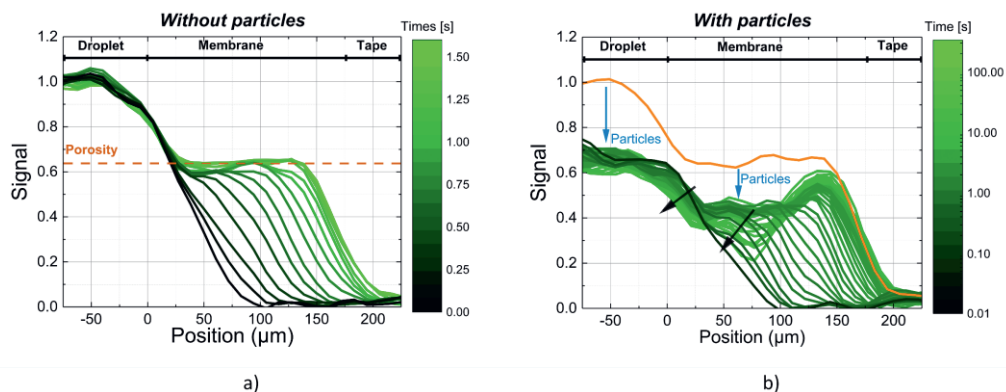


Figure 5.9 UFI-NMR signal profiles measured for different times during the penetration of a 70 wt% glycerol mixtures with no particles (a) and with 5 wt% of  $\text{Fe}_3\text{O}_4$  latex particles that contain 0.5 wt% of  $\text{Fe}_3\text{O}_4$  (b) inside nylon membrane II. The orange line in figure b, is drawn as a reference and corresponds to a profile of a filled membrane with a solution containing no particles as seen in figure a. The black arrows are used to indicate how the profiles change over time. In both figures, a green color map is used to mark the specific time of each profile. Note the huge time difference in timescales of both figures.

In this section, the UFI-NMR method is used to study particle transport during imbibition, by comparing two imbibition experiments on a nylon 0.45 membrane. The experiments are performed with a solution containing no particles (G70P0) and 5 wt% of particles (G70P5F0.5). Both solutions contain 70 wt% of glycerol, used to slow down the penetration and increase the signal-to-noise ratio. The section starts by comparing the measured UFI-NMR signal profiles. Thereafter, the calibration curves in Figure 5.8 is used to determine particle concentration profiles, which in the final part will be compared to SEM-images.

Figure 5.9a, shows the signal profiles for the G70P0 liquid. Similar profiles were also shown in chapter 4, with the penetration of a glycerol mixture inside PVDF and nylon membranes. As explained before, the liquid profiles can be divided in three main regions: the droplet ( $x < 0$ ,  $S = 1$ ), membrane ( $0 < x < 170$ ,  $S \approx 0.65$ ) and tape ( $170 < x$ ,  $S = 0$ ). With no particles, Figure 5.9a, the droplet has signal intensity 1, referring to a fully saturated region. Inside the membrane, the volume percentage of liquid drops, because of the membrane porosity. This results in a decrease in signal intensity equal to the porosity of the membrane, which in this membrane is around 65%. The tape has a signal intensity of 0 because of the absence of liquid.

Figure 5.9b, shows the signal profiles for the penetration of the G70P5F0.5 liquid. The time of each profile is indicated with a green color map. Because particles keep penetrating after the liquid reaches the bottom of the membrane, profiles are measured for longer times than in Figure 5.9a. The addition of particles affects the measured liquid profiles, which are marked by arrows. Blue arrows indicate changes observed from the beginning of the experiment, therefore showing where particles are present, and black

arrows indicate how the profiles change over time, which therefore give information about particle accumulation through time. The changes are marked by blue arrows. For comparison a signal profile of a fully saturated membrane containing the G70P0 is added (orange). In the droplet, the signal decreases from 1 to 0.65, in correspondence with the black calibration curve in Figure 5.8. Inside the membrane, a decrease in signal intensity is observed in the upper part of the membrane ( $0 < x < 100$ ) while, in the bottom part of the membrane ( $x > 100$ ) the signal intensity increases again. These profiles correspond to case C from Figure 5.2, the situation that the particle front lags the liquid front. A clear signal increase is only observed behind  $100 \mu\text{m}$ , which indicates that the splitting before this distance is not large enough to be picked up by our setup. The particle's final penetration depth can be determined to be  $100 \mu\text{m}$ , the position where the signal intensity starts to increase again.

After the liquid has reached the bottom of the membrane, the droplet keeps spreading, allowing more particles to enter. The increase in particle concentration can be observed by the continuous decrease in signal intensity, as marked by a black arrow. The signal decrease is observed in the upper part of the membrane, which indicates that particles do not penetrate deeper than  $100 \mu\text{m}$ . Besides the signal increase within the membrane, a slight signal decrease on top of the membrane is also observed, which is probably due to a buildup of particles that are unable to penetrate inside the medium.

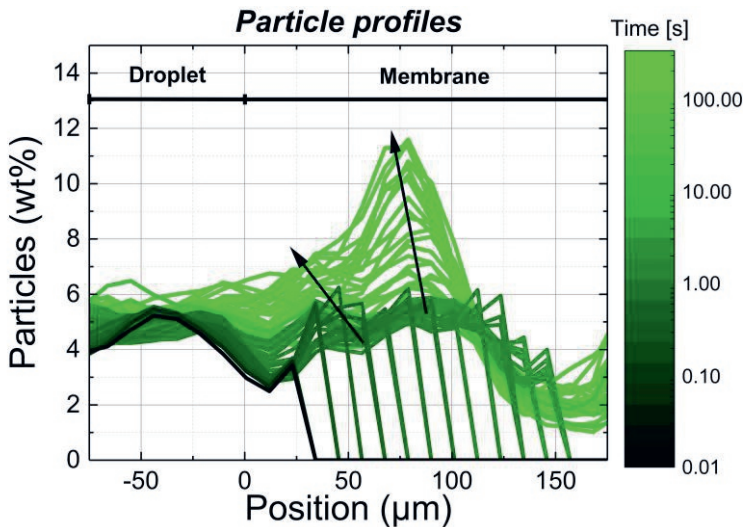


Figure 5.10 Particle concentration profiles corresponding to the profiles of Figure 5.9b.

Using the black calibration curve in Figure 5.8, particle density profiles can be calculated for every signal profile shown in Figure 5.9b. However, before this can be done, the effect of porosity on the signal intensity should be taken into account. This is done by dividing the signal profiles of Figure 5.9b (green) by a profile of a fully saturated membrane (orange) containing only liquid. This will result in signal intensity profiles that are completely determined by the particle concentration, for which the calibration curve can be used to determine the particle concentration profiles. Figure 5.10, shows the particle concentration profiles that correspond to the signal profiles shown in Figure 5.9b.

However, there are still some limitations when determining the particle concentration profiles. First, the particle concentration can only be determined behind the liquid front, where the signal intensity has reached its maximum and is not affected by the limits in resolution. If concentrations are determined too close to the liquid front, the incline due to the resolution limit will result in an overestimation of the particle concentration. Therefore, particle concentrations are determined until 20  $\mu\text{m}$  behind the liquid front. For the same reason, particle concentration profiles are only shown until 175  $\mu\text{m}$ . However, some profiles still have the problem of an overestimation near the end of the particle concentration profiles. The resolution problems will also lead to difficulties in determining particle concentrations near the droplet-membrane interface.

The particle concentration profiles in Figure 5.10 show that the particle concentration inside the droplet and top part of the membrane varies around 5 wt%, in line with the initial concentration of the droplet. This shows that the particles are not hindered by the interface and move together inside the porous medium. This small decline observed at the droplet-membrane interface is probably due to difficulties in determining the particle concentration around interfaces, as it will become more homogeneous through time. During penetration, it is observed that the particle concentration will start to decrease around 100  $\mu\text{m}$ . However, the particle concentration does not decrease towards 0, which suggests that some particles penetrate deeper than 100  $\mu\text{m}$ . Another explanation may originate from the NMR-resolution. If the experimental resolution is 18  $\mu\text{m}$ , a complete signal recovery would require that the particles are at least 36  $\mu\text{m}$  separated from the end of the membrane. In practice, this distance to require complete signal recovery can be somewhat higher. However, our measurement, shows that particles are able to penetrate up to 100  $\mu\text{m}$  and the sample is around 170  $\mu\text{m}$  in thickness. Therefore, there are probably particles that do penetrate a little further than 100  $\mu\text{m}$ .

After the liquid has reached the end of the membrane, the continuous spreading of the droplet in lateral direction will keep bringing particles into the membrane. Because the lateral penetration of liquid takes place beyond the measurements area, this movement cannot be observed within the UFI measurement. However, the additional particles that are brought in are observed by an increase in the particle concentration, which is marked by black arrows in Figure 5.10. It is seen that the particle concentration does not increase homogeneously throughout the medium. The concentration increases first inside the membrane, at 100  $\mu\text{m}$ , which is the depth the particles could penetrate during the process of vertical liquid penetration. Followed by a particle concentration increase that will travel towards the droplet-membrane interface. The final profiles show that the particle concentration has increased to 12 wt% within 330s.

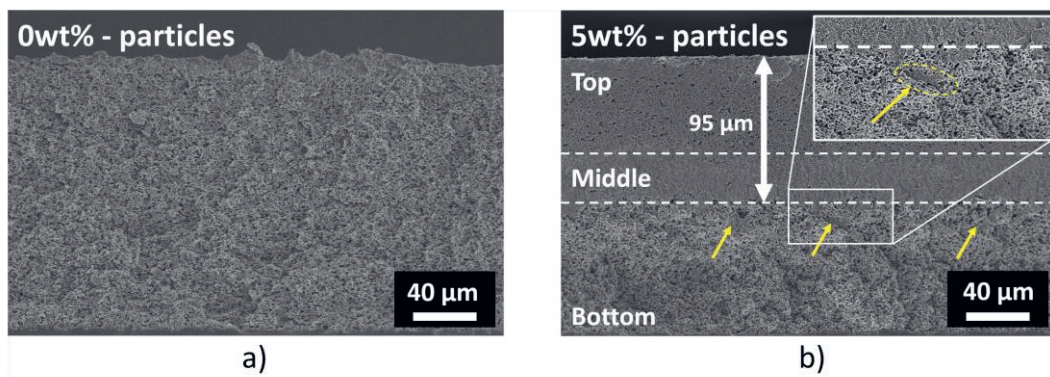


*Figure 5.11 SEM-images of the cross section of a nylon membrane after the penetration of a droplet containing no particles (a) and containing 5 wt% of particles (b). Both droplets also contained 70 wt% of glycerol. The white line marks the particle penetration depth and the red lines refer to particles that were able to penetrate behind the final particle penetration depth.*

To verify these findings, SEM-images of the samples cross-section were taken after penetration. Figure 5.11 a and b show the SEM-images, corresponding to the samples used for the experiments shown in Figure 5.9a (no particles) and Figure 5.9b (5 wt% of particles). In samples without particles (reference), the membranes texture is homogeneous throughout the whole cross-section. No particles are visible and only nylon fibers can be seen. The situation is completely different after the penetration of a dispersion containing 5 wt% of particles Figure 5.11b). Based on the texture, three different regions can be distinguished. The top, which looks denser and completely different than the reference sample, the middle, appearing even denser (between white dashed lines) and the bottom with a similar texture as the reference sample. Figure 5.12 shows close-up pictures of the top (a), middle (b) and bottom (c) part of the picture in Figure 5.11b. In the top of the membrane, particles are clearly visible. The particles cover the entire surface of the nylon membrane and almost no fibers are visible. Particles are also visible in the middle part of the membrane, but here the density of particles is higher compared to the top part. Whereas open pores are still visible at the top of the membrane, almost no open pores are visible in the middle part of the membrane. From the SEM pictures, the dense particle layer is determined to have a thickness around 30  $\mu\text{m}$ , white dashed lines in Figure 5.11b. The gradient in particle concentration, as well as the dense particle layer, are in line with the observation made by the UFI-NMR experiment in Figure 5.10. Where particles are present at the top and middle part of the membrane, they are not visible in the bottom part, Figure 5.12c. This underlines the existence of a final particle penetration depth, in line with the UFI-NMR observation. The final penetration depth extracted from the SEM images is 95  $\mu\text{m}$  (indicated with a white arrow). A closer look to Figure 5.11b, reveals that there are some particles beyond the dense particle layer (yellow arrows). This is probably the reason for the non-zero particle concentration found beyond 100  $\mu\text{m}$  in Figure 5.10.

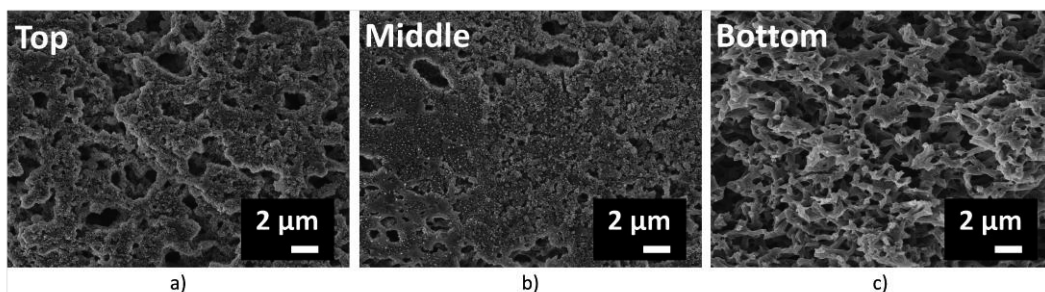


Figure 5.12 SEM images of the top (a), middle (b) and bottom (c) part of the cross-section shown in Figure 5.11b

## 5.10 Conclusions

In this chapter, it was demonstrated how the UFI method introduced in 4 is also able to study particle transport in thin, porous membranes. The chapter gave an extensive explanation about the effect of  $\text{Fe}_3\text{O}_4$  latex particles on the UFI-NMR signal. In this part, a calibration curve was found that linked the UFI-NMR signal to the particle's concentration. The curves showed that  $\text{Fe}_3\text{O}_4$  latex particles decrease the UFI-NMR signal due to  $T_2$  relaxation and lowering the water molecule fraction.

The second part of this chapter demonstrated how UFI-NMR can be used to study the particle penetration during imbibition into thin, porous media. UFI-NMR measurements of the penetration of a 70 wt% glycerol mixture containing 5 wt% of  $\text{Fe}_3\text{O}_4$  latex particles revealed that the particles were able to penetrate inside a 170  $\mu\text{m}$  thick nylon membrane. The measurements also showed a splitting between the liquid and particle front, which resulted in a final particle penetration depth of 100  $\mu\text{m}$ . The UFI-NMR profiles could be used to determine particle concentration profiles during penetration, revealing an inhomogeneous buildup of particles within the membrane. The concentration increases first within the membrane, at the final particle penetration depth of 100  $\mu\text{m}$ , after which the concentration also increases more at the top of the membrane. The measurements showed that the particle concentration has increased from 5 to 12 wt% within 330 s within the membrane.

Both the final particle penetration depth and gradient in particle concentration were verified with Scanning Electron Microscopy images of the samples.

## 5.11 Appendix A: NMR decay curves as a function of $\text{Fe}_3\text{O}_4$ content

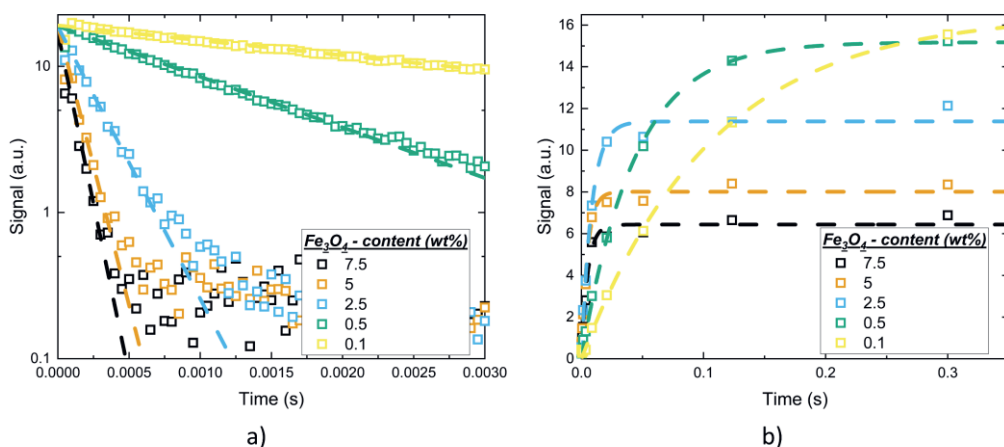


Figure 5.13 a)  $T_2$  relaxation measurement performed by an OW-sequence for solutions containing 30 wt% of latex particles with varying  $\text{Fe}_3\text{O}_4$  content ranging between 0.1 and 7.5 wt%. Dots are used for measured data while lines are the corresponding fits. b)  $T_1$  relaxation measurements performed by a saturation recovery sequence on the same solutions found in figure a.

To study the effect of  $\text{Fe}_3\text{O}_4$  within the latex particles on the NMR relaxation times of the liquid dispersion, signal decays were measured by an OW-sequence ( $t_e = 50 \mu\text{s}$ ) for the  $T_2$  time and by a saturation recovery sequence for the  $T_1$  time. Figure 5.13 shows measured signal decays for the  $T_2$  measurement (a) and the  $T_1$  measurement (b) for solution containing 30 wt% of  $\text{Fe}_3\text{O}_4$  latex particles with varying iron oxide contents between 0.1 and 7.5 wt%. In both cases, increasing the  $\text{Fe}_3\text{O}_4$  content increases the signal decay rates. Decay curves of the data are fitted with dotted lines and can be used to extract the  $T_2$  (Figure 5.7b) and  $T_1$  time (Figure 5.7a). Besides the changes in relaxation time, it is observed that by increasing the  $\text{Fe}_3\text{O}_4$  content, the maximum NMR-signal decreases. The decreasing NMR signal can partly be understood by the replacement of polystyrene with iron oxide which lowers the hydrogen atom density. However, the signal change is larger than would be expected based on only the replacement of polystyrene with iron oxide. A possible reason for this behavior would be that the iron oxide bleaches part of the signal around it. Further research is required to quantify this effect, but this lies beyond the scope of this research and is therefore not given.

## 5.12 Appendix B: Decay curves as a function of particle concentration

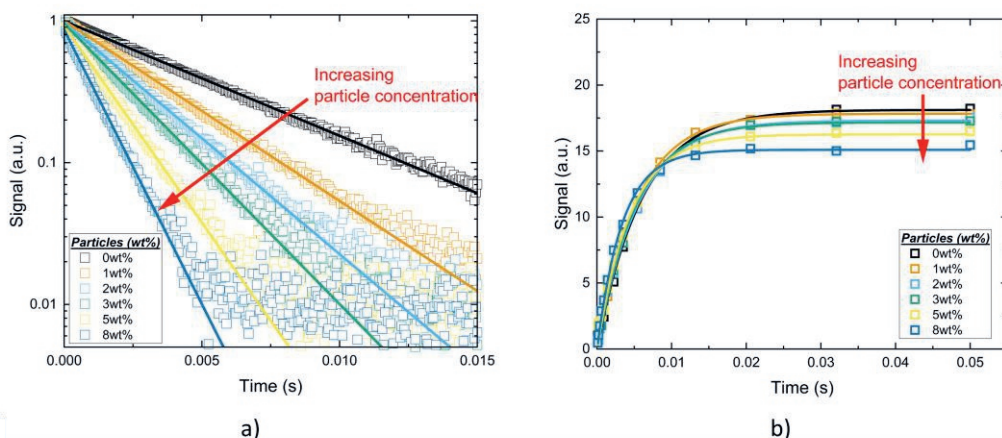


Figure 5.14 a) Signal decays measured by an OW-sequence for liquid solutions containing varying amounts of latex particles, 70 wt% of glycerol and 0.5 wt%  $\text{Fe}_3\text{O}_4$ .

b) Signal decays measured by a saturation recovery sequence for liquid solutions containing varying amounts of latex particles, 70 wt% of glycerol and 0.5 wt%  $\text{Fe}_3\text{O}_4$

In this section, the NMR  $T_2$  and  $T_1$  decay curves are shown for solutions containing 70 wt% glycerol, 0.005 M Clariscan and varying particle concentrations. The particles in the measurements that are shown contain 0.5 wt% of iron oxide. The data is measured with an OW-sequence ( $t_e = 50 \mu\text{s}$ ) and saturation recovery sequence for the  $T_2$  and  $T_1$  respectively. Figure 5.14 shows the signal decay curves for  $T_2$  (a) and  $T_1$  (b). By fitting the relaxation data with  $S = S_{\max}(\exp(-t/T_2))$  and  $S = S_{\max}(1 - \exp(-t/T_1))$ , the relaxation data and maximum signal intensities can be extracted. For the  $T_2$  decays, fits were made on the first 32 echoes. The reason for choosing only the first 32 echoes is because UFI uses the first 32 echoes to build up a liquid profile [24]. Therefore, the relaxation characteristics of these first 32 points are most relevant and are used for fitting. In both measurements, the relaxation time and maximum signal intensity decreases when increasing the particle concentration, marked by a red arrow.

The determined relaxation times and maximum signal intensities can be used to determine the relaxation rates ( $R_1$ ,  $R_2$ ), required determining the signal intensity  $S$  as given in equation (5.2). The value for  $R_2$  is determined in Figure 5.7 of section 5.8.2 while the value for  $R_1$  is determined within this section Figure 5.15.

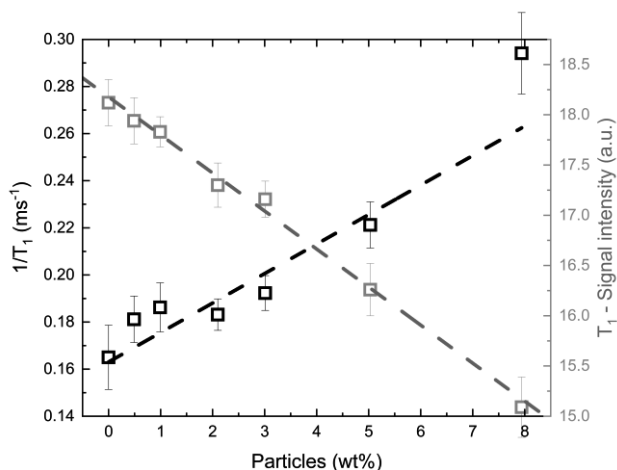


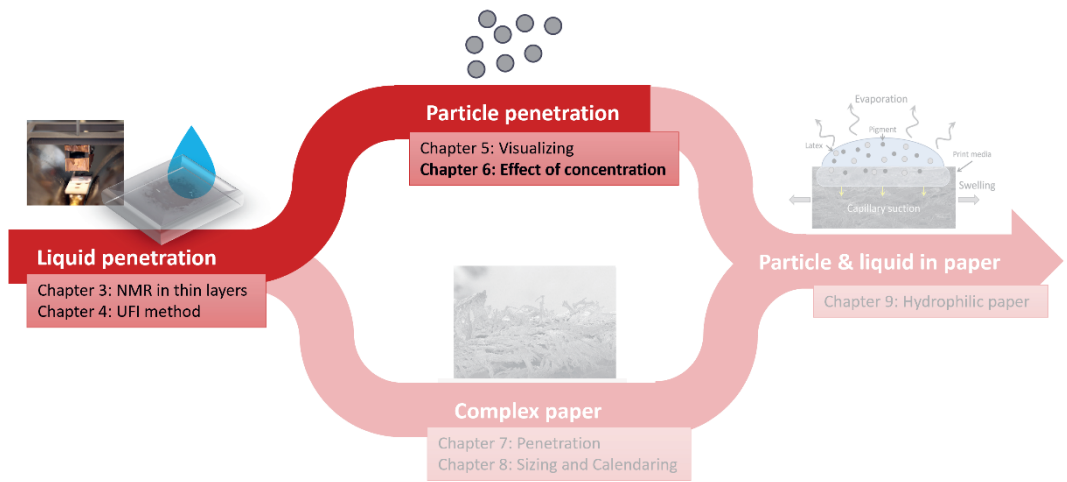
Figure 5.15 Inverse  $T_1$  relaxation time and maximum signal intensity in function of particle concentration for a solution containing 70 wt% of glycerol and  $\text{Fe}_3\text{O}_4$ -latex particles with 0.5 wt% of iron oxide.

The relaxation parameters are determined for  $\text{Fe}_3\text{O}_4$ -latex particles with an iron oxide content of 0.5 wt% in a solution containing 70 wt% glycerol and 0.005 M Clariscan. However, this procedure was repeated to determine the relaxation characteristics of the  $\text{Fe}_3\text{O}_4$ -latex particles in varying glycerol contents (0, 25, 50 and 70 wt%) and with varying iron oxide contents (0.5, 2.5 and 5 wt%), see Table 5.3.

Table 5.3 Relaxivities ( $R_1$  and  $R_2$ ) and  $a$  for three different  $\text{Fe}_3\text{O}_4$ -latex particles with varying iron oxide contents (0.5, 2.5 and 5 wt%) in varying glycerol content environments (0, 25, 50 and 70 wt%).

Glycerol content (wt%)	$\text{Fe}_3\text{O}_4$ content (wt%)	$a$ (wt%-1)	$R_2$ (ms.wt%-1)	$R_1$ (ms.wt%-1)
0	0.5	0.011	0.042	0.003
	2.5	0.017	0.24	0.005
	5	0.026	0.40	0.007
25	0.5	0.012	0.06	0.005
	2.5	0.017	0.28	0.005
	5	0.025	0.50	0.008
50	0.5	0.013	0.088	0.005
	2.5	0.020	0.32	0.006
	5	0.028	0.58	0.006
70	0.5	0.016	0.095	0.013
	2.5	0.026	0.26	0.009
	5	0.035	0.54	0.014





# 6

## Effect of particle concentration on capillary uptake

The transport of particles within thin, porous media is a complex process which received growing attention due to its applications in filtration, printing and microfluidics devices. The effect of particles on liquid imbibition and particle clogging can reduce the performance and lifetime of these applications. However, these processes are still not clearly understood and are challenging to investigate. The goal of this study is to increase our understanding about the effect of particle concentration on the imbibition process in thin fibrous membrane filters. In this study, an Ultra-Fast Imaging NMR method is used to study the particle penetration inside nylon membrane filters for particle suspensions with varying particle concentrations ( $C_0$ ). The measurements revealed that increasing the particle concentration increases the particle penetration depth  $S(t)$  as governed by a Langmuir isotherm given by  $S(t)=l(t)(1+\kappa C_0)/(1+\kappa(C_0+C_{b,m}))$ , with  $C_{b,m}$  the bound particles and  $\kappa$  the binding constant. Secondly, in droplet penetration, particles slow down liquid penetration in a Darcy like manner where effect on viscosity ( $\eta$ ) and surface tension ( $\sigma$ ) determine the penetration speed rather than changes within permeability ( $K_0$ ). The final liquid front ( $l$ ), scaled according to  $l^2 \propto \sigma t / \eta$ . The particle penetration depths were verified using scanning electron microscopy images.

*Adapted from:*

*Nicasy, R. J. K. et al. Increasing particle concentration enhances particle penetration depth but slows down liquid imbibition in thin fibrous filters. Colloids Surfaces A Physicochem. Eng. Asp. 684, 133146 (2024).*

### 6.1 Introduction

Equation Section (Next)As explained in chapter 5, transport, deposition and clogging of nanoparticles within porous media is important in multiple industries such as waste water treatment [309]–[312] and industrial separation (food [313], beverage [290], [314] and pharmaceutical industry [315]), ink penetration [1], [270] and microfluidic devices [41], [316]. A major challenge in filtration processes is filter fouling. In most cases, membrane fouling is caused by particle deposition. Particles such as contaminants will tend to clog pores or form a filter cake. This will significantly lower the flux through your membrane and in some cases even terminate the filtration process, which directly impacts the efficiency of the application. Therefore, a proper understanding of the particle penetration behavior and clogging is of great importance.

Multiple studies are devoted to understanding phenomena involved in particle capture within a porous media. In most research, four different capture mechanisms are distinguished [317]–[319]: (1) sieving, where the particle radius exceeds the pore radius and the particles are blocked due to size exclusion, (2) arching/cake formation, where multiple particles form an arch or cake over a pore or the complete porous media which prevents other particles to enter, (3) flow-induced aggregation, where multiple particles will form an aggregate that will increase in size until it completely blocks a pore and (4) depth filtration, where particles are captured by the porous medium due to physicochemical interactions with the pore walls. The effect of each phenomenon depends on parameters such as the particle size, porosity, initial particle concentration, density of surface pores and physicochemical interactions.

Multiple studies have been performed to improve our understanding about particle transport and the effect of multiple physicochemical parameters on the transport processes. These studies showed that the particle retention and clogging depends on parameters such as the flow rate [41], [42], porosity [43], effect of particle size and the formation of a filter cake [320], and matrix-particle interactions [12], [41]. Also, the effect of particle deposition on the porous matrix could be investigated, showing the change in porosity and permeability during particle capture [321], [322]. In a study performed by Derekx *et al.* [309] the effect of particle size was investigated, which showed that when the particle size was larger than half the pore radius, the particles were unable to penetrate within the porous media. In the same study, it was shown that smaller particles were able to penetrate deeper within the porous membrane. Commonly used particles to study particle transport and characterize filter and membrane performance are latex particles. Studies with latex particles also provided information about parameters such as the retention value [318], [320], [323], the effect of particle size [309] [318], [323], flow velocity [42] and particle-particle interaction [41] on the transport processes.

As explained in chapter 1, the main problem with current research studies is that no experimental techniques allow to measure the particle distribution throughout a porous membrane with sufficient temporal and spatial resolution. Chapter 5 showed how the Ultra-Fast Imaging (UFI) NMR method is able to measure spatial resolved information about the transport of latex nanoparticles within a thin, porous media. The aim of this chapter is to use the UFI method to study how the particle concentration impacts the penetration depth of particles and the speed of fluid imbibition. In order to accomplish this, UFI-NMR profiles are measured during the penetration of particle suspension with varying particle concentrations (Table 5.2) within nylon membrane II (Table 4.1). From these profiles, the particle penetration depth and particle distributions can be extracted. First, the time evolution of UFI signal profiles are discussed. Secondly, the UFI signal profiles will be used to extract particle concentration profiles and particle penetration depth which will be compared to Scanning Electron Microscopy images. Finally, the effect of particle concentration on liquid imbibition speed will be studied and compared to Darcy's model.

## 6.2 Capillary uptake in function of particle concentration (UFI-signal profiles)

Figure 6.1 shows UFI signal profiles measured during the penetration of the particle suspensions outlined in Table 5.2 within nylon membrane II the membrane with a pore radius of  $0.27\ \mu\text{m}$ , see Table 4.1. The profiles are presented for 6 different time steps: a (0.05-0.1 s), b (0.50 s), c (0.75 s), d (1.25 s), e (4.00 s) and f (90-95 s). Profiles are marked with varying colors to indicate the initial particle concentration within the droplet: 0 wt% (black), 1 wt% (orange), 2 wt% (light blue), 3 wt% (green), 5 wt% yellow and 8 wt% (dark blue). The UFI-profiles mainly consist of three regions: (1) the droplet ( $x < 0\ \mu\text{m}$ ), (2) the membrane ( $0\ \mu\text{m} < x < 170\ \mu\text{m}$ ) and (3) the double side tape and glass plate ( $x > 170\ \mu\text{m}$ ). Inside a profile, the signal intensity changes within every region. In the droplet, where the measurement area is fully saturated with liquid, the signal is given by equation (5.2). Inside the membrane, the signal drops, due to the porosity  $\phi$  of the nylon membrane, see equation (5.3). In final part of the profile,  $x > 170\ \mu\text{m}$ , the tape and glass plate, the signal intensity drops to zero, because no liquid is present.

Based on the profiles, the process could be split into several phases: (I), before penetration, (II) early phase liquid penetration (homogeneous), (III) late phase of liquid uptake (front splitting, particles lag behind) and (IV) end state (lateral liquid penetration with vertical particle penetration). Figure 6.2, shows a schematic representation of these four phases. In this figure, the droplet, membrane and tape are shown, and a blue color is used to indicate water, while brown circles indicate particles.

Phase I is shown in Figure 6.1a which shows profiles before liquid penetration. In these profiles, there is only signal within the droplet because no liquid has entered the porous media, as shown in Figure 6.2. The signal intensity within the droplet varies for every profile and depends on the initial particle concentration of the suspension as given by equation (5.2).

In phase II where  $t = 0.5\ \text{s} - 0.75\ \text{s}$ , shown in Figure 6.1b and c, the liquid starts to penetrate the membrane. As explained before, the signal intensity of liquid is lower in porous media due to the porosity  $\phi$ . The profiles show that liquids with higher particle concentrations imbibe slower into the porous media. Furthermore, the signal intensities within the membrane are rather homogeneous. Because the signal is directly linked to the particle concentration, see equation (5.3), a homogeneous signal profile indicates a constant particle concentration. Therefore, at the early stage of penetration, the liquid and particles penetrated as a homogeneous suspension, see Figure 6.2 phase II. Another possibility is that the particle-liquid front splitting does not exceed the NMR resolution ( $18\ \mu\text{m}$ ).

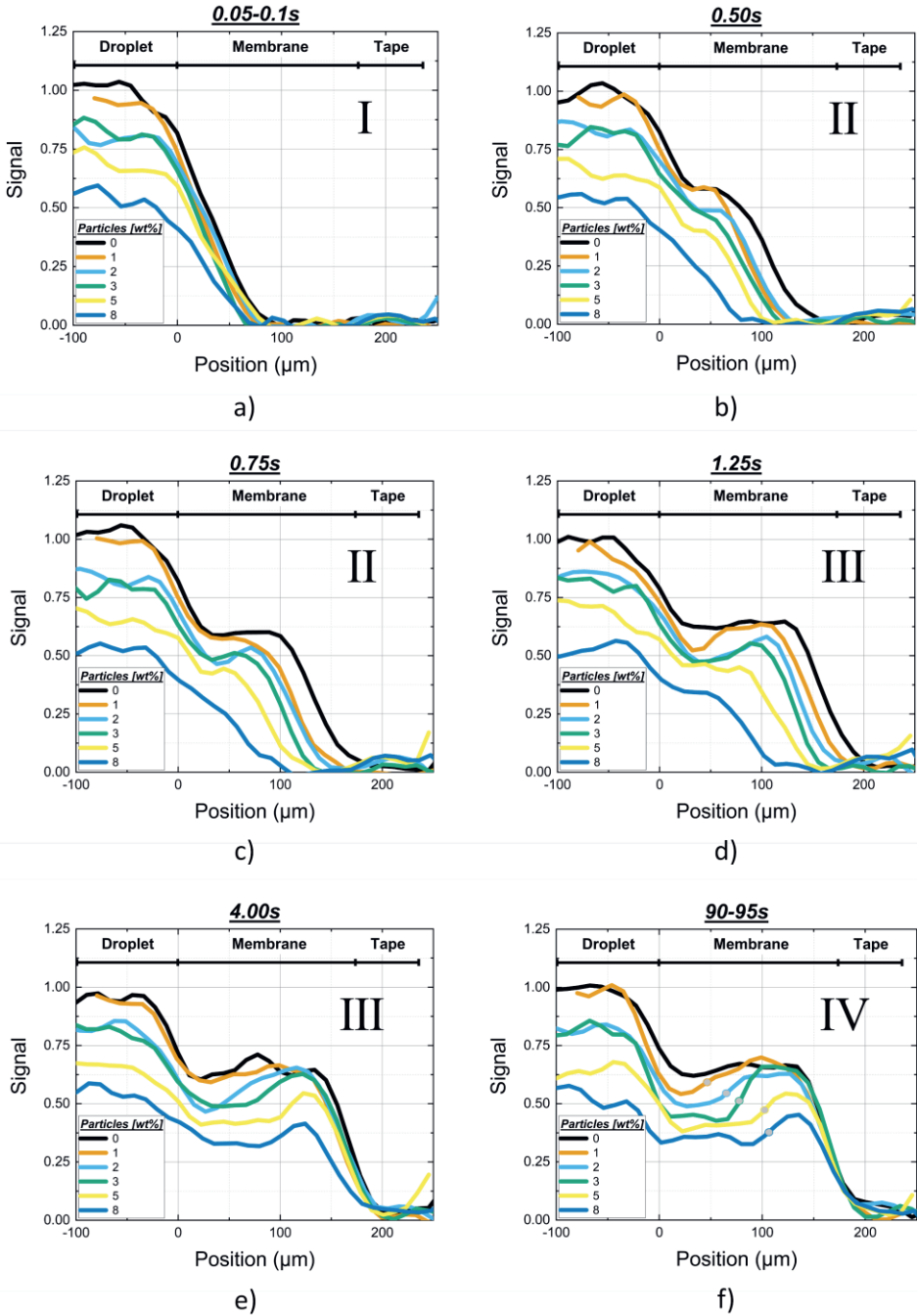


Figure 6.1 UFI-signal profiles measured at different times (a:0.05 - 0.1 s, b:0.50 s, c:0.75 s, d:1.25 s, e:4.00 s and f: 90 - 95 s) during the penetration of liquids containing 70 wt% of glycerol and varying particle concentration inside a nylon membrane. Colors are used to mark the initial particle concentrations:0 wt% (black), 1 wt% (orange), 2 wt% (light blue), 3 wt% (green), 5 wt% yellow and 8 wt% (dark blue). In figure f, dots are used to mark the final particle penetration depth.

Figure 6.1d-e show phase III of the penetration process. During this phase, the signal profiles start to become inhomogeneous and develop a signal increase near the liquid front. This is the case for the lower particle's concentrations (1, 2 and 3 wt%) in Figure 6.1d and for all liquids in Figure 6.1e. Therefore, it can be concluded that the particle concentration starts to decrease near the liquid front. This situation was shown in section 5.4.3, where it was shown that this signal increase indicated the splitting between particle and liquid front, see Figure 6.2 phase III. In Figure 6.1e, at a time of 4.0s, most of the liquid has reached the membrane-tape interface. A closer look at the signal intensities reveals that signal intensities of the lower particle concentrations (1, 2 and 3 wt%) became equal to the signal of the reference solution containing no particles (black). Because the signal intensity is similar to the reference sample, there are no particles within this region. For the higher concentrations, 5 wt% (yellow) and 8 wt% (dark blue), the signal does not completely recover. This either means that some particles are able to penetrate within this area or that the resolution of the setup is unable to resolve the splitting between the particles and liquid front.

Profiles of phase IV are shown in Figure 6.1f. At this stage, the liquid suspension has reached the membrane-tape interface and vertical penetration of liquid is stopped. However, liquid from the droplet is still entering the membrane due to lateral penetration. Due to this penetration, particles are still penetrating the membrane which further increases the particle concentration. This situation is schematically shown in phase IV of Figure 6.2. The increase in particle concentration within the measurement area continues to affect the signal intensity. When comparing Figure 6.1f and e, the influence of the particles can be seen by a further decrease in the signal intensity near the droplet-membrane interface. In Figure 6.1f, the position of the particle front can be clearly observed by the increase in signal intensity within the membrane. These positions are marked with circles.

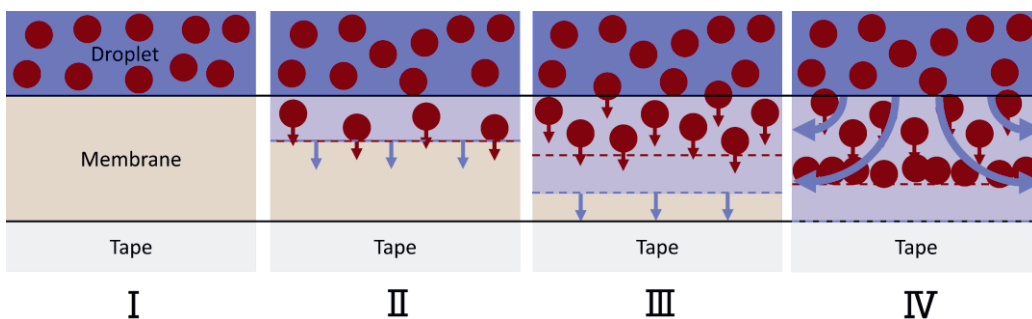


Figure 6.2 Schematic representation of the penetration process.

### 6.3 Influence of particle concentration on particle penetration depth

In the previous section, the UFI profiles revealed that during penetration, a particle front develops that lagged the liquid front. Furthermore, the particles are unable to penetrate the full thickness of the membrane. In this section, the particle penetration depth and concentration profiles will be extracted with the goal of studying the influence of particle concentration on the particle penetration behavior. This data will then be compared to SEM images of the cross sections of the samples.

The profiles shown in Figure 6.1 gave a good idea about the particles position within the membrane. However, due to limits in resolution and the small thickness of the membrane, only a few positions could be extracted to gain information about the particle front through time. With a larger separation between the particle and liquid front or with larger membranes ( $> 250 \mu\text{m}$ ), more particle fronts could be extracted making this technique valuable in multiple applications. In this study, particle concentrations and fronts were extracted at later timescales. In a chapter 5.9, it was shown that by using equation (5.3), the UFI profiles can be turned into particle concentrations. Figure 6.3 shows the particle concentration profiles that were determined from the UFI-profiles in Figure 6.1f.

A first observation of the particle concentration profiles reveals that no jump in concentration is observed at the droplet-membrane interface, therefore the particles are not hindered by the interface. It seems that the difference between the pore radius of the membrane (540 nm) and the particle radius (50 - 100 nm) is large enough for the particles to move freely inside the membrane. This is in line with a study performed by Derekx et al. [309] where the effect of particle size was investigated, which showed particles were hindered if the particle size was larger than half the pore radius.

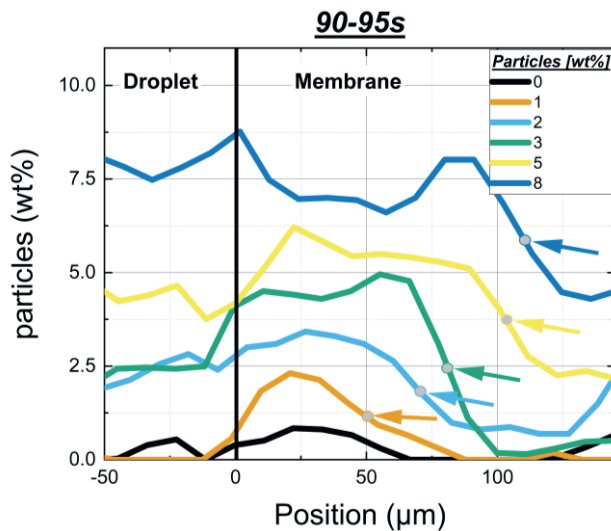


Figure 6.3 Particle concentration profiles as determined from the UFI-profiles shown in Figure 6.2e. Marked with colored dots are the particle penetration depths.

Furthermore, the data shows again that the membrane region can be divided into two regions. A region near the droplet-membrane interface, containing the same particle concentration as inside the droplet, and a region near the membrane-tape interface, containing no or almost no particles. Particle liquid splitting and a final particle penetration depth are also observed in other porous systems found in literature [324].

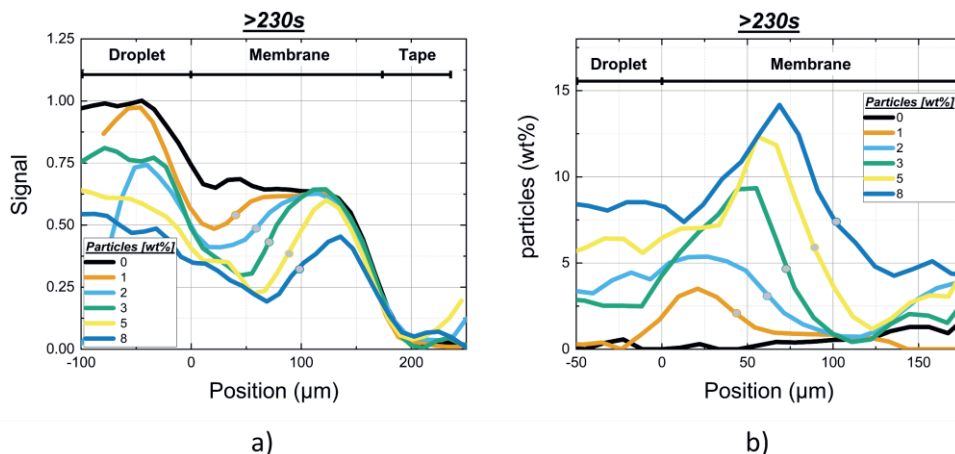


Figure 6.4 a) UFI-NMR signal profiles for the penetration of liquids containing 70 wt% of glycerol with varying particle concentration: 0 wt% (black), 1 wt% (orange), 2 wt% (light blue), 3 wt% (green), 5 wt% (yellow) and 8 wt% (dark blue). The profiles are measured at timescales beyond 230s, just before the droplet disappears. These times can vary because the penetration and evaporation rate are different for all solutions.

The particle penetration depths for all signal profiles are marked with circles. b) particle concentration profiles corresponding to figure a. A similar color code is used to mark the varying initial particle concentrations.

The interface between both regions can be identified as the particle penetration depth and is marked in Figure 6.2f and Figure 6.3 with colored dots. These particle penetration depths reveal that with increasing particle concentration, particles are able to penetrate deeper within the nylon membrane.

In the final part of this section, the UFI measurements are compared to SEM images. Because SEM images of the cross-section can only be taken after the penetration has finished, the SEM images should be compared to profiles measured just before the droplet disappears and the penetration process stops. Figure 6.4 shows UFI - profiles (a) and the corresponding particle concentration profiles (b) after 230 s, just before the penetration process finishes. In two profiles, the one of 1 wt% (orange) and the one of 2 wt% (light blue), the disappearance of the droplet can be observed by the decrease in signal intensity around -75 μm, indicating that no liquid is present. The exact time at which the profiles were measured varied slightly for all liquids due to differences in penetration and evaporation rates.

When comparing the particle concentration profiles of Figure 6.3 and Figure 6.4b, it can be seen that the particle concentrations within the membrane further increase but that the particle penetration depth is unchanged. The increase in particle concentration is however not homogenous but the particles seem to build up from the inside towards the droplet-membrane interface.

The particle penetration depths and profiles of Figure 6.4 can now be verified using SEM images. Figure 6.5 shows SEM-images of the cross-section of the samples used for the UFI measurements shown in Figure 6.4 for all particle concentrations: a (0 wt%), b (1 wt%), c (2 wt%), d (3 wt%), e (5 wt%) and d (8 wt%).



In these figures, the position of the particles is marked with a white line and the particle penetration depth is given by a white arrow. In Figure 6.5f, a filter cake of particles can be seen on top of the membrane. This particle layer was not observed within the UFI-signal profiles, probably because the measurement was stopped too early and the thickness of the filter cake formed during penetration was too small to be picked up with the experimental resolution of 18  $\mu\text{m}$ .

Similar to the NMR results, a final particle penetration depth is observed, that increased with the particle concentration. Furthermore, a similar concentration gradient is observed where a dense particle layer had built up from the inside towards the droplet-membrane interface, similar to what was observed in Figure 6.4b. This is most visible in Figure 6.5e, where a dense particle concentration can be seen near the white line.

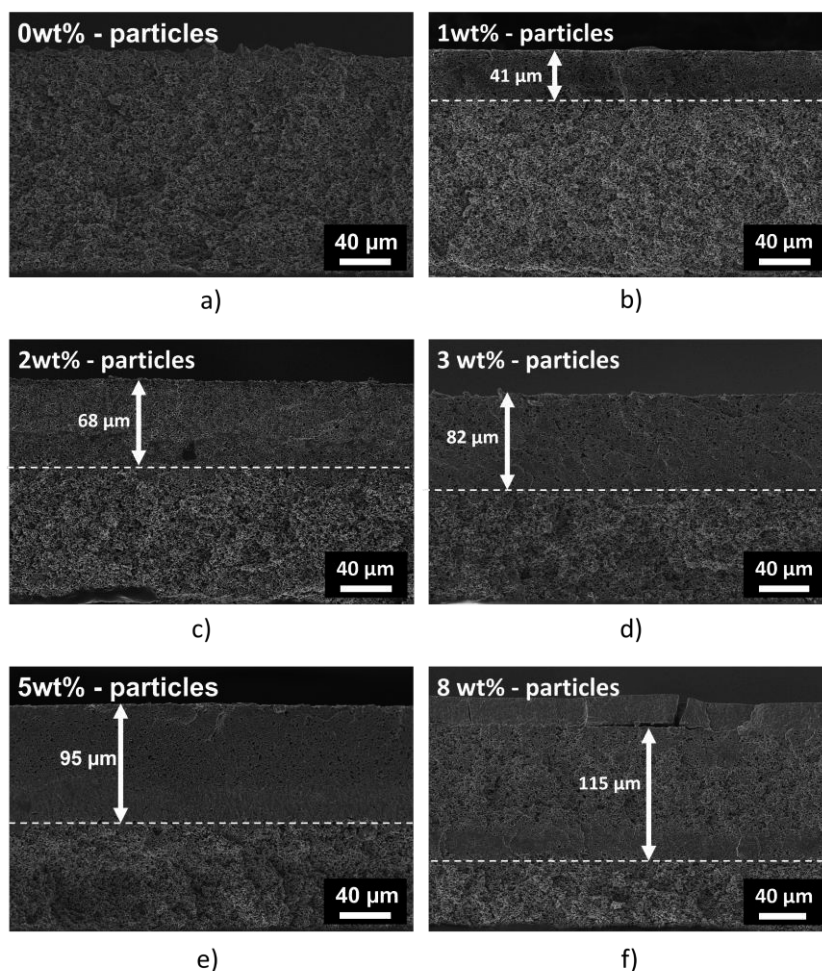


Figure 6.5 Scanning electron microscopy images of the cross-section of nylon membrane II, after penetration of a liquid containing 70 wt% glycerol and varying particle concentrations: a) 0 wt%, b) 1 wt%, c) 2 wt%, d) 3 wt%, e) 5 wt% and f) 8 wt%. The samples correspond to the ones used for measuring the UFI signals in Figure 6.1 and Figure 6.4. Marked with white arrows are the particles penetration depths.

To investigate the effect of particle concentration on the particle penetration depth and compare both the UFI and SEM results, Figure 6.6 shows the particle penetration depths as determined by UFI (black) and SEM (orange). The particle penetration depths for UFI are taken from Figure 6.3. Clearly a good correlation exists between both measurements.

In order to explain the final particle penetration depth, a formula for the particle front  $S(t)$  [m] as a function of the liquid front  $l(t)$  [m] is taken from Kuijpers *et al.* [65], given by,

$$S(t) = l(t) \frac{1 + \kappa C_0}{1 + \kappa (C_0 + C_{b,m})}, \quad (6.1)$$

where  $\kappa$  [m<sup>3</sup>] is the binding constant,  $C_0$  [m<sup>-3</sup>] the initial particle concentration and  $C_{b,m}$  [m<sup>-3</sup>] the maximum concentration of bound particles. In this model, it is assumed that the particles will attach on the membrane following a Langmuir model,  $C_b = C_{b,m} \kappa C_0 / (1 + \kappa C_0)$ . The use of Langmuir models for the attachment of small molecules in thin fibrous membranes has already been used in several other research studies [325], [326]. When  $\kappa$  and  $C_{b,m}$  are used as fitting parameters, this formula can be used to fit the data found for the particle penetration depths by setting  $l(t) = 170 \mu\text{m}$ , the membrane thickness. The corresponding fit for both the UFI-NMR and SEM results are shown in Figure 6.6 with dashed lines. From these fits, values for  $C_{b,m} = 1.35 \text{ E}20 \text{ m}^{-3}$  and  $\kappa = 2.35\text{E}-19 \text{ m}^3$  were found. It can be seen that equation (6.1) is able to describe the final particle front positions quite well. Therefore, it is reasonable to think that the particles during migration adsorb to the membrane in a Langmuir fashion. This means that for low particle concentrations, increasing the particle concentration will result in more surface coverage. However, for larger concentrations, the binding of particles to the surface becomes harder and the total surface coverage stays similar. Therefore, with higher particles concentrations, the particles will on average move faster throughout the medium because they spend less time near the surface, and it becomes less likely to bind to the surface. The increased penetration depth when increasing particle concentration was also observed in a few other research studies on modeling of deep bed filtration [327] and on column experiments [65].

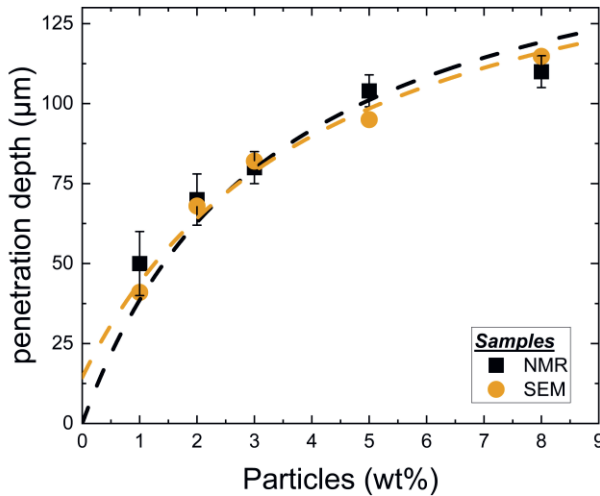


Figure 6.6 Final particle penetration depth as determined by UFI-NMR (black) and Scanning Electron Microscopy (orange). Shown in dashed lines are the fitted penetration depths based on equation.

## 6.4 Influence of particle concentration on liquid imbibition speed

Increasing the particle concentration will influence the imbibition behavior of the liquid mixtures. While the previous section focused on the particle's, this section will investigate the effect of the particle concentration on the liquid imbibition behavior.

From the liquid profiles shown in Figure 6.1, it was concluded that liquid mixtures containing more particles, move slower inside the nylon membrane. For a more in-depth discussion of the imbibition behavior, liquid front positions were extracted from the UFI-signal profiles at half the maximum signal intensity, similarly to chapter 4.5.3.

Figure 6.7a shows the liquid front position as a function of time for all particle concentrations. Every experiment was performed three times, from which an average liquid front position and deviation could be extracted.

The data clearly shows that increasing the particle concentration slows down liquid penetration speed. Explanations for this observation can be searched in two directions: (1) modification of the porous media leading to permeability reduction, commonly reported in literature [328], [329], or a change in the properties of the liquid (i.e. viscosity, surface tension, ...)

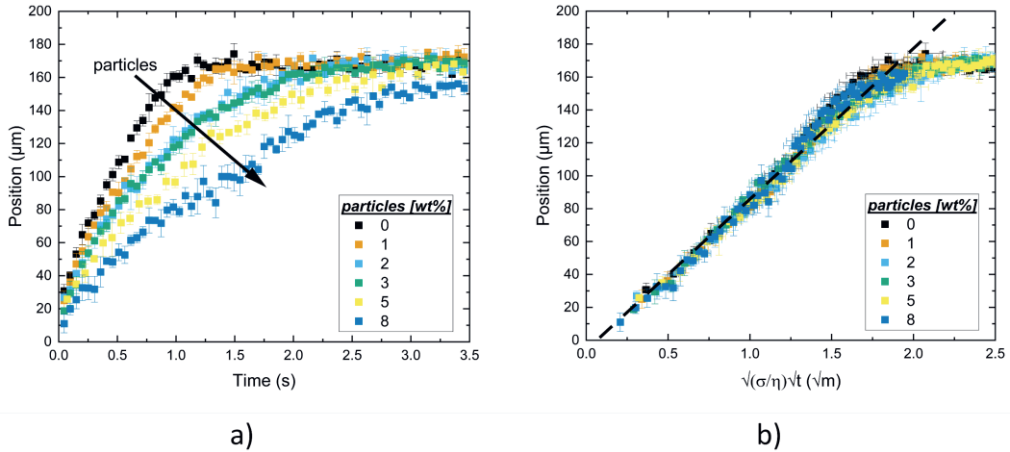


Figure 6.7 Liquid front positions ( $l$ ) as a function of a) time and b) rescaled time ( $\sqrt{\sigma/\eta}\sqrt{t}$ ) for solutions containing varying particle concentrations. All liquids contain 70 wt% of glycerol and are carried out on a nylon membrane. The black dotted line shown in b, is drawn as a guide to the eye.

To investigate if the change in viscosity and surface tension is responsible for the slower penetration, the data is compared to a particular form of Darcy's Law within 1D,  $l^2 = 4K_0 \cos(\theta) \sigma t / \eta$ , [23], [330]. This form of Darcy's Law predicts the fluid front position in function of the viscosity and surface tension. In chapter 4.5.3, it was shown that this equation holds for water-glycerol mixtures within the same nylon membrane. When replotting the liquid fronts of Figure 6.7a on a rescaled time axis given by  $\sqrt{\sigma/\eta}\sqrt{t}$ , the effects of surface tension and viscosity as given by Darcy, can be accounted for. Figure 6.7b shows the liquid front position of Figure 6.7a as a function of  $\sqrt{\sigma/\eta}\sqrt{t}$ . Because all liquid fronts fall onto one master curve, it can be concluded that the predicted scaling with surface tension, viscosity and square root of time holds for particle suspension within the nylon membranes. Therefore, it can also be concluded that the particles will change the penetration speed due to their influence on the liquid properties rather than altering the porous media structure.

This indicates that on short timescales, particle attachment will not influence the liquid penetration speed. This is probably due to the relative low increase in particle concentration in the early stages of penetration which can be seen in Figure 6.3 and Figure 6.4. These profiles show that no significant particle concentration increase is observed before 95 s and that only on later timescales ( $t > 230$  s) significant clogging is observed where the particle concentrations doubled. Within our experiment, vertical penetration happens on timescales two orders of magnitude faster ( $t < 3$  s) which can explain that particle attachment will not influence the measured liquid fronts.

On longer times scales ( $t > 230$  s) shown in Figure 6.4, a clear increase in particle concentration is observed. Therefore, on timescales exceeding 230 s particle attachment and clogging will probably effect the liquid imbibition speed similar to what is observed in several studies where particle concentration increases will reduce the porous media permeability [328], [329], [331]. However, due to the thin membranes used within this study, liquid fronts could only be extracted on much shorter timescales.

## 6.5 Conclusions

In this chapter, the Ultra-Fast Imaging NMR method (UFI) was used to study the effect of particle concentration on the imbibition process within a nylon filter membrane. The effect was investigated by performing imbibition experiments with particle suspensions containing varying particle concentrations. Compared to existing techniques, UFI allows to collect spatially resolved information on timescales going below 1 s and with temporal resolutions below 15  $\mu\text{m}$ . This spatially resolved approach enabled to examine particle and liquid transport throughout the membrane rather than measuring the contribution of the whole membrane as in most studies performed.

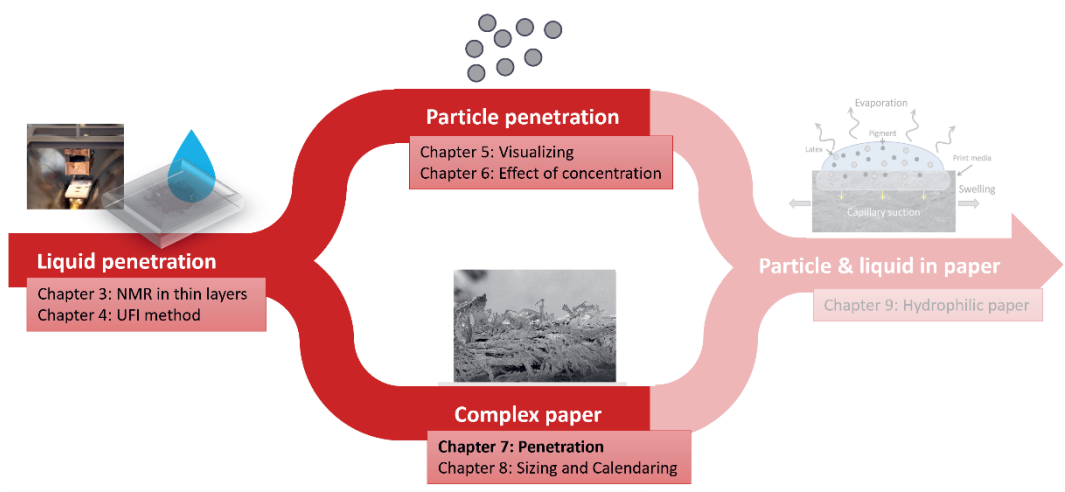
Due to the limited studies on the effect of particle concentration on penetration in thin, porous media, the primary aim of this chapter was to investigate the influence of particle concentration on the penetration dynamics, which resulted in two main findings related to the particle penetration depth and the imbibition speed.

First, increasing the particle concentration led to an increase in the particle's penetration depth. The dependence of the particle penetration depth on the particle concentration was verified by scanning electron microscopy images of the samples cross-sections. The dependence could be linked to a theoretical model based on a Langmuir adsorption model. This aligns with other studies performed on particle suction in porous media that report changes in particle penetration depths [65], [327] or report attachment based upon a Langmuir Isotherm within thin porous media [325], [326], [332].

Secondly, the study demonstrated that increasing the particle concentration slowed down the imbibition speed of the particle suspensions. This change in penetration speed could be linked to an increase in viscosity and decrease in surface tension, as described by Darcy's Law. This study also showed that when the time of penetration is 2 orders of magnitude faster than the typical time to double to particle concentration, the particle suspensions behave according to Darcy's Law and that particle attachment will not affect the liquid imbibition process. This is in contrast with continuous flow on longer time scales where over time particle clogging will change the permeability and porous structure of your medium as reported by several studies [321], [322], [331].

Therefore, it is concluded that a distinction should be made between fast unsaturated droplet penetration, where permeability reduction does not play a role, and long-term saturated flow where particles can influence the permeability of the porous media.





# 7

## Penetration, swelling and air displacement in cellulose sheets.

Liquid penetration in porous cellulosic materials is crucial in many technological fields. The complex geometry, small pore size, and often fast timescale of liquid uptake makes the process hard to capture. Effects such as swelling, vapor transport, film flow and water transport within cellulosic material makes transport deviate from well-known relations such as Lucas-Washburn and Darcy's Law. In this work it is demonstrated how Ultra-Fast Imaging NMR can be used to simultaneously monitor the liquid distribution and swelling during capillary uptake of water with a temporal- and spatial resolution of 10 ms and 14.5–18  $\mu\text{m}$  respectively. The measurements show that in a cellulose fiber sheet liquid first penetrates between the fibers ( $t < 65$  ms) before swelling takes place ( $100$  ms  $< t < 30$  s). Furthermore, the liquid front traps 15 v% of air which is slowly replaced by water during the final stage of liquid uptake. Our method makes it possible to simultaneously quantify the concentration of all three phases (solid, liquid and air) within porous materials during processes exceeding 50 ms (5 times the temporal resolution). We hence believe that the proposed method should also be useful to study liquid penetration, or water diffusion, into other porous cellulosic materials like foams, membranes, nonwovens, textiles and films.

*Adapted from:*

R. J. K. Nicasy, C. Waldner, S. J. F. Erich, O. C. G. Adan, U. Hirn, and H. P. Huinink, "Liquid uptake in porous cellulose sheets studied with UFI-NMR: Penetration, swelling and air displacement," *Carbohydr. Polym.*, vol. 326, p. 121615, Feb. 2024, doi: 10.1016/J.CARBPOL.2023.121615.

### 7.1 Introduction

Liquid uptake and swelling in biopolymer-based fiber sheets is crucial for multiple applications such as printing [82], [333], [334], packaging [78], [335]–[338], fiber-based microfluidic arrays, the textile industry [339]–[341] and even the cleanup of spilled-oil [342]. The material offers multiple advantages such as low cost, biodegradability and the easy manufacturing process [343]. In microfluidic devices such as bio-assays, fiber networks allow to operate without external pumps by using capillary forces to drive the liquids [344]. This makes fiber-based microfluidics highly valuable in low-income countries. To increase the efficiency of biopolymer-based applications, the biopolymers are often modified in order to improve the water absorbency, strength, and functionality [340]. In packaging materials such as foams [335] or biopolymer-based



films the fibers are often made hydrophobic to strengthen the material and increase the water repellency [335], [345]. The performance of these applications relies on both the liquid flow through the sheet and their swelling behavior. Therefore, controlling and predicting liquid flow and swelling are of great importance. Several studies are focused on the improvement of the swelling properties [346], [347] and the dynamic wicking, [339] e.g. to improve the wear comfort of textiles [341] or the usability of edible films.

Another important example is paper, which is a complex system consisting of a network of wood pulp fibers [45]. When liquid comes in contact with a cellulose fiber network, the liquid enters the pores between the fibers due to capillary forces. This process is mostly described by models such as Lucas-Washburn [36]–[39] or Darcy's Law [14], [23], [36]. While both models show great potential to predict the fluid flow, deviations are commonly observed due to the complexity of the paper sheet [37]. Other processes effecting the imbibition are water transport through internal pores within the fibers (lumen) [38], [47], vapor transport, evaporation, inertia effects [48], [49], a precursor front [50] and swelling [51]. The latter process deforms the porous structure during imbibition, resulting in deviations in the capillary uptake behavior. Efforts have been made to extend the existing models and incorporate processes such as swelling [52] or liquid uptake by fibers [47]. Due to the short timescale and small sizescale of the liquid penetration, it is hard to quantitatively capture and analyze these different processes in real time.

The aim of this chapter is to use the UFI method introduced within chapter 4 to study the complex penetration process of water into porous hydrophilic cellulosic materials by simultaneously monitoring the liquid distribution profile, material swelling, and displacement of entrapped air. While this technique is still not fast enough to image processes such as inertia effects which are often described by the Bosanquet equation [348], it offers great potential to study processes that exceed 50 ms such as capillary uptake, swelling, film flow and entrapment of air. It is believed that water uptake in hydrophilic cellulosic materials is governed by a capillary driven fluid front accompanied by swelling and that both processes can be decoupled. In the first part of this chapter, NMR-relaxation measurements on saturated paper samples are studied to identify which elements contribute to the UFI signal. In the second part, droplet uptake experiments are performed where the liquid distribution and swelling of a hydrophilic porous material will be analyzed. Finally, the acquired knowledge will be combined to come up with a model, describing the complex penetration process of water into the substrate. While the measurements are performed on cellulose paper sheets, they can provide information about various processes such as swelling and their influence on liquid imbibition in materials beyond paper such as foams, textiles and biopolymer-based films.

## 7.2 Materials & methods

### 7.2.1. Substrate

In this work paper sheets were investigated, which were also used by Waldner et al. [17], [18], [39]. The sheets are from industrially produced uncoated printing paper (89.6 g/m<sup>2</sup>). The paper is composed of cellulose pulp (bleached eucalyptus kraft) and calcium carbonate filler particles (scalenohedral, precipitated calcium carbonate, filler content 21.25%). The paper has a thickness of 120 - 130  $\mu\text{m}$  and an average pore radius

of 2.8  $\mu\text{m}$ . The pore radii were measured by Waldner et al. by mercury intrusion porosometry, using an Autopore IV 9500 instrument from Micromeritics Instrument Corp, [39]. Figure 7.1 shows Scanning Electron Microscopy images from the cross-section (a) and the surface (b) of the paper sample. The SEM images were taken on a FEI Quanta 600 using 10 kV. In the cross-section, fiber lumen can be seen, which are marked with red arrows. Because the sample was dry, the lumen were closed. However, it could be observed that the lumen at the top of the image extended to a couple of micrometers (blue line). The white parts in the image correspond to scalenohedral precipitated calcium carbonate filler particles.

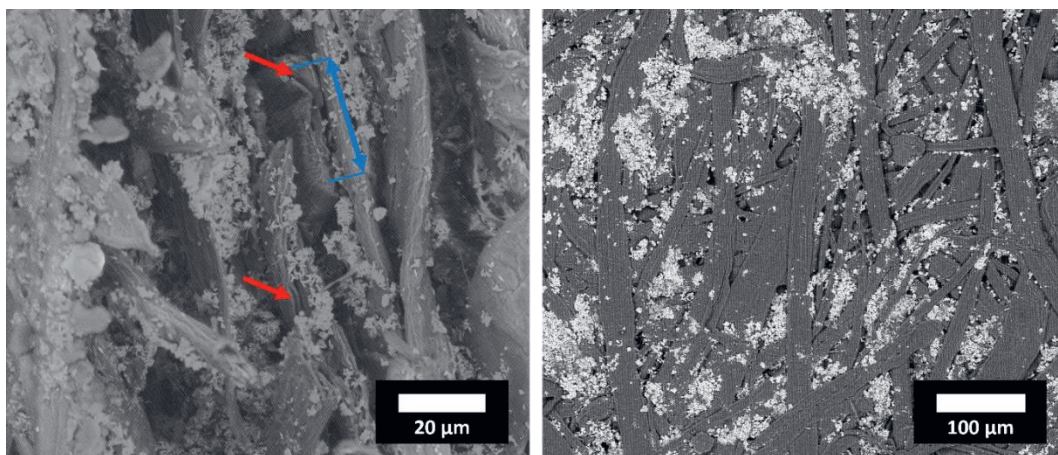


*Figure 7.1 scanning electron microscopy image of the cross-section and surface of the paper used. Red arrows are used to mark examples of fiber lumen while the blue arrow is used to mark the total length of the one lumen.*

### 7.2.2. Liquid uptake experiments

Liquid uptake experiments were performed using the same experimental setup as shown in Figure 4.7. However, in paper, where processes such as swelling, deformations and liquid redistributions can take place on longer timescales, a slightly different experimental procedure is used. Figure 7.2 shows the experimental procedures used within paper samples. For these experiments, samples were prepared by first glueing a piece of paper on top of a glass plate using double sided tape. Thereafter, the sample is surrounded by a glass cylinder which could be closed to prevent evaporation of the droplet and make sure the paper was wetted for a longer time.

Experiment type I was used to measure the liquid profiles during fast and slow liquid uptake processes for a water-Clariscan solution while experiment type II was used to study the slow liquid uptake processes for demineralized water.

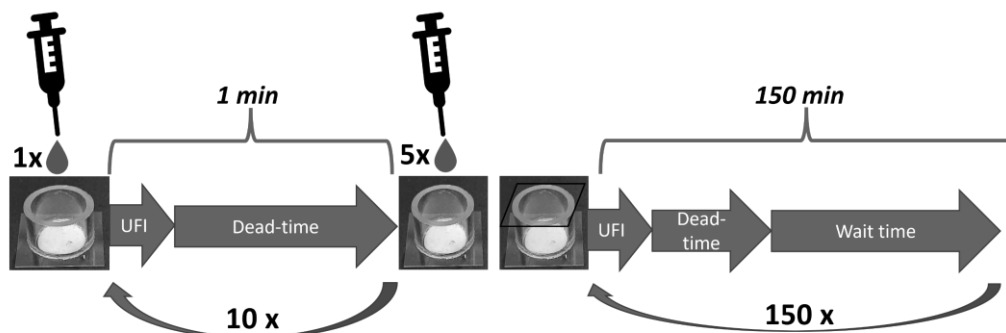
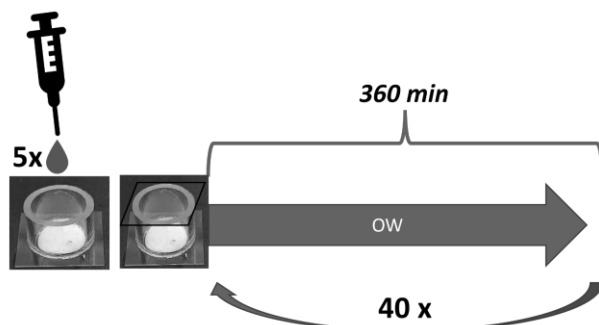
Experiment Type IExperiment Type II

Figure 7.2 a) Experiment type I to measure the liquid profiles during fast and slow liquid uptake of a Clariscan-water solution in paper. Part one of the measurement consists of a UFI measurement (0.8s) followed by a 6-8s dead-time which is repeated 10 times (total time = 1 min). Part two consists of the same UFI measurement (0.8s) and dead time (6-8s) but is now followed by a 1 min wait time. This part is repeated 150 times which results in a total time of 150 min. b) Experiment type II to study the liquid profiles and T2 relaxation time for slow liquid uptake processes of demineralized water. The OW measurement takes 9 minutes and is repeated 40 times which results in a total measurement time of 360 min.

Experiment type I starts by jetting a droplet (8 - 12  $\mu\text{L}$ ) of the water-Clariscan solution on top of the paper sample, which triggers a light sensor that will start the NMR-pulse sequence. In all experiments the droplet radius ( $R$ ), when in contact with the paper, is larger than 4 mm. This ensures that the droplet will not come in contact with the glass cylinder but is large enough to cover the whole measurement area, which is around 4 mm in diameter. Liquid profiles are then measured using the UFI-pulse sequence. This is repeated 10 times and results in a 1 min window in which the fast processes are measured. To measure processes on longer timescales, the system is saturated by adding 5 more droplets and the compartment is closed with a glass plate to prevent evaporation. After closing the system, liquid profiles are measured by UFI every minute for a period of 150 min.

Experiment type II was performed to study the slower uptake processes in more detail by using demineralized water, where the  $T_2$  relaxation time can provide extra valuable information. Because the procedure focusses on the slower processes, the system is directly saturated with 5 droplets of water and closed with a glass plate. After closing the system, the  $T_2$  relaxation time and liquid profile are recorded by an OW sequence every 9 minutes for a time span of 4 h.

### 7.3 NMR signal: the various hydrogen pools in wet paper

Water containing cellulose fiber sheets are complex media, which consist of different hydrogen pools. To interpret UFI signal profiles, it is crucial to identify which hydrogen pools contribute to the measured signal. From the literature, it is known that within cellulose fiber networks such as paper different groups of hydrogen atoms can be discriminated, namely hydrogen from the fibers (cellulose, hemi-cellulose, lignin,...), strongly bound water,  $^1\text{H}$  atoms of fillers, sizing agents, liquid water inside the fiber lumen and liquid water between the fibers [157], [349]. The main goal of this section is to identify which hydrogen pools will contribute to the signal as measured by UFI. Additionally, the measurements provide more insight on the paper samples' morphology and composition, which can be used in later discussions.

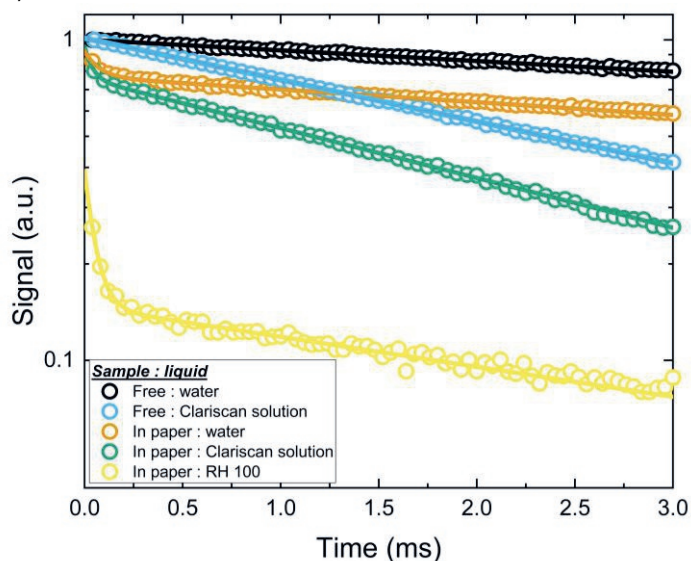


Figure 7.3  $T_2$  signal decay measurements of demineralized water (black), a Clariscan reference solution (blue), demineralized water in a paper sample (orange) and Clariscan reference solution (green) in a paper sample. Also shown is a  $T_2$  decay from a paper conditioned at a temperature of 25 °C with a relative humidity of 100%.

To identify and characterize the NMR signal,  $T_2$  measurements were performed on a saturated paper sheet containing various liquid solutions. As the measurements were performed in the presence of a constant magnetic gradient (41.5 T/m), the  $T_2$  times reported within this study were effective  $T_2$  times and not the true  $T_2$  times. The samples were all saturated for at least 24 h to ensure that all transport processes were finished and that the samples were completely saturated. Figure 7.3 shows the decay curves of demineralized water (black), demineralized water in paper (orange), a Clariscan solution

(blue), a Clariscan solution in paper (green), and a paper sheet conditioned at a relative humidity of 100 % (yellow). The signal intensities of all experiments were rescaled always using the first echo of the free water signal intensity. For the measurements within paper, a multiexponential decay was observed which indicates the presence of various hydrogen pools, as explained in section 3.2.1. This was most visible in case the sample was conditioned at a relative humidity of 100 %, in which there was almost no liquid water. For a sample containing multiple hydrogen pools, the signal intensity is governed by a multiexponential decay as given by equation (3.17). Because the repetition time in all experiments was higher than  $3 T_1$  the influence of the  $T_1$  factor is small and was neglected within the fitting procedure.

The  $T_2$  relaxation time which can be extracted from the data is a complex parameter which depends on several factors as given by equation (3.8). All factors contribution to the relaxation time such as dipolar interactions, diffusion, porous media and a contrast agent were thoroughly described in chapter 3.2.1. In the high-gradient GARField NMR, used in this study, the relaxation time for free water is mainly dominated by the diffusion term of eq. (3.8) due to the high magnetic gradient. When taken a magnetic gradient of 41.5 T/m, a diffusion constant of  $2.1\text{E}^{-9} \text{ m}^2/\text{s}$ , an echo time of 50  $\mu\text{s}$  and a prefactor  $\alpha$  of 0.14, a theoretical  $T_{2\text{dif}}$  can be calculated by  $(\alpha D \gamma^2 G^2 t_e^2)^{-1} \approx 11 \text{ ms}$  [255], and the dipolar interaction ( $T_{2\text{dip}}$ ), which is around a few seconds, can be neglected. When using equation (3.17), the decays of Figure 7.3 can be fitted by setting  $\beta = 1$  in a free solution and  $\beta = 2$  within paper. The corresponding fits are shown as lines with similar colors.

Table 7.1 gives the fit parameters which we labeled long and short  $T_2$  component respectively. It should be noted that in most NMR studies on paper samples, more hydrogen pools are discriminated such as bound water, cellulose, and other paper additives [157], [349]. The relaxation times of these components often lie between 0.1 ms and 2 ms. Due to the limited points within this time period and the rather low signal, these components could not be separated within our study and were therefore all combined within one component (short  $T_2$  component).

When comparing the long  $T_2$  component of demineralized water and demineralized water within a paper sheet, similar  $T_2$  relaxation times were found ( $T_2 \approx 12 \text{ ms}$ ). In all cases the short component had a relaxation time around 50  $\mu\text{s}$ .

The relaxation time of the long  $T_2$  component was close to its theoretical value of 11 ms as calculated from the diffusion term. Therefore, it could be concluded that water within paper acted as free water. This behavior could be explained considering the large pore radius of the paper samples. When, after a pulse, hydrogen atoms were unable to diffuse to the fiber surfaces before a next refocusing pulse was given, surface relaxation, represented by the term  $\sigma(A/V)$  in equation (3.17), would not occur. When using the self-diffusion coefficient of water at 22°C,  $D=2.1\text{E}^{-9} \text{ m}^2/\text{s}$ , and an echo time of 50  $\mu\text{s}$ , the diffusion length scale for free water could be calculated by  $l = \sqrt{6Dt_e} = 0.25 \mu\text{m}$ . Because the pores of the paper sample are 2.8  $\mu\text{m}$ , hence more than 10 times larger, the water behaved as free water within these experimental settings. The same could be said about water in completely swollen lumen [350]. From literature, it is known that lumen are typically one or more micrometers wide, therefore water within lumen will act as free water. As a result, the performed  $T_2$  measurements could not discriminate water between fibers and water in lumen.

Table 7.1 Short and long  $T_2$  components for demineralized water, Clariscan solution, demineralized water within paper, Clariscan solution within paper and a paper conditioned at a temperature of 25 °C with a relative humidity of 100%

Sample	Short $T_2$ comp.		Long $T_2$ comp.	
	$T_2$ [ms]	$\rho_1$	$T_2$ [ms]	$\rho_2$
<b>Demineralized water</b>	/	/	11.90	1.00
<b>Clariscan solution</b>	/	/	3.34	1.01
<b>Demineralized water in paper</b>	0.07	0.16	12.00	0.74
<b>Clariscan solution in paper</b>	0.05	0.20	2.90	0.80
<b>Paper at RH100</b>	0.053	0.24	4.64	0.17

In the measurements that involve paper, a second  $T_2$  component appeared. This was most visible in case the sample was conditioned at a relative humidity of 100 %, in which there was almost no liquid water. In all cases the short component had a relaxation time around 50  $\mu$ s, which corresponded to values found in literature for cellulose fibers and bound water, as reported by Rostom et al. [349]. Therefore, this component could mainly be attributed to the cellulose fibers but also other hydrogen groups such as bound water and hydrogen groups from fillers probably contributed to this signal. With a  $T_2$  time of 50  $\mu$ s and a density of 20 v/v% the signal intensity of the small  $T_2$  component was calculated to be 0.003. This was much lower than the actual noise level and therefore did not contribute to the UFI signal. Using this data, the relative fraction could provide information about the fiber content within the paper samples. In most cases, the fiber content occupied around 16 – 20 v% of a fully wet paper.

For a free Clariscan solution and a Clariscan solution within paper, similar decay curves were observed. For a Clariscan solution within paper, again a short and long  $T_2$  component were observed. The short component had a similar signal intensity as observed with free demineralized water and was around 16 - 20 v%. The difference compared to free water was that the long  $T_2$  components relaxation time was shortened from 12 to 3 ms due to the addition of a contrast agent.

Using these results, the following conclusions about the signal intensity within UFI could be made. The relaxation times of liquid within fiber lumen and between fibers were similar to those of free water. Therefore, signal from water within fiber lumen and in between fibers could not be discriminated and were both visible within the moisture profiles measured by UFI. The contribution of the signal of cellulose fibers, fillers and bound water, was too low to be measured by UFI. Therefore, the signal that was measured with UFI only came from liquid water between the fibers and within the fiber lumen. In chapter 4.5.2, it was shown that by the addition of Clariscan, the relaxation times ( $T_1$  and  $T_2$ ) do not depend on the porous media and that the signal intensity is completely determined by the moisture content  $\rho$ . In the remainder of this study, all data will be represented by the moisture content instead of the signal intensity.

## 7.4 Water uptake in cellulose fiber networks: a three-phase process

The penetration of a Clariscan-water solution in paper was measured. This experiment revealed that water uptake in paper happened in 3 phases: a liquid front penetration

phase, a swelling phase and liquid penetration on longer timescales. This section starts by showing the liquid distribution profiles, liquid front position, swelling and moisture content within the paper sheet. Next, the three phases will be introduced. Afterwards, every phase will be discussed in more detail in the subsequent subsections.

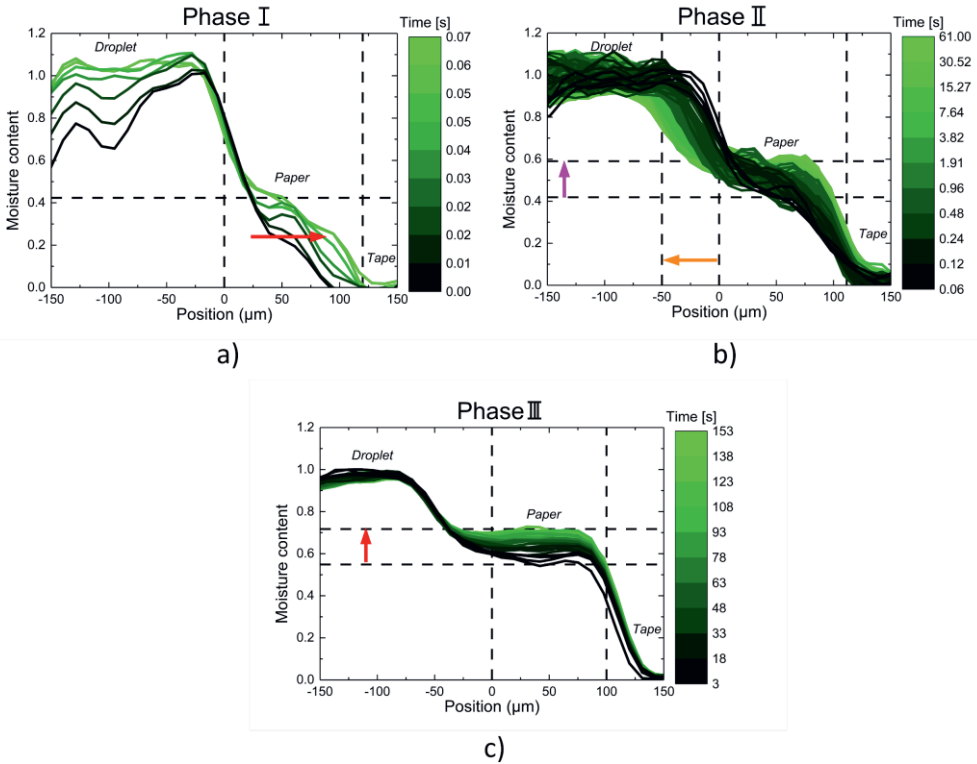


*Figure 7.4 Liquid profiles for the penetration of a water-Clariscan solution in paper sheets. Profiles are measured every 11.6 ms and are given for phase I ( $0\text{ s} < t < 0.07\text{ s}$ ) (a), phase II ( $0.07\text{ s} < t < 61\text{ s}$ ) (b) and phase III ( $61\text{ s} < t$ ) (c). In all figures, a green colormap is used to specify the time of the corresponding liquid profile. Marked with lines are the interfaces and orange arrows are used to indicate the thickness increase that occurs in the paper during swelling.*

Measurements were performed using experiment type I. The moisture profiles for a Clariscan solution penetrating in paper are shown in Figure 7.4. Figure 7.4a shows profiles between 0 and 75 ms, Figure 7.4b between 75 ms and 60 s, and Figure 7.4c between 1 min and 180 min. In Figure 7.4a-c, a green scale is used to identify the time at which the liquid profile was measured. In Figure 7.4a and b, the paper is situated between 0 and 120  $\mu\text{m}$  with the droplet on top ( $x < 0\text{ }\mu\text{m}$ ) and the double-sided tape at the bottom ( $x > 120\text{ }\mu\text{m}$ ). In Figure 7.4c, the paper has increased in thickness and is situated between -50 and 120  $\mu\text{m}$  with the droplet on top ( $x < -50\text{ }\mu\text{m}$ ) and the double-sided tape at the bottom ( $x > 120\text{ }\mu\text{m}$ ). More information about the 3D interpretation of these regions and profiles can be found in Figure 4.7. Figure 7.4a-c all represent another phase of the liquid uptake process. Figure 5a, shows a liquid front penetrating inside the paper (arrow) while maintaining constant paper thickness.

The increase in moisture content observed within the droplet during phase I was attributed to oscillations in the droplet. These oscillations lasted for approximately 50 ms and led to a movement of the hydrogen atoms during the pulse sequence. When the spatial displacement of the atoms was large compared to the spatial resolution of the setup, the misalignment of the spins during the refocusing pulses were large enough to significantly reduce the measured signal intensity. Figure 7.4b illustrates the rapid increase in paper size (orange arrow) due to swelling and increase in moisture content (purple arrow). Finally, Figure 7.4c shows how the moisture content within the paper kept increasing (arrow) even in the absence of further swelling.

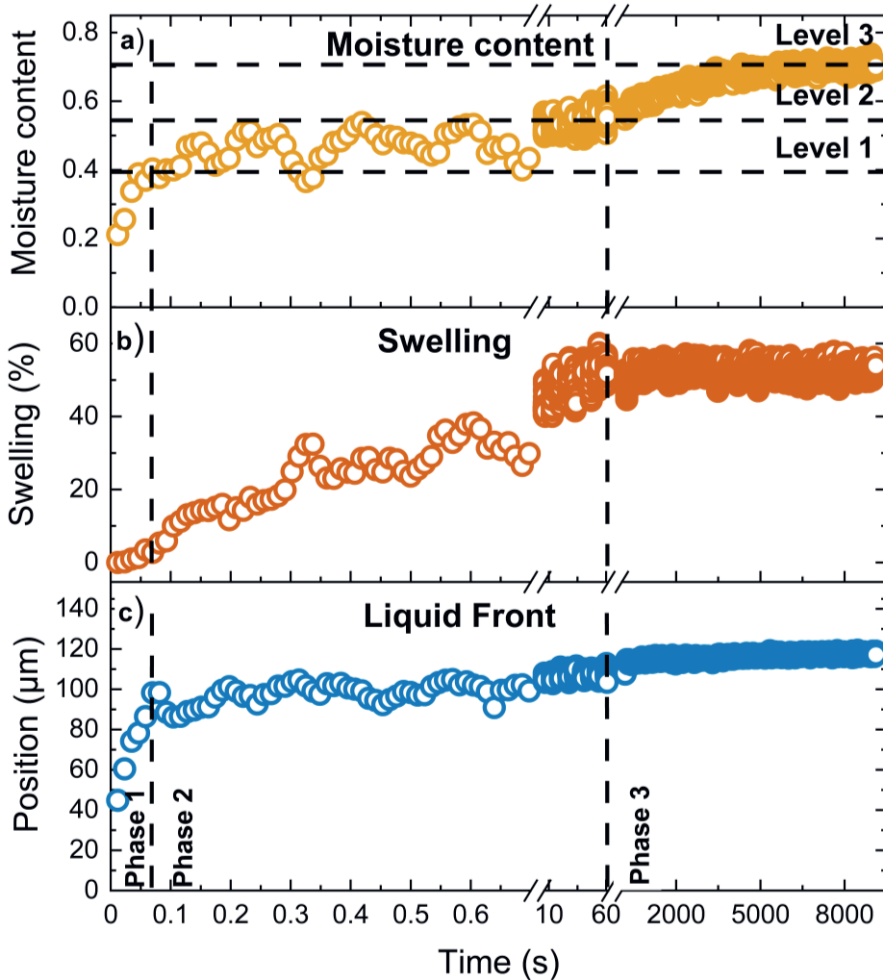


Figure 7.5 a) Moisture content (yellow), b) swelling (orange) and c) liquid front position (blue) in a cellulose fiber sheet during uptake of a water-Clariscan solution. Marked with lines are the different phases, all having a typical moisture content.

Using the liquid profiles of Figure 7.4, the liquid front position, paper swelling and moisture content within the paper sample could be extracted, which are shown in Figure 7.5. The moisture content (Figure 7.5a) was extracted from the profiles in Figure 7.4 between 38 and 50  $\mu\text{m}$ . Swelling (Figure 7.5b), gives the thickness increase of the paper



sheet in percent. The thickness of the paper sheet could be determined by the droplet-paper surface, which was extracted from the profiles of Figure 7.4 at the position where the moisture content equals 0.8. The position of the liquid front (Figure 7.5c) was extracted from the profiles of Figure 7.4 by taking the position where the moisture content equals 0.2. The data showed how the moisture content rose in 3 different phases, all having their typical timescale. Besides the changes in moisture content, liquid front penetration mainly occurred in phase I, swelling mainly occurred in phase II and that both become negligible in phase III. The remainder of this section takes a closer look at every phase in order to explain the physical processes in the three phases.

#### 7.4.1. Phase I: liquid penetration

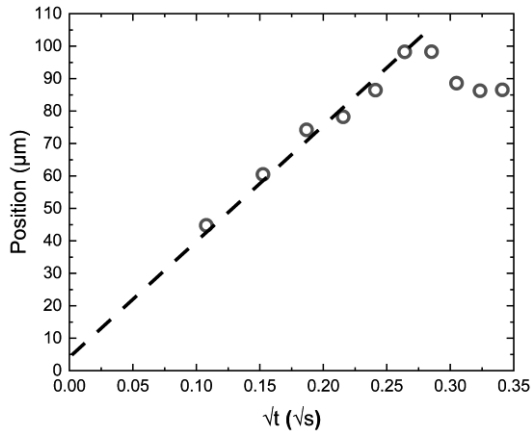


Figure 7.6 Liquid front position as a function of  $\sqrt{t}$  for the penetration of a water-Clariscan solution in paper.

After the droplet came in contact with the paper, liquid started to penetrate due to capillary forces. Figure 7.4a shows how liquid penetrated with a front inside the paper. Figure 7.6 shows the liquid front position as a function of  $\sqrt{t}$  for phase I. A linear relationship existed between the liquid front position and the  $\sqrt{t}$ , which could be related to Lucas Washburn and Darcy's law with a sharp front formalism where for both, the liquid front scaled with the square root of time [40]. After 65 ms the liquid front reached the end of the membrane, which marks the end of phase I. In this experiment, no swelling was observed during penetration. The moisture content after phase I was around 0.4 which meant that 60 v/v% of the area was filled with either air or fibers.

#### 7.4.2. Phase II: swelling

After phase I (capillary uptake) was finished, the paper started to swell. Figure 7.4b shows the moisture profiles during phase II. Swelling of the paper sheet became apparent from the movement of the droplet-paper interface, indicated by the horizontal arrow. The total time taken for the paper to reach maximum swelling was around 30 s. The swelling could be investigated by tracking the droplet-paper interface over time. Figure 7.7 shows both the liquid front positions (yellow) and swelling (black) for phase I and phase II in more detail. The data showed that during phase I, the liquid front position advanced while the swelling front stayed rather constant and that the opposite happened during phase II.

To analyze the swelling kinetics in more detail, a formula was adopted from literature ([8], [351], [352]) where the paper thickness increase ( $S$  [%]) is related to a rate constant  $k$  [ $s^{-1}$ ] by:

$$S = S_{\max} \left(1 - e^{-kt}\right), \quad (2)$$

Where  $S_{\max}$  stands for the maximum thickness increase. A fit of this model is shown in Figure 7.7a (blue line) which gives a rate constant  $k = 2.06 s^{-1}$  and an  $S_{\max} = 45\%$ .

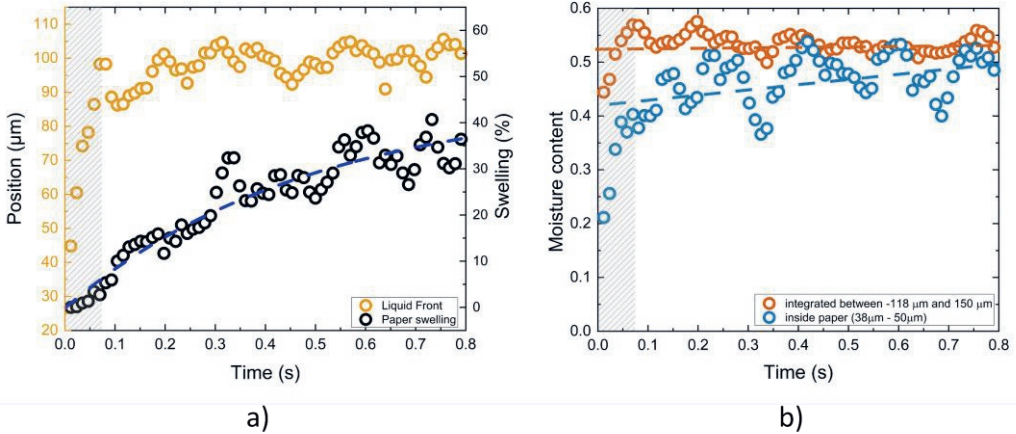


Figure 7.7 a) Liquid front position (yellow) and swelling (black) for the penetration of a Clariscan-solution in paper. Phase I (penetration) and phase II (swelling) are marked by a different gray background. Shown in blue is a fit for the swelling kinetics. b) Moisture between 38 and 50  $\mu\text{m}$  (blue) and the integrated moisture content between -118 and 150  $\mu\text{m}$  (orange). The lines are drawn as a guide for the eye.

Besides swelling, also the moisture content increased from 0.4 to 0.55 during phase II, see Figure 7.4b. Figure 7.7b shows the local moisture content within the paper between 38 and 50  $\mu\text{m}$  (blue). To investigate in more depth the relation between the swelling of the paper and the observed moisture increase within the paper, the integrated moisture content between -118  $\mu\text{m}$  and 150  $\mu\text{m}$  is also given in Figure 7.7b (orange). This integrated moisture content, represents the total moisture content within the paper and part of the droplet that was replaced by paper after swelling, see Figure 7.4b. At both ends, a margin was taken into account for the resolution of our setup. The figure illustrates how the integrated moisture content increased until 0.065 s, which corresponded to the entering of the liquid front (phase I). However, during phase II the total integrated moisture content between -118  $\mu\text{m}$  and 150  $\mu\text{m}$  stayed constant. It can be shown that when the moisture content stays constant, the fiber content must remain constant, which has been done in Nicasy et al [353]. Therefore, the total fiber content within the paper stayed constant during swelling. When the fiber content within the paper stays constant and the paper thickness increases, the fiber concentration must go down. Therefore, swelling resulted in a redistribution of the fibers but leaves the total fiber content unchanged. A decrease in fiber concentration will in turn increase the porosity and increase the local moisture content.

Therefore, the increased moisture content in phase II could be linked to an increase in porosity when the paper swells. The end of phase II was marked by the end of swelling and by a constant moisture content of 0.55 within the paper.

### 7.4.3. Phase III: trapped air release leads to further moisture increase

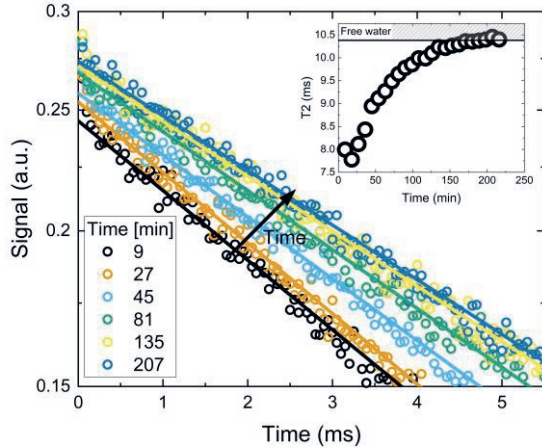


Figure 7.8 OW-Signal decays during the penetration of water within a paper sheet between 30 and 60  $\mu\text{m}$ . Corresponding  $T_2$  fits are shown with lines. The insert shows the extracted  $T_2$  values as a function of time. The relaxation time of free demineralized water (10.3 ms) is also shown.

After swelling, a third phase started, where the moisture content within paper continued to increase, see Figure 7.4c. Figure 7.5a shows how the moisture content increased from 0.55 to 0.72. An increase in the moisture content is accompanied by either a decrease in fiber content or a decrease in air content. Because no further changes in paper thickness were observed, Figure 7.4b, the fiber content had to remain constant. Therefore, there was still air within the paper sample which was gradually replaced by water and thereby increased the hydrogen content  $\rho$  measured by UFI. To confirm that the signal increase could not be attributed to changes in the  $T_1$  and  $T_2$  relaxation time, OW – and saturation recovery measurements were conducted during phase III for a Clariscan solution, the same solution used for the experiments. The  $T_1$  and  $T_2$  relaxation time as a function of time during phase III are given in Figure 7.13 in appendix A of this chapter. These measurements confirmed that both relaxation times were unchanged during phase III and could therefore not be responsible for the observed signal increase.

To investigate what happened during this last phase, OW experiments were performed to determine the  $T_2$  of demineralized water on these later timescales. As explained in chapter 3.2.1, the  $T_2$  of demineralized water can provide valuable information about the environment of the hydrogen content. The measurements were performed according to experiment type II, see Figure 7.2b. Figure 7.8 shows the  $T_2$  decays of demineralized water within a paper sheet during phase III. The data shows how the signal decay changed over time. From the signal decays,  $T_2$  times were extracted which are shown in the indent of Figure 7.8, where a line is used to mark the  $T_2$  time of free water.

The initial  $T_2$  time of water was lower than the one of free water but increased to a value similar to free water. That water within paper acted similar to free water was already observed in Figure 7.3. The period during which the  $T_2$  changed, aligns closely with the time of the signal increase observed in Figure 7.5a. Therefore, the mechanism responsible for the moisture increase was also responsible for the changes in the relaxation time.

It was already concluded that the release of trapped air was responsible for the increase in moisture content during phase III. The  $T_2$  decay however can provide more information about the location of the trapped air. A closer look at Figure 7.8 revealed that the change in decay time happened in the long component of the  $T_2$  decay, which represents the majority of the signal. Because most of the water was between the fibers, the change in  $T_2$  should be attributed to a phenomenon that took place between the fibers rather than within the fiber lumen. If the filling of the fiber lumen would be responsible for the signal increase, the relaxation behavior of the liquid between the fibers would be unchanged which was not observed. Therefore, it was concluded that the air was trapped between the fibers.

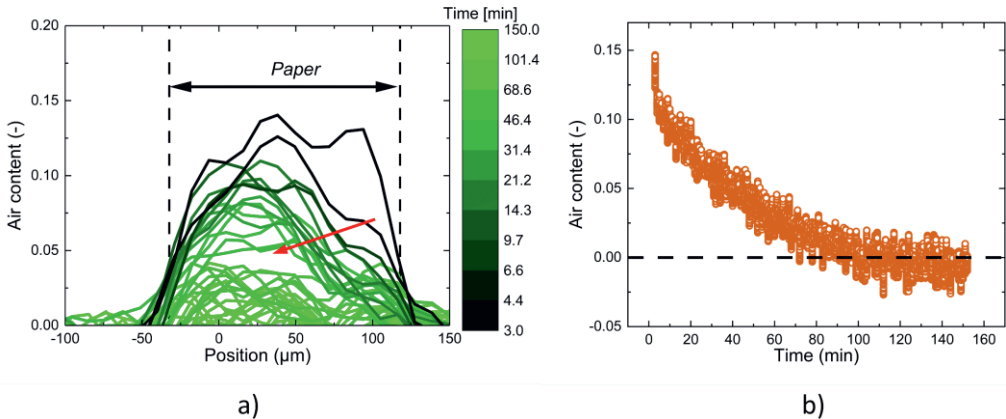


Figure 7.9 a) Air fraction profiles in paper during phase III. The position of the paper sheet at the start of phase III is marked with dashed lines. Red arrow is used to mark the movement of the arrow within the paper through time. b) Air fraction integrated over the whole paper samples as a function of time.

Since trapped air was responsible for the signal increase in phase III, the air content within the paper could be estimated by subtracting the liquid profiles in Figure 7.4c from a fully saturated paper sample. Figure 7.9 shows the air profiles calculated for phase III. The data shows that at the beginning of phase III, 14 v/v% of the paper was filled with air, and that the air was homogeneously distributed throughout the sample.

Over time the air escaped from the paper. Because of the experimental setup, the air could only escape from the top of the paper. The movement of air to the top of the paper can be observed in the profiles of Figure 7.9a marked with an arrow. From these profiles, the total air content within the paper could be calculated over time, which is shown in Figure 7.9b.

## 7.5 Discussion

In this section, the previously introduced data are used to build up a physical understanding about the water-filling mechanism inside a cellulose fiber network. Figure 7.10 illustrates the relations between liquid front, swelling and moisture content in the network, with a green scale marking the time of each data point. Figure 7.11 provides a schematic representation of the liquid filling mechanism. In this figure, the glass plate, network, and part of the droplet are shown. Gray is used for fibers, blue indicates liquid and white represents air. The orange circle marks the development of an air bubble within the paper sample.

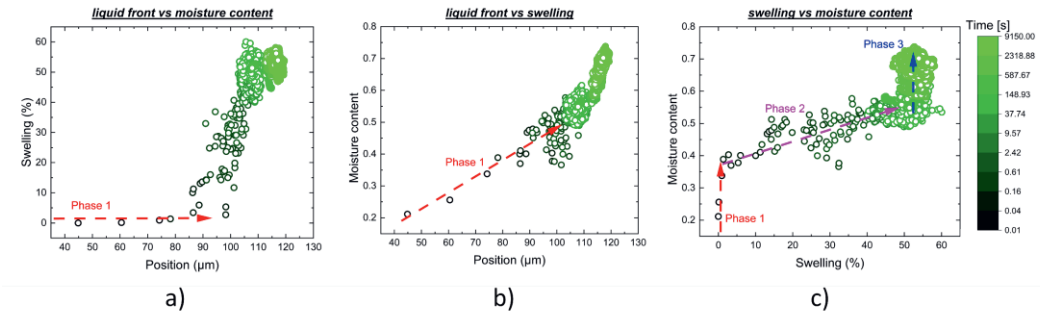


Figure 7.10 a) Swelling as a function of liquid front. b) Moisture content as a function of liquid front. c) Moisture content as a function of swelling.

During phase I, Figure 7.11a, the liquid front (red line) enters the paper because of capillary forces. Capillary penetration leads to a rise in the moisture content as the liquid front moves. Therefore, a correlation existed between the liquid front and moisture content during the first measurement points (Figure 7.10b). During capillary penetration, no swelling took place which can be seen in Figure 7.10a, where the liquid front advanced while swelling is constant. Therefore, it was assumed that the penetration process is unaffected by swelling. In other types of paper, swelling can become important. This should subsequently be taken into account for the penetration process, which is done in some theoretical models [51]. From section 7.4.3, we know that the liquid front will trap air within the liquid system. The orange circle in Figure 7.11a shows the development of an air bubble.

During phase II, the swelling phase, the paper swells from its initial thickness  $h_1$  to a new thickness  $h_2$ , see Figure 7.11b. It was found in section 7.4.2 that a decrease in fiber density was responsible for a further increase in the moisture content. This relation between swelling and moisture content can be seen in Figure 7.10c where a linear relationship exists between moisture content and swelling during phase II (yellow arrow). In this stage, air is surrounded by water and becomes completely trapped (orange circle).

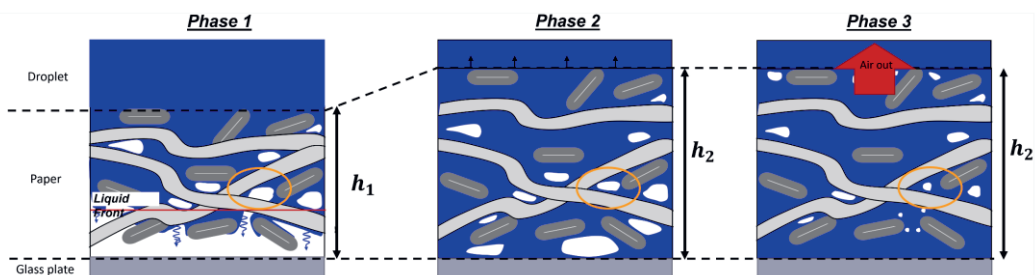


Figure 7.11 Schematic representation of the liquid uptake in paper. Shown are the three different phases: capillary liquid uptake, swelling and the release of trapped air. The orange circle follows the development of an air bubble within the paper sample.

In the final phase, the moisture content increased without a change in swelling or front position (Figure 7.10b,c). In section 4.2.3 it was shown that the release of trapped air is responsible for the increase in moisture content. Figure 7.11c shows how during this phase, the paper thickness stays constant and the air bubbles get smaller (orange circle). It was also shown that the air escaped via the surface of the paper sample. A similar observation was made by Waldner et al. where the presence of air bubbles in the paper after capillary penetration, and their subsequent release, was observed in ultrasonic testing of liquid penetration [18].

## 7.6 Conclusions

In this chapter, the liquid penetration mechanism inside a cellulose fiber network was investigated with UFI NMR. We were able to simultaneously measure the liquid distribution, swelling and trapped air within a paper sample. The liquid penetration process could be split into 3 different phases: 1) liquid front penetration, 2) swelling and 3) the release of entrapped air. During the first phase, capillary forces drove water into the system. This phase lasted for only 65 ms and resulted in a water saturation of 40 v/v%. During the penetration, around 15 v/v% of air is entrapped within the system. Following capillary uptake, the paper entered a 30 second swelling phase. During this phase, the paper swelled around 45 % which led to a further increase in the water density towards 55 v/v% attributed to a reduction in the fiber content. During the final phase, the air that was entrapped during capillary uptake was slowly replaced by water. This phase lasted around 3 h. The study confirmed the hypothesis that, within hydrophilic paper, liquid penetration is governed by capillary uptake and that it can be decoupled from swelling.

The UFI method employed in this study allowed to study the liquid uptake in cellulose fiber networks in much more spatial- and temporal detail than most existing methods. However, further improvements on temporal resolution and signal-to-noise ratio could increase the impact of this technique. The strength of the method is that it becomes possible to quantify the concentration of all three phases, solid, liquid and air within the network at high temporal resolution. We hence believe that the proposed method should also be useful to study liquid penetration, or water diffusion, into other porous cellulosic materials like foams, membranes, nonwovens, textiles and films.

## 7.7 Appendix A: $T_1$ and $T_2$ relaxation times in paper during phase III

To prove that the  $T_1$  and  $T_2$  relaxation time are not responsible for the measured signal changes during phase III of the absorption process, an extended NMR pulse experiment was performed. The experimental procedure is shown in Figure 7.12. Because the focus lies on the later uptake process, 5 drops are directly added, followed by closing the sample holder. After the paper comes in contact with the water the NMR will start to measure the UFI signal, the  $T_2$  relaxation time with an OW sequence ( $t_e = 50 \mu\text{s}$ ,  $t_r = 0.1 \text{ s}$ ) and the  $T_1$  time with a saturation recovery sequence. Because the  $T_1$  time of a Clariscan solution is low enough to ensure fast recovery of the spins. All measurements can be performed within 5 min.

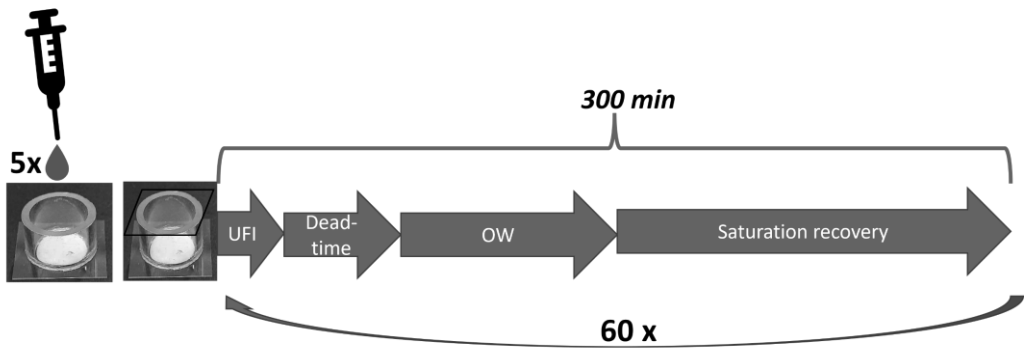


Figure 7.12 Experiment type II, to measure the UFI-signal intensity,  $T_2$  relaxation time and  $T_1$  relaxation time during phase III for a Clariscan-water solution within paper. The measurements together take approximately 5 minutes to perform. This sequence is then repeated 60 times which results in a total measurement time of 300 min.

Figure 7.13a shows the signal intensity, measured with all three pulse sequences, UFI (blue), OW-measurement (orange) and saturation recovery (black). The signal intensities from the OW- and saturation recovery sequence do not depend on the relaxation times and are comparable to the signal intensity measured with UFI. Therefore, the change in signal intensity measured by UFI cannot be linked to a change in  $T_2$  or  $T_1$  time. Besides the signal intensities, Figure 7.13b shows the  $T_1$  and  $T_2$  times measured during phase III which show that both relaxations times stay constant over the course of 300 min, again showing that, the signal change should be attributed to an increase in  $\rho$ , the water content.

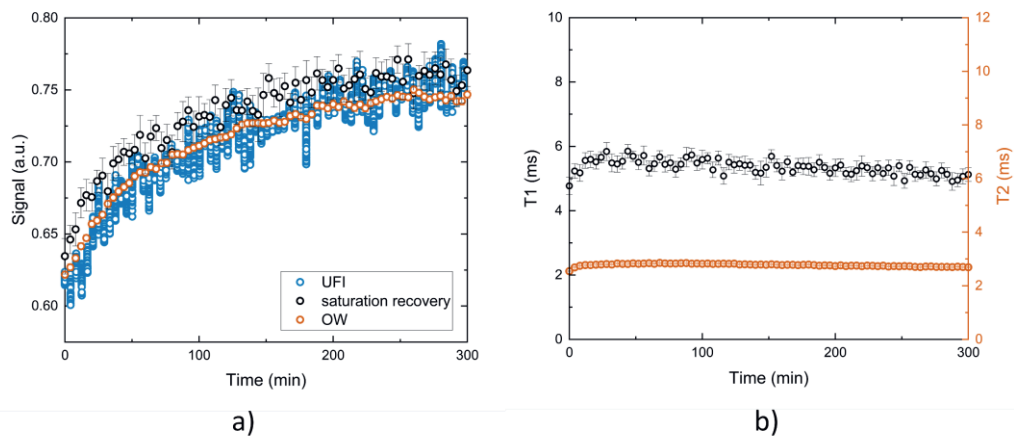
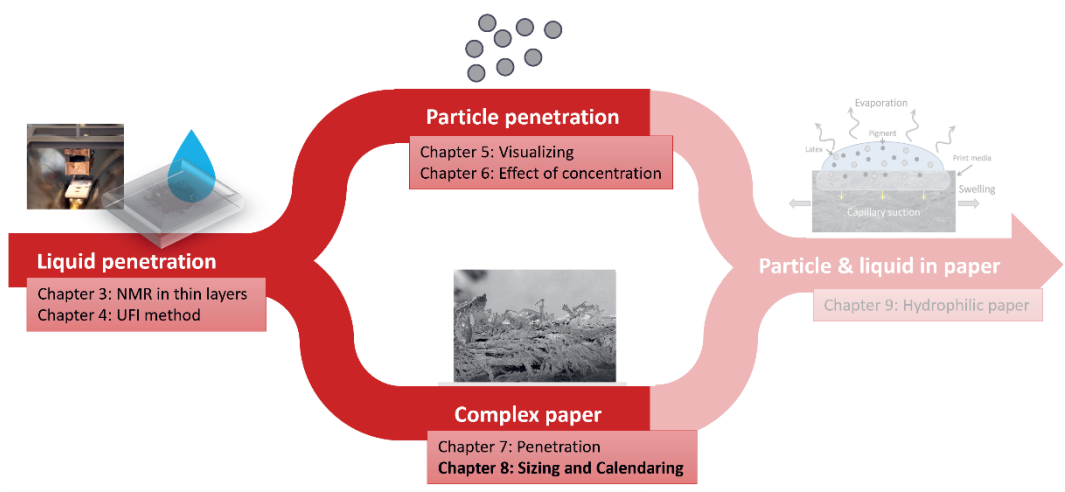


Figure 7.13 a) Signal intensities during the uptake of a Clariscan-water solution in a paper sheet as measured by UFI (blue), OW-measurement (orange) and saturation recovery (black). b)  $T_1$  and  $T_2$  relaxation times during the uptake of a Clariscan-water solution in a.





# 8

## Liquid penetration in hydrophobized and calendered paper sheets.

---

Controlling the liquid transport within cellulose-based materials is crucial for numerous applications, including printing, bio-assays, packaging, and cleaning. To control liquid transport and quality, post-processes such as calendering, a way of compressing and smoothen the paper using hard pressure rollers, and hydrophobization, are commonly employed. To understand how these processes influence liquid uptake, this study uses an Ultra Fast Imaging (UFI) NMR method to analyze moisture profiles during liquid uptake in various cellulose-based paper sheets with diverse levels of hydrophobization and calendering. It is demonstrated that calendering decreases penetration speed and increases swelling. The reduction in penetration speed could be linked to a decrease in permeability upon calendering, as measured by the Gurley air permeance. Additionally, hydrophobization delayed and slowed down liquid uptake in the paper samples, and, in extreme cases, completely altered the liquid uptake phenomena. With substantial hydrophobization, liquid penetration no longer proceeded with a well-defined liquid front but exhibited huge levels of fingering. Furthermore, it was observed that within highly hydrophobized paper, fibers were first prewetted, initiating a first swelling, before the pores between fibers could be filled. Subsequently, water could enter the pores between, allowing fiber bonds to be broken, leading to a second swelling of the paper sheet. The improved understanding contributes to a better control of the flow within cellulose-based materials, benefiting applications such as printing, packaging and microfluidics.

*Adapted from:*

*R. J. K. Nicasy, C. Waldner, S. J. F. Erich, O. C. G. Adan, U. Hirn, and H. P. Huinink, "Liquid penetration in hydrophobised cellulose based sheets," Cellul. 2024 1–18 (2024) doi:10.1007/S10570-024-05934-5.*

### 8.1 Introduction

Cellulose-based materials such as paper, have experienced growing interest in the last decades in application such as packaging, driven by their renewable and biodegradable nature and the rising environmental concerns imposed by materials such as plastics [354], [355]. In the pursuit of minimizing environmental impact and develop circular economies, efforts are made to replace existing materials with paper and other biopolymers [356], [357]. However, paper and biopolymers-based materials exhibit

complex structures, which greatly influence the end-use properties such as printability and packaging performance. Consequently, extensive research focuses on the effects of introducing these materials for packaging systems [343], [358], [359], barrier layers [347] and paper-based diagnostics [36], [268]. Beyond enhancing the biodegradability of existing and new applications, research is also devoted to understanding and refining the printability of paper products [30], [334]. This can drastically reduce the usage of harmful chemical components such as inks.

To enable fiber-based cellulosic materials, such as paper, to compete with existing applications or to enhance printability, the materials are often modified to influence the penetration behavior of liquids, their strength or smoothness. While certain materials such as tissues are specially designed to absorb water, other applications, including textiles, medical applications or food packaging require resistance to water [78]. Fully controlling water transport in cellulosic materials through specific liquid-surface interaction has advantages in general printing, printable electronics [360], microfluidic devices and lab-on-chip devices [64], [268], [361], [362]. Therefore, multiple processes are employed to influence the penetration behavior in the final applications [361], [362]. Two factors that significantly influence the penetration behavior are the porous structure and the surface chemistry of the biopolymer fibers. Calendering and sizing are two commonly used processes to adjust the porous structure or surface chemistry. In sizing, the surface chemistry of the fiber is modified to change the hydrophobicity, while calendering influences the porous structure by compressing. In sizing, a hydrophobic sizing agent is applied to the paper sample (surface sizing) or attached to the fibers (internal sizing), which hydrophobizes the paper [78]. By increasing the hydrophobicity, the paper becomes more resistant to water and moisture. The vulnerability of biopolymers and paper to wetting is a significant concern in packaging and barrier materials which can be overcome by sizing. Szlek et al. [363] provide a detailed description of various sizing treatments to improve the hydrophobic nature of cellulose-based and other polysaccharide barriers for sustainable food packaging. Besides protection against water damage, controlled hydrophobicity can be employed to adjust the penetration speed for desired properties, and for example to define the flow path within paper-based microfluidic devices by selectively hydrophobizing certain areas of the sheet [362]. While sizing is used to modify the hydrophobicity of the paper, as previously mentioned, calendering is used to adjust the porous structure. During calendering, paper is passed through a series of steel rollers that press the fibers together [76]. In some cases, these forces are accompanied by a heat treatment. Calendering increases the density of the paper, reduces surface roughness, enhances uniformity and increase paper gloss [364]. A smoother surface primarily improves print quality, while uniformity in the paper improves workability or folding. Both outcomes contribute to improvements in the quality of the finished products.

Given that both sizing and calendering significantly influence processes such as ink or liquid penetration, swelling, and water resistance, it is crucial to improve our understanding of these processes in respect to wetting behaviour. This will lead to improvements in production speed, production cost, and quality of the paper-based materials in a variety of applications. Penetration behavior in cellulosic material mainly depends on four processes: 1) liquid phase penetration in the capillaries (inter-fiber space), 2) surface transport along the fibers, 3) diffusion within fibers and 4) vapor phase transport. The contribution of these processes depend on the porous structure

and chemical nature of the fibers which are both adjusted by processes such as calendering and sizing. While there is extensive research on the penetration of water and aqueous liquids into materials such as paper [53], cellulosic materials [54], and random fiber network [55], [56], the research on effects such as calendering and hydrophobization on that penetration is significantly less. However, several studies address the effects of sizing and calendering on phenomena such as print dot spreading [57], [58], wettability [59], [60], mechanical strength [61], changes in local roughness [62], ink setting behavior [365] and printability [64]. Although, these studies offer information about the effect on parameters such as printability, gloss, and water resistance, they provide limited insight into the physics and exact penetration behavior.

To enhance our understanding about effects such as calendering and hydrophobization on liquid penetration and provide validation for existing models, an experimental study providing moisture distributions on relevant time scales is necessary. In chapter 7, it was shown how the Ultra Fast Imaging (UFI) NMR method was able to measure the moisture distribution within paper samples with a temporal resolution of 10 ms and spatial resolution of 18  $\mu\text{m}$ . These profiles enabled information to be extracted about moisture density, swelling and structural deformation during and after liquid penetration. chapter 7 also showed that within hydrophilic, lightly calendered paper, the penetration process could be divided into three phases: liquid uptake, swelling and release of trapped air.

The aim of this current chapter is to study the effect of hydrophobization and calendering on the liquid uptake behavior by providing spatial resolved moisture distributions during penetration of a water-based solutions within a diverse range of calendered and hydrophobized paper samples. The resulting moisture profiles offer valuable insights into the liquid penetration behavior, swelling kinetics and structural changes within the paper samples during and after penetration. With these findings we can deepen our understanding of the physics governing liquid penetration within paper and the contribution and importance of varying processes such as calendering and hydrophobization to target specific product properties.

## 8.2 Materials

### 8.2.1. Substrates

Various paper sheets with differing degrees of calendering and hydrophobization were examined. The papers were taken from a study performed by Waldner et al. [39]. Table 8.1 summarizes the most important parameters and characteristics. The sheets are made from an industrially produced uncoated paper composed of cellulose pulp (bleached eucalyptus kraft) and calcium carbonate filler (scaleno-hedral, precipitated calcium carbonate, filler content 21.25%). The surface energy of the paper was modified using chemical vapor deposition. The hydrophobization agent was hexamethyldisilazene (HMDS, from Carl Roth, 98%). Four hydrophobization levels were obtained by applying either 0 (H00), 10 (H10), 20 (H20), 40 mL (H40) of HDMS per 10 A4 sheets. After hydrophobization, the papers were calendered using a force of 0 (C00), 15 (C15), 30 (C30) or 60 (C60) kN, which resulted in a line load of 0, 71, 143, and 286  $\text{kN m}^{-1}$ . The Gurley method (ISO 5636-5) is used to obtain a first approximation about the paper permeability. The Gurley air permeance  $\kappa_c [\mu\text{m Pa}^{-1} \text{S}^{-1}]$  gives the volumetric air flow,

averaged over the measurement area and pressure. For a detailed description of the paper samples, the Gurley air permeance measurements and the preparation process, readers are referred to the original paper by Waldner et al. [39].

Table 8.1 Physical properties of the paper samples, data from Waldner et al. [39].

Paper	Thickness [μm]	Apparent density [g.cm <sup>-3</sup> ]	Mean pore diameter [μm]	Water contact angle θ [°]	Gurley air permeance κ <sub>G</sub> [μm.Pa <sup>-1</sup> .S <sup>-1</sup> ]
<b>C00H00</b>	132.4 ± 1.9	0.68	2.80	38.0	11.5 ± 0.2
<b>C15H00</b>	100.0 ± 1.2	0.90	2.16	39.0	5.0 ± 0.1
<b>C30H00</b>	94.9 ± 2.6.	0.94	1.89	41.0	3.0 ± 0.1
<b>C60H00</b>	92.3 ± 2.1	0.97	1.51	46.9.0	2.1 ± 0.1
<b>C00H10</b>	134.3 ± 2.5	0.67	2.80	82.8	11.9 ± 0.3
<b>C00H20</b>	132.4 ± 1.7	0.68	2.80	104.5	11.6 ± 0.5
<b>C00H40</b>	132.0 ± 2.8	0.68	2.80	114.6	11.7 ± 0.4

### 8.3 Effect of calendering

To study the influence of calendering, liquid penetration experiments were performed using a Clariscan-water mixture on a reference paper (C00H00) and several non-hydrophobized calendered papers (C15H00, C30H00 and C60H00). The moisture profiles are measured using the UFI method as shown in Figure 4.7. The first part of this section concentrates on a comparison between the moisture distributions during penetration in the reference paper and a heavily calendered paper only, in order to highlight the major changes, thus providing insights into swelling, liquid penetration speed and moisture content during penetration. Later, these three parameters will be discussed in more detail. Finally, the correlation between the liquid front and swelling will be discussed.

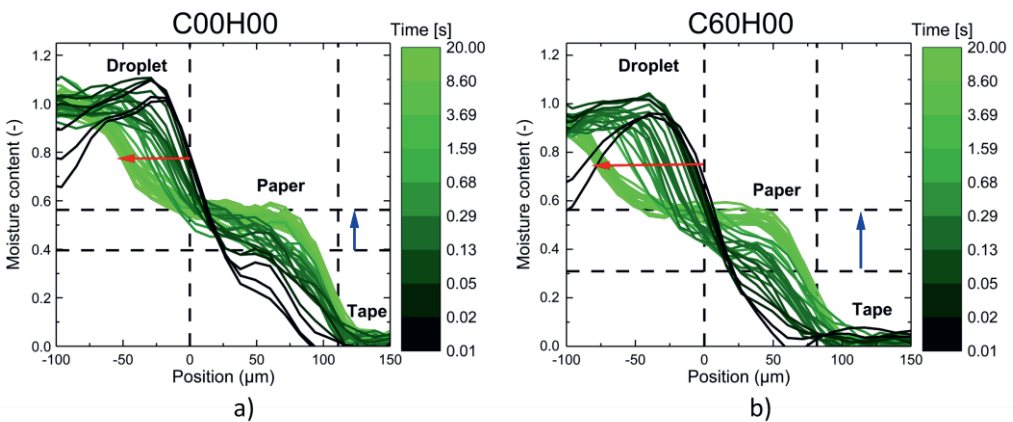


Figure 8.1 Liquid profiles measured during the penetration of a Clariscan-water solution within a) C00H00, a reference paper, and b) C60H00, a calendered paper. A green color map is used to mark the time at which the profile is measured.

Figure 8.1 shows the liquid profiles measured during the penetration of a Clariscan-water solution within a lightly calendered paper (C00H00) and a high-calendered paper (C60H00). For the purpose of this section, the profiles for the samples C15H00 and C30H00 are not shown but can be found Nicasy et al. [366]. The profiles represent the droplet area, paper sample and double-sided tape. In both measurements, at  $t = 0$  s, the droplet is situated at  $x < 0$   $\mu\text{m}$  and has a signal intensity of 1 representing 100% saturation since the droplet consists entirely of liquid. At  $t < 0$ , before the droplet hits the paper sheet, the paper is dry, and no moisture is observed in the paper sheet. These zero signal profiles are not shown on these images.

In Figure 8.1a, the paper has a thickness of approximately 115  $\mu\text{m}$  and is located between 0 and 115  $\mu\text{m}$ . In the case of the highly calendered paper, shown in Figure 8.1b, the paper thickness reduces to 80  $\mu\text{m}$  which is a direct consequence of the calendering process. The decrease in paper thickness upon calendering was also shown in Table 8.1.

For both measurements, swelling was observed as a movement of the droplet-paper interface, indicated by a red arrow. Consistent with what was seen in chapter 7.4.2, a moisture increase was observed within the paper samples after liquid front penetration, as indicated by a blue arrow. The initial moisture content at the start of swelling (marked with dashed line) was taken from the moisture profile just after the liquid front reached the end of the paper,  $t = 80$  ms (C00H00) and  $t = 130$  ms (C60H00). This moisture increase was attributed to two phenomena: swelling, which increased the internal porosity, and the removal of air which was entrapped by the liquid front.

## 8.4 Liquid penetration

The profiles provide information about the influence of calendering on penetration behavior. It was evident from the profiles that calendering affected the penetration speed of the water-Clariscan mixture, as observed by the slower movement of the profiles inside the C60H00 paper. Liquid front positions were extracted over time at a moisture content of 0.2 (-), where a saturation of 1 corresponds with a fully saturated region. It is important to note that ideally, liquid front positions are extracted at half the maximum moisture content. This becomes more challenging in papers with higher levels of calendering as the moisture content varies significantly through time, making the front positions of highly calendered papers less accurate.

Figure 8.2a shows the liquid front position as a function of the square root of time for papers with varying degrees of calendering. The penetration data were analyzed until the water reached the bottom of the paper which varied between 0.2 - 0.4 s depending on the level of calendering. Thereafter, the position slowly increased due to an artefact coming from the further increase in moisture content. In all cases, data reveal a square root of time behavior for the first part of the penetration as predicted by Darcy [14], [23], see dotted lines in Figure 8.2a. The data illustrates how calendering decreased penetration speed. Since both papers were chemically similar (unsized), changes within the porous structure, such as tortuosity, should be responsible for the decrease in penetration speed. This is explained by models such as Darcy and Washburn, where the fluid front position scales with pore radius. In these models, capillary pressure is taken as the driving force and the permeability is a value which represents the porous media properties.

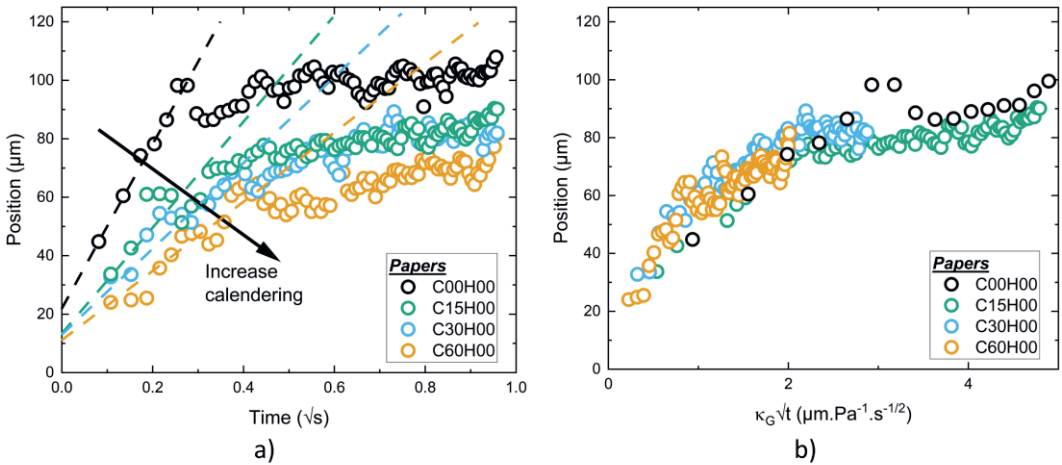


Figure 8.2 Liquid front positions as a function of a)  $t$  and b)  $\kappa_G \sqrt{t}$ , for the penetration of a Clariscan-water solution in a C00H00 reference paper (black) and higher calendered C15H00 (green), C30H00 (blue) and C60H00 (orange) paper. The liquid front positions are taken from the profiles shown in Figure 8.1 at a moisture content of 0.2 (-).

While the capillary pressure scales with  $1/r$ , the permeability scales with  $r^2$  [281]. Therefore, the fluid front scales linearly with the pore radius. A better approximation on the influence of the porous structure can be achieved using the Gurley air permeance  $\kappa_G$ , in Table 8.1. Although  $\kappa_G$  represents the air flow through a specific paper sheet rather than a real permeability, both can be related to each other using paper properties [367]. Because the paper properties of all sample are similar, a rescaling with the Gurley air permeance is justified and can be used as a first approximation to account for the permeability. When rescaling the data using Darcy's Law and the Gurley Air permeance ( $\kappa_G$ ) (Table 8.1) with  $\kappa_G \sqrt{t}$  [ $\mu\text{mPa}^{-1}\text{s}^{-1/2}$ ], the data converge relatively well onto one master curve (Figure 8.2b), suggesting that the Gurley Air permeance is a suitable measure for determining changes in the pore structure of the paper such as permeability or tortuosity for liquid penetration.

## 8.5 Swelling

The profiles also provide insight into the swelling behavior of the papers. By examining the droplet membrane interface, the paper thickness can be followed over time. At  $t = 0$  s, the droplet-membrane interface was located at  $x = 0$   $\mu\text{m}$ . However, paper swelling resulted in a movement of the droplet-membrane interface (indicated by a red arrow in Figure 8.1). By tracking the interface at a moisture content of 0.75, the paper thickness  $d_t$  at time  $t$  was determined. Swelling  $S$  [%] was calculated using the formula,  $S = 100(d_t - d_0)/d_0$ , where  $d_0$  represents the initial paper thickness at  $t = 0$  s. Figure 8.4 illustrates the swelling in percent as a function of time for the C00H00 reference paper (black) and the C60H00 calendered paper (orange). For clarity, only the reference paper and highly calendered paper are shown, while data for other calendered papers can be found in Nicasy et al. [366]. It was observed that the C60H00 paper swelled more than the reference C00H00 paper.

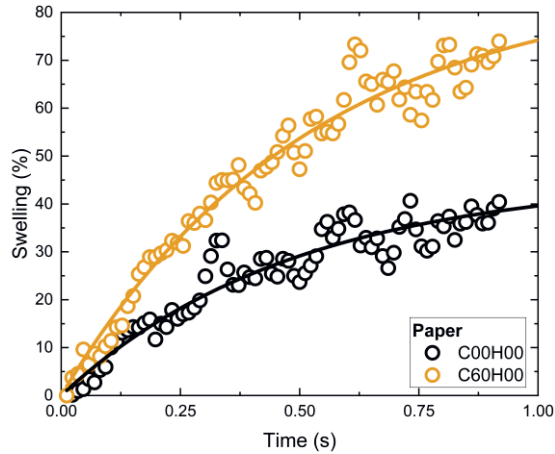


Figure 8.3 Swelling as a function of time for C00H00 (black) and C60H00 (orange).

The lines corresponding to a fit based on a swelling model given by:  $f=f_{\max}(1-e^{-kt})$

The process of swelling arises from internal stresses and water diffusion in fibers. While models exist for this stress-diffusion coupling in fiber-like porous media, they often require numerical solutions due to their complexity [368], [369]. In this chapter, a simpler model is used, see chapter 7.4.2, which links paper swelling to a rate constant  $k$  [ $\text{s}^{-1}$ ] by  $S=S_{\max}(1-e^{-kt})$ . Here,  $S_{\max}$  represents the equilibrium swelling degree (maximum possible swelling), and  $k$  a rate constant which can be associated with diffusion in the fibers, relaxation of the fibers, or a combination of both [370]–[372].  $k$  can also be related to a time  $t_d=1/k$ , where  $t_d$  is the time required for the paper to reach 0.63 of its maximum swelling. The fit for both papers is given in Figure 8.3, yielding values of  $k = 2.06 \pm 0.1 \text{ s}^{-1}$  and  $S_{\max} = 45 \pm 0.4 \%$  for C00H00 and values of  $k = 1.92 \pm 0.1 \text{ s}^{-1}$  and  $S_{\max} = 87 \pm 0.5 \%$  for C60H00. The similarity in rate constants suggests a comparable swelling mechanism. Because the fibers of both papers are identical, diffusion in the fibers should be comparable. On the other hand, the more compressed calendered paper should have an increased relaxation behaviour due to the higher fiber density. This leads to the conclusion that at this time period, diffusion in the fibers is the main driving force behind swelling. The higher swelling of the highly calendered paper compared to lightly calendered paper can be attributed to differences in fiber density between the two papers.

Considering that  $k$  is related to the diffusion in the fiber walls, a first estimation of the diffusion constant can be made. Using Fickian diffusion, the diffusion constant ( $D$ ) can be calculated by  $D=l_d^2/2t_d$ . Taking  $l_d$  as the typical thickness of the fiber wall (2–5  $\mu\text{m}$ ), a diffusion constant  $D = 4.2 \cdot 10^{-11} \text{ m}^2\text{s}^{-1}$  is obtained, which aligns reasonable well with values for radial diffusion in wood fibers as found in literature [373], [374]. This aligns with the observation that initially pores are saturated with water before swelling occurs, meaning that water penetrates from the radial direction into the fibers. This water penetration initiates paper swelling. The maximum swelling is determined by the fiber density of the paper sheets, which is influenced by the degree of calendering.



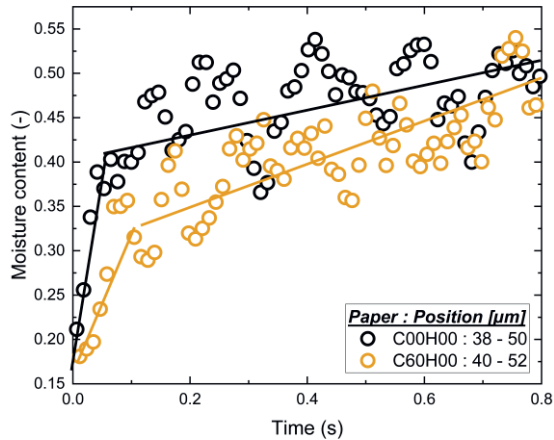


Figure 8.4 Moisture content measured within a C00H00 (black) and C60H00 (orange) paper during the penetration of a Clariscan-water solution. The moisture content was determined between 38 and 50  $\mu\text{m}$  in the C00H00 paper and between 40 – 52  $\mu\text{m}$  for the C60H00 paper.

## 8.6 Moisture content

Finally, the profiles also provide information about the moisture content, indirectly offering insight into the paper structure. In chapter 7.4.2, we demonstrated that, for the reference paper (C00H00), during swelling, the paper's porosity increased, leading to a rise in the moisture content. A similar moisture content increase was also observed within the highly calendered paper as indicated by blue arrows in Figure 8.1. Figure 8.4 shows the moisture content as a function of time for the reference paper as measured in chapter 7.4, represented by the black data points and as measured for the highly calendered paper C60H00, orange data points. The moisture content was integrated between 38 – 50  $\mu\text{m}$  in the reference paper and between 40 – 52  $\mu\text{m}$  for the C60H00 paper. For the reference paper, the moisture content increased from 0.4 to 0.55. However, for the highly calendered paper, the moisture content increased from 0.3 to 0.55. This observation led to two main findings. First, the calendered paper has a lower initial porosity, resulting in a lower moisture content at the start. Second, after swelling, both papers had similar moisture contents, indicating that the effect of calendering disappeared after contact with water, and this again supports the topological nature of compression and its effect on tortuosity.

## 8.7 Liquid front vs swelling

In the final part of this section, the relationship between liquid front and swelling will be discussed. Figure 8.5 shows the liquid front position as a function of swelling for the C00H00 reference paper (filled circles) and the C60H00 calendered paper (open squares). A color code is used to mark the time of the data points. In chapter 7, it was shown that for a lightly calendered hydrophilic paper such as the reference paper, liquid first penetrated the entire paper before swelling occurred, see purple arrow in Figure 8.5. Differently, for a calendered paper, where penetration was significantly slowed down swelling already occurred during penetration, as seen in Figure 8.5 (black arrow).

The relationship between the liquid front and swelling provides valuable information for theoretical models and simulations. The data shows that for our reference paper, (hydrophilic, pore radius  $> 2.8 \mu\text{m}$ , and initial porosity  $> 0.4$ ), theoretical models and simulation for liquid penetration can be simplified by neglecting swelling. However, for higher calendering, which results in papers with lower pore radii and lower porosities, swelling can significantly influence the penetration process and cannot be neglected. In these particular case, incorporating swelling into the model is essential, which has been the focus of several studies [14], [51].

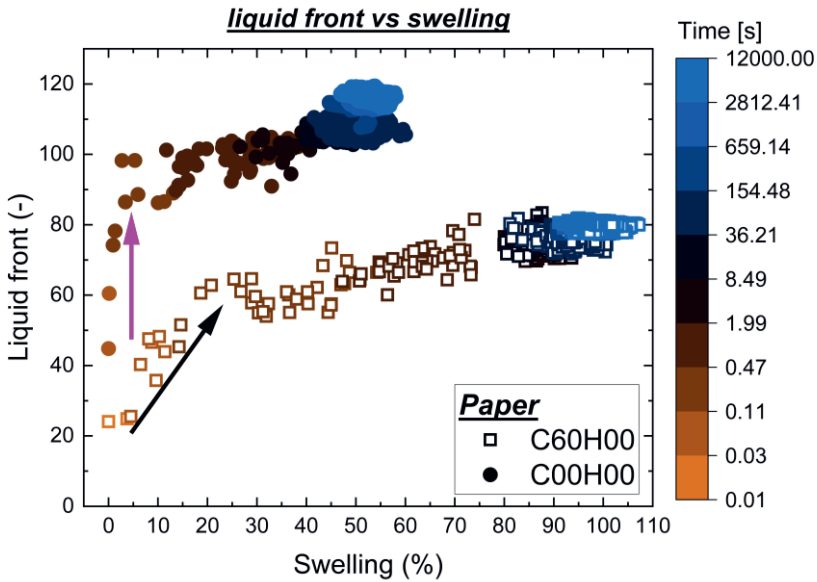


Figure 8.5 Liquid front as a function of paper swelling for the C00H00 reference paper (filled circles) and for the C60H00 calendered paper (open squares). A color code is used to mark the time of the measurement.

## 8.8 Effect of hydrophobization

To study the effect of hydrophobization on liquid transport, penetration experiments were conducted on four papers with varying levels of hydrophobization (C00H00, C00H10, C00H20 and C00H40), as listed in Table 8.1. Figure 8.6 displays the liquid profiles obtained during penetration of a Clariscan-water mixture within C00H10 and C00H40. Due to the similarity between the profiles of C00H20 and C00H10, only the profiles for the C00H10 paper are shown, while those of C00H20 can be found in Nicasy et al. [366]. The liquid profiles for the C00H00 reference paper are shown in Figure 8.1a. In these figures, a green scale is used to indicate the time of measurement.

The liquid profiles revealed that papers with less hydrophobization, such as C00H10 (Figure 8.6a) and C00H20 [366], exhibit similar penetration behavior to the hydrophilic paper (Figure 8.1a), showing comparable moisture profiles. Within these papers, the liquid still penetrated with a well-defined liquid front. The main influence of hydrophobization within these papers was a decrease in penetration speed. However, for higher levels of hydrophobization, as found in the C00H40 paper, the penetration

behavior completely changed, as illustrated in Figure 8.6b. In this paper, the liquid did not penetrate with a well-defined liquid front but shows two distinct phases.

During the first phase, the liquid barely penetrates the paper. This is evident in the liquid profiles of Figure 8.6b, where until 114 s, the liquid profiles remain relatively stationary. Only a small amount of liquid was able to penetrate within the pores of the paper sample, as indicated by a yellow arrow. After a certain moment, a second phase starts around 160 s, where the moisture content within the pore space rapidly increases (red arrow). The highly hydrophobized paper, having a completely different penetration behavior, will be discussed in more detail in section 8.11. But first, in section 8.9, we will take a closer look at the moisture content within the paper and the relationship between moisture content and swelling for all different papers.

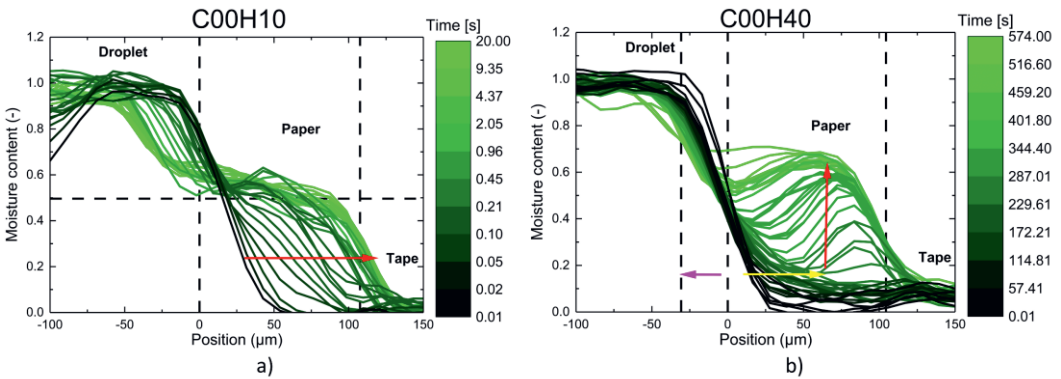


Figure 8.6 Liquid profiles measured during the penetration of a Clariscan-water solution within a) C00H10 and b) C00H40 paper. A green scale is used to identify the time at which the profile is measured.

## 8.9 Moisture content

To investigate the effect of hydrophobization on moisture uptake, the moisture content within the papers was monitored over time. Figure 8.7 shows the moisture content as a function of time for the penetration of a Clariscan-water solution within papers with four levels of hydrophobization: C00H00 (black), C00H10 (orange), C00H20 (blue) and C00H40 (green). The moisture content was extracted from the moisture profiles between 38  $\mu\text{m}$  and 60  $\mu\text{m}$  for the C00H00 paper and between 28  $\mu\text{m}$  and 62  $\mu\text{m}$  for the other papers. In this figure, time is plotted logarithmically. Based on this data, the liquid uptake could be divided into three main regions: 1) a delay time, in which moisture penetration is remarkably slow, only observed in hydrophobized papers, 2) a rapid moisture increase and 3) a slower moisture increase at the end.

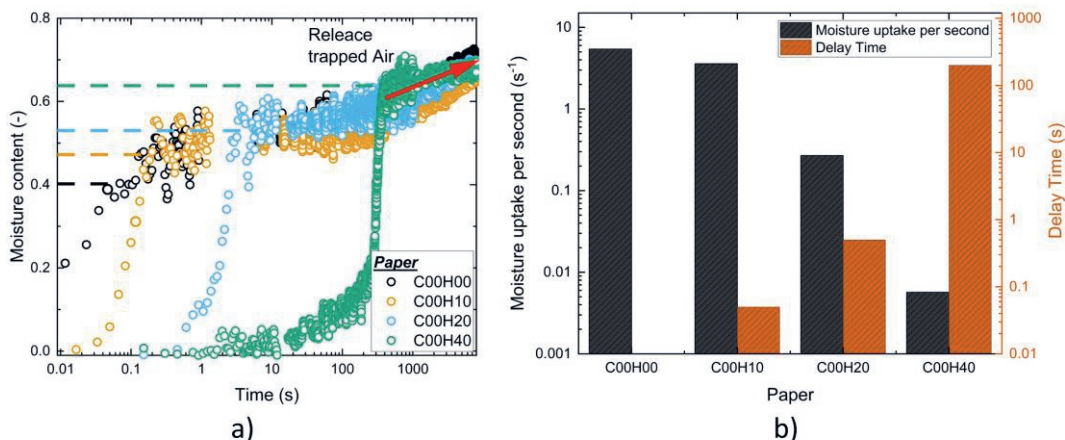


Figure 8.7 Moisture content as a function of time for penetration experiment performed with a Clariscan-water solution on varying sized papers: C00H00 (black), C00H10 (orange), C00H20 (blue) and C00H40 (green).

The data indicates that hydrophobization significantly decreased and delayed moisture uptake within a paper sheet. To acquire a first approximation of the moisture uptake rate, a linear fit is used around the point of highest moisture uptake rate. The slope of these fits are used for the moisture uptake rate. The fits were determined between 0.01 - 0.05 s (C00H00), 0.03 - 0.14 s (C00H10), 1.6 - 2.6 s (C00H20), and 290 - 330 s (C00H40). Figure 8.7b shows the observed delay times for all papers in orange columns and the determined moisture uptake rates by grey columns.

The delay time scaled almost logarithmically with hydrophobization, doubling the hydrophobization agent concentration delayed penetration by one or more orders of magnitude, as shown in Figure 8.7b by orange columns. During this delay time, moisture slowly penetrated within the paper sample, most markedly for the highly hydrophobized C00H40 paper.

After this delay time, the moisture content rapidly increased, and the pore space was filled with water. In the data of the C00H00, C00H10 and C00H20 papers, the sudden increase in moisture content corresponded with the movement of the liquid front through the paper sample. However, within the C00H40 paper, liquid penetration occurred differently, without a liquid front. Therefore, the sudden increase did not correspond to a liquid front but to a rapid filling of the pore space, as observed within the profiles in Figure 8.6b. Therefore, it can be concluded that from a certain level of hydrophobization, liquid penetration transitions from a liquid front towards a non-liquid front like behavior. The particular behaviour of these systems and the sudden increase in explained in more detail in section 8.11.

Another observation, made from Figure 8.7a, was that after filling of the pore space, the moisture content became larger with increased levels of hydrophobization, as indicated by dotted lines. In chapter 7, it was shown that for a C00H00 reference paper, the moisture content after filling first increased to 0.4 due to the movement of a liquid front[353]. Thereafter, other effects, such as swelling, and air removal further increased the moisture content towards 0.75. The phenomena of air removal was proven in chapter

7.4.3, where NMR relaxation measurements showed that air was trapped during liquid front movement. Thereafter, the air slowly diffused out of the system through the top of the paper sample as shown in Figure 7.11. Because the saturation after filling of the pore space increased with higher levels of hydrophobization, it was believed that by decreasing the penetration speed, the paper was already able to increase its porosity due to swelling, or less air was entrapped during penetration. Since, for the lightly hydrophobized papers (C00H00, C00H10 and C00H20), the moisture increase on later timescales was quite similar as shown by the red arrow, the release of trapped air was quite similar in all cases. Therefore, the reason for a higher moisture content after front penetration was linked to paper swelling during penetration.

For the highly hydrophobized paper, the need for release of trapped air disappeared, and the moisture content is seen to increase directly towards the highest level of 0.75, green data points in Figure 8.7b. Therefore, in highly hydrophobized papers, the paper already swelled before penetration and the distinct penetration behavior entrapped less air.

## 8.10 Swelling vs moisture content

Figure 8.8 illustrates the moisture content as a function of swelling to investigate the penetration behavior in more detail. In chapter 7, it was found that for a reference paper (C00H00, filled squares) swelling occurred after liquid front penetration. Slightly hydrophobized papers, C00H10 (open circles) and C00H20 (filled triangles), exhibited similar behavior as seen in Figure 8.8. However, for the highly hydrophobized paper, C00H40 (open triangles) swelling took place before moisture appeared within the pores of the paper sample. Since swelling of paper sheets can only occur in the presence of moisture, this indicates that water must be present within the fibers before water can fill the pore space between the fibers, indicating a different wetting mechanism than for hydrophilic paper. Where for hydrophilic paper, liquid can directly penetrate due to capillary forces, in hydrophobized paper, fibers first need to be wetted before liquid uptake can take place.

This also suggests a change in the surface of the pore space which also causes swelling. Therefore, water must for sure be present along the fibers. If water were only present within the fibers, the pore spaces would remain unchanged, preventing water from entering the paper samples. The next section is devoted to understanding the different mechanisms of wetting, such as wetting delay, moisture vapor diffusion, swelling, and fingering observed in highly hydrophobized papers.

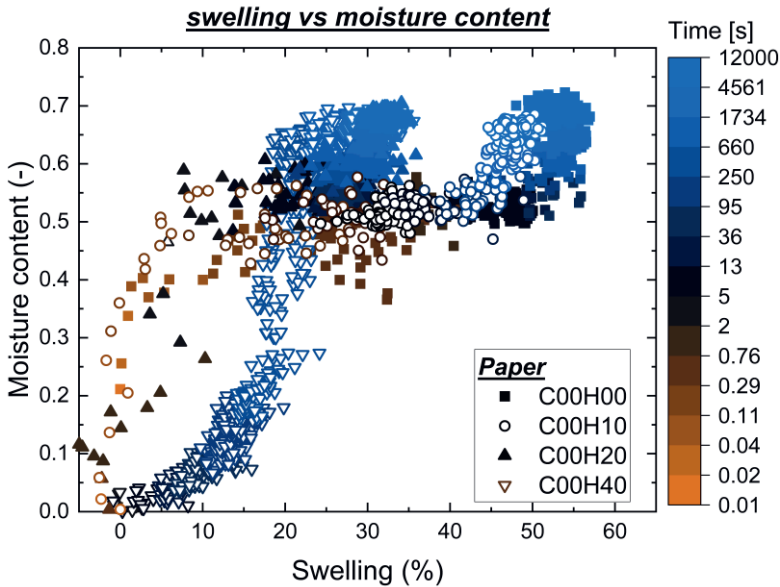


Figure 8.8 Moisture content as a function of swelling for the penetration of a Clariscan-water solution within four papers with varying levels of hydrophobization: C00H00 (filled squares), C00H10 (open circles), C00H20 (filled triangles) and C00H40 (open triangles).

## 8.11 Highly hydrophobized papers

Given the distinctive penetration mechanism of the highly hydrophobized C00H40 paper, a dedicated section is devoted to supporting the understanding of the penetration within highly hydrophobized papers.

Figure 8.9 presents a graph depicting swelling and moisture content as a function of time for hydrophobised C00H40 paper. Based on the moisture uptake, penetration could be divided into two regimes: a slow almost linear moisture uptake and a second, faster uptake. This slow and fast uptake was also observed within the profiles in Figure 8.6b. Another observation was that immediately after the paper came into contact with the droplet, the paper started to swell even when there was almost no moisture within the paper pores. This swelling continued until the paper swelled by 12.5% in thickness after which the swelling rate decreased. Furthermore, the onset of fast moisture uptake triggered another swelling stage. Therefore, water within the pores is required to swell the paper sheets completely. This indicates that there are two swelling mechanisms: first a swelling caused by moisture uptake of the fibers and swelling caused by moisture between the fibers, probably loosening up the bonding between fibers.

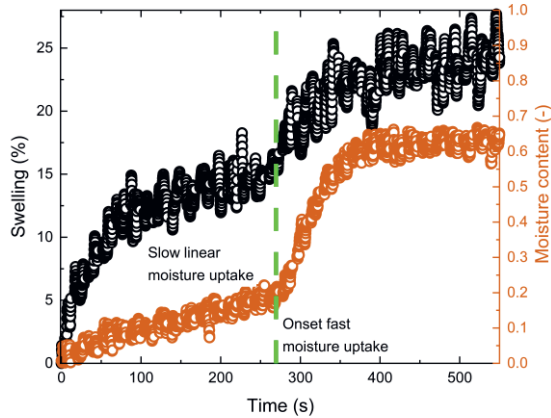


Figure 8.9 Swelling (black) and moisture content (orange) as a function of time for the penetration of a Clariscan-water solution within a highly sized C00H40 paper.

The peculiar behavior of the moisture profiles in Figure 8.6b and the two-phase moisture uptake can be explained by fingering. To illustrate this behavior, pictures from the top of the C00H40 paper during penetration were captured and are shown in Figure 8.10. At the start of the penetration, the droplet was clearly visible, and the paper appeared completely white. Over time, darker spots began to emerge, corresponding to saturated areas within the paper sample. The darkening is due to a change in refractive index when the paper becomes wet, making it transparent and less white as explained in other research [29]. The onset of the darker spots could be related to the onset of the fast moisture uptake around 270 s after initial liquid contact. Furthermore, these spots were observed to gradually expand gradually over time. A typical spot is marked by a red arrow in Figure 8.10. This illustrates that wet zones act as nucleation zones, attracting more water until the paper was fully wet and completely transparent. This mechanism of pore space filling clarifies why no liquid fronts were observed in highly sized paper in Figure 8.6b.

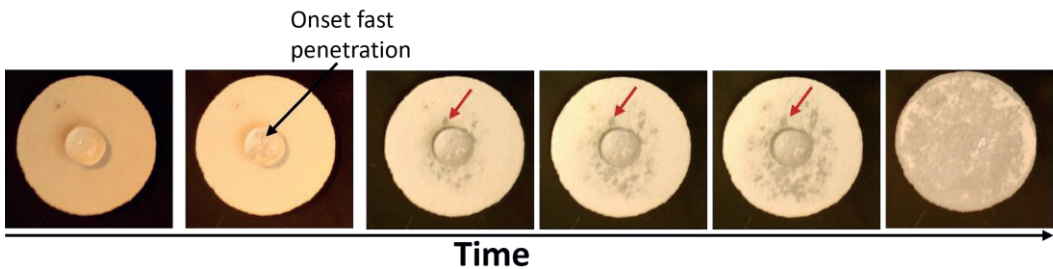


Figure 8.10 Top images of the C00H40 highly sized paper during the penetration of a Clariscan-water solution. The darker spots correspond to areas which are fully saturated which make the paper more transparent.

For a better understanding of the filling mechanism in highly hydrophobized paper, a schematic representation given in Figure 8.11. The mechanism can be split into three phases.

In phase 1, a delay with very slow increasing moisture content was observed. This was attributed to the paper's hydrophobic nature, making it challenging for water to enter the pore spaces. During this slow uptake, water attempts to find a path on the fibers which is probably a combination of film flow along the fibers, gas vapor transport and flow within the fibers.

During and after this transport, within a 2<sup>nd</sup> phase, water is present within the fibers which was observed by a first swelling of the paper in Figure 8.9 even though no moisture was observed within the pore spaces. This swelling is attributed to an increase in fiber volume when they absorb water, see section 8.5. After swelling, water was observed to enter the pore space (Figure 8.8), therefore, fibers first need to be wetted before water can enter the pore space. A similar observation was made by Akinli-Koçak [20], which showed that sorption along the interfibre pores is delayed by a wetting delay and that water first absorbed into the fiber walls before interfibre sorption occurs. This fiber wetting reduces the hydrophobicity of the surface, enabling water to enter a fully wetted pore space.

The reduction in hydrophobicity (contact angle) can be linked to various phenomena such as swelling, and water vapor transport. These processes are time dependent and will therefore contribute to the dynamic character of the imbibition process. Swelling increases the surface area of the fibers, at the same time, the amount of HDMS bonded to the surface stays constant. Therefore, the surface coverage drops and the contact angle decreases. There are also some suggestions that water diffusion into the fibers lowers the glass transition temperature of the amorphous cellulose in the surface, thereby allowing polar hydroxyl groups to rotate outwards, leading to a reduction of the contact angle ahead of the liquid front [20].

The change in contact angle can also be influenced by sorption of water molecules from the vapor phase on to the fiber wall ahead of the liquid front. The high water concentration in the vapor phase close to the liquid surface result in a diffusion of water in the vapor phase into the paper sample. The water can then condense back onto the fibers, thereby lowering the contact angle and inducing water penetration. The transport of vapor is discussed in multiple studies [38], [273], [375]. Because in sized paper, the contact angle is above 90°, which inhibits capillary flow, gas vapor flow is probably the most important contribution to water transport in sized papers.

These processes are inhomogeneous which leads to fiber areas with varying contact angle and therefore capillary forces. This will result in a finger-like behavior and explains the absence of a clear liquid front. Furthermore, liquid can start making bridges between regions separated by hydrophobised surfaces, a phenomenon called Haines jump [376]–[378]. These sudden jumps are accompanied by a quick fluid redistribution within the medium. At a certain point, the water reaches the bottom of the paper samples, making this area transparent as seen in Figure 8.10.

In a final 3<sup>rd</sup> phase, water will fill the porous medium through areas that were prewetted. During this wetting period, water finds it easier to enter through regions that are already wet, initiating a rapid increase in moisture along these existing paths, as shown in Figure 8.11. This was also verified by the growing transparent spots in Figure 8.10. When the pore space is completely filled, the water will break the hydrogen bonds and allows the paper to start a second swelling process and reach its final thickness.



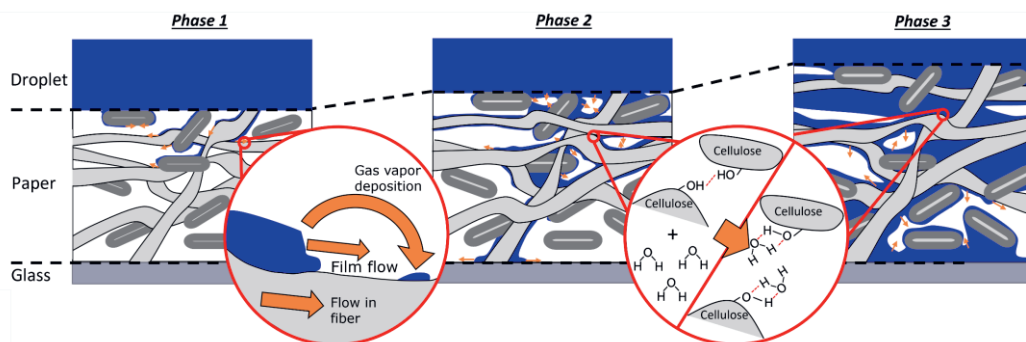


Figure 8.11 Schematic representation of the liquid penetration within highly hydrophobized paper.

## 8.12 Conclusions

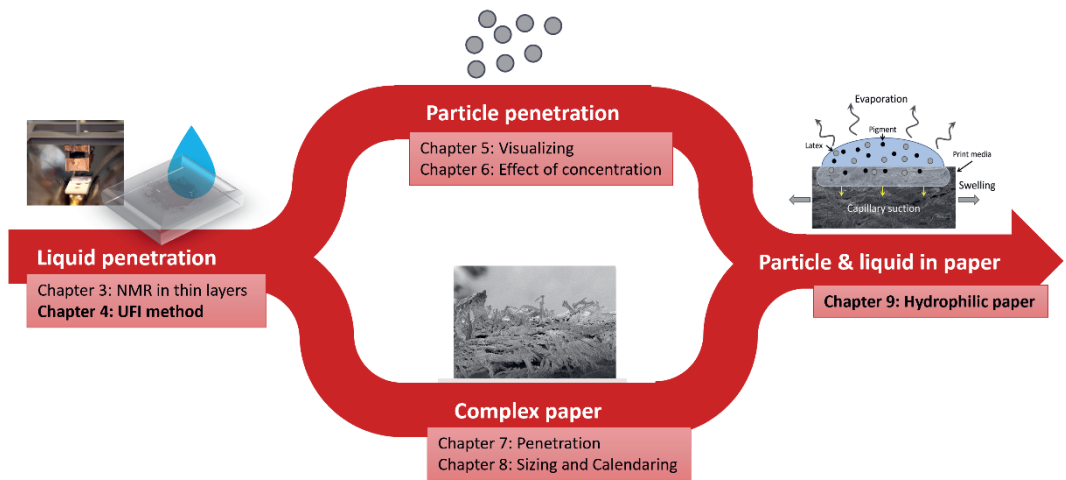
In this chapter, liquid penetration experiments were conducted on papers with varying levels of calendering and hydrophobization.

The first part of this study demonstrated that calendering decreased liquid front penetration speed, and the Gurley air permeance proved to be a good measure for the reduction in permeability. It could be concluded according to this convergence that calendering effects a topological compression of the matrix structure retaining the original nodal contact between fibers, such that the porosity decreases and the tortuosity in the depth direction increases. Furthermore, a guideline was presented for modeling liquid penetration in hydrophilic paper which indicated that for hydrophilic low-calendered paper, swelling could be neglected in penetration models. However, for highly calendered papers, swelling significantly influenced the penetration behavior and cannot be neglected.

The second part of this chapter focused on the effect of hydrophobization, which revealed that hydrophobization delayed and slowed down liquid uptake in paper samples and in extreme cases even completely changed the uptake behavior. In highly hydrophobized papers, liquid penetration was governed prewetting of the fibers, most likely by liquid vapor transport. During this period a first swelling stage of the paper took place which was linked to an increase in fiber thickness. Both vapor transport and swelling decreased the hydrophobisation of the fibers. After fibers were prewet, the hydrophobicity dropped, allowing water to fill the paper pore space. This further increases the paper thickness due to the breaking of hydrogen bonds between fibers.

By performing through-thickness moisture profiles during penetration, this paper could contribute to enhance our understanding of the complex penetration in paper and the effects of post processes such as calendering and hydrophobization. A better understanding of these processes on the penetration characteristics will result in an improved control of the flow mechanisms, benefiting applications such as printing, microfluidics, cleaning papers and much more.





## 9

## Particle dynamics in hydrophilic uncoated paper sheets

---

Understanding particle dynamics in paper-based media is crucial for achieving optimal print quality in multiple applications such as office printing and packaging. The goal of this chapter is to use the Ultra-Fast Imaging (UFI) NMR method for studying the transport of particle suspensions within hydrophilic uncoated paper. For this purpose, penetration experiments will be performed within paper sheets with particle suspensions having varying particle concentrations. These measurements will be used to extract information about liquid imbibition, by monitoring the fluid front over time, and particle penetration, by analyzing the signal intensity profiles. The measurements reveal that the latex particles are carried along with the liquid solution and are evenly distributed throughout the medium. The resulting particle concentrations within the paper sheet was determined and showed to be similar to ones found within the droplet. Furthermore, it is shown that the penetration of the suspensions can be described using a Darcy Model. While the measurements are performed on a particular paper medium and model ink, the chapter demonstrates how UFI can be extended towards other media and model inks.

### 9.1 Introduction

The transport of ink into paper-based substrates is a complicated process, crucial for achieving optimal print quality in printing applications such as packaging. As the variety of products sold in today's world rapidly increases, packaging materials and inks are constantly evolving. Because print quality should be guaranteed in every application, printing should be understood in a wide variety of material and ink combinations. Furthermore, there is a rising trend in recent years to replace current solvent-based inks by more renewable water-based inks [379]–[381]. Water-based inks are believed to overtake solvent-based inks due to environmental concerns, and their improvements in overall print quality. These water-based inks use polymeric binder resins such as acrylic or latex for a proper binding between the pigment and the substrate. Therefore, understanding the transport of these resin particles is of great importance.

For particle penetration, optimal print quality is achieved when ink particles remain at the surface. Uncontrolled particle penetration can lead to various undesired effects, such as ink spreading beyond the desired drop area (bleeding), and particles penetrating to deep which results in intensity loss and potential print-through. In water-based inks, resin particles are used to fixate pigment particles. Therefore, the penetration and position of ink particles is determined by these resin particles. This explains why current

research studies on water-based inks are focused on understanding the penetration of these particles within paper-based materials [381]–[383]. However, the vast array of media and ink compositions, combined with the predominant focus of research on specific ink and media combinations, greatly restricts the applicability of most studies. This leaves numerous penetration characteristics and ink-media interactions unresolved. To fill these gaps, more research studies are required.

However, there are several studies on the penetration of ink and particle suspensions within paper based materials that focus on effects such as viscosity and surface tension [120], [384] or coating layers [30]. In a study by Li et al., the penetration of ink pigment within coated papers revealed that size, and arrangement of pores highly affected the penetration depth and distribution of ink pigment [30]. Studies on uncoated paper, revealed that a more hydrophilic surface, led to a faster and deeper ink penetration and that calendering reduced the penetration depth [301]. However, as explained in the introduction, the experimental methods commonly used to study these processes such as microscopic techniques [301], [385], grinding the paper layer-by-layer [386], Drop adsorption [17], [19] or Ultrasonic Liquid penetration [17], [18] are unable to measure dynamic processes with spatial resolution required to obtain crucial information. Therefore, a complete picture of the particle transport dynamics is missing. Within this thesis, it has been shown that Ultra Fast Imaging UFI NMR as explained in chapter 4 is able to measure spatial resolved information for both particle transport (chapter 5 and 6) and liquid transport in paper sheets (chapter 7 and 8). Therefore, the technique should also be able to measure particle transport within paper sheets.

The goal of this chapter is to demonstrate how UFI can measure the penetration of a model ink within a paper sheet and to get a better understanding on the penetration of a polystyrene latex particle suspensions in hydrophilic uncoated paper. This is studied by performing penetration experiments on hydrophilic uncoated paper sheets with particle suspensions having varying particle concentrations.

First, Ultra Fast Imaging NMR signal profiles during penetration of the varying suspensions are analyzed. Secondly, the profiles will be used to gain information about the influence of particles on liquid penetration and swelling. Finally, the particle penetration depth is discussed.

## 9.2 Materials and methods

In this chapter, penetration experiments are performed on a non-coated hydrophilic C00H00 paper sheets as described in chapter 7.2.1. For liquid, the particle suspensions discussed in chapter 5, see Table 5.2, are taken. These suspensions contain 70 wt% of glycerol and a varying latex particle concentration of 0 (G70P0), 1 (G70P1), 2 (G70P2), 3 (G70P3), 5 (G70P5), and 8 (G70P8) wt%. Droplets are jetted on top of the paper sample. From the moment the droplet contacts the paper, UFI is used to measure the signal profiles during penetration. A detailed description of the experiment is given in chapter 4.4.5, Figure 4.7.

## 9.3 UFI signal profiles during capillary uptake

The goal of this section is to demonstrate how particles influence the UFI signal profiles measured during penetration. This section starts by showing the signal profiles within

the paper sheets. Because all particle solutions resulted in similar signal profiles, the discussion is limited to signal profiles measured for the G70P0 and G70P8 liquid.

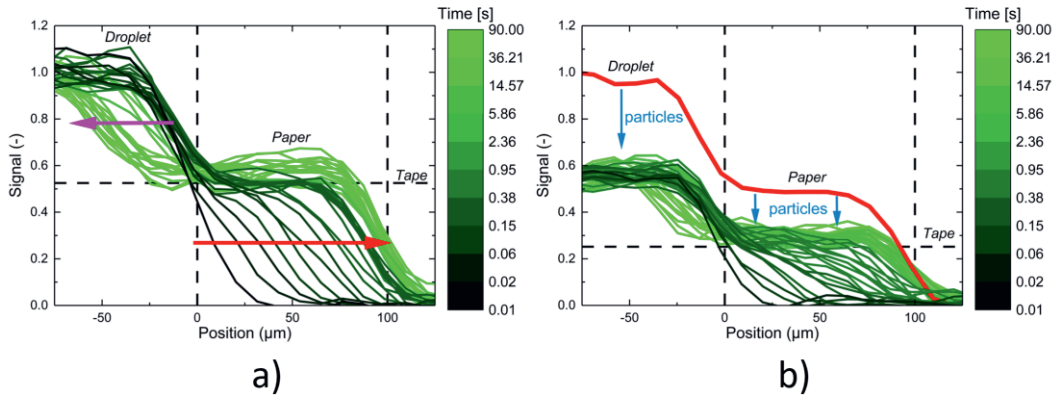


*Figure 9.1 UFI-signal profiles measured during the penetration of a suspensions containing 70 wt% of glycerol and a) 0 or b) 8 wt% of particles. The red line in b is added as comparison and shows a UFI profile of a filled C00H00 paper at  $t = 0.86$  s with a suspension containing no particles (G70P0) as shown in a. The blue arrow indicates changes which arise by the addition of particles.*

Figure 9.1 shows the UFI signal profiles measured during the penetration of the reference liquid G70P0 without particles (a) and of the G70P8 suspension with 8 wt% of particles (b). In both figures, an identical scale is used to mark the time at which the profiles are measured. For the reference liquid, the profiles are similar to the once found in chapter 7, Figure 7.4 for a for Clariscan-water mixture without glycerol. In these profiles, liquid penetration (red arrow) and swelling (purple arrow) can be observed. As explained earlier in this thesis, the profiles of Figure 9.1b provide information about penetration speed, by looking at the front position, and the particle position and concentration, by looking at the relative signal compared to the reference liquid. In case, particles are introduced, Figure 9.1b, the signal intensity becomes a function of both the total moisture content  $\rho$ , and the particle concentration  $C$ , as given by equation (5.1).

When comparing the profiles of Figure 9.1a and Figure 9.1b, it can be seen that by adding particles, the penetration speed is lowered. Furthermore, the signal profiles during the penetration of a suspension containing 8 wt% of particles (Figure 9.1b) had similar shapes than the ones of a fluid without particles (Figure 9.1a). In chapter 5.4.2, it was shown that in this case, particles were able to penetrate the whole paper sheet while remaining homogeneously distributed throughout the fluid.

## 9.4 Influence of particles on liquid dynamics and swelling

In this chapter, the UFI profiles in chapter 9.3, are used to gain information about the effect of particles on liquid penetration and swelling, by extracting the fluid front positions and swelling through time. The liquid front positions were extracted from the UFI profiles at a signal intensity that corresponded to 50% of the maximum signal found within the paper, red arrow in Figure 9.1a as described in chapter 4.5.3. Figure 9.2a shows the liquid front as a function of time. The data shows that the liquid imbibition

speed slows down when the particle concentration increases. It follows from Table 5.2, that particles alter the viscosity and surface tension of the suspensions. To investigate if these changes are responsible for the decreased penetration speed, time is rescaled by  $\sqrt{\sigma/\eta}\sqrt{t}$ , in line with eq. (4.10). The rescaled data is shown in Figure 9.2b and falls onto a master curve. This shows that liquid penetration can be described by Darcy's law, similar to what was observed within nylon-6,6 membranes as discussed in chapter 6.4.

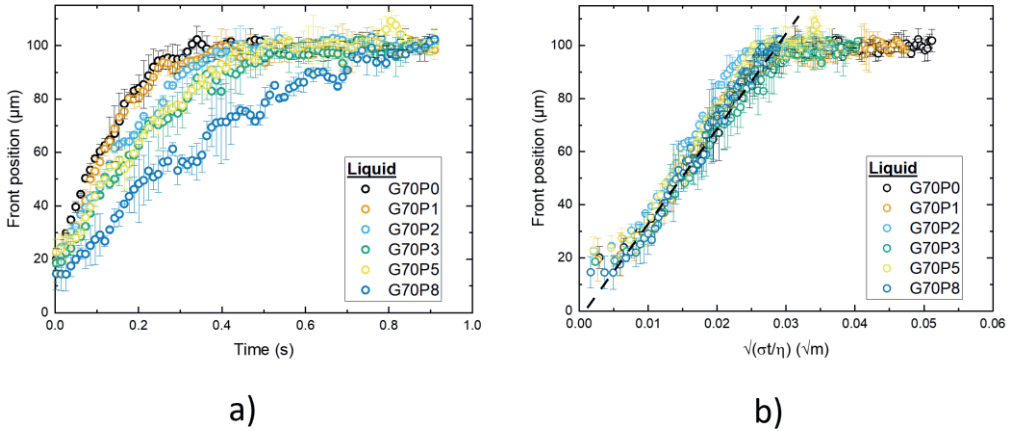


Figure 9.2 Liquid front positions ( $l$ ) as a function of a) time and b) rescaled time ( $\sqrt{\sigma/\eta}\sqrt{t}$ ) within a C00H00 paper during wetting with particle suspensions containing 70 wt% of glycerol and 0 wt% (black), 1 wt% (orange), 2 wt% (blue), 3 wt% (green), 5 wt% (yellow), and 8 wt% (blue). The black dotted line (b) is a guide to the eye.

Besides the liquid fronts, swelling can be monitored by extracting the paper thickness over time. The paper thicknesses are extracted in a similar manner than the front positions, but now at a signal that lies between 1 (the droplet) and the signal within the paper (fluid dependent), see purple arrow Figure 9.1a. Figure 9.3a depicts the swelling in percent as function of time while. It can be concluded that particles slow down swelling of the paper sheet. To investigate if the scaling, used for the liquid fronts, can explain the swelling behavior, a similar rescaling is performed. Figure 9.3a shows the swelling as function of  $\sqrt{\sigma/\eta}\sqrt{t}$ . Again, the rescaled data falls onto a master curve. This shows that swelling also obeys Darcy scaling.

## 9.5 Particle penetration depth

The goal of this section is to gain information about the particle concentrations within the paper sheet and see how this is affected by the initial particle concentration within the fluid. To gain information about the particle concentrations, the UFI signal profiles are analyzed and transferred to particle concentrations using the calibration curves of Figure 5.8, as described in chapter 5.9. For clarity, this will be done for the penetration of only 4 dispersions: the reference liquid with 0 wt% of particles and the liquids containing 2 wt%, 5 wt% and 8 wt% of particles. In the first part, the signal profiles of these experiments will be analyzed at two specific times: after liquid penetration ( $t = 0.9$  s), and second after the majority of swelling has happened ( $t = 80$  s). Thereafter,

the signal intensity within the paper sheets and within the droplet will be used for further analysis to determine the particle concentrations at these two time intervals.

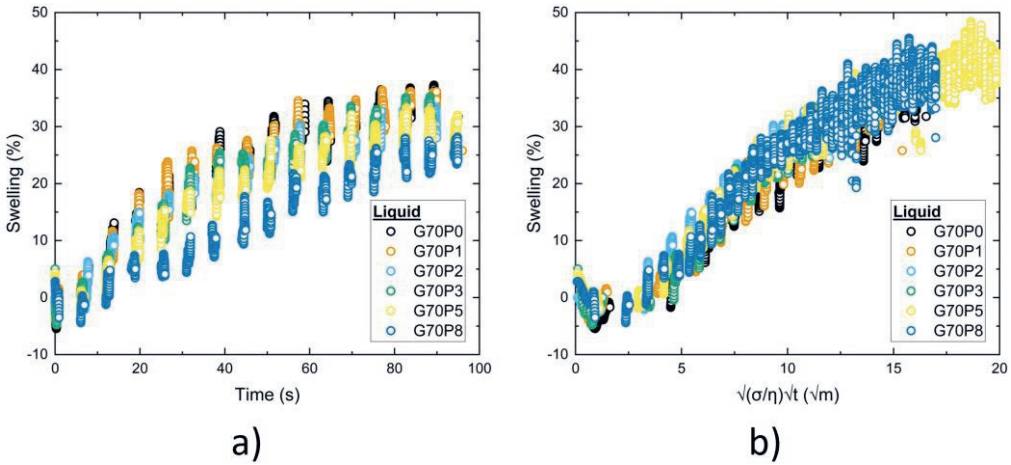


Figure 9.3 Swelling as a function of a) time and b)  $(\sqrt{\sigma/\eta}\sqrt{t})$  for C00H00 paper during wetting with particle suspensions containing 70 wt% of glycerol and 0 wt% (black), 1 wt% (orange), 2 wt% (blue), 3 wt% (green), 5 wt% (yellow), and 8 wt% (blue).

### 9.5.1. Signal profiles

Figure 9.4a shows the signal profiles after the paper has been wetted by the droplet for about 0.9 s. These profiles correspond to the situation where the liquid front has reached the end of the membrane for all particles suspensions (Figure 9.2a) and swelling was minimal (Figure 9.3). Figure 9.4b shows the signal profiles after the paper has been wetted by the droplet for about 85 s. In this case, the majority of swelling has happened. However, it should be noted that some minor swelling is still going on. In both figures, the signal for the reference liquid with 0 wt% of particles (black) and the liquids containing 2 wt% (orange), 5 wt% (blue) and 8 wt% (green) of particles are shown. For clearness, the droplet-membrane and paper-tape interface are marked with black dotted lines.

The major difference between both times is that at 80 s, the paper has swollen between 30 % and 35 %, which can be seen by the displacement of the droplet-paper interface from  $-5 \mu\text{m}$  in Figure 9.4a to  $-45 \mu\text{m}$  in Figure 9.4b.

Besides this swelling effect, the profiles are quite similar. At both times, increasing the particle concentration drops the signal intensity in correspondence with the calibration curve in Figure 5.8. Furthermore, the signal change is observed throughout the whole paper sheet, which as explained in chapter 5.4.2, shows that particles evenly distributed throughout the measurement area. Therefore, it can be concluded that differently to the nylon-6,6 membranes shown in chapter 6.3, during liquid penetration and swelling, no particle accumulation takes place and particles are able to penetrate the whole paper sheet. It is believed that this difference in particle penetration can be explained by the huge difference in pore radius between the paper sheets ( $2.8 \mu\text{m}$ ) and the nylon membranes ( $0.53 \mu\text{m}$ ).



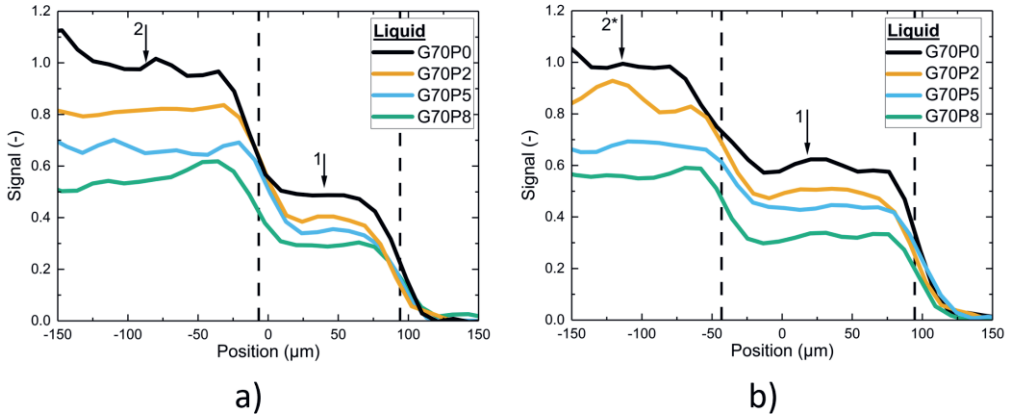


Figure 9.4 UFI signal profiles measured at a) 0.9 s and b) 80 s for a particle suspensions containing 70 wt% glycerol and 0 wt% (black), 2 wt% (orange), 5 wt% (blue) and 8 wt% (green) of particles.

### 9.5.2. Particle concentration inside the paper sheet

In this section, the profiles shown in Figure 9.4 are used to extract information about the particle concentrations within the paper sheets after liquid front penetration (0.9 s) and after swelling (80 s). Figure 9.5 shows the signal intensities as function of the liquids initial particle concentration at 0.9 s (circles) and at 80 s (squares). For both times, the signal is given within the droplet (black) and within the paper sheet (orange). The black line is the calibration curve for the signal as function of the particle concentration as given in chapter 5.8.3, Figure 5.8, used to determine the particle concentration within a solution. To use the particle calibration curve within a porous media, the calibration curve should be rescaled with porosity in correspondence with eq. (5.3). Because the porosity of a paper sheet during wetting is time dependent as described in chapter 7.4, the calibration curve should be determined for both times separately. To correct the calibration curve with the porosity of the paper sheet at a specific time, the black calibration curve is rescaled using the signal intensity for the solution containing no particles, where porosity should be the only effect on signal intensity. These rescaled calibration curves are given at 0.9 s (orange dashed line) and at 80 s (orange dotted line).

The data points within the droplet are independent of time and lie on top of the calibration curve. This shows that the particle concentration within the droplet stays constant through time and equal to the initial concentration of the liquid.

Within the paper sheets, the signal increases slightly over time which can be attributed an increase in the porosity linked to swelling of the paper media as discussed in chapter 7.4.2. However, the signal within the paper sheet lies on top of the rescaled calibration curve. This indicates that the difference in signal can be totally attributed to changes in the porosity and that the particle concentrations within the paper sheet are equal to the ones found within the droplet.

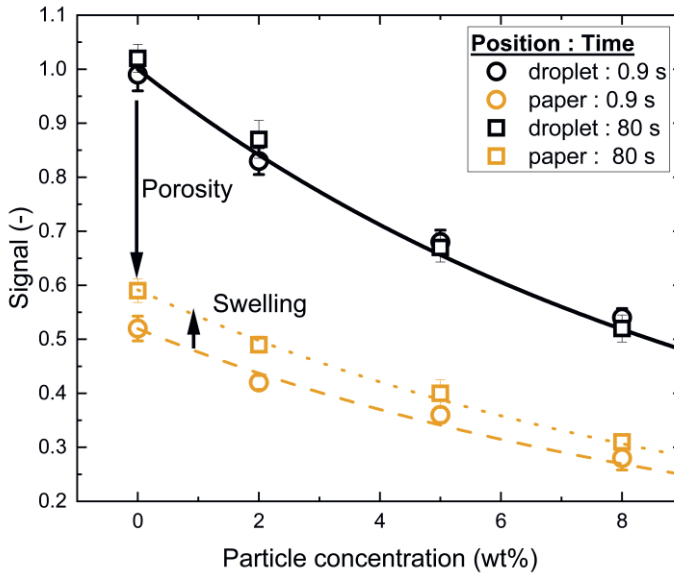


Figure 9.5 Signal intensities measured as a function of the liquids particle concentration within the droplet (black) and within the paper (orange). The signals are given for two specific times after wetting: 0.9 s (circles) and 80 s (squares). Shown in lines are the calibration curves for a liquid solution (black) and the calibration curve as corrected for the papers porosity (orange). The corrections are based on the signal intensities measured for a solution containing no particles, where porosity should be the only effect on signal intensity.

## 9.6 Conclusions

In this chapter, particle dynamics within hydrophilic non-coated paper has been studied. Experiments were performed with particle suspensions containing 70wt% of glycerol and particle concentrations between 0 and 8 wt%.

The experiments revealed that the penetration could be described by a Darcy model. The experiments showed that by increasing the particle concentration, the liquid penetration slows down. The decrease in penetration speed could be linked to changes within the viscosity and surface tension introduced by the particles.

Furthermore, it was shown that the particles were carried along with the suspensions and that they were homogeneously distributed throughout the medium. Furthermore, by looking at the signal intensity within the paper sheet, it was shown that a similar particle concentration existed within the droplet and membrane. This implies that particles are not hindered by sorption to the paper fibers and that particles can penetrate quite deeply within hydrophilic non-coated paper.



# 10

## Conclusions

---

The aim of this study was to develop an NMR-based method to study penetration of complex particle suspensions in thin, porous media, with a primary goal of advancing our understanding of liquid transport, particle transport, and deformations in porous media. These processes are key features in printing and define the final print density, gloss, sharpness, and quality of the print. In this thesis, penetration of complex mixtures within unsaturated membrane filters and paper sheets were measured using an NMR-based method which simultaneously determined the moisture profile, particle concentrations and paper thickness. The main conclusions of this work are summarized in this chapter.

***"For the first time, ink penetration could be monitored with NMR in real time."***

With this study, significant progress in NMR imaging of ink was achieved by developing an Ultra-Fast Imaging (UFI) NMR method, which enhanced both the temporal and spatial resolution for NMR imaging, allowing visualization of capillary imbibition in thin, porous media such as polymer membranes and paper.

***"Darcy's Law correctly models penetration of liquids in thin, membrane layers."***

Studies on thin membrane layers revealed capillary driven front dynamics similar to large scale experiments, justifying models, such as Darcy. This implies that liquid propagated via a sharp capillary driven liquid front with dynamics linked to the viscosity and surface tension of the liquid mixture and the pore radius of the membrane.

It was revealed that latex particles impact ink droplet dynamics in unsaturated porous media. The particles affected the liquid imbibition and particles penetration depth. Both effects are described in the paragraphs below.

***"Darcy's Law correctly models the penetration dynamics of inks, containing typical latex particles with diameters of 80 nm, in paper, having micrometer sized pores, by taking into account the corrected viscosity and surface tension characteristic of the particle-laden mixture."***

Droplets containing particles penetrate similarly to other liquids. The penetration process can be described by laws such as Darcy, where variations in viscosity and surface tension, due to the presence of particles, change the liquid uptake dynamics. In the performed experiment, where particles had a diameter of 80 nm and the medium a pore radius of 500 nm, the penetration could be completely described by Darcy's Law. Thus,

it seems, that within these systems, changes in permeability due to the presence of particles are negligible.

***"For ink penetration in non-coated hydrophilic paper, with typical micrometer sized pore radii, the results reveal that particles, having a much smaller pore radii, follow the liquid phase and do not split from the liquid front."***

The absorption of latex particles during capillary suction was highly dependent on the pore radius of the medium. Particles absorb if the pore radius is small enough. In the systems used in this study, with a pore radius of about 500 nm and particle diameter of about 80 nm, the particle penetration depth depends on the particle concentration. Paper has a much larger pore radii ( $> 2 \mu\text{m}$ ), and, consequently particles did not absorb but instead penetrate throughout the full medium.

The results show that liquid transport in paper goes beyond simple models and strongly depends on the structure and chemical nature of the paper sheet. This study differentiated between three types of paper: 1) *Hydrophilic low calendered paper*, 2) *Hydrophilic high calendered paper* and 3) *Highly Hydrophobic paper*.

***"The study shows that liquid transport in hydrophilic paper is governed by capillary uptake and can be described by models such as Darcy. Further, the decrease in penetration speed due to calendering can be predicted using Darcy's law."***

In hydrophilic low calendered paper, water penetrates in three phases, occurring on three different timescales: capillary uptake (0 - 0.1 s), swelling of the paper sheet (0.1 - 30 s) and removal of entrapped air (0 - 3 h). In this case, absorption dynamics could be described by Darcy's Law. Due to the differences in timescales, capillary uptake was independent of swelling. The quantification of these timescales opens a door to more accurate and simplified models to describe ink penetration in paper.

In hydrophilic highly calendered paper, swelling can significantly influence the penetration process and cannot be neglected in penetration models. Because calendering reduces the porosity and pore radius, capillary uptake slows down. Due to this slower uptake dynamics, capillary uptake and swelling now appeared at similar timescales. Ergo, swelling should be included when modeling the fluid flow in these systems. Whereas Darcy's Law readily describes penetration in hydrophilic low-calendered paper, the model must be adjusted to include effects of swelling in the case of hydrophilic highly calendered paper.

***"In hydrophobic paper, water first wets the fibers which introduces a delay in the uptake process. The wetting period is followed by a finger-like filling of the pore spaces."***

In highly hydrophobic paper, where water cannot penetrate via capillary uptake, liquid penetration occurs in a fingering pattern. In this paper, fibers were first prewet by phenomena such as liquid vapor transport, film flow and intra-fiber flow water. This induced an initial swelling of the paper sheet linked to an increase in fiber thickness. Due to the wetting of the fibers, the surface becomes more hydrophilic, which eventually allows water to enter the inter-fiber pore space. This water intrusion breaks the fiber

---

bonds and initiates a second swelling phase. This complex process causes the water to follow heterogeneous paths and therefore no liquid front is observed.

The developed NMR technique makes it possible for the first time to monitor ink penetration in real time. These spatially resolved images provide significant information about ink penetration and the influence of the print media, ink composition and varying processes. The technique enables groundbreaking results in ink penetration dynamics which could lead to highly improved print quality, cost reductions and a reduction of the environmental impact required to meet the Net Zero Emission climate goals set by the European Union.



# 11

## Outlook

---

In this thesis an Ultra-Fast Imaging NMR method was developed to image liquid and particle redistributions in thin, porous media, such as paper or membrane filters. Although this technique has solved multiple questions, it also has opened a door for studying many topics that could not be studied before. The aim of this chapter is to discuss some of the important new questions and give recommendations for follow-up work.

### **11.1 Determining particle concentrations during penetration and swelling**

In this thesis, particle concentrations could be determined within membrane filters during penetration. In paper, particle concentrations were only determined at two fixed times: after penetration ( $t = 0.9$  s) and just after swelling ( $t = 80$  s), as the liquid contents are well defined at these moments, see chapter 9.

In chapter 7, it was shown that within paper, liquid uptake happened in multiple phases: front movement, swelling, and air removal. Therefore, the liquid content varies over time and is not well-defined. Consequently, it becomes hard to link signal changes to particle concentration only, leading to either an over or underestimated particle concentration.

To solve this problem, methods must be found enabling quantification of the particle concentrations during processes such as liquid uptake, swelling, and air entrapment. This will lead to a better interpretation of the signal intensities and a correct determination of the particle concentration. Because the contribution of these phases can depend on the medium and type of particle suspensions, future research should aim to quantify the contributions of all different phases for all particle suspensions and paper media, as was done in chapter 7, for a Clariscan-water in hydrophilic uncoated paper. After determining the contributions of the different phases such as air entrapment and swelling on the NMR signal intensity, the signal changes coming from particles can be extracted, which allows quantitative determination of the particle concentration during penetration and swelling.

### **11.2 Finding the relation between delay time and paper hydrophobization**

In chapter 8, it was shown that water first wets the fibers when it comes in contact with hydrophobized paper. The processes such as vapor transport, film flow and transport



through the fibers responsible for wetting continue until the fiber surface becomes sufficiently hydrophilic for water to enter the pores between the fibers. The time it takes for water to enter the pore spaces of a paper sample is characterized by a delay time, which is highly dependent on the level of hydrophobization (see chapter 8). However, an exact relation between the delay time and the level of hydrophobization has not been found. The delay time has been reported in other studies, yet the precise relationship remains ambiguous [38], [60], [387]. Multiple applications benefit from hydrophobized paper and their ability to resist moisture. Therefore, a relation between the delay time and the level of hydrophobization is very important. This relation would also help to identify the most important factors to control water repellency. This could lead to improved paper-based packaging materials and make them compete with plastic counter parts in for example the food industry [357], [358].

Future research could benefit from using UFI in determining the relationship between the delay time and parameters, such as contact angle, fiber density, and paper roughness.

Based on our research, future research could start by identifying the relation between the contact angle  $\theta$  and the delay time  $t_d$ . Because filling of the pore spaces can only occur with hydrophilic contact angles, we believe that the delay time is a function of the contact angle. This can be achieved by performing penetration experiments on a set of papers with varying levels of hydrophobicity and measure the delay time with UFI, as illustrate by the preliminary measurements shown in Figure 11.1. Thereafter, the contact angle on all the papers should be measured and linked to the measured delay times, in order to identify a possible relation.

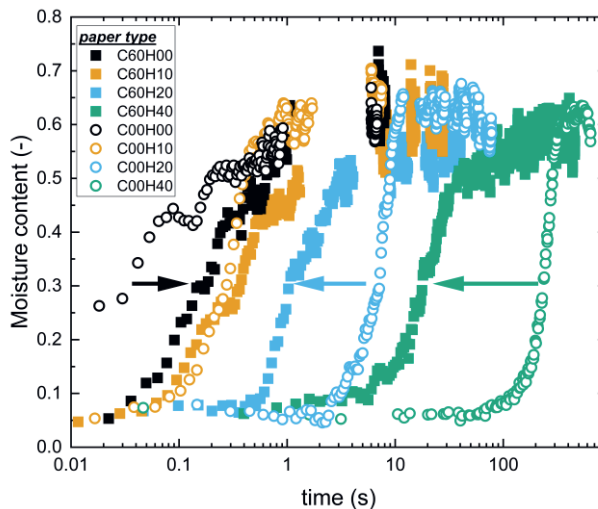


Figure 11.1 Moisture content measured in papers with varying levels of calendering (C) (~ fiber density) and varying levels of hydrophobization (H), for sample coding we refer to Table 8.1.

Figure 11.1 shows the moisture contents for a series of paper with two different calendering levels (fiber densities) and four levels of hydrophobization. Similarly to chapter 8, the paper hydrophobization was obtained by applying either 0 (H00), 10 (H10), 20 (H20), 40 ml (H40) of HDMS per 10 A4 sheets, whereas calendering was performed by compressing the sheets using a force of 0 (C00), or 60 (C60) kN. Heavily calendered C60 papers are shown in filled squares, while lowly calendered C00 papers are represented by open circles. The colors are used to mark different levels of hydrophobization. For both calendering forces (C00 and C60), hydrophobization slowed down liquid uptake and increased the observed delay time. However, as discussed in chapter 8, calendering slows down penetration in a hydrophilic C00H00 paper due the decrease in permeability, shown by a black arrow. However, the situation becomes different for higher levels of hydrophobization. In these papers calendering increased penetration speed (blue and green arrows). This implies that a higher fiber density slows down penetration in hydrophilic paper, but that the opposite is true for hydrophobic paper. This shows that within hydrophobic paper, fiber density plays a crucial role in the penetration process and that the delay is probably a function of the fiber density  $\phi_{fibers}$ .

Based on these findings, we believe that the delay time becomes a function of the contact angle and fiber density and therefore future research should start by identifying a relation of the following form,

$$t_d = f(\theta, \phi_{fibers}). \quad (6.3)$$

### 11.3 The effect of increasing substrate complexity

UFI can also be used for studying more complex substrates and ink compositions, that more closely resemble real applications and involve unexplored materials and ink parameters. Future research could aim to study dynamics of particle dispersions in modified substrates and more complex model inks using particle modifications. This section will discuss the effect of hydrophobized paper on liquid transport and particle transport, the effect of a coating layer and the effect of primers.

#### 11.3.1. Effect of particles on transport in hydrophobized paper

In chapter 9, it was shown that particles decrease the penetration speed within hydrophilic paper. Because penetration in hydrophobic paper is completely different, see Chapter 8, it is unclear how particles influence liquid penetration in hydrophobized paper. In hydrophobized paper, water repellency is an important feature, used in printing, packaging, microfluids and lab-on-chip devices. Consequently, it is crucial to understand how and if the particles change the water repellent nature of these papers. UFI is an ideal tool for studying this process, by measuring the penetration of various particle dispersions in hydrophobic paper.

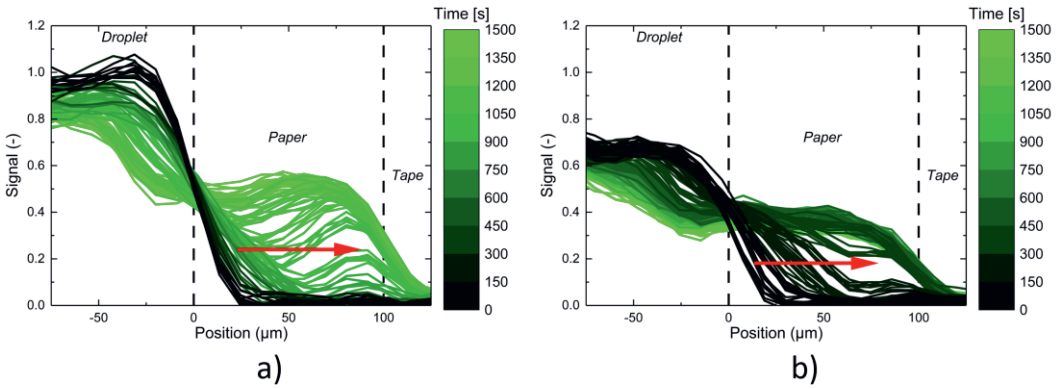


Figure 11.2 Signal profiles during penetration of a liquid containing 70 wt% of glycerol with a) 0 wt% and b) 5 wt% of particles within a hydrophobic C00H40 paper. In both figures, a similar green scale is used to identify the time at which the profiles are taken. Red arrows are used to identify the direction of penetration.

Figure 11.2 shows some preliminary results measured on the penetration of a reference liquid G70P0 (a) and a liquid containing 5 wt% of particles (b) within a hydrophobized C00H40 paper, for details the reader is referred to chapter 8. The data shows that adding particles increases the penetration speed and that the penetration changes from a non-front-like behavior to a more front-like behavior. In both figures, a similar scale is used to identify the time at which the signal profile is taken. Using these profiles, the signal in the paper can be measured through time. Figure 11.3 shows the integrated signal intensity between 25 – 75 μm as a function of time for G70P0 (black) and G70P5 (orange).

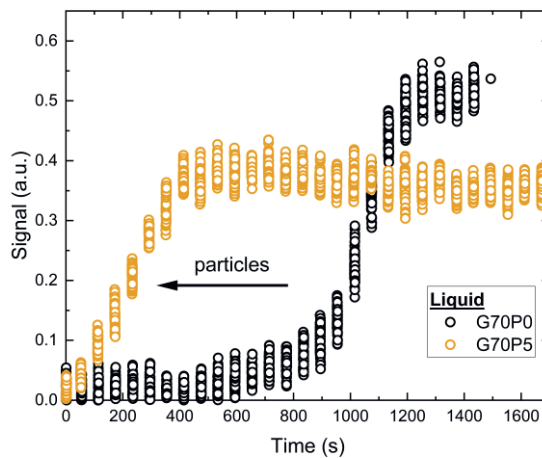


Figure 11.3 Integrated signal as a function of time for the penetration of a G70P0 (black) liquid and a G70P5 (orange) liquid penetration inside a hydrophobic C00H40 paper.

In hydrophobic paper, particles increase penetration speed. A possible reason for this behavior lies in a lowering of the relative contact angle when introducing particles into the suspension. This lower contact angle will increase the penetration speed and increase the capillary nature of the penetration process, as can be seen the more front like behavior in the liquid profiles in Figure 11.2b.

However, a comprehensive investigation is needed to understand this behavior. Research should start by measuring the penetration of model inks containing varying particle concentrations. These measurements can be utilized to establish a relationship between penetration speed and particle concentration. Subsequently, this relation should be linked to physical parameters such as the contact angle, surface tension and viscosity induced by the particles.

### 11.3.2. Effect of hydrophobicity on particle transport

Chapter 8 shows that the penetration of liquid within hydrophobic paper deviates from penetration in hydrophilic paper. Therefore, the question arises: how do particles penetrate within hydrophobic paper and what is the final penetration depth? Particle penetration is probably most important as it determines the final print quality.

The signal profiles of Figure 11.2 can provide some preliminary results about particle transport and particle penetration depth by studying the signal intensity. Figure 11.4a shows the signal through time for the penetration of a particle suspension containing 5 wt% of particles within a hydrophobic (black) and hydrophilic paper (orange). Figure 11.4b shows the signal profiles of a hydrophobic (black) and hydrophilic paper (orange) after the droplet has penetrated and swelling was completed. For the hydrophobic paper, this corresponds to a time of 800 s, whereas for the hydrophilic paper this corresponds to a time of 60 s. Both times are marked with an arrow in Figure 11.4a.

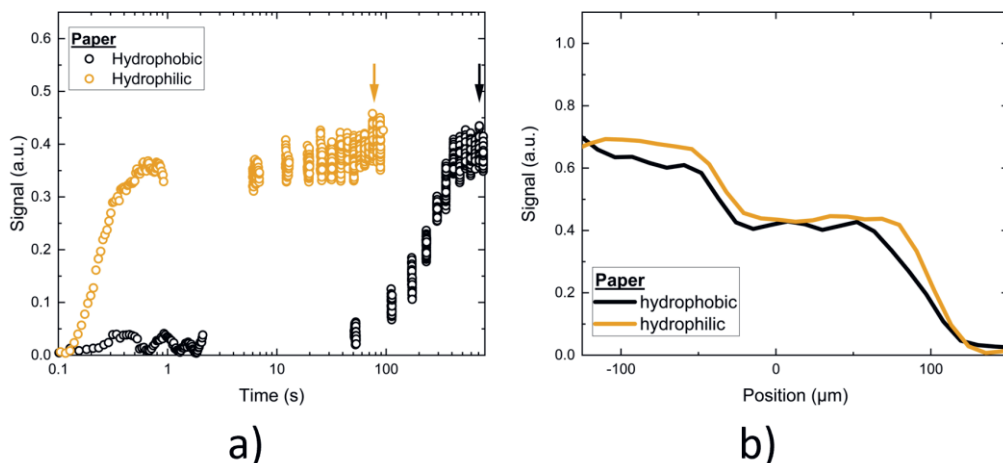


Figure 11.4 Signal intensity comparison between the penetration of a particle suspension containing 5 wt% of particles and 70 wt% of glycerol within a hydrophilic (orange) and hydrophobic paper (paper). Shown are the signal intensity profiles after the penetration is finished (a) and the signal intensity as a function of time (b).

Figure 11.4a, shows that the hydrophilic and hydrophobic case end up with a similar signal intensity. This can also be seen when looking at the signal profiles in Figure 11.4b, which show almost identical profiles. This indicates that both papers end up with a similar end situation. This situation was explained in chapter 9, and corresponds to a homogeneously distribution of the particles throughout the medium. Although the final signal is quite similar, the processes are quite different. In hydrophilic paper, the signal rises almost directly to 0.4, while in hydrophobic paper, a delay time is observed. If sufficient liquid is available to fill the entire pore space, both systems end up in a similar situation.

Future research should aim to understand the processes that lead to these final situations, where the paper is homogeneously filled with latex particles. The study can start by measuring the penetration of model inks having varying particle concentrations. This will help to determine if particles are still homogeneously distributed when fewer particles are available within the ink droplet. Additionally, the effect of drop size can be investigated by performing penetration experiments with ink droplets having different volumes. By decreasing the drop size, the importance of evaporation increases. In the case of hydrophobic paper, which exhibits a significant delay time, we expect that the competition between evaporation and penetration becomes important in small droplets, which can lead to changes in particle penetration depths upon chemical modification of the paper surface [388], [389].

### 11.3.3. The influence of a coating layer on liquid penetration

A coating layer increases the complexity of the porous system and influences the transport of water and particles [32], [82], [390], [391]. The coating layer, having a small pore radius (0.05–0.5  $\mu\text{m}$ ), traps particles. How liquid transports through this layer and how its affected by the porous layer is still unclear. Many applications benefit from coating layers. In printing, coatings are used to prevent deep penetration within the fibrous layer and increase print quality. Furthermore, coated paper is an example of a multi-layer porous system. Characterizing transport in these systems provides relevant modeling tools for all sorts of multi-layer systems with are relevant in biological/chemical protection or desalination. Therefore, UFI can provide valuable information within these systems.

It would be beneficial to visualize the coating layer during a UFI measurement. Figure 11.5 shows some preliminary measurements of a coated paper. Figure 11.5a shows the measured profiles while Figure 11.5b gives swelling as a function of liquid front position. In the profiles, a red arrow is used to mark a signal decrease within the profiles that correspond to the position of the coating layer. To make this coating layer visible, the pulse sequence was adjusted. Because the coating layer was about 10  $\mu\text{m}$  thick, the resolution was increased by setting the window width and echo time to 100  $\mu\text{s}$  and 90  $\mu\text{s}$ , resulting in a theoretical resolution about 6  $\mu\text{m}$ . Because the signal intensity of the echoes depends on the echo time, and the echo time was doubled, now only 16 echoes were used to make UFI profiles instead of the normal 32 used throughout this thesis. Finally, the delay time was set to 0.050 seconds.

The reason for the intensity decrease should be investigated in more detail but is probably due to a lower porosity of the coating layer compared to the base material. The measurements presented in this chapter clearly show that coating layers can be

made visible and that investigation on coated materials can benefit from UFI measurements. Future research should start by characterizing the signal changes found within the coating layer, as seen in Figure 11.5a. Thereafter, penetration studies should be performed on coating paper with variations in coating thickness and porosity in order to reveal the effect of coating parameters on liquid and particle penetration.

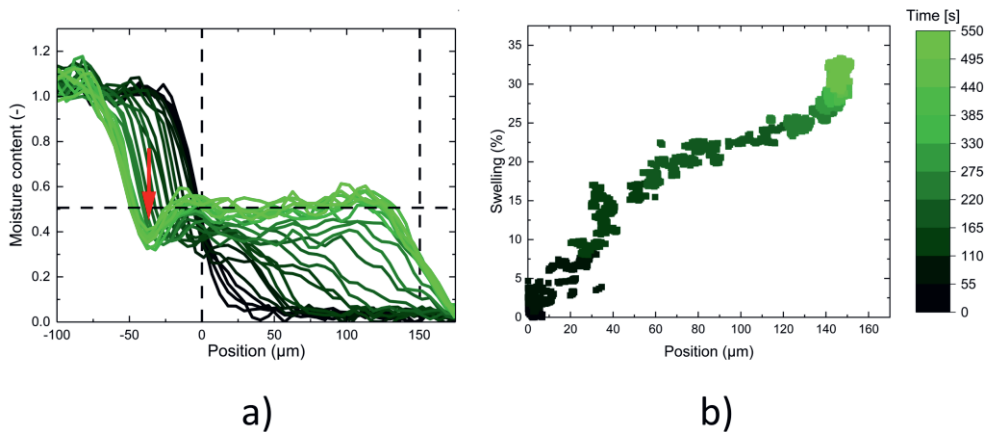


Figure 11.5 Liquid penetration experiments with a Clariscan-water solution in a coated paper, showing (a) profiles and (b) swelling as a function of liquid front position. In both graphs, a color scale is used to identify the time of the data point.

#### 11.3.4. The effect of a primer on ink penetration

To enhance the adhesion between particles and substrates, primers are widely used in inkjet printing and packaging materials [82], [392], [393]. A primer is a type of coating, to enhance the interactions between substrate and ink aiming to improve print quality. Think of divalent ions, that bind latex particles by complexation. A good primer keeps the ink particles near the surface by fixating the pigment particles. This fixation minimizes the amount of particles that are absorbed by the medium, helps to control dot size, and increases the resistivity against rubbing. This helps to reduce costs and climate impact and allows more robust packages. For water-based inks, which can contain 90 - 95 % of liquid, primers also enable faster drying, which increases the production speed. Another task of primers, is to minimize curl, which can result in printing damage as the medium does not fit through the printer.

UFI can play a crucial role in studying the effects of a primer upon the printing process by imaging particles during liquid uptake and swelling with high spatial and temporal resolution. Studying the transport of particle suspensions in paper with and without primers can reveal effects of primers on liquid penetration and particle transport. Performing penetration experiments with varying primer types can reveal if models such as Dary and Washburn are still able to predict liquid and particle or if adjustments are needed.

## 11.4 The effect of particle properties on ink penetration

Chapter 6 demonstrated the correlation between particle concentration and penetration depth. Since particles pose significant environmental concerns within ink, lowering particle content by controlling particle deposition is of great importance. UFI facilitates significant scientific progress in studying the impact of particle modifications on ink penetration with minimal effort. Future research should prioritize investigating particle modifications, such as particle size, glass transition temperature ( $t_g$ ) and charge, with UFI and provide handling tools for particle deposition control. The following sections offer recommendations for future research, beginning with what we consider to be the most crucial modification.

### 11.4.1. Clarifying the influence of multi-sized particles on ink penetration

Inks are composed of multiple particles such as pigment particles and resins like latex. Therefore, it is beneficial to study the penetration of systems with multiple particle sizes.

Latex particles with varying sizes can easily be produced [394]–[396]. Consequently, studies should focus on investigating if inks with varying latex particles sizes allow for an improved print quality. UFI experiments on the penetration of these model inks within various systems can provide insight into the effect of these particle variations on particle penetration depth and fluid penetration.

Research should start with well-defined membranes, such as nylon membranes. This allows for studying the effect of multiple particle sizes while minimizing factors like swelling or air entrapment. We propose to start with the simplest case, using two particle sizes, a small and larger one. Additionally, two model inks should be prepared: one with labelling for small particles and another for large particles. This enables to perform experiments focused on tracking a single particle. Due to the limitations in UFI, which tracks particles using a single signal intensity, simultaneously tracking both particles is not possible. By combining the results, data can reveal information about the individual movement of the small and large particles.

### 11.4.2. The effect of glass transition temperature on ink penetration

In water-based inks, latex particles are used to fixate the pigment particles. Depending on the glass transition temperature of these particles, film formation can occur. How film formation effects particle deposition is still unclear.

In this study, the glass transition temperature  $t_g$  of the latex is about 100 °C, preventing film formation and leaving individual particles visible, see Figure 11.6, which shows a SEM image of a the edge of a dried droplet on top of a PVDF membrane filter.

Future research should investigate the effects of the glass transition temperature and film formation on particle deposition, as this provides an easy to modify handling tool for controlling ink deposition. This can be achieved by performing penetration experiments with model inks containing latex particles having varying glass transition temperatures, which can be achieved by adjusting the particles composition [382], [397]–[399].

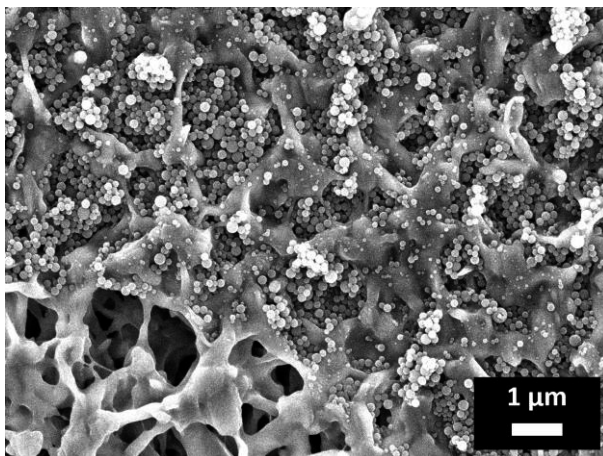


*Figure 11.6 SEM image of a PVDF membrane filter after the imbibition and drying of a droplet containing 5 wt % of Latex Particles tagged with iron oxide.*

#### 11.4.3. The effect of surface charge on ink penetration

Charges are used to stabilize latex particles in ink, by introducing repulsive forces between the particles [110], [400], and adjust ink transport in paper [82]. Decreasing the surface charge density decreases these repulsive forces. This leads to coagulation of the particles, increasing the effective particle size. This can induce particle clogging which keeps particles closer to the surface. UFI NMR would be an ideal tool to study this behavior. Ultimately, when the effect of surface charge on the penetration process is known, it could provide handles to optimize print quality and decrease particle usage.





# References

- [1] M. Singh, H. M. Haverinen, P. Dhagat, and G. E. Jabbour, "Inkjet Printing-Process and Its Applications," *Adv. Mater.*, vol. 22, no. 6, pp. 673–685, 2010, doi: 10.1002/adma.200901141.
- [2] N. Yousefi Shiviyari, M. Tajvidi, D. W. Bousfield, and D. J. Gardner, "Production and Characterization of Laminates of Paper and Cellulose Nanofibrils," *ACS Appl. Mater. Interfaces*, vol. 8, no. 38, pp. 25520–25528, Sep. 2016, doi: 10.1021/ACSAMI.6B07655/ASSET/IMAGES/LARGE/AM-2016-076554\_0008.JPEG.
- [3] R. Göttinger, M. Hill, S. Schabel, and J. Schneider, "Glass-paper-laminates: examination of manufacturing methods, properties and discussion of potentials," *Glas. Struct. Eng.*, vol. 6, no. 1, pp. 119–128, Mar. 2021, doi: 10.1007/S40940-020-00144-4/FIGURES/6.
- [4] M. Aktas, N. Kiziltoprak, I. Avci, and J. Schneider, "Bearing-strength of paper laminates in single bolt connections," 2022, doi: 10.1016/j.conbuildmat.2022.126462.
- [5] D. Foti *et al.*, "Microstructure and compressive strength of gypsum-bonded composites with papers, paperboards and Tetra Pak recycled materials," doi: 10.1186/s10086-019-1821-5.
- [6] C. Cai *et al.*, "Ultralight Programmable Bioinspired Aerogels with an Integrated Multifunctional Surface for Self-Cleaning, Oil Absorption, and Thermal Insulation via Coassembly," *Cite This ACS Appl. Mater. Interfaces*, vol. 12, pp. 11273–11286, 2020, doi: 10.1021/acsami.0c00308.
- [7] William T. Tze and Douglas J. Gardner, "Swelling of recycled wood pulp fibers: Effect on hydroxyl availability and surface chemistry | Request PDF," *Wood Fiber Sci.*, vol. 33, no. 3, pp. 364–376, 2001, Accessed: Aug. 22, 2023. [Online]. Available: [https://www.researchgate.net/publication/287495991\\_Swelling\\_of\\_recycled\\_wood\\_pulp\\_fibers\\_Effect\\_on\\_hydroxyl\\_availability\\_and\\_surface\\_chemistry](https://www.researchgate.net/publication/287495991_Swelling_of_recycled_wood_pulp_fibers_Effect_on_hydroxyl_availability_and_surface_chemistry).
- [8] E. Letková, M. Letko, and M. Vrška, "Influence of recycling and temperature on the swelling ability of paper," *Chem. Pap.*, vol. 65, no. 6, pp. 822–828, Dec. 2011, doi: 10.2478/S11696-011-0089-Z.
- [9] S. Kopacic, A. Walz, A. Zankel, E. Leitner, and W. Bauer, "Alginate and chitosan as a functional barrier for paper-based packaging materials," *Coatings*, vol. 8, no. 7, Apr. 2018, doi: 10.3390/COATINGS8070235.
- [10] J. Alamán, R. Alicante, J. I. Peña, and C. Sánchez-Somolinos, "Inkjet Printing of Functional Materials for Optical and Photonic Applications," *Materials (Basel)*, vol. 9, no. 11, Nov. 2016, doi: 10.3390/MA9110910.
- [11] H. Siringhaus and T. Shimoda, "Inkjet Printing of Functional Materials," *MRS Bull.*, vol. 28, no. 11, pp. 802–804, Jan. 2003, doi: 10.1557/MRS2003.228/METRICS.
- [12] A. Elrahmani, R. I. Al-Raoush, H. Abugazia, and T. Seers, "Pore-scale simulation of fine particles migration in porous media using coupled CFD-DEM," *Powder Technol.*, vol. 398, p. 117130, Jan. 2022, doi: 10.1016/J.POWTEC.2022.117130.
- [13] Y. Zhou, L. Chen, Y. Gong, and S. Wang, "Pore-Scale Simulations of Particles Migration and Deposition in Porous Media Using LBM-DEM Coupling Method," *Process. 2021, Vol. 9, Page 465*, vol. 9, no. 3, p. 465, Mar. 2021, doi: 10.3390/PR9030465.
- [14] R. Masoodi and K. M. Pillai, "Darcy's law-based model for wicking in paper-like swelling porous media," *AICHE J.*, vol. 56, no. 9, pp. 2257–2267, Sep. 2010, doi: 10.1002/AIC.12163.
- [15] C. G. Van Der Sman, E. Bosco, and R. H. J. Peerlings, "A model for moisture-induced dimensional instability in printing paper," *Nord. Pulp Pap. Res. J.*, vol. 31, no. 4, pp. 676–683, Dec. 2016, doi: 10.3183/NPPRJ-2016-31-04-P676-683/MACHINEREADABLECITATION/RIS.
- [16] A. Geffert, O. Vacek, A. Jankech, J. Geffertová, and M. Milichovský, "Swelling of cellulosic porous materials - Mathematical description and verification," *BioResources*, vol. 12, no. 3, pp. 5017–5030, Aug. 2017, doi: 10.15376/BIORES.12.3.5017-5030.
- [17] C. Waldner, A. Mayrhofer, and U. Hirn, "Measuring liquid penetration in thin, porous sheets with ultrasound and drop absorption – scope and limitations," *Colloids Surfaces A Physicochem. Eng. Asp.*, vol. 650, p. 129551, Oct. 2022, doi: 10.1016/J.COLSURFA.2022.129551.
- [18] C. Waldner and U. Hirn, "Ultrasonic Liquid Penetration Measurement in Thin Sheets—Physical Mechanisms and Interpretation," *Mater. 2020, Vol. 13, Page 2754*, vol. 13, no. 12, p. 2754, Jun. 2020, doi: 10.3390/MA13122754.
- [19] X. Chen, J. Chen, X. Ouyang, Y. Song, R. Xu, and P. Jiang, "Water Droplet Spreading and Wicking on Nanostructured Surfaces," *Langmuir*, vol. 33, no. 27, pp. 6701–6707, Jul. 2017, doi: 10.1021/ACS.LANGMUIR.7B01223/ASSET/IMAGES/LARGE/LA-2017-01223S\_0010.JPEG.
- [20] S. Akinli-Kogak, "THE INFLUENCE OF FIBER SWELLING ON PAPER WETTING," 1997.
- [21] H. Ramada, D. W. Bousfield, and W. T. Luu, "The absorption mechanism of aqueous and solvent inks into synthetic nonwoven fabrics," *Int. Conf. Digit. Print. Technol.*, pp. 549–552, 2008, doi: 10.2352/j.imagingsci.technol.2009.53.5.050201.
- [22] S. Gruener and P. Huber, "Capillarity-Driven Oil Flow in Nanopores: Darcy Scale Analysis of Lucas–Washburn Imbibition Dynamics," *Transp. Porous Media*, vol. 126, no. 3, pp. 599–614, 2019, doi: 10.1007/s11242-018-1133-z.
- [23] C. J. Kuijpers, T. A. P. van Stiphout, H. P. Huinink, N. Tomozeiu, S. J. F. Erich, and O. C. G. Adan, "Quantitative measurements of capillary absorption in thin porous media by the Automatic Scanning Absorptometer," *Chem. Eng. Sci.*, vol. 178, pp. 70–81, 2018, doi: 10.1016/j.ces.2017.12.024.
- [24] R. J. K. Nicasy, H. P. Huinink, S. J. F. Erich, O. C. G. Adan, and N. Tomozeiu, "Ultra Fast Imaging NMR method for measuring fast transport processes in thin porous media," *Magn. Reson. Imaging*, vol. 103, pp. 61–74, Nov. 2023, doi: 10.1016/j.mri.2023.06.009.
- [25] R. Balamurugan, S. Sundarrajan, and S. Ramakrishna, "Recent Trends in Nanofibrous Membranes and Their Suitability for Air and Water Filtrations," *Membr. 2011, Vol. 1, Pages 232-248*, vol. 1, no. 3, pp. 232–248, Aug. 2011, doi: 10.3390/MEMBRANES1030232.

- [26] A. Benamar, N. D. Ahfir, H. Q. Wang, and A. Alem, "Particle transport in a saturated porous medium: Pore structure effects," *Comptes Rendus - Geosci.*, vol. 339, no. 10, pp. 674–681, Oct. 2007, doi: 10.1016/J.CRTE.2007.07.012.
- [27] T. Ikni, A. Benamar, M. Kadri, N. D. Ahfir, and H. Q. Wang, "Particle transport within water-saturated porous media: Effect of pore size on retention kinetics and size selection," *Comptes Rendus Geosci.*, vol. 345, no. 9–10, pp. 392–400, Sep. 2013, doi: 10.1016/J.CRTE.2013.09.001.
- [28] M. G. Wijburg, S. Wang, and A. A. Darhuber, "Transport and evaporation of aqueous co-solvent solutions in thin porous media," *Colloids Surfaces A Physicochem. Eng. Asp.*, vol. 656, p. 130268, Jan. 2023, doi: 10.1016/J.COLSURFA.2022.130268.
- [29] V. Murali, G. Venditti, J. C. H. Zeegers, and A. A. Darhuber, "Inkjet deposition of lines onto thin moving porous media - experiments and simulations," *Int. J. Heat Mass Transf.*, vol. 176, p. 121466, Sep. 2021, doi: 10.1016/J.IJHEATMASTRANSFER.2021.121466.
- [30] Y. Li and B. He, "Characterization of ink pigment penetration and distribution related to surface topography of paper using confocal laser scanning microscopy," *BioResources*, vol. 6, no. 3, pp. 2690–2702, 2011.
- [31] H. Aslannejad, H. Fathi, S. M. Hassanizadeh, A. Raoof, and N. Tomozeiu, "Movement of a liquid droplet within a fibrous layer: Direct pore-scale modeling and experimental observations," *Chem. Eng. Sci.*, vol. 191, pp. 78–86, Dec. 2018, doi: 10.1016/J.CES.2018.06.054.
- [32] H. Aslannejad, S. M. Hassanizadeh, and M. A. Celia, "Characterization of the Interface Between Coating and Fibrous Layers of Paper," *Transp. Porous Media*, vol. 127, no. 1, pp. 143–155, Mar. 2019, doi: 10.1007/S11242-018-1183-2/FIGURES/8.
- [33] N. Riefler, M. Ulrich, M. Morshäuser, and U. Fritsching, "Particle penetration in fiber filters," *Particuology*, vol. 40, pp. 70–79, Oct. 2018, doi: 10.1016/J.PARTIC.2017.11.008.
- [34] P. Heard, J. Preston, D. Parsons, J. Cox, and G. Allen, "Visualisation of the distribution of ink components in printed coated paper using focused ion beam techniques," *Physicochem. Eng. Asp.*, vol. 244, pp. 67–71, 2004, doi: 10.1016/j.colsurfa.2004.05.012.
- [35] T. Senden *et al.*, "Experimental imaging of fluid penetration into papers," 2007, Accessed: Jul. 24, 2023. [Online]. Available: [https://www.researchgate.net/publication/237837566\\_Experimental\\_imaging\\_of\\_fluid\\_penetration\\_into\\_papers](https://www.researchgate.net/publication/237837566_Experimental_imaging_of_fluid_penetration_into_papers).
- [36] M. M. Gong and D. Sinton, "Turning the Page: Advancing Paper-Based Microfluidics for Broad Diagnostic Application," *Chem. Rev.*, vol. 117, no. 12, pp. 8447–8480, Jun. 2017, doi: 10.1021/ACS.CHEMREV.7B00024.
- [37] S. Patari and P. S. Mahapatra, "Liquid Wicking in a Paper Strip: An Experimental and Numerical Study," *ACS Omega*, vol. 5, no. 36, pp. 22931–22939, 2020, doi: 10.1021/acsomega.0c02407.
- [38] P. Salminen, "Studies of water transport in paper during short contact times. Ph.D Thesis," Abo Akademi University, Turku, Finland, 1988.
- [39] C. Waldner and U. Hirn, "Modeling liquid penetration into porous materials based on substrate and liquid surface energies," *J. Colloid Interface Sci.*, vol. 640, pp. 445–455, Jun. 2023, doi: 10.1016/J.JCIS.2023.02.116.
- [40] C. J. Kuijpers, H. P. Huinink, N. Tomozeiu, S. J. F. Erich, and O. C. G. Adan, "Sorption of water-glycerol mixtures in porous Al2O3 studied with NMR imaging," *Chem. Eng. Sci.*, vol. 173, pp. 218–229, 2017, doi: 10.1016/j.ces.2017.07.035.
- [41] P. Bacchin, A. Marty, P. Duru, M. Meireles, and P. Aimar, "Colloidal surface interactions and membrane fouling: Investigations at pore scale," *Adv. Colloid Interface Sci.*, vol. 164, no. 1–2, pp. 2–11, May 2011, doi: 10.1016/J.CIS.2010.10.005.
- [42] N.-D. Ahfir, A. Hammadi, A. Alem, H. Wang, G. Le Bras, and T. Ouahbi, "Porous media grain size distribution and hydrodynamic forces effects on transport and deposition of suspended particles," 2016, doi: 10.1016/j.jes.2016.01.032.
- [43] P. Schmitz and J. M. Frey, "Particle transport and capture at the membrane surface in cross-flow microfiltration."
- [44] M. A. Mulla, H. N. Yow, H. Zhang, O. J. Cayre, and S. Biggs, *Colloid Particles in Ink Formulations*. John Wiley & Sons, Ltd, 2016.
- [45] M. Alava and K. Niskanen, "The physics of paper," *Prog. Phys. Rep. Prog. Phys.*, vol. 69, pp. 669–723, 2006, doi: 10.1088/0034-4885/69/3/R03.
- [46] J. Schoelkopf, P. A. C. Gane, C. J. Ridgway, and G. P. Matthews, "Practical observation of deviation from Lucas-Washburn scaling in porous media," *Colloids Surfaces A Physicochem. Eng. Asp.*, vol. 206, no. 1–3, pp. 445–454, Jul. 2002, doi: 10.1016/S0927-7757(02)00066-3.
- [47] S. Chang, J. Seo, S. Hong, D.-G. Lee, and W. Kim, "Dynamics of liquid imbibition through paper with intra-fibre pores," *J. Fluid Mech.*, vol. 845, pp. 36–50, 2018, doi: 10.1017/jfm.2018.235.
- [48] C. J. Ridgway, P. A. C. Gane, and J. Schoelkopf, "Effect of Capillary Element Aspect Ratio on the Dynamic Imbibition within Porous Networks," *J. Colloid Interface Sci.*, vol. 252, pp. 373–382, 2002, doi: 10.1006/jcis.2002.8468.
- [49] J. Schoelkopf, C. J. Ridgway, P. A. C. Gane, G. P. Matthews, and D. C. Spielmann, "Measurement and Network Modeling of Liquid Permeation into Compacted Mineral Blocks," *J. Colloid Interface Sci.*, vol. 227, pp. 119–131, 2000, doi: 10.1006/jcis.2000.6885.
- [50] E. N. De Azevedo, L. R. Alme, M. Engelsberg, J. O. Fossum, and P. Dommersnes, "Fluid imbibition in paper fibers: Precursor front," *Phys. Rev. E - Stat. Nonlinear, Soft Matter Phys.*, vol. 78, no. 6, p. 066317, Dec. 2008, doi: 10.1103/PHYSREVE.78.066317/FIGURES/5/MEDIUM.
- [51] S. Chang and W. Kim, "Dynamics of water imbibition through paper with swelling," *J. Fluid Mech.*, vol. 892, p. A39, 2020, doi: 10.1017/JFM.2020.219.
- [52] R. Masoodi and K. M. Pillai, "Darcy's law-based model for wicking in paper-like swelling porous media," *AICHE J.*, vol. 56, no. 9, pp. 2257–2267, 2010, doi: 10.1002/aic.12163.
- [53] J. F. Oliver, L. Agbezuge, and K. Woodcock, "A diffusion approach for modelling penetration of aqueous liquids into paper," *Colloids Surfaces A Physicochem. Eng. Asp.*, vol. 89, no. 2–3, pp. 213–226, Sep. 1994, doi: 10.1016/0927-7757(94)80120-7.
- [54] N. Wu, M. A. Hubbe, O. J. Rojas, and S. Park, "Permeation of Polyelectrolytes and other Solutes into the Pore Spaces of

- Water-Swollen Cellulose: A Review," *Bioresources*, vol. 4, no. 3, pp. 1222–1262, Aug. 2009, doi: 10.15376/BIORES.4.3.1222-1262.
- [55] K. T. Hodgson and J. C. Berg, "The effect of surfactants on wicking flow in fiber networks," *J. Colloid Interface Sci.*, vol. 121, no. 1, pp. 22–31, Jan. 1988, doi: 10.1016/0021-9797(88)90404-3.
- [56] R. Vallabh, J. Ducoste, A. F. Seyam, and P. Banks-Lee, "Modeling tortuosity in thin fibrous porous media using computational fluid dynamics," *J. Porous Media*, vol. 14, no. 9, pp. 791–804, 2011, doi: 10.1615/JPORMEDIA.V14.I9.40.
- [57] C. Waldner, A. Ritzer, and U. Hirn, "Modeling inkjet dots from drop spreading, absorption and evaporation—An engineering approach," 2023, doi: 10.1016/j.colsurfa.2023.131986.
- [58] D. Kannangara and W. Shen, "Roughness effects of cellulose and paper substrates on water drop impact and recoil," *Physicochem. Eng. Asp.*, vol. 330, pp. 151–160, 2008, doi: 10.1016/j.colsurfa.2008.07.056.
- [59] M. von Bahr, R. Seppanen, F. Tilberg, and B. Zhmud, "Dynamic wetting of AKD-sized papers," *J. Pul Pap. Sci.*, vol. 30, no. 3, pp. 74–81, Mar. 2004.
- [60] H. Modaressi and G. Garnier, "Mechanism of wetting and absorption of water droplets on sized paper: Effects of chemical and physical heterogeneity," *Langmuir*, vol. 18, no. 3, pp. 642–649, Feb. 2002, doi: 10.1021/LA0104931/ASSET/IMAGES/MEDIUM/LA0104931E00012.GIF.
- [61] A. Korpela, A. K. Jaiswal, and J. Asikainen, "Effects of Hydrophobic Sizing on Paper Dry and Wet-Strength Properties: A Comparative Study between AKD Sizing of NBSK Handsheets and Rosin Sizing of CTMP Handsheets," *BioResources*, vol. 16, no. 3, pp. 5350–5360, 2021, doi: 10.15376/BIORES.16.3.5350-5360.
- [62] X. Xie, F. Samsudeen, R. Farnood, M. T. Kortschot, and J. K. Spelt, "Roughening Due to Ink Jet Rewetting: Effect of Paper Treatment and Composition," *J. Imaging Sci.*, vol. 52, no. 1, pp. 10506-1-10506-7, Jan. 2008, doi: 10.2352/J.ImagingSci.Technol.(2008)52:1(010506).
- [63] U. Hirn and W. Bauer, "Calendering effects on coating pore structure and ink setting behavior."
- [64] P. Wulz, C. Waldner, S. Krainer, E. Kontturi, U. Hirn, and S. Spirk, "Surface hydrophobization of pulp fibers in paper sheets via gas phase reactions," *Int. J. Biol. Macromol.*, vol. 180, pp. 80–87, Jun. 2021, doi: 10.1016/J.IJBIOMAC.2021.03.049.
- [65] C. J. Kuijpers, H. P. Huinink, N. Tomozeiu, S. J. F. Erich, and O. C. G. Adan, "Nano-particle dynamics during capillary suction," *J. Colloid Interface Sci.*, vol. 521, pp. 69–80, Jul. 2018, doi: 10.1016/J.JCIS.2018.03.023.
- [66] T. Baumann and C. J. Werth, "Visualization of colloid transport through heterogeneous porous media using magnetic resonance imaging," *Physicochem. Eng. Asp.*, vol. 265, pp. 2–10, 2005, doi: 10.1016/j.colsurfa.2004.11.052.
- [67] E. O. Fridjonsson, S. L. Codd, and J. D. Seymour, "Application of PFG-NMR to Study the Impact of Colloidal Deposition on Hydrodynamic Dispersion in a Porous Medium," *Transp Porous Med*, vol. 103, pp. 117–130, 2014, doi: 10.1007/s11242-014-0290-y.
- [68] S. Krainer, C. Smit, and U. Hirn, "The effect of viscosity and surface tension on inkjet printed picoliter dots," *RSC Adv.*, vol. 9, no. 54, pp. 31708–31719, 2019, doi: 10.1039/c9ra04993b.
- [69] Robert C. Williams Museum of Papermaking, "The Invention of Paper," *Georgia Institute of Technology*. <https://paper.gatech.edu/early-papermaking> (accessed Aug. 21, 2023).
- [70] Dard Hunter, *Papermaking: the history and technique of an ancient craft*. New York: Dover Publications, 1978.
- [71] Christopher J. Biermann, *Handbook of Pulping and Papermaking*. Elsevier, 1996.
- [72] T. Barrett, "Enzymatic Pretreatment during 15 th to 18 th Century Papermaking in Europe," *BioResources*, vol. 11, no. 2, pp. 2964–2967, Accessed: Aug. 22, 2023. [Online]. Available: <http://paper.lib.uiowa.edu/european.php>.
- [73] B. Hubbe, M. A. Hubbe, and C. Bowden, "Handmade paper, review," *BioResources*, vol. 4, no. 4, pp. 1736–1792, 2009.
- [74] Timothy Barrett, "Paper through Time: Nondestructive Analysis of 14th- through 19th-Century PapersNo Title," *University of Iowa Libraries*, 2012. <https://paper.lib.uiowa.edu/european.php> (accessed Aug. 21, 2023).
- [75] W. M. Bundy and J. N. Ishley, "Kaolin in paper filling and coating," *Appl. Clay Sci.*, vol. 5, pp. 397–420, 1991.
- [76] T. Browne and R. Crotagino, "FUTURE DIRECTIONS IN CALENDERING RESEARCH," *BioResources*, pp. 1001–1036, 2018, doi: 10.15376/FRC.2001.2.1001.
- [77] P. Vernhes, M. Dubé, and J.-F. Bloch, "Effect of calendering on paper surface properties," *Appl. Surf. Sci.*, vol. 256, pp. 6923–6927, 2010, doi: 10.1016/j.apsusc.2010.05.004.
- [78] P. Samyn, "Wetting and hydrophobic modification of cellulose surfaces for paper applications," *J. Mater. Sci.*, vol. 48, no. 19, pp. 6455–6498, Jun. 2013, doi: 10.1007/S10853-013-7519-Y.
- [79] S. Kumar, V. S. Chauhan, and S. K. Chakrabarti, "Separation and analysis techniques for bound and unbound alkyl ketene dimer (AKD) in paper: A review," 2012, doi: 10.1016/j.arabjc.2012.04.019.
- [80] H. Kipphan, *Handbook of Print Media*, 1st ed. Springer Berlin, Heidelberg, 2001.
- [81] F. Rees, *Johannes Gutenberg: inventor of the printing press*. Minneapolis: Compass Point Books, 2006.
- [82] T. T. Lamminmäki, J. P. Kettle, and P. A. C. Gane, "Absorption and adsorption of dye-based inkjet inks by coating layer components and the implications for print quality," *Colloids Surfaces A Physicochem. Eng. Asp.*, vol. 380, no. 1–3, pp. 79–88, May 2011, doi: 10.1016/J.COLSURFA.2011.02.015.
- [83] Jiri George Drobny, "Applications of Fluoropolymer Films," *Appl. Fluoropolymer Film.*, 2020, doi: 10.1016/C2017-0-04740-7.
- [84] A.-L. Anderson, S. Chen, L. Romero, I. Top, and R. Binions, "Thin Films for Advanced Glazing Applications," *Build. 2016*, Vol. 6, Page 37, vol. 6, no. 3, p. 37, Sep. 2016, doi: 10.3390/BUILDINGS6030037.
- [85] J. P. B. Silva, K. C. Sekhar, H. Pan, J. L. MacManus-Driscoll, and M. Pereira, "Advances in Dielectric Thin Films for Energy Storage Applications, Revealing the Promise of Group IV Binary Oxides," *ACS Energy Lett.*, vol. 6, pp. 2208–2217, 2021, doi: 10.1021/ACSENERGYLETT.1C00313.
- [86] Z. Pan *et al.*, "Substantially improved energy storage capability of ferroelectric thin films for application in high-temperature capacitors," *J. Mater. Chem. A*, vol. 9, no. 14, pp. 9281–9290, Apr. 2021, doi: 10.1039/D0TA08335F.

- [87] N. S. Gü *et al.*, "Real-time evaluation of thin film drying kinetics using an advanced, multi-probe optical setup †," *J. Mater. Chem. C*, vol. 4, p. 2178, 2018, doi: 10.1039/c5tc03448e.
- [88] C. Schaefer, J. J. Michels, and P. van der Schoot, "Dynamic Surface Enrichment in Drying Thin-Film Binary Polymer Solutions," *Macromolecules*, vol. 50, no. 15, pp. 5914–5919, Aug. 2017, doi: 10.1021/ACS.MACROMOL.7B01224.
- [89] B. Blumich, F. Casanova, J. Perlo, F. Presciutti, C. Anselmi, and B. Doherty, "Noninvasive Testing of Art and Cultural Heritage by Mobile NMR†," *Acc. Chem. Res.*, vol. 43, no. 6, pp. 761–770, Jun. 2010, doi: 10.1021/AR900277H.
- [90] C. Rehorn and B. Blümich, "Cultural Heritage Studies with Mobile NMR," *Angew. Chemie - Int. Ed.*, vol. 57, no. 25, pp. 7304–7312, Jun. 2018, doi: 10.1002/ANIE.201713009.
- [91] S. Gupta, W. T. Navaraj, L. Lorenzelli, and R. Dahiya, "Ultra-thin chips for high-performance flexible electronics," *npj Flex. Electron.* 2018 21, vol. 2, no. 1, pp. 1–17, Mar. 2018, doi: 10.1038/s41528-018-0021-5.
- [92] M. C. Rao and M. S. Shekhawat, "A BRIEF SURVEY ON BASIC PROPERTIES OF THIN FILMS FOR DEVICE APPLICATION," *India Int. J. Mod. Phys. Conf. Ser.*, vol. 22, pp. 576–582, 2013, doi: 10.1142/S2010194513010696.
- [93] T. J. Miranda, "The Future of the Coatings Industry," *Surf. Coatings*, pp. 1–10, 1993, doi: 10.1007/978-94-011-1220-8\_1.
- [94] M. Ma *et al.*, "Microstructure development in drying latex coatings," *Prog. Org. Coatings*, vol. 52, no. 1, pp. 46–62, Jan. 2005, doi: 10.1016/J.PORGCOAT.2004.07.023.
- [95] A. Du Chesne, A. Bojkova, J. Gapinski, D. Seip, and P. Fischer, "Film Formation and Redispersion of Waterborne Latex Coatings," *J. Colloid Interface Sci.*, vol. 224, no. 1, pp. 91–98, Apr. 2000, doi: 10.1006/JCIS.1999.6645.
- [96] L. A. Felton, "Mechanisms of polymeric film formation," *Int. J. Pharm.*, vol. 457, no. 2, pp. 423–427, Dec. 2013, doi: 10.1016/J.IJPHARM.2012.12.027.
- [97] J. L. Keddie and A. F. Routh, *Fundamentals of Latex Film Formation*. Dordrecht: Springer Netherlands, 2010.
- [98] E. Ciampi and P. J. McDonald, "Skin formation and water distribution in semicrystalline polymer layers cast from solution A magnetic resonance imaging study," *Macromolecules*, vol. 36, no. 22, pp. 8398–8405, Nov. 2003, doi: 10.1021/ma034951j.
- [99] J. Mallégol, G. Bennett, P. J. McDonald, J. L. Keddie, and O. Dupont, "Skin Development during the Film Formation of Waterborne Acrylic Pressure-Sensitive Adhesives Containing Tackifying Resin," *J. Adhes.*, vol. 82, no. 3, pp. 217–238, Mar. 2007, doi: 10.1080/00218460600646461.
- [100] M. A. Frommer and R. M. Messalem, "Mechanism of Membrane Formation. VI. Convective Flows and Large Void Formation during Membrane Precipitation," *Ind. Eng. Chem. Prod. Res. Dev.*, vol. 12, no. 4, pp. 328–333, Dec. 2002, doi: 10.1021/I360048A015.
- [101] L. Y and W. DE, "The Effects of Curing and Casting Methods on the Physicochemical Properties of Polymer Films," *AAPS PharmSciTech*, vol. 19, no. 6, pp. 2740–2749, Aug. 2018, doi: 10.1208/S12249-018-1113-1.
- [102] Z. Mo, S. Lu, and M. Shao, "Volatile organic compound (VOC) emissions and health risk assessment in paint and coatings industry in the Yangtze River Delta, China," *Environ. Pollut.*, vol. 269, p. 115740, Jan. 2021, doi: 10.1016/J.ENVPOL.2020.115740.
- [103] C. E. Stockwell *et al.*, "Volatile organic compound emissions from solvent-and water-borne coatings-compositional differences and tracer compound identifications," *Atmos. Chem. Phys.*, vol. 21, no. 8, pp. 6005–6022, Apr. 2021, doi: 10.5194/ACP-21-6005-2021.
- [104] T. Salthammer, "Emission of Volatile Organic Compounds from Furniture Coatings," *Indoor Air*, vol. 7, no. 3, pp. 189–197, Sep. 1997, doi: 10.1111/J.1600-0668.1997.T01-1-00004.X.
- [105] Concepción Jiménez-González, D. J. C. Constable, and C. S. Ponder, "Evaluating the 'Greenness' of chemical processes and products in the pharmaceutical industry—a green metrics primer," *Chem. Soc. Rev.*, vol. 41, no. 4, pp. 1485–1498, Jan. 2012, doi: 10.1039/C1CS15215G.
- [106] J. Cummings, J. S. Lowengrub, B. G. Sumpter, S. M. Wise, and R. Kumar, "Modeling solvent evaporation during thin film formation in phase separating polymer mixtures † ‡," *Soft Matter*, vol. 14, p. 1833, 2018, doi: 10.1039/c7sm02560b.
- [107] C. M. Hansen, "Polymer Coatings. Concepts of Solvent Evaporation Phenomena," *Ind. Eng. Chem. Prod. Res. Dev.*, vol. 9, no. 3, pp. 282–286, 2002, doi: 10.1021/I360035A004.
- [108] T. Narita, P. Hébraud, and F. Lequeux, "Effects of the rate of evaporation and film thickness on nonuniform drying of film-forming concentrated colloidal suspensions," *Eur. Phys. J. E* 2005 171, vol. 17, no. 1, pp. 69–76, Mar. 2005, doi: 10.1140/EPJE/I2004-10109-X.
- [109] J. W. Vanderhoff, "LATEX FILM FORMATION.," *Polym. News*, vol. 3, no. 4, pp. 194–203, 1977, doi: 10.1016/S1359-0294(97)80026-X.
- [110] P. A. Steward, J. Hearn, and M. C. Wilkinson, "An overview of polymer latex film formation and properties," *Adv. Colloid Interface Sci.*, vol. 86, no. 3, pp. 195–267, Jul. 2000, doi: 10.1016/S0001-8686(99)00037-8.
- [111] M. Dušková-smrčková and K. Dušek, "Processes and states during polymer film formation by simultaneous crosslinking and solvent evaporation," *J. Mater. Sci.* 2002 3722, vol. 37, no. 22, pp. 4733–4741, Nov. 2002, doi: 10.1023/A:1020843020379.
- [112] J. Feng *et al.*, "Formation and crosslinking of latex films through the reaction of acetoacetoxy groups with diamines under ambient conditions," *J. Coatings Technol.* 1998 70881, vol. 70, no. 881, pp. 57–68, 1998, doi: 10.1007/BF02730151.
- [113] I. Ichinose, S. Mizuki, S. Ohno, H. Shiraishi, and T. Kunitake, "Preparation of Cross-Linked Ultrathin Films Based on Layer-by-Layer Assembly of Polymers," *Polym. J.* 1999 3111, vol. 31, no. 11, pp. 1065–1070, 1999, doi: 10.1295/polymj.31.1065.
- [114] C. A. Kumins, "Transport through polymer films," *J. Polym. Sci. Part C Polym. Symp.*, vol. 10, no. 1, pp. 1–9, Jan. 1965, doi: 10.1002/POLC.5070100103.
- [115] S. Gårdebjer, M. Larsson, T. Gebäck, M. Skepö, and A. Larsson, "An overview of the transport of liquid molecules through structured polymer films, barriers and composites – Experiments correlated to structure-based simulations," *Adv. Colloid Interface Sci.*, vol. 256, pp. 48–64, Jun. 2018, doi: 10.1016/J.CIS.2018.05.004.

- [116] A. I. Visan, G. Popescu-Pelin, and G. Socol, "Degradation Behavior of Polymers Used as Coating Materials for Drug Delivery—A Basic Review," *Polymers (Basel)*, vol. 13, no. 8, Apr. 2021, doi: 10.3390/POLYM13081272.
- [117] David Cheneler and James Bowen, "Degradation of polymer films," *Soft Matter*, vol. 9, no. 2, pp. 344–358, Dec. 2012, doi: 10.1039/C2SM26502H.
- [118] N. J. W. Reuvers, *Water and ion transport in nylon as studied by NMR*. Technische Universiteit Eindhoven, 2012.
- [119] T. J. Senden, M. A. Knackstedt, and M. B. Lyne, "Droplet penetration into porous networks: Role of pore morphology," *Nord. Pulp Pap. Res. J.*, vol. 15, no. 5, pp. 554–563, 2000, doi: 10.3183/NPPRJ-2000-15-05-P554-563.
- [120] S. Krainer, L. Saes, and U. Hirn, "Predicting inkjet dot spreading and print through from liquid penetration- and picoliter contact angle measurement," *Nord. Pulp Pap. Res. J.*, vol. 35, no. 1, pp. 124–136, Mar. 2020, doi: 10.1515/NPPRJ-2019-0088.
- [121] K. Sarah and H. Ulrich, "Short timescale wetting and penetration on porous sheets measured with ultrasound, direct absorption and contact angle," *RSC Adv.*, vol. 8, no. 23, pp. 12861–12869, Apr. 2018, doi: 10.1039/C8RA01434E.
- [122] W. Kappel, C. and Hirn, Ulrich and Donoser, Michael and Bauer, "Measurement of printing ink penetration in uncoated papers and its influence on print quality," 2008, Accessed: Oct. 20, 2021. [Online]. Available: <https://www.researchgate.net/publication/267694165>.
- [123] P. Lepoutre, "The structure of paper coatings: an update," *Prog. Org. Coatings*, vol. 17, no. 2, pp. 89–106, Jul. 1989, doi: 10.1016/0033-0655(89)80016-0.
- [124] C. E et al., "Dynamic in vivo mapping of model moisturiser ingress into human skin by GARfield MRI," *NMR Biomed.*, vol. 24, no. 2, pp. 135–144, Feb. 2011, doi: 10.1002/NBM.1562.
- [125] P. J. McDonald, A. Akhmerov, L. J. Backhouse, and S. Pitts, "Magnetic resonance profiling of human skin in vivo using GARField magnets," *J. Pharm. Sci.*, vol. 94, no. 8, pp. 1850–1860, 2005, doi: 10.1002/JPS.20401.
- [126] L. Backhouse, M. Dias, J. P. Gorce, J. Hadgraft, P. J. McDonald, and J. W. Wiechers, "GARField magnetic resonance profiling of the ingress of model skin-care product ingredients into human skin in vitro," *J. Pharm. Sci.*, vol. 93, no. 9, pp. 2274–2283, Sep. 2004, doi: 10.1002/JPS.20137.
- [127] P. J. McDonald, J. Mitchell, M. Mulheron, L. Monteilhet, and J. P. Korb, "Two-dimensional correlation relaxation studies of cement pastes," *Magn. Reson. Imaging*, vol. 25, no. 4, pp. 470–473, May 2007, doi: 10.1016/j.mri.2006.11.013.
- [128] P. J. McDonald, O. Istok, M. Janota, A. M. Gajewicz-Jaromin, and D. A. Faux, "Sorption, anomalous water transport and dynamic porosity in cement paste: A spatially localised 1H NMR relaxation study and a proposed mechanism," *Cem. Concr. Res.*, vol. 133, p. 106045, Jul. 2020, doi: 10.1016/j.cemconres.2020.106045.
- [129] A. N. Garroway, P. K. Grannell, and P. Mansfield, "Image formation in NMR by a selective irradiative process," *J. Phys. C Solid State Phys.*, vol. 7, no. 24, p. L457, Dec. 1974, doi: 10.1088/0022-3719/7/24/006.
- [130] P. C. LAUTERBUR, "Image Formation by Induced Local Interactions: Examples Employing Nuclear Magnetic Resonance," *Nat.* 1973 2425394, vol. 242, no. 5394, pp. 190–191, 1973, doi: 10.1038/242190a0.
- [131] B. Blumich, *NMR Imaging of Materials*. Oxford University Press, 2000.
- [132] A. Adams, "Analysis of solid technical polymers by compact NMR," *TrAC - Trends Anal. Chem.*, vol. 83, pp. 107–119, Oct. 2016, doi: 10.1016/J.TRAC.2016.04.003.
- [133] S. Ligot et al., "Correlation Between Mechanical Properties and Cross-Linking Degree of Ethyl Lactate Plasma Polymer Films," *Plasma Process. Polym.*, vol. 12, no. 6, pp. 508–518, Jun. 2015, doi: 10.1002/PPAP.201400162.
- [134] J. M. Spruell et al., "Reactive, multifunctional polymer films through thermal cross-linking of orthogonal click groups," *J. Am. Chem. Soc.*, vol. 133, no. 41, pp. 16698–16706, Oct. 2011, doi: 10.1021/JA207635F/SUPPL\_FILE/JA207635F\_SI\_001.PDF.
- [135] G. T. Carroll, M. E. Sojka, X. Lei, N. J. Turro, and J. T. Koberstein, "Photoactive additives for cross-linking polymer films: Inhibition of dewetting in thin polymer films," *Langmuir*, vol. 22, no. 18, pp. 7748–7754, Aug. 2006, doi: 10.1021/LA0611099/SUPPL\_FILE/LA0611099SI20060609\_101113.PDF.
- [136] K. Schmidt-Rohr and H. W. Spiess, *Multidimensional solid-state NMR and polymers*. 1994.
- [137] F. A. (Frank A. Bovey and P. A. Mirau, *NMR of polymers*. Academic Press, 1996.
- [138] K. Hatada and T. Kitayama, *NMR Spectroscopy of Polymers*. Springer Netherlands, 1993.
- [139] A. J. Brandolini and D. D. Hills, *NMR spectra of polymers and polymer additives*. Marcel Dekker, 2000.
- [140] P. M. Glover, P. S. Aptaker, J. R. Bowler, E. Ciampi, and P. J. McDonald, "A Novel High-Gradient Permanent Magnet for the Profiling of Planar Films and Coatings," *J. Magn. Reson.*, vol. 139, no. 1, pp. 90–97, 1999, doi: 10.1006/jmre.1999.1772.
- [141] A. A. Samoilenko and K. Zick, "Stray-Field Imaging of Solids (STRAFI)," *25th Congr. Ampere Magn. Reson. Relat. Phenom.*, pp. 92–93, 1990, doi: 10.1007/978-3-642-76072-3\_44.
- [142] B. Blümich, S. Anferova, S. Sharma, A. L. Segre, and C. Federici, "Degradation of historical paper: nondestructive analysis by the NMR-MOUSE," *J. Magn. Reson.*, vol. 161, no. 2, pp. 204–209, Apr. 2003, doi: 10.1016/S1090-7807(03)00034-X.
- [143] F. Bloch, "The principle of nuclear induction," *Science (80- )*, vol. 118, no. 3068, pp. 425–430, 1953, doi: 10.1126/SCIENCE.118.3068.425.
- [144] E. M. Purcell, "Research in nuclear magnetism," *Science (80- )*, vol. 118, no. 3068, pp. 431–436, 1953, doi: 10.1126/SCIENCE.118.3068.431.
- [145] T. Dikić et al., "Fluorine depth profiling by high-resolution 1D magnetic resonance imaging," *Polymer (Guildf)*, vol. 48, no. 14, pp. 4063–4067, Jun. 2007, doi: 10.1016/J.POLYMER.2007.05.017.
- [146] R. P. Suggate and W. W. Dickinson, "Carbon NMR of coals: the effects of coal type and rank," *Int. J. Coal Geol.*, vol. 57, no. 1, pp. 1–22, Jan. 2004, doi: 10.1016/S0166-5162(03)00116-2.
- [147] M. Saqib, N. S. Francis, and N. J. Francis, "Design and Development of Helmholtz Coils for Magnetic Field," *Proc. 2nd 2020 Int. Youth Conf. Radio Electron. Electr. Power Eng. REEPE 2020*, Mar. 2020, doi: 10.1109/REEPE49198.2020.9059109.

- [148] E. L. Hahn, "Spin Echoes," *Phys. Rev.*, vol. 80, no. 4, p. 580, Nov. 1950, doi: 10.1103/PhysRev.80.580.
- [149] E. L. Hahn and D. E. Maxwell, "Spin Echo Measurements of Nuclear Spin Coupling in Molecules," *Phys. Rev.*, vol. 88, no. 5, p. 1070, Dec. 1952, doi: 10.1103/PhysRev.88.1070.
- [150] A. A. Behroozmand, K. Keating, and E. Auken, "A Review of the Principles and Applications of the NMR Technique for Near-Surface Characterization," *Surv. Geophys.* 2014 361, vol. 36, no. 1, pp. 27–85, Sep. 2014, doi: 10.1007/S10712-014-9304-0.
- [151] G. B. Chavhan, P. S. Babyn, B. Thomas, M. M. Shroff, and E. Mark Haacke, "Principles, techniques, and applications of T2\*-based MR imaging and its special applications," *Radiographics*, vol. 29, no. 5, pp. 1433–1449, Sep. 2009, doi: 10.1148/RG.295095034/ASSET/IMAGES/LARGE/G09SE10G09B.JPEG.
- [152] H. Y. Carr and E. M. Purcell, "Effects of Diffusion on Free Precession in Nuclear Magnetic Resonance Experiments," *Phys. Rev.*, vol. 94, no. 3, p. 630, May 1954, doi: 10.1103/PhysRev.94.630.
- [153] S. Meiboom, D. Gill, and D. Gillt, "Modified SpinEcho Method for Measuring Nuclear Relaxation Times Modified Spin-Echo Method for Measuring Nuclear Relaxation Times\*," *Cit. Rev. Instrum.*, vol. 29, p. 688, 1958, doi: 10.1063/1.1716296.
- [154] D. Cohen and H. Hosaka, "Part II magnetic field produced by a current dipole," *J. Electrocardiol.*, vol. 9, no. 4, pp. 409–417, Jan. 1976, doi: 10.1016/S0022-0736(76)80041-6.
- [155] N. Bloembergen, E. M. Purcell, and R. V. Pound, "Relaxation Effects in Nuclear Magnetic Resonance Absorption," *Phys. Rev.*, vol. 73, no. 7, p. 679, Apr. 1948, doi: 10.1103/PhysRev.73.679.
- [156] H. È. Ggkvist, "Effects of drying and pressing on the pore structure in the cellulose @bre wall studied by 1 H and 2 H NMR relaxation."
- [157] Ö. Gezici-Koç, S. J. F. Erich, H. P. Huinink, L. G. J. van der Ven, and O. C. G. Adan, "Bound and free water distribution in wood during water uptake and drying as measured by 1D magnetic resonance imaging," *Cellulose*, vol. 24, no. 2, pp. 535–553, Feb. 2017, doi: 10.1007/S10570-016-1173-X/TABLES/4.
- [158] S. J. F. Erich, "NMR imaging of curing processes in alkyd coatings," Technische Universiteit Eindhoven, 2006.
- [159] S. J. F. Erich, J. Laven, L. Pel, H. P. Huinink, and K. Kopinga, "Comparison of NMR and confocal Raman microscopy as coatings research tools," *Prog. Org. Coatings*, vol. 52, no. 3, pp. 210–216, Mar. 2005, doi: 10.1016/j.porgcoat.2004.12.002.
- [160] K. R. Keshari and D. M. Wilson, "Chemistry and biochemistry of 13C hyperpolarized magnetic resonance using dynamic nuclear polarization," *Chem. Soc. Rev.*, vol. 43, no. 5, pp. 1627–1659, Feb. 2014, doi: 10.1039/C3CS60124B.
- [161] B. Voogt, H. Huinink, B. Erich, J. Scheerder, P. Venema, and O. Adan, "Water mobility during drying of hard and soft type latex: Systematic GARField 1H NMR relaxometry studies," *Prog. Org. Coatings*, vol. 123, pp. 111–119, Oct. 2018, doi: 10.1016/J.PORGOAT.2018.06.011.
- [162] K. R. Brownstein and C. E. Tarr, "Importance of classical diffusion in NMR studies of water in biological cells," *Phys. Rev. A*, vol. 19, no. 6, p. 2446, Jun. 1979, doi: 10.1103/PhysRevA.19.2446.
- [163] O. Mohnke and B. Hughes, "Jointly deriving NMR surface relaxivity and pore size distributions by NMR relaxation experiments on partially desaturated rocks," *Water Resour. Res.*, vol. 50, no. 6, pp. 5309–5321, 2014, doi: 10.1002/2014WR015282.
- [164] P. Zhao *et al.*, "Nuclear magnetic resonance surface relaxivity and its advanced application in calculating pore size distributions," *Mar. Pet. Geol.*, vol. 111, pp. 66–74, Jan. 2020, doi: 10.1016/J.MARPETGEO.2019.08.002.
- [165] M. Fleury, "NMR SURFACE RELAXIVITY DETERMINATION USING NMR APPARENT DIFFUSION CURVES AND BET MEASUREMENTS."
- [166] Z. Zhang and A. Weller, "Estimating the nuclear magnetic resonance surface relaxivity of Eocene sandstones: A comparison of different approaches," <https://doi.org/10.1190/geo2020-0501.1>, vol. 86, no. 2, pp. JM11–JM22, Feb. 2021, doi: 10.1190/GEO2020-0501.1.
- [167] S. Falzone and K. Keating, "A laboratory study to determine the effect of pore size, surface relaxivity, and saturation on NMR T2 relaxation measurements," *Near Surf. Geophys.*, vol. 14, no. 1, pp. 57–69, 2016, doi: 10.3997/1873-0604.2016001.
- [168] M. Müller-Petke, R. Dlugosch, J. Lehmann-Horn, and M. Ronczka, "Nuclear magnetic resonance average pore-size estimations outside the fast-diffusion regime," *Geophysics*, vol. 80, no. 3, pp. D195–D206, Mar. 2015, doi: 10.1190/GEO2014-0167.1.
- [169] P. Bendel, "Spin-echo attenuation by diffusion in nonuniform field gradients," *J. Magn. Reson.*, vol. 86, no. 3, pp. 509–515, Feb. 1990, doi: 10.1016/0022-2364(90)90028-8.
- [170] M. D. Hürlimann, "Diffusion and relaxation effects in general stray field NMR experiments," *J. Magn. Reson.*, vol. 148, no. 2, pp. 367–378, 2001, doi: 10.1006/JMRE.2000.2263.
- [171] A. Merbach, L. Helm, and È. Toth, "The Chemistry of Contrast Agents in Medical Magnetic Resonance Imaging: Second Edition," *The Chemistry of Contrast Agents in Medical Magnetic Resonance Imaging: Second Edition*, Feb. 18, 2013. .
- [172] Y. D. Xiao, R. Paudel, J. Liu, C. Ma, Z. S. Zhang, and S. K. Zhou, "MRI contrast agents: Classification and application (Review)," *Int. J. Mol. Med.*, vol. 38, no. 5, pp. 1319–1326, Nov. 2016, doi: 10.3892/IJMM.2016.2744.
- [173] C. P. Sales *et al.*, "Evaluation of different magnetic resonance imaging contrast materialsto be used as dummy markers in image-guided brachytherapy for gynecologicmalignancies," *Radiol. Bras.*, vol. 49, no. 3, p. 165, May 2016, doi: 10.1590/0100-3984.2015.0004.
- [174] È. Toth, L. Helm, and A. E. Merbach, *Relaxivity of MRI Contrast Agents*. Springer, Berlin, Heidelberg, 2002.
- [175] P. Szomolanyi *et al.*, "Comparison of the Relaxivities of Macrocylic Gadolinium-Based Contrast Agents in Human Plasma at 1.5, 3, and 7 T, and Blood at 3 T," *Invest. Radiol.*, vol. 54, no. 9, p. 559, Sep. 2019, doi: 10.1097/RLI.0000000000000577.
- [176] S. Gaudin, D. Lourdin, D. Le Botlan, J. L. Ilari, and P. Colonna, "Plasticisation and Mobility in Starch-Sorbitol Films," *J. Cereal Sci.*, vol. 29, no. 3, pp. 273–284, May 1999, doi: 10.1006/JCRS.1999.0236.
- [177] Q. Xiao, L. T. Lim, Y. Zhou, and Z. Zhao, "Drying process of pullulan edible films forming solutions studied by low-field

- NMR," *Food Chem.*, vol. 230, pp. 611–617, Sep. 2017, doi: 10.1016/J.FOODCHEM.2017.03.097.
- [178] Q. Xiao, "Drying process of sodium alginate edible films forming solutions studied by LF NMR," *Food Chem.*, vol. 250, pp. 83–88, Jun. 2018, doi: 10.1016/J.FOODCHEM.2018.01.043.
- [179] K. Ulrich, S. A. Centeno, J. Arslanoglu, and E. Del Federico, "Absorption and diffusion measurements of water in acrylic paint films by single-sided NMR," *Prog. Org. Coatings*, vol. 71, no. 3, pp. 283–289, Jul. 2011, doi: 10.1016/J.PORGCOAT.2011.03.019.
- [180] L. M. A. Silva, F. D. Andrade, E. G. A. Filho, M. R. Monteiro, E. R. de Azevedo, and T. Venâncio, "NMR investigation of commercial carbon black filled vulcanized natural rubber exposed to petrodiesel/biodiesel mixtures," *Fuel*, vol. 186, pp. 50–57, Dec. 2016, doi: 10.1016/J.FUEL.2016.08.060.
- [181] B. Voogt *et al.*, "Film Formation of High Tg Latex Using Hydroplasticization: Explanations from NMR Relaxometry," *Langmuir*, vol. 35, no. 38, pp. 12418–12427, Sep. 2019, doi: 10.1021/acs.langmuir.9b01353.
- [182] P. Galvosas and P. T. Callaghan, "Multi-dimensional inverse Laplace spectroscopy in the NMR of porous media," *Comptes Rendus Phys.*, vol. 11, no. 2, pp. 172–180, Mar. 2010, doi: 10.1016/J.CRHY.2010.06.014.
- [183] H. J. R. J. H. S. M. R. Halse, "Diffusion and molecular mobility in microporous media: applications to rubber and zeolite 4A powders," *Physica B*, vol. 203, pp. 196–199, 1994. <https://reader.elsevier.com/reader/sd/pii/S0730725X96001592?token=D8B02FD6209FEB6E11C7F51A8E6684C534D4DAF130D51536D29A298EDFE4EAD6C6636F8ECBBD434A4DDDC48F86C8EAB5&originRegion=eu-west-1&originCreation=20210913125615> (accessed Sep. 13, 2021).
- [184] E. D. Ostroff and J. S. Waugh, "Multiple spin echoes and spin locking in solids," *Phys. Rev. Lett.*, vol. 16, no. 24, pp. 1097–1098, 1966, doi: 10.1103/PHYSREVLETT.16.1097.
- [185] J. L. Markley, W. J. Horsley, and M. P. Klein, "Spin-lattice relaxation measurements in slowly relaxing complex spectra," *J. Chem. Phys.*, vol. 55, no. 7, pp. 3169–3177, 1971, doi: 10.1063/1.1676626.
- [186] R. Nicasy, H. Huinink, B. Erich, and O. Adan, "NMR Profiling of Reaction and Transport in Thin Layers: A Review," *Polym. 2022, Vol. 14, Page 798*, vol. 14, no. 4, p. 798, Feb. 2022, doi: 10.3390/POLYM14040798.
- [187] M. H. Levitt, *Spin Dynamics: Basics of Nuclear Magnetic Resonance*. John Wiley & Sons, Ltd, 2013.
- [188] M. Levitt, *Spin dynamics: basics of nuclear magnetic resonance*. WILEY, 2013.
- [189] P. J. McDonald and B. Newling, "Stray field magnetic resonance imaging," *Reports Prog. Phys.*, vol. 61, no. 11, pp. 1441–1493, Nov. 1998, doi: 10.1088/0034-4885/61/11/001.
- [190] B. Blümich, J. Perlo, and F. Casanova, "Mobile single-sided NMR," *Prog. Nucl. Magn. Reson. Spectrosc.*, vol. 52, no. 4, pp. 197–269, May 2008, doi: 10.1016/j.pnmrs.2007.10.002.
- [191] B. Blümich *et al.*, "Advances of unilateral mobile NMR in nondestructive materials testing," *Magn. Reson. Imaging*, vol. 23, no. 2, pp. 197–201, Feb. 2005, doi: 10.1016/J.MRI.2004.11.058.
- [192] S. J. F. Erich, O. C. G. Adan, L. Pel, H. P. Huinink, and K. Kopinga, "NMR imaging of coatings on porous substrates," *Chem. Mater.*, vol. 18, no. 18, pp. 4500–4504, Sep. 2006, doi: 10.1021/cm060744x.
- [193] P. M. Glover, P. J. McDonald, and B. Newling, "Stray-Field Imaging of Planar Films Using a Novel Surface Coil," *J. Magn. Reson.*, vol. 126, no. 2, pp. 207–212, Jun. 1997, doi: 10.1006/JMRE.1997.1174.
- [194] T. G. Nunes, R. Pires, J. Perdigão, A. Amorim, and M. Polido, "The study of a commercial dental resin by 1H stray-field magnetic resonance imaging," *Polymer (Guildf.)*, vol. 42, no. 19, pp. 8051–8054, Jun. 2001, doi: 10.1016/S0032-3861(01)00296-8.
- [195] F. Simon, S. Kunkel, H. Oehler, D. Lellinger, P. Spahn, and I. Alig, "Investigation of deformation mechanisms during latex film formation by combination of unilateral NMR and near infrared measurements," *Prog. Org. Coatings*, vol. 70, no. 4, pp. 230–239, Apr. 2011, doi: 10.1016/J.PORGCOAT.2010.08.015.
- [196] P. J. McDonald, "Stray field magnetic resonance imaging," *Prog. Nucl. Magn. Reson. Spectrosc.*, vol. 30, no. 1–2, pp. 69–99, Mar. 1997, doi: 10.1016/S0079-6565(96)01035-7.
- [197] T. G. Nunes, E. W. Randall, and G. Guillot, "The first proton NMR imaging of ice: Stray-field imaging and relaxation studies," *Solid State Nucl. Magn. Reson.*, vol. 32, no. 2, pp. 59–65, Oct. 2007, doi: 10.1016/J.SSNMR.2007.08.002.
- [198] K. J. Carlton, M. R. Halse, and J. H. Strange, "Diffusion-Weighted Imaging of Bacteria Colonies in the STRAFI Plane," *J. Magn. Reson.*, vol. 143, no. 1, pp. 24–29, Mar. 2000, doi: 10.1006/JMRE.1999.1959.
- [199] I. Hopkinson, R. A. L. Jones, S. Black, D. M. Lane, and P. J. McDonald, "Fickian and Case II diffusion of water into amylose: A stray field NMR study," *Carbohydr. Polym.*, vol. 34, no. 1–2, pp. 39–47, Dec. 1997, doi: 10.1016/S0144-8617(97)00106-9.
- [200] H. Zhu, H. P. Huinink, S. J. F. Erich, V. Baukh, O. C. G. Adan, and K. Kopinga, "High spatial resolution NMR imaging of polymer layers on metallic substrates," *J. Magn. Reson.*, vol. 214, pp. 227–236, 2012, doi: 10.1016/j.jmr.2011.11.009.
- [201] G. Eidmann, R. Savelsberg, P. Blümler, and B. Blümich, "The NMR MOUSE, a Mobile Universal Surface Explorer," *J. Magn. Reson. Ser. A*, vol. 122, no. 1, pp. 104–109, Sep. 1996, doi: 10.1006/JMRA.1996.0185.
- [202] P. J. Prado, "NMR hand-held moisture sensor," *Magn. Reson. Imaging*, vol. 19, no. 3–4, pp. 505–508, Apr. 2001, doi: 10.1016/S0730-725X(01)00279-X.
- [203] F. Casanova and B. Blümich, "Two-dimensional imaging with a single-sided NMR probe," *J. Magn. Reson.*, vol. 163, no. 1, pp. 38–45, Jul. 2003, doi: 10.1016/S1090-7807(03)00123-X.
- [204] J. Perlo, F. Casanova, and B. Blümich, "Profiles with microscopic resolution by single-sided NMR," *J. Magn. Reson.*, vol. 176, no. 1, pp. 64–70, Sep. 2005, doi: 10.1016/J.JMR.2005.05.017.
- [205] M. D. Hürlimann, "Well Logging," *Encycl. Magn. Reson.*, Jun. 2012, doi: 10.1002/9780470034590.EMRSTM0593.PUB2.
- [206] R. Freedman and N. Heaton, "Fluid Characterization using Nuclear Magnetic Resonance Logging | Petrophysics | OnePetro," *PetroPhys*, vol. 45, no. 03, 2004, Accessed Sep. 17, 2021. [Online]. Available: <https://onepetro.org/petrophysics/article-abstract/171033/Fluid-Characterization-using-Nuclear-Magnetic?redirectedFrom=fulltext>.
- [207] G. R. Coates, L. Xiao, and M. G. Prammer, *NMR Logging Principles and Applications*. Halliburton Energy Services



- Publication, 1999.
- [208] P. J. McDonald, J.-P. Korb, J. Mitchell, and L. Monteilhet, "Surface relaxation and chemical exchange in hydrating cement pastes: A two-dimensional NMR relaxation study," *Phys. Rev. E*, vol. 72, no. 1, p. 011409, Jul. 2005, doi: 10.1103/PhysRevE.72.011409.
- [209] T. Nunes, E. W. Randall, A. A. Samoilenko, P. Bodart, and G. Feio, "The hardening of Portland cement studied by 1H NMR stray-field imaging," *J. Phys. D. Appl. Phys.*, vol. 29, no. 3, pp. 805–808, Mar. 1996, doi: 10.1088/0022-3727/29/3/044.
- [210] M. Van Landeghem, J. B. D'Espinoze De Lacaillerie, B. Blümich, J. P. Korb, and B. Bresson, "The roles of hydration and evaporation during the drying of a cement paste by localized NMR," *Cem. Concr. Res.*, vol. 48, pp. 86–96, Jun. 2013, doi: 10.1016/J.CEMCONRES.2013.01.012.
- [211] A. Leventis, D. A. Verganelakis, M. R. Halse, J. B. Webber, and J. H. Strange, "Capillary Imbibition and Pore Characterisation in Cement Pastes," *Transp. Porous Media* 2000 392, vol. 39, no. 2, pp. 143–157, 2000, doi: 10.1023/A:1006687114424.
- [212] J. Boguszynska *et al.*, "Magnetic resonance studies of cement based materials in inhomogeneous magnetic fields," *Cem. Concr. Res.*, vol. 35, no. 10, pp. 2033–2040, Oct. 2005, doi: 10.1016/J.CEMCONRES.2005.06.012.
- [213] B. Voogt, H. Huinink, B. Erich, J. Scheerder, P. Venema, and O. Adan, "Water mobility during drying of hard and soft type latex: Systematic GARField 1H NMR relaxometry studies," *Prog. Org. Coatings*, vol. 123, pp. 111–119, Oct. 2018, doi: 10.1016/j.porgcoat.2018.06.011.
- [214] B. E *et al.*, "In vivo assessment of aged human skin with a unilateral NMR scanner," *NMR Biomed.*, vol. 28, no. 6, pp. 656–666, Jun. 2015, doi: 10.1002/NBM.3304.
- [215] H. Zhu, H. P. Huinink, O. C. G. Adan, and K. Kopinga, "NMR study of the microstructures and water-polymer interactions in cross-linked polyurethane coatings," *Macromolecules*, vol. 46, no. 15, pp. 6124–6131, Aug. 2013, doi: 10.1021/MA401256N.
- [216] N. Reuvers, H. Huinink, and O. Adan, "Water plasticizes only a small part of the amorphous phase in nylon-6," *Macromol. Rapid Commun.*, vol. 34, no. 11, pp. 949–953, Jun. 2013, doi: 10.1002/MARC.201300009.
- [217] V. Baukh, H. P. Huinink, O. C. G. Adan, S. J. F. Erich, and L. G. J. van der Ven, "Water-Polymer Interaction during Water Uptake," *Macromolecules*, vol. 44, no. 12, pp. 4863–4871, Jun. 2011, doi: 10.1021/MA102889U.
- [218] A. Adams and B. Blümich, "Single-Sided NMR of Semicrystalline Polymers," *Macromol. Symp.*, vol. 327, no. 1, pp. 29–38, May 2013, doi: 10.1002/MASY.201350503.
- [219] S. G. Pereira, N. Reis, and T. G. Nunes, "Spatially resolved studies on the photopolymerization of dimethacrylate monomers," *Polymer (Guildf.)*, vol. 46, no. 19, pp. 8034–8044, Sep. 2005, doi: 10.1016/J.POLYMER.2005.06.086.
- [220] H. P. Huinink *et al.*, "High-resolution NMR imaging of paramagnetic liposomes targeted to a functionalized surface," *Magn. Reson. Med.*, vol. 59, no. 6, pp. 1282–1286, Jun. 2008, doi: 10.1002/MRM.21587.
- [221] H. M. H. F. Sanders *et al.*, "Morphology, binding behavior and MR-properties of paramagnetic collagen-binding liposomes," *Contrast Media Mol. Imaging*, vol. 4, no. 2, pp. 81–88, 2009, doi: 10.1002/CMMI.266.
- [222] P. R. Laity, P. M. Glover, J. Godward, P. J. McDonald, and J. N. Hay, "Structural studies and diffusion measurements of water-swollen cellophane by NMR imaging," *Cellulose*, vol. 7, no. 3, pp. 227–246, 2000, doi: 10.1023/A:1009249332222.
- [223] M. Dias, J. Hadgraft, P. M. Glover, and P. J. McDonald, "Stray field magnetic resonance imaging: A preliminary study of skin hydration," *J. Phys. D. Appl. Phys.*, vol. 36, no. 4, pp. 364–368, Feb. 2003, doi: 10.1088/0022-3727/36/4/306.
- [224] V. L. M. D. E. P. J. B. B. and C. F., "Low-gradient single-sided NMR sensor for one-shot profiling of human skin," *J. Magn. Reson.*, vol. 215, pp. 74–84, Feb. 2012, doi: 10.1016/J.JMR.2011.12.010.
- [225] R. Kwamen, B. Blümich, and A. Adams, "Estimation of self-diffusion coefficients of small penetrants in semicrystalline polymers using single-sided NMR," *Macromol. Rapid Commun.*, vol. 33, no. 10, pp. 943–947, May 2012, doi: 10.1002/MARC.201100847.
- [226] Z. Fu, A. Hejl, A. Swartz, K. Beshah, and G. Dombrowski, "Film Formation Through Designed Diffusion Technology," *Prot. Coatings Film Form. Prop.*, pp. 153–168, May 2017, doi: 10.1007/978-3-319-51627-1\_7.
- [227] G. JP, B. D, M. PJ, P. P, T. D, and K. JL, "Vertical water distribution during the drying of polymer films cast from aqueous emulsions," *Eur. Phys. J. E. Soft Matter*, vol. 8, no. 4, pp. 421–429, 2002, doi: 10.1140/EPJE/I2002-10023-3.
- [228] P. Ekanayake, P. J. McDonald, and J. L. Keddie, "An experimental test of the scaling prediction for the spatial distribution of water during the drying of colloidal films," *Eur. Phys. J. Spec. Top. 2009 1661*, vol. 166, no. 1, pp. 21–27, Feb. 2009, doi: 10.1140/EPJST/E2009-00872-4.
- [229] S. J. F. Erich, J. Laven, L. Pel, H. P. Huinink, and K. Kopinga, "Dynamics of cross linking fronts in alkyd coatings," *Appl. Phys. Lett.*, vol. 86, no. 13, pp. 1–3, Mar. 2005, doi: 10.1063/1.1886913.
- [230] G. Bennett, J. P. Gorce, J. L. Keddie, P. J. McDonald, and H. Berglind, "Magnetic resonance profiling studies of the drying of film-forming aqueous dispersions and glue layers," *Magn. Reson. Imaging*, vol. 21, no. 3–4, pp. 235–241, Apr. 2003, doi: 10.1016/S0730-725X(03)00130-9.
- [231] S. Ghoshal, C. Mattea, and S. Stapf, "Inhomogeneity in the drying process of gelatin film formation: NMR microscopy and relaxation study," *Chem. Phys. Lett.*, vol. 485, no. 4–6, pp. 343–347, Jan. 2010, doi: 10.1016/J.CPLETT.2009.12.064.
- [232] S. G. Pereira, R. Fulgêncio, T. G. Nunes, M. Toledano, R. Osorio, and R. M. Carvalho, "Effect of curing protocol on the polymerization of dual-cured resin cements," *Dent. Mater.*, vol. 26, no. 7, pp. 710–718, Jul. 2010, doi: 10.1016/j.dental.2010.03.016.
- [233] T. G. Nunes, F. C. P. Garcia, R. Osorio, R. Carvalho, and M. Toledano, "Polymerization efficacy of simplified adhesive systems studied by NMR and MRI techniques," *Dent. Mater.*, vol. 22, no. 10, pp. 963–972, Oct. 2006, doi: 10.1016/j.dental.2005.10.008.
- [234] G. Hunter, D. M. Lane, S. N. Scrimgeour, P. J. McDonald, and C. H. Lloyd, "Measurement of the diffusion of liquids into dental restorative resins by stray-field nuclear magnetic resonance imaging (STRAFI)," *Dent. Mater.*, vol. 19, no. 7, pp. 632–638, Nov. 2003, doi: 10.1016/S0109-5641(03)00006-X.
- [235] S. J. F. Erich, J. Laven, L. Pel, H. P. Huinink, and K. Kopinga, "Influence of catalyst type on the curing process and network structure of alkyd coatings," *Polymer (Guildf.)*, vol. 47, no. 4, pp. 1141–1149, Feb. 2006, doi:

- 10.1016/j.polymer.2005.12.081.
- [236] O. Gezici-Koç *et al.*, "In-depth study of drying solvent-borne alkyd coatings in presence of Mn- and Fe- based catalysts as cobalt alternatives," *Mater. Today Commun.*, vol. 7, pp. 22–31, Jun. 2016, doi: 10.1016/J.MTCOMM.2016.03.001.
- [237] J. Mallégol *et al.*, "Influence of drier combination on through-drying in waterborne alkyd emulsion coatings observed with magnetic resonance profiling," *J. Coatings Technol.* 2002 74933, vol. 74, no. 933, pp. 113–124, 2002, doi: 10.1007/BF02697951.
- [238] S. J. F. Erich *et al.*, "The influence of calcium and zirconium based secondary driers on drying solvent borne alkyd coatings," *Polymer (Guildf.)*, vol. 121, pp. 262–273, Jul. 2017, doi: 10.1016/J.POLYMER.2017.06.031.
- [239] S. J. F. Erich, O. C. G. Adan, H. P. Huinink, J. Laven, A. C. Esteves, and T. B. en Ondergrond, "The influence of the pigment volume concentration on the curing of alkyd coatings: A 1D MRI depth profiling study," *Prog. Org. Coatings*, vol. 63, no. 4, p. 4, 2008, Accessed: Aug. 23, 2021. [Online]. Available: <https://repository.tno.nl/islandora/object/uuid%3A1000cfa0-64f1-446a-8f30-da3792c37144>.
- [240] S. Croll, "Drying of latex paint," *J. Coatings Technol.*, 1984.
- [241] E. W. S. Hagan, M. N. Charalambides, C. T. Young, Thomas, J. S. Learner, and S. Hackney, "Tensile properties of latex paint films with TiO<sub>2</sub> pigment," *Mech Time-Depend Mater*, vol. 13, pp. 149–161, 2009, doi: 10.1007/s11043-009-9076-y.
- [242] E. W. S. Hagan, M. N. Charalambides, C. R. T. Young, T. J. S. Learner, and S. Hackney, "Viscoelastic properties of latex paint films in tension: The contribution of the inorganic phase and surfactants," *Prog. Org. Coatings*, vol. 69, no. 1, pp. 73–81, Sep. 2010, doi: 10.1016/J.PORCOAT.2010.05.008.
- [243] S. Croll, "Heat and mass transfer in latex paints during drying," *J. Coatings Technol.*, 1987.
- [244] J. Mallégol, J.-P. Gorce, O. Dupont, C. Jaynes, P. J. McDonald, and J. L. Keddie, "Origins and Effects of a Surfactant Excess near the Surface of Waterborne Acrylic Pressure-Sensitive Adhesives," *Langmuir*, vol. 18, no. 11, pp. 4478–4487, May 2002, doi: 10.1021/LA0117698.
- [245] T. Kaewpetch and J. F. Gilchrist, "Chemical vs. mechanical microstructure evolution in drying colloid and polymer coatings," *Sci. Reports 2020 101*, vol. 10, no. 1, pp. 1–10, Jun. 2020, doi: 10.1038/s41598-020-66875-0.
- [246] M. Soleimani, J. C. Haley, W. Lau, and M. A. Winnik, "Effect of Hydroplasticization on Polymer Diffusion in Poly(butyl acrylate-co-methyl methacrylate) and Poly(2-ethylhexyl acrylate-co-tert-butyl methacrylate) Latex Films," *Macromolecules*, vol. 43, no. 2, pp. 975–985, Jan. 2009, doi: 10.1021/MA9020483.
- [247] N. Q and R. Y., "Various modes of void closure during dry sintering of close-packed nanoparticles," *Langmuir*, vol. 26, no. 2, pp. 1226–1231, Jan. 2010, doi: 10.1021/LA902381B.
- [248] R. Rodríguez *et al.*, "Correlation of Silicone Incorporation into Hybrid Acrylic Coatings with the Resulting Hydrophobic and Thermal Properties," *Macromolecules*, vol. 41, no. 22, pp. 8537–8546, Nov. 2008, doi: 10.1021/MA8006015.
- [249] F. T. Carter, R. M. Kowalczyk, I. Millichamp, M. Chainey, and J. L. Keddie, "Correlating Particle Deformation with Water Concentration Profiles during Latex Film Formation: Reasons That Softer Latex Films Take Longer to Dry," *Langmuir*, vol. 30, no. 32, pp. 9672–9681, Aug. 2014, doi: 10.1021/LA5023505.
- [250] A. M. König, T. G. Weerakkody, J. L. Keddie, and D. Johannsmann, "Heterogeneous Drying of Colloidal Polymer Films: Dependence on Added Salt," *Langmuir*, vol. 24, no. 14, pp. 7580–7589, Jul. 2008, doi: 10.1021/LA800525N.
- [251] K. Kawasaki and Y. Sekita, "Sorption and diffusion of water vapor by nylon 6," *J. Polym. Sci. Part A Gen. Pap.*, vol. 2, no. 5, pp. 2437–2443, May 1964, doi: 10.1002/POL.1964.100020532.
- [252] N. J. W. Reuvers, H. P. Huinink, H. R. Fischer, and O. C. G. Adan, "Quantitative Water Uptake Study in Thin Nylon-6 Films with NMR Imaging," *Macromolecules*, vol. 45, no. 4, pp. 1937–1945, Feb. 2012, doi: 10.1021/MA202719X.
- [253] N. J. W. Reuvers, H. P. Huinink, and O. C. G. Adan, "Plasticization lags behind water migration in nylon-6: An NMR imaging and relaxation study," *Polym. (United Kingdom)*, vol. 63, p. 127, Apr. 2015, doi: 10.1016/J.POLYMER.2015.03.005.
- [254] B. Newling, D. R. Ward, and V. Vijayakrishnan, "Stray Field Magnetic Resonance Imaging (STRAFI) of Water Transport in Ceramic Substrates," *J. Porous Mater.* 2001 83, vol. 8, no. 3, pp. 193–199, Oct. 2001, doi: 10.1023/A:1012228421764.
- [255] V. Baukh, H. P. Huinink, O. C. G. Adan, S. J. F. Erich, and van der L.G.J. Ven, "Predicting water transport in multilayer coatings," *Polymer (Guildf.)*, vol. 53, no. 15, pp. 3304–3312, Jul. 2012, doi: 10.1016/J.POLYMER.2012.05.043.
- [256] A. Webb and L. Hall, "Evaluation of the use of nuclear magnetic resonance imaging in the study of Fickian diffusion in rubbery polymers. I, Unicomponent solvent ingress," *undefined*, 1990.
- [257] N. J. W. Reuvers, H. P. Huinink, H. R. Fischer, and O. C. G. Adan, "Migration of divalent ions in nylon 6 films," *Polymer (Guildf.)*, vol. 55, no. 8, pp. 2051–2058, Apr. 2014, doi: 10.1016/J.POLYMER.2014.02.059.
- [258] N. J. W. Reuvers, H. P. Huinink, H. R. Fischer, and O. C. G. Adan, "The influence of ions on water transport in nylon 6 films," *Polymer (Guildf.)*, vol. 54, no. 20, pp. 5419–5428, Sep. 2013, doi: 10.1016/J.POLYMER.2013.07.054.
- [259] K. PERRY, P. McDONALD, E. RANDALL, and K. ZICK, "STRAY FIELD MAGNETIC-RESONANCE-IMAGING OF THE DIFFUSION OF ACETONE INTO POLY(VINYL CHLORIDE)," *Polymer (Guildf.)*, vol. 35, no. 13, pp. 2744–2748, 1994, doi: 10.1016/0032-3861(94)90302-6.
- [260] D. Lane and P. McDonald, "The visualization of spatial gradients in polymer and solvent dynamics for mixed solvents ingressing poly(methyl methacrylate) using stray field magnetic resonance imaging," *Polymer (Guildf.)*, vol. 38, no. 10, pp. 2329–2335, 1997, doi: 10.1016/S0032-3861(96)00787-2.
- [261] V. Baukh, H. P. Huinink, O. C. G. Adan, S. J. F. Erich, L. G. J. van der Ven, and T. B. en Ondergrond, "NMR Imaging of Water Uptake in Multilayer Polymeric Films: Stressing the role of Mechanical Stress," *Macromolecules*, vol. 43, no. 8, p. 3882, Apr. 2010, doi: 10.1021/MA1001996.
- [262] D. Capitani, V. Di Tullio, and N. Proietti, "Nuclear Magnetic Resonance to characterize and monitor Cultural Heritage," *Prog. Nucl. Magn. Reson. Spectrosc.*, vol. 64, pp. 29–69, Jul. 2012, doi: 10.1016/J.PNMRS.2011.11.001.
- [263] B. Blümich, S. Anferova, K. Kremer, S. Sharma, V. Herrmann, and A. Segre, "Unilateral Nuclear Magnetic Resonance for Quality Control The NMR-MOUSE," 2003.
- [264] L. V. Angelova, B. Ormsby, and E. Richardson, "Diffusion of water from a range of conservation treatment gels into paint

- films studied by unilateral NMR: Part I: Acrylic emulsion paint," *Microchem. J.*, vol. 124, pp. 311–320, Jan. 2016, doi: 10.1016/J.MICROC.2015.09.012.
- [265] S. Prati *et al.*, "Cleaning oil paintings: NMR relaxometry and SPME to evaluate the effects of green solvents and innovative green gels," *New J. Chem.*, vol. 43, no. 21, pp. 8229–8238, May 2019, doi: 10.1039/C9NJ00186G.
- [266] F. Busse, C. Rehorn, M. Küppers, N. Ruiz, H. Stege, and B. Blümich, "NMR relaxometry of oil paint binders," *Magn. Reson. Chem.*, vol. 58, no. 9, pp. 830–839, Sep. 2020, doi: 10.1002/MRC.5020.
- [267] H. Noh and S. T. Phillips, "Metering the capillary-driven flow of fluids in paper-based microfluidic devices," *Anal. Chem.*, vol. 82, no. 10, pp. 4181–4187, May 2010, doi: 10.1021/AC100431Y/SUPPL\_FILE/AC100431Y\_SI\_005.PDF.
- [268] J. Songok and M. Toivakka, "Controlling capillary-driven surface flow on a paper-based microfluidic channel," *Microfluid. Nanofluidics*, vol. 20, no. 4, pp. 1–9, Apr. 2016, doi: 10.1007/S10404-016-1726-1/FIGURES/10.
- [269] B. Li, L. Yu, J. Qi, L. Fu, P. Zhang, and L. Chen, "Controlling Capillary-Driven Fluid Transport in Paper-Based Microfluidic Devices Using a Movable Valve," *Anal. Chem.*, vol. 89, no. 11, pp. 5707–5712, Jun. 2017, doi: 10.1021/ACS.ANALCHEM.7B00726/ASSET/IMAGES/LARGE/AC-2017-00726T\_0003.JPEG.
- [270] S. Krainer, C. Smit, and U. Hirn, "The effect of viscosity and surface tension on inkjet printed picoliter dots," *RSC Adv.*, vol. 9, no. 54, pp. 31708–31719, 2019, doi: 10.1039/C9RA04993B.
- [271] F. P. Morais and J. M. R. Curto, "Challenges in computational materials modelling and simulation: A case-study to predict tissue paper properties," *Heliyon*, vol. 8, no. 5, May 2022, doi: 10.1016/J.HELIYON.2022.E09356.
- [272] J. Gigac, M. Fišerová, M. Stankovská, and M. Maholányiová, "Prediction of water-absorption capacity and surface softness of tissue paper products using photoclinometry," *O Pap.*, vol. 80, no. 08, pp. 91–97, 2019.
- [273] J. Songok, P. Salminen, and M. Toivakka, "Temperature effects on dynamic water absorption into paper," *J. Colloid Interface Sci.*, vol. 418, pp. 373–377, Mar. 2014, doi: 10.1016/J.JCIS.2013.12.017.
- [274] E. W. Washburn, "The dynamics of capillary flow," *Phys. Rev.*, vol. 17, no. 3, pp. 273–283, 1921, doi: 10.1103/PHYSREV.17.273.
- [275] R. Lucas, "Ueber das Zeitgesetz des kapillaren Aufstiegs von Flüssigkeiten," *Kolloid-Zeitschrift 1918 231*, vol. 23, no. 1, pp. 15–22, Jul. 1918, doi: 10.1007/BF01461107.
- [276] H. Darcy, *Les fontaines publiques de la ville de Dijon*. Paris, 1856.
- [277] J. Andersson, A. Ström, T. Gebäck, and A. Larsson, "Dynamics of capillary transport in semi-solid channels," *Soft Matter*, vol. 13, no. 14, pp. 2562–2570, Apr. 2017, doi: 10.1039/C6SM02305C.
- [278] A. Terzis *et al.*, "Heat release at the wetting front during capillary filling of cellulose micro-substrates," *J. Colloid Interface Sci.*, vol. 504, pp. 751–757, Oct. 2017, doi: 10.1016/J.JCIS.2017.06.027.
- [279] R. Roberts, T. Senden, M. Knackstedt, and M. Lyne, "Spreading of aqueous liquids in unsized papers is by film flow," *J. Pulp Pap. Sci.*, vol. 29, pp. 123–131, 2003.
- [280] B. D. MacDonald, "Flow of liquids through paper," *J. Fluid Mech.*, vol. 852, pp. 1–4, Oct. 2018, doi: 10.1017/JFM.2018.536.
- [281] H. Huinink, *Fluids in porous media: Transport and phase changes*. 2016.
- [282] myHealthbox, "Clariscan 0.5 mmol/ml Oplissing voor | myHealthbox," 2022. <https://myhealthbox.eu/nl/clariscan-05-mmol-ml-oplissing-voor-injectie/5135676> (accessed Mar. 08, 2022).
- [283] G. P. Association, *Physical Properties of Glycerine and Its Solutions*. New York: Glycerine Producers' Association, 1963.
- [284] J. Bolden, Z. Corder, C. Higdon, and C. Miller, "Measuring Surface Tension Using the Pendant Drop Method," 2015, doi: 10675.2/552630.
- [285] J. Anthony Bristow, "Liquid absorption into paper during short time intervals," *Sven. Pap.*, vol. 70, no. 19, pp. 623–629, 1967.
- [286] M. Rohrer, H. Bauer, J. Mintorovitch, M. Requardt, and H. J. Weinmann, "Comparison of magnetic properties of MRI contrast media solutions at different magnetic field strengths," *Invest. Radiol.*, vol. 40, no. 11, pp. 715–724, Nov. 2005, doi: 10.1097/01.RLI.0000184756.66360.D3.
- [287] T. H. Kim, "Pulsed NMR: Relaxation times as function of viscosity and impurities," 2008, pp. 1–5.
- [288] N. Bloembergen, *NUCLEAR MAGNETIC RELAXATION*, 1st ed. Dordrecht: Springer Dordrecht.
- [289] M. M. Tomadakis and T. J. Robertson, "Viscous permeability of random fiber structures: Comparison of electrical and diffusional estimates with experimental and analytical results," *J. Compos. Mater.*, vol. 39, no. 2, pp. 163–188, 2005, doi: 10.1177/0021998305046438.
- [290] W. Hoffmann *et al.*, "Processing of extended shelf life milk using microfiltration," *Int. J. Dairy Technol.*, vol. 59, no. 4, pp. 229–235, Nov. 2006, doi: 10.1111/J.1471-0307.2006.00275.X.
- [291] S. Y. Yang, I. Ryu, H. Y. Kim, J. K. Kim, S. K. Jang, and T. P. Russell, "Nanoporous membranes with ultrahigh selectivity and flux for the filtration of viruses," *Adv. Mater.*, vol. 18, no. 6, pp. 709–712, Mar. 2006, doi: 10.1002/ADMA.200501500.
- [292] J. Chatterjee, S. Pratap, and S. Abdulkareem, "Dual-deposition rates in colloid filtration caused by coupled heterogeneities in a colloidal population," *J. Colloid Interface Sci.*, vol. 356, no. 1, pp. 362–368, Apr. 2011, doi: 10.1016/J.JCIS.2010.12.029.
- [293] B. Jalvo, A. Aguilar-Sanchez, M. X. Ruiz-Caldas, and A. P. Mathew, "Water filtration membranes based on non-woven cellulose fabrics: Effect of nanopolysaccharide coatings on selective particle rejection, antifouling, and antibacterial properties," *Nanomaterials*, vol. 11, no. 7, p. 1752, Jul. 2021, doi: 10.3390/NANO11071752/S1.
- [294] L. M. McDowell-Boyer, J. R. Hunt, and N. Sitar, "Particle transport through porous media," *Water Resour. Res.*, vol. 22, no. 13, pp. 1901–1921, Dec. 1986, doi: 10.1029/WR022I013P01901.
- [295] X. Wang *et al.*, "Surface Wettability for Skin-Interfaced Sensors and Devices," 2022, doi: 10.1002/adfm.202200260.
- [296] W. Liu, H. Cheng, and X. Wang, "Skin-interfaced colorimetric microfluidic devices for on-demand sweat analysis," *npj Flex. Electron.*, vol. 7, no. 1, p. 43, 2023, doi: 10.1038/s41528-023-00275-y.
- [297] Y. Liu *et al.*, "Skin-Interfaced Superhydrophobic Insensible Sweat Sensors for Evaluating Body Thermoregulation and Skin Barrier Functions," *ACS Nano*, vol. 17, no. 6, pp. 5588–5599, Mar. 2023, doi:

- 10.1021/ACSNANO.2C11267/SUPPL\_FILE/NN2C11267\_SI\_002.MP4.
- [298] R. C. Daniel and J. C. Berg, "Spreading on and penetration into thin, permeable print media: Application to ink-jet printing," *Adv. Colloid Interface Sci.*, vol. 123–126, no. SPEC. ISS., pp. 439–469, Nov. 2006, doi: 10.1016/J.CIS.2006.05.012.
- [299] K. Bülow *et al.*, "The penetration depth and lateral distribution of pigment related to the pigment grain size and the calendaring of paper," *Nucl. Instruments Methods Phys. Res. Sect. B Beam Interact. with Mater. Atoms*, vol. 189, no. 1–4, pp. 308–314, Apr. 2002, doi: 10.1016/S0168-583X(01)01076-X.
- [300] D. M. Desjumaux, D. W. Bousfield, T. P. Glatter, and R. L. Van Gilder, "Influence of latex type and concentration on ink gloss dynamics," *Prog. Org. Coatings*, vol. 38, no. 2, pp. 89–95, 2000, doi: 10.1016/S0300-9440(00)00078-3.
- [301] R. Li, Y. Zhang, Y. Cao, and Z. Liu, "Ink Penetration of Uncoated Inkjet Paper and Impact on Printing Quality," *BioResources*, vol. 10, no. 4, pp. 8135–8147, 2015, doi: 10.15376/BIORES.10.4.8135-8147.
- [302] C. H. Koo, A. W. Mohammad, and F. Suja', "Effect of cross-flow velocity on membrane filtration performance in relation to membrane properties," *New pub Balaban*, vol. 55, no. 3, pp. 678–692, Jul. 2014, doi: 10.1080/19443994.2014.953594.
- [303] K. J. Howe and M. M. Clark, "Effect of coagulation pretreatment on membrane filtration performance," *J. / Am. Water Work. Assoc.*, vol. 98, no. 4, 2006, doi: 10.1002/J.1551-8833.2006.TB07641.X.
- [304] G. Boccardo *et al.*, "A review of transport of nanoparticles in porous media: From pore- to macroscale using computational methods," *Nanomater. Detect. Remov. Wastewater Pollut.*, pp. 351–381, Jan. 2020, doi: 10.1016/B978-0-12-818489-9.00013-X.
- [305] S. Lu and J. Forcada, "Preparation and characterization of magnetic polymeric composite particles by miniemulsion polymerization," *J. Polym. Sci. Part A Polym. Chem.*, vol. 44, no. 13, pp. 4187–4203, Jul. 2006, doi: 10.1002/POLA.21525.
- [306] Y. Zhang, J. Cheng, and W. Liu, "Characterization and Relaxation Properties of a Series of Monodispersed Magnetic Nanoparticles," 2019, doi: 10.3390/s19153396.
- [307] Y. Gossuin *et al.*, "Characterization of commercial iron oxide clusters with high transverse relaxivity," *J. Magn. Reson. Open*, vol. 10–11, p. 100054, Jun. 2022, doi: 10.1016/J.JMRO.2022.100054.
- [308] R. J. K. Nicasy *et al.*, "Magnetite-latex nanoparticle motion during capillary uptake in thin, porous layers studied with UFI-NMR," *Colloids Surfaces A Physicochem. Eng. Asp.*, vol. 683, p. 133011, Feb. 2024, Accessed: Dec. 30, 2023. [Online]. Available: <https://linkinghub.elsevier.com/retrieve/pii/S0927775723020952>.
- [309] Q. Dereckx, P. Bacchin, D. Veyret, K. Glucina, and P. Moulin, "Simulation of particle capture in a microfiltration membrane," *Water Sci. Technol.*, vol. 64, no. 6, pp. 1368–1373, 2011, doi: 10.2166/WST.2011.349.
- [310] K.-M. Yao, M. T. Habibian, and C. R. O'melia2, "current research Water and Waste Water Filtration: Concepts and Applications," vol. 5, no. 11, p. 59, 1971, Accessed: Jul. 18, 2023. [Online]. Available: <https://pubs.acs.org/sharingguidelines>.
- [311] P. Le-Clech, V. Chen, and T. A. G. Fane, "Fouling in membrane bioreactors used in wastewater treatment," *J. Memb. Sci.*, vol. 284, pp. 17–53, 2006, doi: 10.1016/j.memsci.2006.08.019.
- [312] S. Song, P. Le-Clech, and Y. Shen, "Microscale fluid and particle dynamics in filtration processes in water treatment: A review," *Water Res.*, vol. 233, p. 119746, 2023, doi: 10.1016/j.watres.2023.119746.
- [313] L. K. Wang, N. K. Shammias, M. Cheryan, Y.-M. Zheng, and S.-W. Zou, "Treatment of Food Industry Foods and Wastes by Membrane Filtration," *Membr. Desalin. Technol.*, pp. 237–269, 2011, doi: 10.1007/978-1-59745-278-6\_6.
- [314] G. Brans, C. G. P. H. Schroën, R. G. M. Van Der Sman, and R. M. Boom, "Membrane fractionation of milk: state of the art and challenges," *J. Memb. Sci.*, vol. 243, pp. 263–272, 2004, doi: 10.1016/j.memsci.2004.06.029.
- [315] Nathalie Tufenkji and Menachem Elimelech, "Correlation Equation for Predicting Single-Collector Efficiency in Physicochemical Filtration in Saturated Porous Media," *Environ. Sci. Technol.*, vol. 38, no. 2, pp. 529–536, 2004, doi: 10.1021/es034049r.
- [316] P. Bacchin, Q. Dereckx, D. Veyret, K. Glucina, and P. Moulin, "Clogging of microporous channels networks: role of connectivity and tortuosity," doi: 10.1007/s10404-013-1288-4.
- [317] R. Van Zwieten, T. Van De Laar, J. Sprakel, and K. Schroën, "From cooperative to uncorrelated clogging in cross-flow microfluidic membranes OPEN," *Sci. RepoRtS* |, vol. 8, p. 5687, 2018, doi: 10.1038/s41598-018-24088-6.
- [318] J.-K. Lee' and B. Y. H. Liu, "A Filtration Model of Microporous Membrane Filters In Liquids," *KSME J.*, vol. 8, no. I, pp. 78–87, 1994.
- [319] C. Lu, Y. Bao, and J.-Y. Huang, "Fouling in membrane filtration for juice processing," 2021, doi: 10.1016/j.cofs.2021.05.004.
- [320] J.-K. Lee and B. Y. H. Liu, "An Experimental Study of Particulate Retention by Microporous Membranes in Liquid Filtration," *KSME J.*, vol. 8, no. I, pp. 69–77, 1994.
- [321] A. Alem, A. Elkawafi, N.-D. Ahfir, and H. Wang, "Filtration of kaolinite particles in a saturated porous medium: hydrodynamic effects," doi: 10.1007/s10040-012-0948-x.
- [322] A. Parvan, S. Jafari, M. Rahnama, S. Norouzi Apourvari, and A. Raouf, "Insight into particle retention and clogging in porous media; a pore scale study using lattice Boltzmann method," *Adv. Water Resour.*, vol. 138, p. 103530, 2020, doi: 10.1016/j.advwatres.2020.103530.
- [323] and D. Y. H. P. Tsz Yan Ling, Jing Wang, "Measurement of Retention Efficiency of Filters against Nanoparticles in Liquids using an Aerosolization Technique," *Environ. Sci. Technol.*, vol. 44, no. 2, pp. 774–779, 2010, doi: 10.1021/es901955e.
- [324] M. Berlin and G. Suresh Kumar, "Numerical modelling on sorption kinetics of nitrogen species in wastewater-applied agricultural field," *Appl. Water Sci.*, vol. 8, no. 8, pp. 1–16, Dec. 2018, doi: 10.1007/S13201-018-0869-5/FIGURES/9.
- [325] K. T. Kubra, M. S. Salman, M. N. Hasan, A. Islam, M. M. Hasan, and M. R. Aual, "Utilizing an alternative composite material for effective copper(II) ion capturing from wastewater," *J. Mol. Liq.*, vol. 336, p. 116325, Aug. 2021, doi: 10.1016/J.MOLLIQ.2021.116325.
- [326] M. R. Aual *et al.*, "Green and robust adsorption and recovery of Europium(III) with a mechanism using hybrid donor

- conjugate materials," *Sep. Purif. Technol.*, vol. 319, p. 124088, Aug. 2023, doi: 10.1016/J.SEPPUR.2023.124088.
- [327] J. Lee and J. Koplik, "Network model for deep bed filtration," *Phys. Fluids*, vol. 13, no. 5, pp. 1076–1086, May 2001, doi: 10.1063/1.1359747.
- [328] A. Zamani and B. Maini, "Flow of dispersed particles through porous media - Deep bed filtration," *J. Pet. Sci. Eng.*, vol. 69, no. 1–2, pp. 71–88, Nov. 2009, doi: 10.1016/J.PETROL.2009.06.016.
- [329] Q. Feng, L. Cha, C. Dai, G. Zhao, and S. Wang, "Effect of particle size and concentration on the migration behavior in porous media by coupling computational fluid dynamics and discrete element method," *Powder Technol.*, vol. 360, pp. 704–714, Jan. 2020, doi: 10.1016/J.POWTEC.2019.10.011.
- [330] J. Fabricius, J. G. I. Hellström, T. S. Lundström, E. Miroshnikov, and P. Wall, "Darcy's Law for Flow in a Periodic Thin Porous Medium Confined Between Two Parallel Plates," *Transp. Porous Media*, vol. 115, no. 3, pp. 473–493, 2016, doi: 10.1007/s11242-016-0702-2.
- [331] J. Moghadasi, H. Müller-Steinhagen, M. Jamialahmadi, and A. Sharif, "Theoretical and experimental study of particle movement and deposition in porous media during water injection," *J. Pet. Sci. Eng.*, vol. 43, no. 3–4, pp. 163–181, Aug. 2004, doi: 10.1016/J.PETROL.2004.01.005.
- [332] K. T. Kubra *et al.*, "The heavy lanthanide of Thulium(III) separation and recovery using specific ligand-based facial composite adsorbent," *Colloids Surfaces A Physicochem. Eng. Asp.*, vol. 667, p. 131415, Jun. 2023, doi: 10.1016/J.COLSURFA.2023.131415.
- [333] P. J. Heard, J. S. Preston, D. J. Parsons, J. Cox, and G. C. Allen, "Visualisation of the distribution of ink components in printed coated paper using focused ion beam techniques," *Colloids Surfaces A Physicochem. Eng. Asp.*, vol. 244, no. 1–3, pp. 67–71, Sep. 2004, doi: 10.1016/J.COLSURFA.2004.05.012.
- [334] A. Lundberg, J. Örtengren, E. Alfthan, and G. Ström, "Paper-ink interactions: Microscale droplet absorption into paper for inkjet printing," *Nord. Pulp Pap. Res. J.*, vol. 26, no. 1, pp. 142–150, 2011, doi: 10.3183/NPPRJ-2011-26-01-P142-150.
- [335] Y. Han, S. O. Manolach, F. Denes, and R. M. Rowell, "Cold plasma treatment on starch foam reinforced with wood fiber for its surface hydrophobicity," *Carbohydr. Polym.*, vol. 86, pp. 1031–1037, 2011, doi: 10.1016/j.carbpol.2011.05.056.
- [336] P. Kumar Kunam, D. Ramakanth, K. Akhila, and K. K. Gaikwad, "Bio-based materials for barrier coatings on paper packaging," *Biomass Convers. Biorefinery*, 2022, doi: 10.1007/s13399-022-03241-2.
- [337] S. Kumar, A. Mukherjee, and J. Dutta, "Biopolymer-Based Food Packaging: Innovations and Technology Applications," *Biopolym. Food Packag. Innov. Technol. Appl.*, pp. 1–490, Apr. 2022, doi: 10.1002/9781119702313.
- [338] K. S. Salem, V. Naithani, H. Jameel, L. Lucia, and L. Pal, "A systematic examination of the dynamics of water-cellulose interactions on capillary force-induced fiber collapse," *Carbohydr. Polym.*, vol. 295, p. 119856, Nov. 2022, doi: 10.1016/J.CARBPOL.2022.119856.
- [339] M. Parada, Peter Vontobel, R. M. Rossi, D. Derome, and J. Carmeliet, "Dynamic Wicking Process in Textiles," *Transp. Porous Media*, vol. 119, pp. 611–632, 2017, doi: 10.1007/s11242-017-0901-5.
- [340] A. Salam, R. A. Venditti, J. J. Pawlak, and K. El-Tahlawy, "Crosslinked hemicellulose citrate-chitosan aerogel foams," *Carbohydr. Polym.*, vol. 84, pp. 1221–1229, 2011, doi: 10.1016/j.carbpol.2011.01.008.
- [341] K. P. M. Tang, Y. S. Wu, K. H. Chau, C. W. Kan, and J. T. Fan, "Characterizing the transplanar and in-plane water transport of textiles with gravimetric and image analysis technique: Spontaneous Uptake Water Transport Tester," *Sci. Rep.*, vol. 5, no. 1, pp. 1–6, 2015, doi: 10.1038/srep09689.
- [342] H. Zhang *et al.*, "A sustainable nanocellulose-based superabsorbent from kapok fiber with advanced oil absorption and recyclability," *Carbohydr. Polym.*, vol. 278, p. 118948, 2022, doi: 10.1016/j.carbpol.2021.118948.
- [343] X. Z. Tang, P. Kumar, S. Alavi, and K. P. Sandeep, "Recent Advances in Biopolymers and Biopolymer-Based Nanocomposites for Food Packaging Materials," *Crit Rev Food Sci Nutr.*, vol. 52, no. 5, pp. 426–442, May 2012, doi: 10.1080/10408398.2010.500508.
- [344] C. Berli, S. Claudio, L. A. Berli, E. Elizalde, R. Urteaga, and C. L. A. Berli, "Rational design of capillary-driven flows for paper-based microfluidics," *Lab Chip*, vol. 15, no. 10, pp. 2173–2180, May 2015, doi: 10.1039/C4LC01487A.
- [345] C. Cui *et al.*, "Hydrophobic Biopolymer-Based Films: Strategies, Properties, and Food Applications," *Food Eng. Rev.* 2023 152, vol. 15, no. 2, pp. 360–379, Apr. 2023, doi: 10.1007/S12393-023-09342-6.
- [346] T. N. T. Rohadi, M. J. M. Ridzuan, M. S. A. Majid, E. M. Cheng, M. J. Norasni, and N. Marsi, "Swelling Behaviors of Composite film with Alternating Fibre Reinforcement and Aqueous Media," *J. Phys. Conf. Ser.*, vol. 2051, no. 1, 2021, doi: 10.1088/1742-6596/2051/1/012024.
- [347] J. Xu, F. Liu, T. Wang, H. D. Goff, and F. Zhong, "Fabrication of films with tailored properties by regulating the swelling of collagen fiber through pH adjustment," *Food Hydrocoll.*, vol. 108, p. 106016, Nov. 2020, doi: 10.1016/j.foodhyd.2020.106016.
- [348] C. M. Bosanquet, "On the flow of liquid into capillary tubes," *London, Edinburgh, Dublin Philos. Mag. J. Sci.*, vol. 45, no. 267, pp. 525–531, 1923, doi: 10.1080/14786442308634144.
- [349] L. Rostom, S. Caré, and | Denis Courtier-Murias, "Analysis of water content in wood material through 1D and 2D 1 H NMR relaxometry: Application to the determination of the dry mass of wood," *Magn. Reson. Chem.*, vol. 59, no. 6, pp. 614–627, 2021, doi: 10.1002/mrc.5125.
- [350] D. Topgaard and O. Söderman, "Diffusion of water absorbed in cellulose fibers studied with 1H-NMR," *Langmuir*, vol. 17, no. 9, pp. 2694–2702, May 2001, doi: 10.1021/LA000982L/ASSET/IMAGES/LARGE/LA000982LF00016.JPEG.
- [351] M. Jablonsky, M. Botková, Š. Šutý, L. Šmatko, and Š. Jozef, "Accelerated Ageing of Newsprint Paper: Changes in Swelling Ability, WRV and Electrokinetic Properties of Fibres," *FIBRES Text. East. Eur.*, vol. 22, no. 2, pp. 108–113, Jan. 2014, Accessed: Jun. 09, 2023. [Online]. Available: [https://www.academia.edu/79471062/Accelerated\\_Ageing\\_of\\_Newsprint\\_Paper\\_Changes\\_in\\_Swelling\\_Ability\\_WRV\\_and\\_Electrokinetic\\_Properties\\_of\\_Fibres](https://www.academia.edu/79471062/Accelerated_Ageing_of_Newsprint_Paper_Changes_in_Swelling_Ability_WRV_and_Electrokinetic_Properties_of_Fibres).
- [352] M. Botková, Š. Šutý, M. Jablonský, L. Kucerová, and M. Vrška, "Monitoring of kraft pulps swelling in water," *Cellul. Chem. Technol.*, vol. 47, no. 2, pp. 95–102, 2013, Accessed: Feb. 01, 2023. [Online]. Available: [https://www.academia.edu/31875970/Monitoring\\_of\\_kraft\\_pulps\\_swelling\\_in\\_water](https://www.academia.edu/31875970/Monitoring_of_kraft_pulps_swelling_in_water).

- [353] R. J. K. Nicasy, C. Waldner, S. J. F. Erich, O. C. G. Adan, U. Hirn, and H. P. Huinink, "Liquid uptake in porous cellulose sheets studied with UFI-NMR: Penetration, swelling and air displacement," *Carbohydr. Polym.*, vol. 326, p. 121615, Feb. 2024, doi: 10.1016/J.CARBPOL.2023.121615.
- [354] M. Ilyas, W. Ahmad, H. Khan, S. Yousaf, K. Khan, and S. Nazir, "Plastic waste as a significant threat to environment - A systematic literature review," *Rev. Environ. Health*, vol. 33, no. 4, pp. 383–406, Dec. 2018, doi: 10.1515/REVEH-2017-0035/ASSET/GRAPHIC/J\_REVEH-2017-0035\_FIG\_005.JPG.
- [355] J. G. B. Derraik, "The pollution of the marine environment by plastic debris: a review Jos e e G," *Mar. Pollut. Bull.*, vol. 44, no. 9, pp. 842–852, 2002, doi: 10.1016/S0025-326X(02)00220-5.
- [356] R. Dziuba, M. Kucharska, L. Madej-Kielbik, K. Sulak, and M. Wiśniewska-Wrona, "Biopolymers and Biomaterials for Special Applications within the Context of the Circular Economy," *Mater. 2021, Vol. 14, Page 7704*, vol. 14, no. 24, p. 7704, Dec. 2021, doi: 10.3390/MA14247704.
- [357] K. Babaremu, O. P. Oladijo, and E. Akinlabi, "Biopolymers: A suitable replacement for plastics in product packaging," *Adv. Ind. Eng. Polym. Res.*, vol. 6, no. 4, pp. 333–340, Oct. 2023, doi: 10.1016/J.AIEPR.2023.01.001.
- [358] V. T. Weligama Thuppahige and M. A. Karim, "A comprehensive review on the properties and functionalities of biodegradable and semibiodegradable food packaging materials," *Compr. Rev. Food Sci. Food Saf.*, vol. 21, no. 1, pp. 689–718, Jan. 2022, doi: 10.1111/1541-4337.12873.
- [359] A. H. Tayeb, M. Tajvidi, and D. Bousfield, "Paper-Based Oil Barrier Packaging using Lignin-Containing Cellulose Nanofibrils," *Mol. 2020, Vol. 25, Page 1344*, vol. 25, no. 6, p. 1344, Mar. 2020, doi: 10.3390/MOLECULES25061344.
- [360] A. Rida, L. Yang, R. Vyas, and M. M. Tentzeris, "Conductive inkjet-printed antennas on flexible low-cost paper-based substrates for RFID and WSN applications," *IEEE Antennas Propag. Mag.*, vol. 51, no. 3, pp. 13–23, 2009, doi: 10.1109/MAP.2009.5251188.
- [361] A. Böhm and M. Biesalski, "Paper-based microfluidic devices: A complex low-cost material in high-tech applications," *MRS Bull.*, vol. 42, no. 5, pp. 356–364, May 2017, doi: 10.1557/MRS.2017.92.
- [362] X. Li, J. Tian, and W. Shen, "Progress in patterned paper sizing for fabrication of paper-based microfluidic sensors," *Cellulose*, vol. 17, no. 3, pp. 649–659, Jun. 2010, doi: 10.1007/S10570-010-9401-2/FIGURES/8.
- [363] D. B. Szlek, B. Reynolds, and M. A. Hubbe, "Hydrophobic Molecular Treatments of Cellulose-based or Other Polysaccharide Barrier Layers for Sustainable Food Packaging: A Review," *BioResources*, vol. 17, no. 2, pp. 3551–3673, 2022, doi: 10.15376/BIORES.17.2.SZLEK.
- [364] P. Vernhes, J. F. Bloch, A. Blayo, and B. Pineaux, "Effect of calendaring on paper surface micro-structure: A multi-scale analysis," *J. Mater. Process. Technol.*, vol. 209, no. 11, pp. 5204–5210, Jun. 2009, doi: 10.1016/j.jmatprotec.2009.03.005.
- [365] P. Resch, U. Hirn, and W. Bauer, "Calendering effects on coating pore structure and ink setting behavior," *TAPPI J.*, vol. 9, no. 1, pp. 27–35, 2010.
- [366] R. J. K. Nicasy, C. Waldner, S. J. F. Erich, O. C. G. Adan, U. Hirn, and H. P. Huinink, "Liquid penetration in hydrophobized cellulose based sheets," *Cellulose*, vol. Submitted, 2024.
- [367] P. Shallhorn and N. Gurnagul, "A SIMPLE MODEL OF THE AIR PERMEABILITY OF PAPER," in *Advances in Pulp and Paper Research*, 2009, pp. 475–490, doi: 10.15376/frc.2009.1.475.
- [368] T. Seidlhofer, U. Hirn, S. Teichtmeister, and M. H. Ulz, "Hygro-coupled viscoelastic viscoplastic material model of paper," *J. Mech. Phys. Solids*, vol. 160, p. 104743, Mar. 2022, doi: 10.1016/J.JMPS.2021.104743.
- [369] A. Blanco, G. González, E. Casanova, M. E. Pirela, and A. Briceño, "Mathematical Modeling of Hydrogels Swelling Based on the Finite Element Method," *Appl. Math.*, vol. 2013, no. 08, pp. 161–170, Jul. 2013, doi: 10.4236/AM.2013.48A022.
- [370] N. Benmessaoud, S. Hamri, T. Bouchaour, and U. Maschke, "Swelling and thermal behavior of a cross-linked polymer networks poly(2-phenoxyethyl acrylate): exploitation by the Voigt viscoelastic model," *Polym. Bull.*, vol. 77, no. 10, pp. 5567–5588, Oct. 2020, doi: 10.1007/S00289-019-03040-2/TABLES/3.
- [371] N. Yavari and S. Azizian, "Mixed diffusion and relaxation kinetics model for hydrogels swelling," 2022, doi: 10.1016/j.molliq.2022.119861.
- [372] K. Zhang, W. Feng, and C. Jin, "Protocol efficiently measuring the swelling rate of hydrogels," *MethodsX*, vol. 7, p. 100779, Jan. 2020, doi: 10.1016/J.MEX.2019.100779.
- [373] T. Arends, L. Pel, and D. Smeulders, "Moisture penetration in oak during sinusoidal humidity fluctuations studied by NMR," *Constr. Build. Mater.*, vol. 166, pp. 196–203, Mar. 2018, doi: 10.1016/J.CONBUILDMAT.2018.01.133.
- [374] S. Saft and M. Kaliske, "A hybrid interface-element for the simulation of moisture-induced cracks in wood," *Eng. Fract. Mech.*, vol. 102, pp. 32–50, Apr. 2013, doi: 10.1016/J.ENGFRACTMECH.2013.02.010.
- [375] X. Ma, B. Maillat, L. Brochard, O. Pitois, R. Sidi-Boulouar, and P. Coussot, "Vapor-sorption Coupled Diffusion in Cellulose Fiber Pile Revealed by Magnetic Resonance Imaging," *Phys. Rev. Appl.*, vol. 17, no. 2, p. 024048, Feb. 2022, doi: 10.1103/PHYSREVAPPLIED.17.024048/FIGURES/11/MEDIUM.
- [376] S. Berg *et al.*, "Real-time 3D imaging of Haines jumps in porous media flow," *Proc. Natl. Acad. Sci. U. S. A.*, vol. 110, no. 10, pp. 3755–3759, Mar. 2013, doi: 10.1073/PNAS.1221373110.
- [377] Z. Sun and Z. Santamarina, "Haines jumps: Pore scale mechanisms," *Phys. Rev. E*, vol. 100, no. 2, 2019, doi: 10.1103/physreve.100.023115.
- [378] A. O'Brien, S. Afkhami, and M. Bussmann, "Pore-scale direct numerical simulation of Haines jumps in a porous media model," *Eur. Phys. J. Spec. Top. 2020 22910*, vol. 229, no. 10, pp. 1785–1798, Sep. 2020, doi: 10.1140/EPJST/E2020-000008-0.
- [379] A. Ozcan, S. Sonmez, and D. Tutak, "Effect of coating pigment type on paper printability with water-based inks," *J. Coatings Technol. Res.*, vol. 19, no. 4, pp. 1149–1157, Jul. 2022, doi: 10.1007/S11998-021-00593-8/TABLES/7.
- [380] N. Jürgensen, M. Pietsch, X. Hai, S. Schliske, and G. Hernandez-Sosa, "Green ink formulation for inkjet printed transparent electrodes in OLEDs on biodegradable substrates," *Synth. Met.*, vol. 282, p. 116930, Dec. 2021, doi: 10.1016/J.SYNTHMET.2021.116930.
- [381] L. Zhao, C. Hong, C. Wang, J. Li, H. Ren, and C. Zhou, "Enhancement of the adhesion strength of water-based ink binder

- based on waterborne polyurethane," *Prog. Org. Coatings*, vol. 183, p. 107765, Oct. 2023, doi: 10.1016/J.PORGOAT.2023.107765.
- [382] Y. Duan, Y. Huo, and L. Duan, "Preparation of acrylic resins modified with epoxy resins and their behaviors as binders of waterborne printing ink on plastic film," *Colloids Surfaces A Physicochem. Eng. Asp.*, vol. 535, pp. 225–231, Dec. 2017, doi: 10.1016/J.COLSURFA.2017.09.041.
- [383] N. Toda, T. Nakagawa, N. Hidefumi, J. Furukawa, H. Kobayashi, and K. Nagai, "Advanced water-based latex-inks for film media," *Int. Conf. Digit. Print. Technol.*, vol. 2014-January, pp. 353–356, 2014, Accessed: Feb. 12, 2024. [Online]. Available: [https://jglobal.jst.go.jp/en/detail?JGLOBAL\\_ID=201902204586854732](https://jglobal.jst.go.jp/en/detail?JGLOBAL_ID=201902204586854732).
- [384] C. Gao, T. Xing, X. Hou, and G. Chen, "The influence of ink viscosity, water and fabric construction on the quality of ink-jet printed polyester," *Color. Technol.*, vol. 136, no. 1, pp. 45–59, Feb. 2020, doi: 10.1111/COTE.12439.
- [385] B. A. Arthur, R. P. Smith, S. Lavrykov, and B. V. Ramarao, "Imaging of ink jet penetration in uncoated paper using microscopic techniques," *Tappi J.*, vol. 10, no. 11, pp. 35–40, Dec. 2011, doi: 10.32964/TJ10.11.35.
- [386] U. Mattila, K. Tahkola, S. Nieminen, and M. Kleen, "Penetration and separation of coldset ink resin and oils in uncoated paper studied by chromatographic methods," *Nord. Pulp Pap. Res. J.*, vol. 18, no. 4, pp. 413–420, Dec. 2003, doi: 10.3183/NPPRJ-2003-18-04-P413-420/MACHINEREADABLECITATION/RIS.
- [387] M. A. Hubbe, D. J. Gardner, and W. Shen, "Wettability of cellulotics," *BioResources*, vol. 10, no. 4, pp. 8657–8749, 2015.
- [388] S. Sousa, J. A. Gamelas, A. De Oliveira Mendes, P. T. Fiadeiro, and A. Ramos, "Interactions of ink colourants with chemically modified paper surfaces concerning inkjet print improvement," *Mater. Chem. Phys.*, vol. 139, no. 2–3, pp. 877–884, May 2013, doi: 10.1016/J.MATCHEMPHYS.2013.02.048.
- [389] T. Costa, J. Gamelas, I. Moutinho, M. Figueiredo, and P. Ferreira, "The influence of paper surface sizing on inkjet pigment penetration," *Appita J.*, vol. 63, pp. 392–398, 2010.
- [390] J. Schoelkopf, P. A. C. Gane, C. J. Ridgway, and G. P. Matthews, "Influence of Inertia on Liquid Absorption into Paper Coating Structures."
- [391] J. Kettle, T. Lamminmäki, and P. Gane, "A review of modified surfaces for high speed inkjet coating," 2009, doi: 10.1016/j.surfcoat.2009.10.035.
- [392] M. Zea, A. Moya, R. Villa, and G. Gabriel, "Reliable Paper Surface Treatments for the Development of Inkjet-Printed Electrochemical Sensors," *Adv. Mater. Interfaces*, vol. 9, no. 21, Jul. 2022, doi: 10.1002/ADMI.202200371.
- [393] R. Sang, S. Yang, and Z. Fan, "Effects of MDF Substrate Surface Coating Process on UV Inkjet Print Quality," *Coatings* 2023, Vol. 13, Page 970, vol. 13, no. 5, p. 970, May 2023, doi: 10.3390/COATINGS13050970.
- [394] J. W. Goodwin, R. H. Ottewill, R. Pelton, G. Vianello, and D. E. Yates, "CONTROL OF PARTICLE SIZE IN THE FORMATION OF POLYMER LATICES," *Br Polym J*, vol. 10, no. 3, pp. 173–180, 1978, doi: 10.1002/PI.4980100304.
- [395] I. H. Harding, "Amphoteric polystyrene latex colloids: polymerization pathway and the control of particle size and potential," *Colloid Polym. Sci.*, vol. 263, no. 1, pp. 58–66, Jan. 1985, doi: 10.1007/BF01411249/METRICS.
- [396] S.-E. Shim, Y.-J. Cha, J.-M. Byun, and S. Choe, "Size Control of Polystyrene Beads by Multistage Seeded Emulsion Polymerization," 1999, doi: 10.1002/(SICI)1097-4628(19990328)71:13.
- [397] J. Ding, G. Xue, Q. Dai, and R. Cheng, "Glass transition temperature of polystyrene microparticles," *Polymer (Guildf).*, vol. 34, no. 15, pp. 3325–3327, Jan. 1993, doi: 10.1016/0032-3861(93)90412-4.
- [398] J. C. Grunlan, Y. Ma, M. A. Grunlan, W. W. Gerberich, and L. F. Francis, "Monodisperse latex with variable glass transition temperature and particle size for use as matrix starting material for conductive polymer composites," *Polymer (Guildf).*, vol. 42, no. 16, pp. 6913–6921, Jul. 2001, doi: 10.1016/S0032-3861(01)00158-6.
- [399] C. C. Ho and M. C. Khew, "Low glass transition temperature (Tg) rubber latex film formation studied by atomic force microscopy," *Langmuir*, vol. 16, no. 6, pp. 2436–2449, Mar. 2000, doi: 10.1021/LA990192F/ASSET/IMAGES/LARGE/LA990192FF00013.JPEG.
- [400] I. Szilágyi, D. Rosická, J. Hierrezuelo, and M. Borkovec, "Charging and stability of anionic latex particles in the presence of linear poly(ethylene imine)," *J. Colloid Interface Sci.*, vol. 360, no. 2, pp. 580–585, Aug. 2011, doi: 10.1016/J.JCIS.2011.04.106.

---

# Summary

---

## Towards NMR imaging of ink penetration in paper

The printing industry is undergoing a significant shift towards water-based inks for economic and environmental reasons. These inks are complex mixtures composed of multiple components, such as water, co-solvent, latex, and pigment particles. Furthermore, with the rise of multiple paper-based applications, including various packaging materials, the printing process has become extremely diverse. To increase print quality, sustainability, and performance of these applications, adjustments to the paper, ink and printing processes are required. For water-based inks, the highest print quality is obtained when pigment particles remain at the surface of the medium. However, due to multiple processes, such as capillary suction, ink will carry these pigment particles in the medium. To enhance these applications, a better understanding of the printing process is required, which includes processes such as liquid penetration, particle penetration and deformations within a paper sheet.

Modern printing is characterized by remarkable speed, with industrial digital printers achieving speeds exceeding 100 pages per minute (PPM). Therefore, ink penetration must occur extremely fast, mostly within fractions of a second. Furthermore, most print media are based on paper sheets, having dimensions around 100  $\mu\text{m}$ . These high speeds and thin media put a lot of constraints on temporal and spatial resolution when studying these processes experimentally. Prior to this research, no experimental technique was capable of coping with the extreme spatial and temporal requirements simultaneously. Therefore, spatially resolved information, such as liquid or particle distributions during penetration could not be measured, resulting in a limited amount of information. Consequently, it becomes extremely difficult to verify theoretical models for liquid and particle penetration. **In this thesis, a novel Ultra-Fast Imaging NMR method (UFI) is introduced, which, for the first time, allowed to study the penetration of complex liquids in thin, porous media, such as paper with sufficient temporal (< 10 ms) and spatial resolution (< 14.5 -18  $\mu\text{m}$ ).**

First, the UFI method was introduced, which allowed measurements of moisture distributions and deformations within thin, porous layers. The UFI NMR method uses a GARField NMR setup, a modified Ostroff-Waugh pulse sequence and a contrast agent to optimize the penetrating liquids NMR relaxation times. By studying droplet penetrations, on thin, porous membranes, this work showed that **models for liquid penetration such as Darcy, which are valid in millimeter sized samples, are also valid on the microscale.** After validating the newly invented method, the study was focused on three main topics, which paved the way towards measuring ink penetration in paper, namely: particle transport in thin, porous layer, liquid transport in paper sheets, and finally transport of particle mixtures in paper sheets.

Because one of the main components of water-based inks, crucial for print quality, are latex particles, a large part of this study was devoted to monitoring and understanding latex particle transport. To make the latex particles visible within UFI, iron oxide, a well-known magnetic component, was incorporated within the particles. The iron oxide allowed to quantify latex particle concentrations and visualize them during transport. This was demonstrated by monitoring the transport of particle suspensions within nylon



membrane filters. From these measurements, the particles penetration depth and concentration profiles could be determined experimentally on timescales comparable to printing. These profiles could be verified by Scanning Electron Microscopy images. After establishing the visualization of particles, the effect of particles upon the penetration was investigated. **The penetration of the particle solution could be linked to a Darcy model, which showed that for typical latex particles, having a particle radius around 40 nm, and a paper, with a micrometer sized pore radius, the droplet penetration speed decreases due to particle induced changes in the viscosity and surface tension of the mixtures.** Besides the effect on liquid imbibition, it was shown that for typical latex particles, having a particle radius around 40 nm, and a porous membrane, having a 200 – 500 nm sized pore radius, the **particles also influenced the particle penetration depth, where higher initial particle concentrations resulted in an increase in penetration depth.**

Because printing is mostly performed on paper-based media, penetration should be studied in paper-like materials. However, the penetration in paper is extremely complex due to the interplay of multiple processes, such as capillary action, swelling, inter- and intra-fiber transport, and film flow, this thesis first studied the penetration of water-based liquids in paper sheets before moving to model inks. By measuring the transport of a water-based liquid, crucial features about the penetration process were extracted. First, it was shown that the penetration in paper could be split in different phases, and that the phases are influenced by the paper type. **In hydrophilic, lowly calendered paper, penetration happens in three phases: Darcy based capillary uptake, swelling and the removal of entrapped air.** For hydrophilic, highly calendered paper, swelling started to influence the penetration process. Furthermore, **Darcy correctly predicted a decrease in liquid uptake for calendered papers, coming from a reduction in permeability induced by the compression forces of the calendering process.** Finally, for hydrophobic paper, where capillary uptake is not possible, fibers are first prewet by phenomena such as film flow, vapor transport or flow of liquid in the fibers, and a first swelling phase. **After wetting the fibers, water enters the paper sheet by a finger-like filling of the pore spaces,** which initiates a second swelling phase. Quantification of these phases is crucial when moving towards real model inks. In these systems, UFI signals will be used to extract particle concentrations during penetration. Therefore, it becomes important to identify all liquid phases correctly, which makes these measurements with water-based liquids so crucial.

To approximate the printing process, the transport of a model ink, containing both liquid and particles within a hydrophilic paper sample were studied. These measurements revealed that **within non-coated hydrophilic paper, with typical micrometer sized pores, liquid penetration was governed by a Darcy like model and that particles, having a typical radius of 50 nm, were carried along with the solvent phase and were homogeneously distributed throughout the wet region.** These measurements also revealed that within these systems particles penetrate quite deeply within the medium, which is unwanted for optimum print quality.

In this work, we successfully developed an NMR-based method able to measure the penetration of a model ink within a paper-based media which opens the way towards NMR imaging of ink penetration in all types of paper-based materials. This leads to a better understanding of the printing process and makes way for improved print quality on everyday applications, such as office prints and your daily delivered packages.

# Samenvatting

---

## De weg van NMR naar de beeldvorming van inkt penetratie in papier

Door de vele milieuvriendelijk en economische doelstellingen ondergaat de printindustrie een ware transitie. De printindustrie omvat heel wat drukprocessen. In deze processen zijn inkt en het te bedrukken materiaal (printmedium) een cruciale factor. Wil men aan de nieuwe doelstellingen voldoen en de printkwaliteit behouden, zijn aanpassingen aan inkt, papier en printproces nodig.

Voor de inkt kijkt men naar nieuwe water gebaseerde inkten. Deze inkten zijn complexe mengsels samengesteld uit meerdere componenten, zoals water, co-solvent, latex en pigmentdeeltjes. De hoogste printkwaliteit voor water gebaseerde inkten wordt verkregen wanneer de pigmentdeeltjes aan het oppervlak van het medium blijven. Als gevolg van meerdere processen, zoals capillaire penetratie, zullen de pigmentdeeltjes samen met de inkt het medium binnendringen. Om inktpenetratie te verbeteren, is het belangrijk om processen zoals vloeistofpenetratie, penetratie van deeltjes en papier vervormingen beter te begrijpen.

Daarnaast, is er een toename in papier gebaseerde toepassingen, waaronder verschillende verpakkingsmaterialen die allemaal bedrukt moeten worden. Hierdoor is het drukproces uiterst divers geworden.

De huidige printprocessen worden gekenmerkt door opmerkelijke snelheden. Industriële digitale printers bereiken snelheden van meer dan 100 pagina's per minuut (PPM). Daarom moet inktpenetratie zeer snel plaatsvinden, meestal binnen fracties van een seconde. Bovendien zijn de meeste printmedia gebaseerd op papier met een typische dikte van ongeveer 100  $\mu\text{m}$ . Deze hoge printsnelheden en dunne printmedia leggen veel beperkingen op aan de tijd en ruimtelijke resolutie nodig bij het experimenteel bestuderen van deze processen. Voorafgaand aan deze studie was er geen enkele experimentele techniek in staat om gelijktijdig aan dergelijke extreme eisen te voldoen. Daarom kon plaatsafhankelijke informatie, zoals vloeistof- of deeltjesverdelingen tijdens penetratie, niet worden gemeten, wat resulteerde in een beperkte hoeveelheid informatie. Bijgevolg wordt het uiterst moeilijk om theoretische modellen voor vloeistof- en deeltjespenetratie te verifiëren.

**In deze thesis wordt een nieuwe Ultra-Snelle NMR-methode (UFI) geïntroduceerd, die ons voor het eerst in staat stelt om de penetratie van complexe vloeistoffen in dunne, poreuze media, zoals papier, te bestuderen met voldoende tijdsresolutie ( $< 10$  ms) en plaatsresolutie ( $< 14.5 - 18$   $\mu\text{m}$ ).**

In het eerste deel wordt de UFI methode geïntroduceerd. De methode maakt het mogelijk om vochtverdelingen en vervormingen binnen dunne, poreuze lagen te meten. De Ultra-Snelle (UFI) NMR-methode maakt gebruik van een GARField NMR opstelling, een gemodificeerde Ostroff-Waugh pulssequentie en een contrastmiddel om de NMR relaxatie tijden van de vloeistoffen te optimaliseren. De indringing van druppels op dunne, poreuze membranen, ttonde aan dat **modellen voor vloeistof opname, zoals Darcy, die geldig zijn in millimetergrote samples, ook geldig zijn op microschaal.**

In het tweede deel, na validatie van de nieuw ontwikkelde methode, werd de opname van complexe vloeistoffen in papier en dunne lagen onderzocht. Dit onderzoek werd opgedeeld in drie hoofdonderwerpen: transport van deeltjes in dunne, poreuze lagen, vloeistoftransport in papier en ten slotte transport van deeltjesmengsels in vellen papier.

Omdat latex deeltjes een van de belangrijkste componenten zijn in water gebaseerde inkten, werd een groot deel van dit onderzoek besteed aan het bestuderen en begrijpen van het transport van latexdeeltjes. Om de latexdeeltjes zichtbaar te maken, werd ijzeroxide, een bekende magnetisch component, geïntroduceerd in de deeltjes. Dit ijzeroxide maakt de deeltjes magnetisch actief en zorgt ervoor dat de concentratie latexdeeltjes gekwantificeerd en gevisualiseerd kan worden tijdens transport. Dit werd gedemonstreerd door de opname van deeltjessuspensies in nylon membraanfilters te bestuderen. Uit deze metingen konden de penetratiediepte van de deeltjes en concentratieprofielen experimenteel worden bepaald op tijdschalen vergelijkbaar met een echt print proces. Deze metingen konden worden geverifieerd door Scanning Elektronen Microscopie. Na de visualisatie van de deeltjes werd het effect van de deeltjes op de penetratie onderzocht.

**De opname van de deeltjesoplossingen kon worden gekoppeld aan een Darcy-model. Dit toonde aan dat voor typische latexdeeltjes, met een deeltjesstraal van ongeveer 40 nm, en papier, met een micrometergrootte porie straal, de snelheid van de druppelpenetratie afneemt dankzij veranderingen in de viscositeit en oppervlaktespanning van de oplossingen veroorzaakt door de deeltjes.**

Naast het effect op vloeistofopname werd ook aangetoond dat voor typische latexdeeltjes, met een deeltjesstraal van ongeveer 40 nm, en een poreus membraan, met een porie straal van 200 - 500 nm, de **deeltjes ook een effect hadden op de penetratiediepte van de deeltjes, waarbij hogere initiële concentraties resulteerden in een toename van de penetratiediepte.**

Omdat printen voornamelijk gebeurt op papierachtige media, is het noodzakelijk dat de penetratie wordt bestudeerd in papierachtige materialen. Omdat de penetratie in papier uiterst complex is door de wisselwerking van meerdere processen, zoals capillaire kracht, zwelling, inter- en intra-vezeltransport, en filmstroming, bestudeerde deze thesis eerst de penetratie van water gebaseerde vloeistoffen in vellen papier. Daarna werd geschakeld naar modelinkten.

Door het transport van waterige oplossingen te bestuderen, werden cruciale kenmerken over het penetratieproces onthuld. Ten eerste werd aangetoond dat de penetratie in papier kon worden opgesplitst in verschillende fasen, die beïnvloed worden door het type papier. **In hydrofiel, licht gecalendered papier, vindt penetratie plaats in drie fasen: Darcy-gebaseerde capillaire opname, zwelling en de diffusie van ingesloten lucht.** Voor hydrofiel, sterk gecalendered papier wordt het penetratieproces beïnvloed door zwelling. Bovendien kan Darcy correct een afname in vloeistofopname voorspellen voor gecalendered papier, gerelateerd aan een lagere permeabiliteit afkomstig van de compressiekrachten tijdens het calendering proces. Ten slotte, voor hydrofobe papieren, waar capillaire opname niet mogelijk is, worden vezels eerst bevochtigd door processen zoals filmstroming, damptransport of vloeistoftransport doorheen de vezels, en een eerste zwelfase. **Na het bevochtigen van de vezels,**

**dringt water het papier in met een vingerachtige vulling van de porieruimten,** wat een tweede zwelfase initieert. Het correct in kaart brengen van deze fasen is cruciaal bij de overgang naar echte modelinkten. In deze systemen zullen UFI-signalen worden gebruikt om de deeltjesconcentraties tijdens penetratie te bepalen. Daarom is het cruciaal om alle vloeibare fasen correct te identificeren.

Om het printproces zo goed mogelijk te benaderen, werd de opname van een modelinkt, met zowel vloeistof als deeltjes, in een hydrofiel papier bestudeerd. Deze metingen onthulden dat in niet-gecoate hydrofiële papieren, met typische micrometergrote poriën, de penetratie van vloeistof beschreven kan worden door een Darcy-achtig model en dat deeltjes, met een typische straal van 50 nm, werden meegevoerd door het oplosmiddel en gelijkmatig werden verdeeld over het bevochtigde gebied. Tenslotte werd aangetoond dat in deze systemen de deeltjes vrij diep doordringen in het medium, wat ongewenst is voor optimale printkwaliteit.

In deze thesis hebben we met succes een op NMR gebaseerde methode ontwikkeld die in staat is om de penetratie van een modelinkt binnen een papierachtig medium te meten, wat de weg opent naar NMR-beeldvorming van inktpenetratie in alle soorten materialen van papier. Op die manier kunnen printkwaliteit en printproces beter afgestemd worden op vele en steeds hoger eisende milieu- en economische doelstellingen.



# Acknowledgements

---

Finally, after four wonderful years, I can proudly present my PhD thesis. Despite encountering multiple challenges along the way, I will always remember the beautiful memories and remarkable individuals who crossed my path during this period. Without them, this thesis would never be possible, and therefore they all deserve a word of thanks.

First and foremost, I want to thank my supervisors, Henk, Bart, and Olaf, for believing in me and for giving me the opportunity to follow my dream and pursue a career in research. Without their support, I doubt I could have provided the work you all have in your hands right now. Their support, both scientific and personal, helped me navigate through all obstacles. When I started my PhD journey, some might describe my early approach as somewhat chaotic and challenging to follow. Thanks to Henk and Olaf, this chaotic person transformed into an organized and structured PhD student ready to tackle the world. Next to this was Bart, my NMR mentor, who taught me all the tips and tricks about the experimental setups, his baby's as he called them. Bart is a complex person whose intellect operates at a hypersonic speed, which both helped me a lot but also gave me a lot of headaches. He was always willing to assist, even at the expense of his own workload and I want to thank him for that.

Special recognition goes to Joey, my roommate and colleague for almost four years. In every professional career, the hope is to encounter colleagues like Joey. Someone who not only brings laughter but also provides a helping hand in times of need. He provided me with some beautiful SEM images, including the one on the cover of this thesis. I will always remember our chess breaks, though perhaps extending my PhD timeline. I cannot remember the final score, but I am pretty sure I won. Maybe I should ask Joey.

I am also thankful to Tim, my fellow NMR PhD colleagues, for our shared commitment to our NMR setups. Working side by side on similar setups made us partners in crime, as we navigated through the challenges and triumphs of our NMR experiments and setups. While the setups yielded incredible results, I don't want to count the hours Tim and I dedicated to troubleshooting and repairing these machines.

To all the members of the TPM group who worked alongside me, Jelle, Kevin, Rodrigo, Elena, Dasol, Martina, Michaela, Leo, Klaas, Carola, Aleksandr, Renee, Ahmed, Hartmut, Suzanne, Rozeline, Xiaoxiao, Wendy, Stan, Verena, Lars, Ruben, Natalia, Myrthe, Evelien, Leyla, Suzanne, Anja, Cas, I extend my appreciation for their support and the amazing work environment. Each individual has contributed to the amazing four years and group outings I had in the TU/e.

I am grateful to the bachelor students, Casper Anjo, and Robert, for their contribution to my research and Marc and his father for proofreading my introduction and summary.

For the technical support with my setup, I must thank Hans, Martijn and Jef. The expertise they possessed in electronics, tubing, and various technical aspects played a crucial role in always reaching the perfect experimental setup. Hans with his countless number of books and connections within the TU/e was amazing. For every question, Hans could find a book or person to help you, I still cannot believe how he did it. While

younger people would use the internet, Hans preferred books and people for answers and he always succeeded. I am deeply grateful to all technicians for their support and believe their work cannot be underestimated.

I extend my appreciation to the team at Canon production printing Jasper, Helder, Herman, Louis, Hamid, Henk-Jan, and Rob for their assistance with multiple measurements and scientific expertise. A heartfelt acknowledgment is reserved for Nicolae, my main contact person at Canon, whose mentorship extended beyond the laboratory. He not only guided me professionally within the company and with my PhD but also shared memorable experiences during trips to Abu Dhabi and Edinburgh. During these trips I also met his wonderful wife, Marian. Both of them made these trips a wonderful experience where I really felt like we were a small family. Me as the son and Nicolae and Marian my amazing parents.

I also want to thank Jurgen from Covestro for the broad chemical knowledge he brought to the table. This contributed to the depth of our research and the great results we achieved with respect to the latex particles used in this thesis.

I am grateful to Ulrich and Carina from TU Graz for their expertise and provision of the paper samples, essential to my research. I can still remember the multiple discussions we had about paper samples, both online and at the TU Graz during our visit. During these discussions, they let me realize that an 'ordinary' piece of paper as we all know it, is not at all ordinary, but a complex porous media with all its challenges and complexity. Because of them I will never look at a piece of paper in the same way.

Aitor from Polymat deserves my thanks for the preparation of the Latex particles containing iron oxide. Furthermore, I want to thank Thomas Cools who helped me with the magnetic characterization of the particles.

Peter Lipman's support with MIP measurement is greatly appreciated. The measurements led to some major conclusions about the penetration behaviour of liquids in membranes, improving the knowledge of my thesis.

To all my friends and family outside the academic world, who provided me with energy during weekends and late-night drinks. These gave me energy throughout these four years. For the sport activities I have to thank the people from Korfbal club Vobako and my running friends from the VOBako running team with whom I run countless trails, half-marathons and marathons. Besides sports, I also spend a lot of time in bars and cafes with my friends, the Putze Zatlappen, my friend from KU Leuven and my friend from High school. Besides my friends, I always had my family to count on. A special thanks also goes to my brothers Jonas, Hannes and Sander who made me the person I am today. Despite our various interests, we all ended up where we belong, and for me that was doing a PhD.

Finally, my greatest appreciation goes to my Girlfriend, who stood by my side throughout this four-year period. Especially during the corona pandemic, performing research was quite difficult and I spent a lot of ours together with her. She was always listening to the endless talks about my research and helped me through some tough times. For all the support, I want to thank her. Now that my PhD is over, I hope to spend some more time with her and make some more unforgettable moments.

---

# List of publications

---

## Publications related to this thesis

**R. J. K. Nicasy**, H. P. Huinink, S. J. F. Erich & O. C. G. Adan, High-speed NMR imaging of capillary action in thin nontransparent porous media. *Phys. Rev. E* 104, 2–6 (2021).

**R. J. K. Nicasy**, H. P. Huinink, S. J. F. Erich & O. C. G. Adan, NMR Profiling of Reaction and Transport in Thin Layers: A Review. *Polym. 2022, Vol. 14, Page 798* 14, 798 (2022).

**R. J. K. Nicasy**, H. P. Huinink, S. J. F. Erich, O. C. G. Adan, N. Tomozeiu, Ultra Fast Imaging NMR method for measuring fast transport processes in thin porous media. *Magn. Reson. Imaging* 103, 61–74 (2023).

**R. J. K. Nicasy**, A. Barquero, H. P. Huinink, S. J. F. Erich, O. C. G. Adan, N. Tomozeiu, H. Mansouri & J. Scheerder, Magnetite-latex nanoparticle motion during capillary uptake in thin, porous layers studied with UFI-NMR. *Colloids Surfaces A Physicochem. Eng. Asp.* 683, 133011 (2024).

**R. J. K. Nicasy**, A. Barquero, H. P. Huinink, S. J. F. Erich, O. C. G. Adan, N. Tomozeiu, H. Mansouri & J. Scheerder, Increasing particle concentration enhances particle penetration depth but slows down liquid imbibition in thin fibrous filters. *Colloids Surfaces A Physicochem. Eng. Asp.* 684, 133146 (2024).

**R. J. K. Nicasy**, C. Waldner, S. J. F. Erich, O. C. G. Adan, U. Hirn & , H. P. Huinink, Liquid uptake in porous cellulose sheets studied with UFI-NMR: Penetration, swelling and air displacement. *Carbohydr. Polym.* 326, 121615 (2024).

**R. J. K. Nicasy**, C. Waldner, S. J. F. Erich, O. C. G. Adan, U. Hirn & , H. P. Huinink, Liquid penetration in hydrophobised cellulose based sheets. *Cellul. 2024* 1–18 (2024) doi:10.1007/S10570-024-05934-5.

## Other publications

A. Khaled, L. Ključar, S. Brand, M. Kögel, R. Aertgeerts, **R. J. K. Nicasy** & I. De Wolf, Study of GHz-SAM sensitivity to delamination in BEOL layers. *Microelectron. Reliab.* 76–77, 238–242 (2017).

A. Piovesan, **R. J. K. Nicasy**, B. Dequeker, J. Soete, C. Achille, R. Dochy, C. Parra Cabrera, R. Ameloot, P. Verboven & B. Nicolai, A. *et al.* Multiscale modelling of capillary imbibition in 3D-printed porous microfluidic channels. *Microfluid. Nanofluidics* 26, 1–15 (2022).





---

# Curriculum Vitae

---

Ruben nicasy was born on the 26<sup>th</sup> of December 1996 in Bonheiden, Belgium. In 2014 he started his carrier in science when he studied Physics at KU Leuven. After finishing a Bachelor in Physics, Ruben started a Master in Nanoscience, Nanotechnology and Nanoengineering which he graduated in 2019.

From 2019 he started his PhD project at the Eindhoven University of Technology (TU/e) in the group Transport in Permeable media at the Department of Applied Physics. The results of this PhD project are presented in this dissertation.

